Synthesis, Photo-Physical Properties and Applications of Novel Metal Nanoclusters

A dissertation submitted in partial fulfilment of requirements
for the degree of

Doctor of Philosophy

by

Priyanka Sarkar

Roll No. 186122046

Department of Chemistry
Indian Institute of Technology Guwahati
Guwahati-781039, Assam, India

JULY 2024

Statement

I do hereby declare that the work incorporated in this thesis entitled, "**Synthesis, Photo-Physical Properties, and Applications of Novel Metal Nanoclusters**" is the result of investigations carried out by me under the guidance of Prof. Kalyanasis Sahu, at the Department of Chemistry, Indian Institute of Technology Guwahati, Guwahati, Assam, India.

In keeping with the general practice of reporting scientific observations, acknowledgments have been included for works referenced from other researchers. Additionally, I affirm that this study has not been submitted, in part or full, for the purpose of obtaining any academic degree or diploma at any other institution.

Priyanka Sarkar

IIT Guwahati
April 2024

Priyanka Sarkar

Prof. Kalyanasis Sahu
Professor, Department of Chemistry
Indian Institute of Technology Guwahati
Guwahati-781039, Assam, India
http://www.iitg.ac.in/chemistry/fac/ksahu/

Phone : +91-361-2583302
E-mail : ksahu@iitg.ac.in

Certificate

This is to certify that the work included in this thesis entitled "**Synthesis, Photo-Physical Properties, and Applications of Novel Metal Nanoclusters**" by Priyanka Sarkar, Department of Chemistry, Indian Institute of Technology Guwahati has been carried out under my supervision. I further certify that this work has not been submitted to any other University or Institution in part or full for the award of any degree or diploma.

Kalyanasis Sahu

IIT Guwahati

April 2024

Kalyanasis Sahu
Thesis supervisor
Department of Chemistry
Indian Institute of Technology Guwahati
Guwahati – 781039, Assam, India

Dedicated to my parents

and my brother

Table of Contents

Acknowledgement

Undertaking this PhD has been truly a life-changing experience for me and I am deeply grateful for the invaluable contributions of all those who have played a part in bringing this thesis to fruition. Throughout this remarkable journey, numerous individuals have extended their unwavering support, guiding me with genuine care and expertise. I have tried to acknowledge each person who has contributed sincerely to this endeavour. My heartfelt thanks go out to each and every one of you for your indispensable assistance and encouragement.

I am profoundly grateful to Prof. Kalyanasis Sahu, my supervisor and mentor, for affording me the invaluable opportunity to be a part of his esteemed research group. His unwavering support, insightful suggestions, scholarly guidance, profound understanding, and constant inspiration have not only propelled me forward but also acquainted me with a field that was previously unfamiliar to me. I express my sincere gratitude to him for entrusting me with responsibilities and granting me the freedom to chart my own research path. His patience and accessibility have been exemplary, as he consistently provided invaluable insights and feedback on my thesis work, for which I am deeply thankful.

In addition to my supervisor, I extend my heartfelt gratitude to my doctoral committee members, Prof. Subhendu Sekhar Bag, Prof. A. S. Achalkumar, and Dr. Kalyan Raidongia, for their consistent engagement and invaluable feedback throughout the assessment of my research. Their insightful suggestions and constructive comments during each seminar not only broadened the scope of my research but also played a pivotal role in enhancing the quality of my thesis from diverse angles.

I wholeheartedly extend my appreciation to all my educators from Arya Vidyapeeth College (Guwahati), Assam University (Silchar), B.H College (Howly) and St. Mary’s High School (Barpeta Road) for instilling in me not only valuable knowledge but also fostering a strong foundation of ethics and principles.

I am profoundly thankful to my maa and baba, whose unwavering sacrifices, boundless love, and constant support has always empowered me to navigate my path with courage and determination as I pursue my aspirations. Additionally, I wish to extend my gratitude to my brother, Subham Sarkar, whose support transcends his role as a younger sibling, often offering guidance and assistance akin to that of an elder brother.

One of my good decisions was to start learning with one of my hard-working senior Dillip Kumar Sahu. He is the person who made me learn basic experimental works and instruments handling. I really grateful to him for guiding me in my early phase of research work and really enjoyed a lot working with his company.

Working alongside Nilanjana, Subhashree, Neha, and Tousif da has truly been a highlight of this journey. I thank them for insightful discussions, encouragement and for all the fun, we have had in this entire journey. All of them deserve the best and extreme respect for their hard work, assiduousness, and obligatory input into the overall research work. I wish all of them success in every aspect of their life.

I want to express my heartfelt gratitude to my lifelong friend and my constant source of comfort, Sanjoy Sen. He has always stood by my side, offering unwavering support whenever I needed it. He has constantly amazed me with his encouragement and support whenever I felt demotivated about my failed experiments.

I also offer my heartfelt gratitude to my dear friends Dr. Nilanjana, Priya, and Nikita for the enriching discussions and the cherished memories we've shared throughout this journey. Your unwavering support and companionship have been a source of strength from the very beginning of our knowing each other. I am deeply thankful for the moral support and the time you've generously extended whenever I needed it.

I also wish to express my sincere appreciation to Dr. Rabindranath da and Dr. Mihir da for their invaluable assistance and guidance regarding various aspects of the research whenever I sought their help.

I am also thankful to God for the friendship I share with my M.Sc buddies Rajib Ray, Dr. Samina Easmin, Priyanka Dowerah, Dr. Fillip Sarkar, and Dhanjit Deka. Thank you all for always being there to cheer me up and provide moral support whenever I feel low. Late Runumi Das and Late Arif Nawaj Khan you both will always be remembered.

I am also thankful to all the research scholars and staff of the Department of Chemistry, IIT Guwahati for their kind cooperation and support. Further, I am grateful to the Central Instrument Facility, IIT Guwahati for allowing me to access their facility for the various experiments. I am indebted to the staff of Student Affairs, Academic Affairs, and Finance sections of IIT Guwahati for being kind enough to advise and help in their respective roles.

I express gratitude towards each individual for extending their support, encouragement and remembering me in their prayers.

Priyanka Sarkar

Priyanka Sarkar

Thesis Abstract

This thesis delivers some strategic synthetic route for the production of some novel metal nanoclusters (MNCs) of silver (Ag) and copper (Cu), commonly referred to as silver nanoclusters (AgNCs) and copper nanoclusters (CuNCs). It comprises of the optical and structural characterization of these novel metal nanoclusters (MNCs), followed by exploring their applicability in optical sensing of analytes in aqueous and biological media, bio-imaging and white light emission (WLE). Although MNCs of gold (Au) has been extensively investigated, however MNCs of Ag and Cu are comparatively less explored. The high reactivity and ease of oxidation of Cu and Ag in zero-valent state challenges formation and stability of CuNCs and AgNCs, compared to extensively explored AuNCs. Thus this report primarily aims to document the synthesis of novel AgNCs and CuNCs exhibiting diverse optical characteristics.

In ***Chapter 1***, a systematic overview of the evolution of MNCs, to their identification as potential luminescent materials is discussed. This chapter also describes its distinct photo-physical characteristics, various synthesis strategies, methods for tuning its optical characteristics along with its application across diverse fields.

Chapter 2 provides a broad description of the various materials, instrumental techniques, and methodology used throughout the experiments.

In ***Chapter 3***, selective and efficient detection of Cu^{2+} and Vitamin B_{12} (VB12) is achieved using red-emitting AgNCs synthesized within dithiothreitol-reduced lysozyme (LYS) scaffold. The AgNCs features red emission at 640 nm, quantum yield of 6.1%, massive Stokes shift of 280 nm and solid-state emission. Two contrasting fluorescence (FL)-quenching mechanisms are responsible for the sensing. Cu^{2+}-induced FL quenching occurs via both static and dynamic quenching, whereas the inner filter effect and Förster resonance energy transfer are mainly responsible for VB12-induced FL quenching. A portable paper strip was fabricated using LYS-AgNCs for on-site detection of Cu^{2+} and VB12. The probe was further applied for cell-imaging and detection capability of Cu^{2+} and VB12 inside cells as well.

In ***Chapter 4***, dithiothreitol-reduced bovine serum albumin (BSA) has been employed as a stabilizing agent to produce AgNCs with dual emission: a blue emission band at 450 nm and a far-red emissive band at 680 nm, allowing selective and ratiometric detection of Cu^{2+} and IO_4^-. These two analytes display different effects on both the emission bands. IO_4^- induced a

conformational change in BSA, intensifying the blue emission band at 450 nm along with a dynamic quenching of the AgNCs' emission at 680 nm. In contrast, Cu^{2+} triggered only a metal exchange method-based quenching of the 680 nm emission with almost no effect on the BSA capping. A smartphone-based on-site detection of IO_4^- and Cu^{2+} was also achieved. This investigation will provide important insight into the one-pot synthesis of dual-emissive silver nanoclusters and the ratiometric detection mechanism of IO_4^- and Cu^{2+}.

In ***Chapter 5***, a different synthetic strategy was adopted to synthesize CuNCs via a two-step process. Non emissive copper nanoparticles (CuNPs) were firstly synthesized, followed by introduction of mercaptopropionic acid (MPA), which prompted time-controlled conversion of these CuNPs to green-emissive (G-CuNCs) and blue-emissive CuNCs (B-CuNCs). This B-CuNCs were then utilized for selective detection of Fe^{3+} and Glutathione (GSH) via fluorescence turn-off-on mechanism. The Fl turn-off mechanism by Fe^{3+} involves both static and dynamic quenching processes, whereas restoration of the Fl intensity of B-CuNCs was triggered by the GSH-induced reduction of Fe^{3+} to Fe^{2+} and subsequent release of Fe^{3+} from the surface of B-CuNCs. Further, employing B-CuNCs and G-CuNCs a white light emitting (WLE) system was also generated.

In ***Chapter 6***, two different strategy to produce AIDF based luminescent materials at room temperature was reported, from widely reported Glutathione (GSH) capped CuNCs (GSH-CuNCs) by (1) simply modifying the solvent environment of the system and (2) by introduction of Gadolinium (Gd^{3+}) ions. The synthesized GSH-CuNCs in aqueous solution displayed weak fluorescence (Fl) emission. However, introducing these GSH-CuNCs to ethanol medium led to emergence of enhanced delayed Fl emission with significant delayed lifetime component and high delayed quantum yield (QY). Further, it was observed that, introduction of Gd^{3+} to GSH-CuNCs in aqueous solution can also induce enhanced delayed Fl emission with delayed lifetime component and high delayed QY. TEM and DLS measurements ascribed the fact that both the ethanol solvent and Gd^{3+} endows controlled aggregation of GSH-CuNCs, enabling successful harvesting of triplet states and ultimately leading to AIDF phenomenon. Lastly, the AIDF phenomena harnessed from GSH-CuNCs by Gd^{3+} were successfully employed to detect Cr^{6+} ions in aqueous solution with excellent selectivity.

Chapter 7 offers a concise overview of the thesis along with some future directions of the works presented in the thesis.

List of Figures

List of Schemes

CHAPTER 1

INTRODUCTION

1.1 OVERVIEW

The word “nano” which came from greek word “nanos” meaning “dwarf” or “very small” depicts scale of one thousand millionth of a meter (10^{-9})[1]. A plethora of nanomaterials can be witnessed in nature, existing from magnetotactic bacteria employing iron oxide nanoparticles for magnetic field sensing to the mesmerizing hues found in butterfly wings, stemming from intricate nanoarchitectural interactions with light. Nanomaterials have left their mark on human history since the fourth century AD, as evidenced by the remarkable "Lycurgus Cup."[2] This ancient artifact showcases extraordinary optical properties, with its appearance shifting between red or green in transmitted or reflected light respectively **(Figure 1.1)**. Later in 1857, Michael Faraday concluded that these unusual properties as observed, were attributed to gold metallic nanoparticles[3]. He mentioned that gold at sufficiently small size scales produces such atypical colors. A similar observation of unlike optical properties of gold at small size scales from bulk was also introduced by German physicist Gustav Mie in 1908[4]. However, the idea of intentional engineering of materials at nanoscale level was later introduced by Nobel laureate Richard Feynman in a lecture, by referencing a line “There is Plenty of Room at the Bottom” in 1959[5], during the annual meeting of the American Physical Society at the California Institute of Technology. In 1974, a Japanese scientist Norio Taniguchi was the first to describe the term “Nanotechnology” encompassing the pioneering processes of fabricating materials with nanometer-level precision[6]. Since then, nanotechnology continued to benefit in almost every aspect of science- material science, natural science and engineering, information/communication technologies, medicine, agriculture and the list continues till date. Furthermore, the synergistic potential of nanomaterials and nanotechnology can substantially enhance the efficiency of nanotheranostics processes, benefiting both therapeutic and diagnostic applications[7].

Figure 1.1: Lycurgus Cup viewed (a) in reflected light (b) in transmitted light.

Till date, researchers have come across various luminescent nanomaterials like organic fluorophores, semiconductor quantum dots (QDs), carbon dots (CDs), fluorescent proteins, rare-earth nanoparticles (NPs) and metal nanoclusters (MNCs). The utilization of quantum dots (QDs) and organic fluorophores can pose harmful impact on both human health and the environment due to their inherent toxicity. Since its discovery, MNCs have become a captivating field of interest for researchers due to their unique characteristics, such as discrete energy levels akin to molecules, resulting in distinct HOMO-LUMO transitions, tunable fluorescence, outstanding photostability, and minimal toxicity[8-11]. Furthermore, due to their biocompatibility and extremely small size, MNCs find extensive applications in biological systems[12, 13]. Continuously increasing popularity in utilization of MNCs for analytical applications motivated numerous researchers to develop potential sensors employing nanoclusters and their hybrid systems[14].[15]

Metal nanoclusters represent class of nanomaterials that comprise of metal atoms in the core and organic ligands as shell surrounding the core. It has diameter in the size range less than 2 nm, analogous to Fermi wavelength of electron. This strong confinement generates discrete energy levels, inducing molecule like properties in MNCs, strong luminescence due to discrete electronic transitions, HOMO-LUMO transitions. MNCs emerged as a bridging link between isolated metal atoms and metal nanoparticles (MNPs) **(Figure 1.2)**. In bulk metals, energy gap does not exists between valence band and conduction band, permitting free movement of electrons. The comparable size of MNPs with the electron mean free path allow limited movement of electrons facilitating collective oscillation of surface electrons, that resonate with the incoming electromagnetic field, leading to generation of surface plasmon resonance (SPR) effects[16]. Unlike MNPs, MNCs display fluorescence in the visible to infrared wavelength region via electronic transitions by virtue of discrete energy levels. The unique properties of

MNCs continue to fascinate scientists since decades for potential application in diverse area of research like catalysis, environmentally hazardous chemicals sensing, optoelectronics and biomedical field. Additionally, with the advantage of long lifetime, good solubility, significant Stokes shift, tunable emissive property and favourable biocompatibility, this MNCs serve as a promising fluorescent sensors.

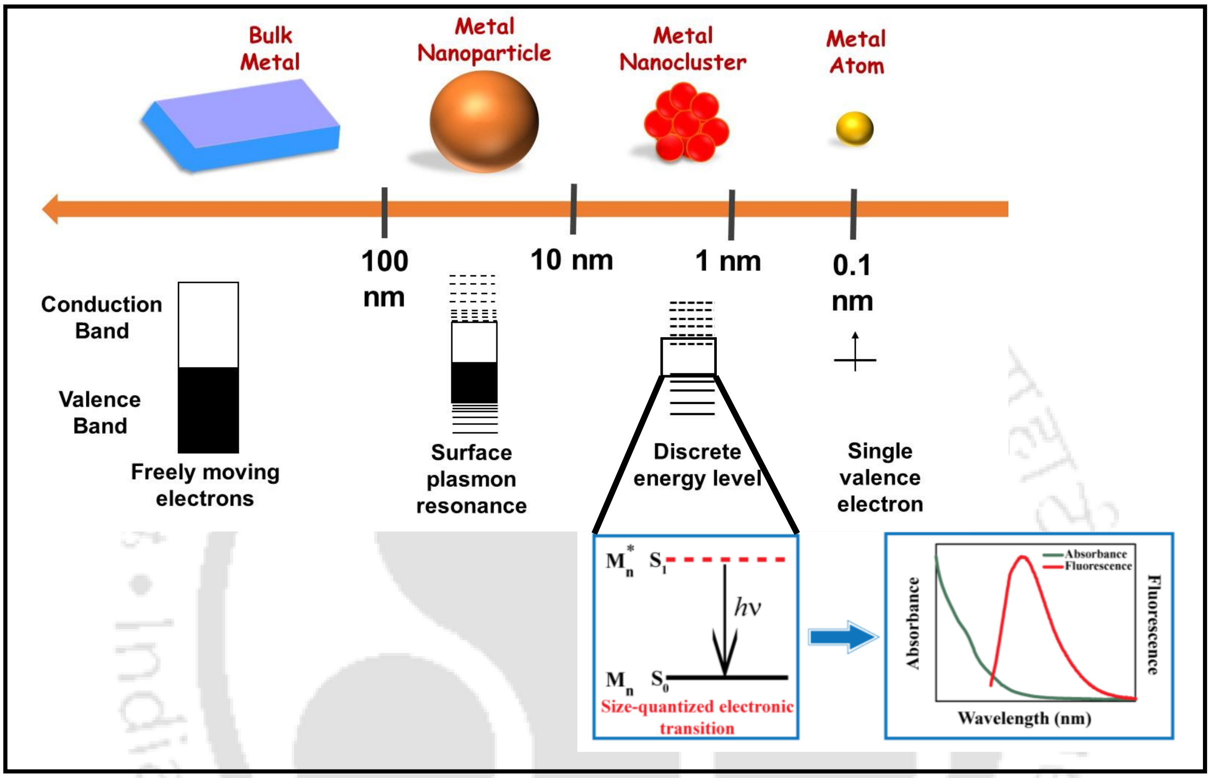

Figure 1.2: Effect of size on metals. Bulk metal and metal nanoparticle exhibit continuous band of energy levels, the limited number of atoms in metal clusters results in discrete energy levels, resulting in electronic transitions between energy levels upon interaction with light. Metal nanoparticle shows absorbance due to surface plasmon resonance, whereas metal cluster exhibits bright fluorescence due to electronic transitions.

1.2 OPTICAL PROPERTIES AND FACTORS AFFECTING OPTICAL PROPERTIES OF METAL NANOCLUSTERS.

1.2.1 Photoluminescence (PL)

After absorbing light, quantum confinement effect in MNCs prompts photon-induced electrons to jump to higher energy levels. The excited state lifetimes ranges from nanoseconds to microseconds, after that they tend to revert back to the ground state via various relaxation mechanisms. When these excited electrons get radiatively relaxed to ground state in the form of light, the phenomenon is called as photoluminescence (PL). Based on the lifetime of the excited state, PL may be classified into fluorescence, phosphorescence and delayed fluorescence **(Figure 1.3)**. Typically, fast relaxation process in the nanosecond lifetime range is classified as fluorescence (Fl). Here absorption of photons results in electronic transitions to singlet excited state followed by reverting back to the ground state via photon emission. Conversely, phosphorescence defines much slower relaxation process, which lies in the microsecond or longer lifetime range. The longer lifetime results because of the change in spin multiplicity of the excited electrons from singlet state to triplet state. Thereafter, resulting in optical radiation while returning from triplet state to ground state[17]. In case of delayed fluorescence (DF), excited electrons undergoes an ISC (Inter system crossing) process from singlet to triplet state followed by RISC (Reverse Inter system crossing) from triplet to singlet state with subsequent radiative decay from singlet to ground state. Typically, small ΔE_{ST} (usually 0.05-0.2 eV) enables an efficient $T_1 \rightarrow S_1$ up-conversion for DF by supressing non-radiative decay process[18]. This inherent PL property of MNCs have proved to be potential feature for wide range of significant applications. Below are some mentioned factors which can majorly contribute to regulate the PL property of MNCs.

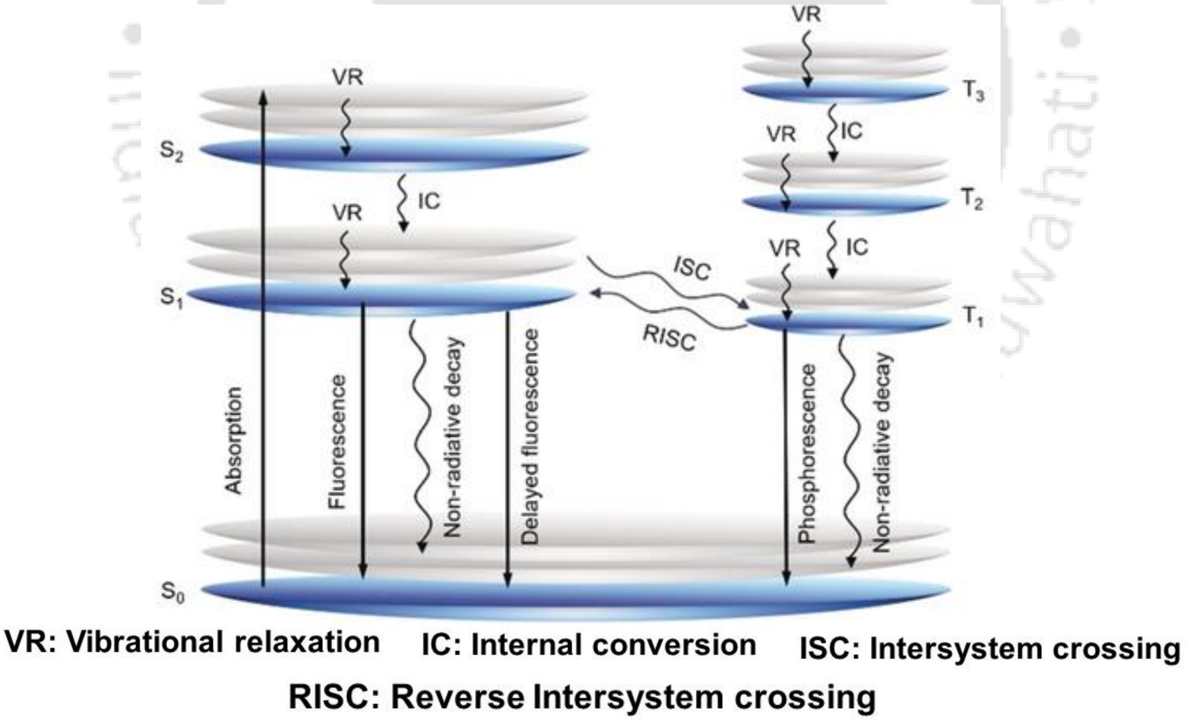

Figure 1.3 Jablonski diagram representing all possible radiative and non-radiative relaxation process. Adapted from ref [19] with permission. Copyright 2020 John Wiley and Sons.

1.2.2 Electronic structure of the core

The electronic structure of MNCs which greatly influence its PL property depends significantly on size, composition and structure of MNCs. In 2003, a literature reported synthesis of atomically precise PAMAM capped AuNCs, consisting of 8 Au atoms with bright blue luminescent property at 455 nm[20]. Following this, another literature reported synthesis of different sized AuNCs, with emission in the range of violet to visible green stemming from Au_5 to Au_{13}. The large sized AuNCs, Au_{23} and Au_{31} displayed emission in the visible red (760 nm) and NIR region (866 nm)[21] **(Figure 1.4).** This red shifting of emission intensity with the increament in size of AuNCs points towards existence of dependency of size of MNCs on the photoemission spectra. This relation between size of MNCs and photoemission spectra has been quantified by the equation-

$$\Delta E_{emission} = {E_{Fermi}}/{N^{1/3}} \tag{1}$$

Where E_{Fermi} represents Fermi level energy of the metal, $\Delta E_{emission}$ represents emission energy and N represents number of atoms[8].

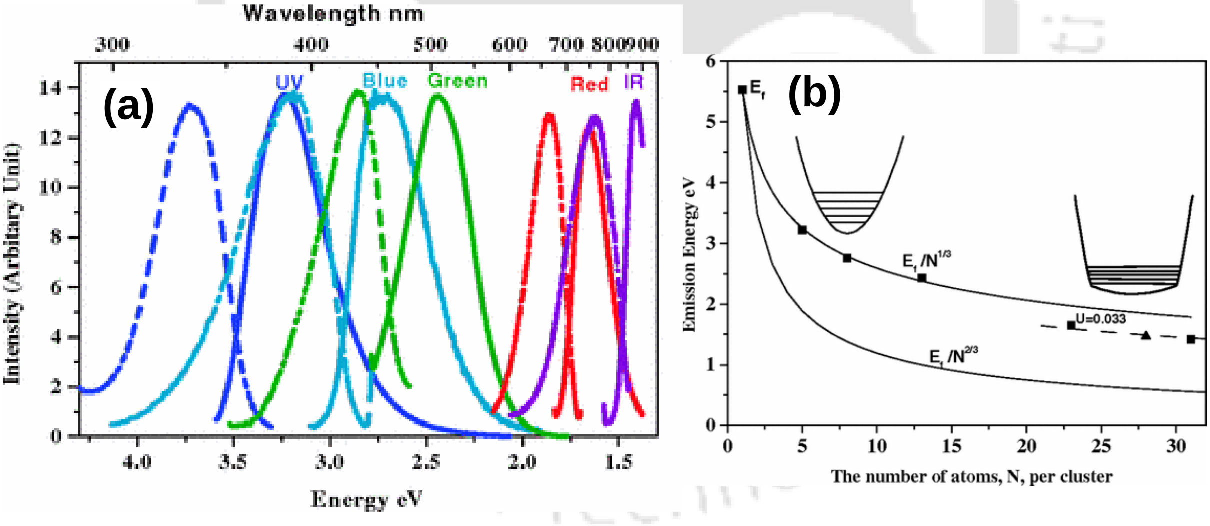

Figure 1.4 (a) Excitation (dashed) and emission (solid) spectra of Au NCs with different core sizes (b) correlation of emission energy with no. of atoms (N) and related to $E_{Fermi}/N^{1/3}$. Adapted from ref [21] with permission. Copyright 2004 American Physical Society

However, with time continuous emphasis on the study of optical properties of MNCs led to findings of certain exceptions related to photoemission from MNCs. Like, a literature reported the synthesis of Au_{25} and Ag_{25}NCs with similar structures, yet they exhibited markedly different photoluminescent characteristics due to the compositional variation **(Figure 1.5)**[22, 23]. In another literature, a mixture of Ag_7 and Ag_8NCs were produced by mercaptosuccinic acid (MSA) induced etching of AgNPs. Later, gel electrophoresis based separation showed bluish green emission (440 nm) from Ag_7NCs and red emission (650 nm) from Ag_8NCs[24]. Excess GSH (Glutathione) ligand induced digestive ripening of polydispersed mixture of CuNPs yielding red emission from $Cu_{34\text{-}32}$NCs synthesized at room temperature, while blue emission from Cu_{25}NCs synthesized at 70 °C. Below are mentioned some additional factors which contribute to influence the photophysical characteristics of MNCs[25].

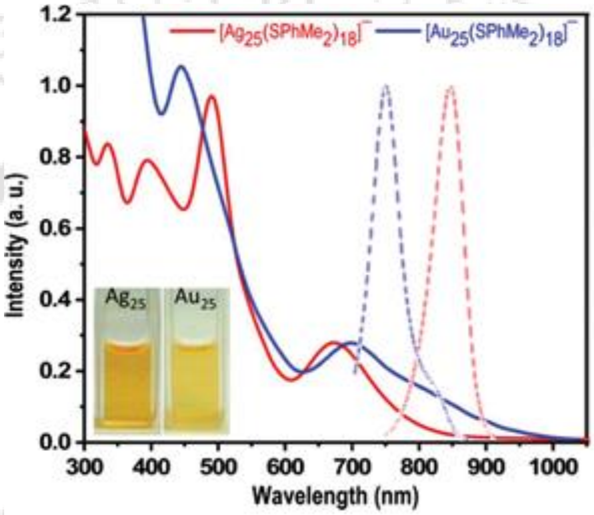

Figure 1.5 Optical absorption (solid lines) and normalized photoemission (dotted lines) spectra of $[Ag_{25}(SPhMe_2)_{18}]^-$ and $[Au_{25}(SPhMe_2)_{18}]^-$. Adapted from ref [22] with permission. Copyright 2015 American Chemical Society.

1.2.3 Effect of ligands

Ligands play significant role in tuning the PL property of MNCs by regulating its electronic structure. Both the emission wavelength and quantum yield of MNCs can be influenced either by ligand anchoring point (refers to the part that interacts with the metal core) or its body[17]. In a literature, Jin and his co-workers extensively and carefully studied the role of ligands over the photoluminescent property of Au_{25}NCs. They suggested the fact that surface ligands can regulate the PL in two ways (i) ligand to MNCs core via Au-S bonds and (ii) donation of delocalized electrons from electron rich atoms or groups present in the ligand to the MNCs core **(Figure 1.6a)**[26]. Their study support the fact that increase in electron donating ability of the ligands can enhance the emission intensity of the MNCs. Furthermore, their study also demonstrated that an increase in electropositivity (or oxidation state) of the metal core can lead to enhancement in emission intensity of MNCs **(Figure 1.6b).** The concept of the influence of ligand and the metal core on the PL property of Ag(0)NCs@Ag(I)-carboxylate complex bearing core-shell structure has also been discussed in another literature[27] . They deliberately proposed that the origin of the photoemission in Ag(I)-carboxylate AgNCs arises due to transfer of electrons from the electron-rich oxygen atoms present in the carboxylate groups of the ligands to the Ag(I) ions to the Ag-atoms in the core followed by subsequent radiative relaxation, a phenomenon referred as ligand-to-metal-metal charge transfer(LMMCT). In a literature, CuNCs capped with aromatic thiols has been synthesized. Their study revealed that increase in electron donating ability of the aromatic ligands can deliberately tune the emission colour from yellow to dark red via the influence of ligand-to-metal charge transfer and/or ligand-to-metal-metal charge transfer[28].

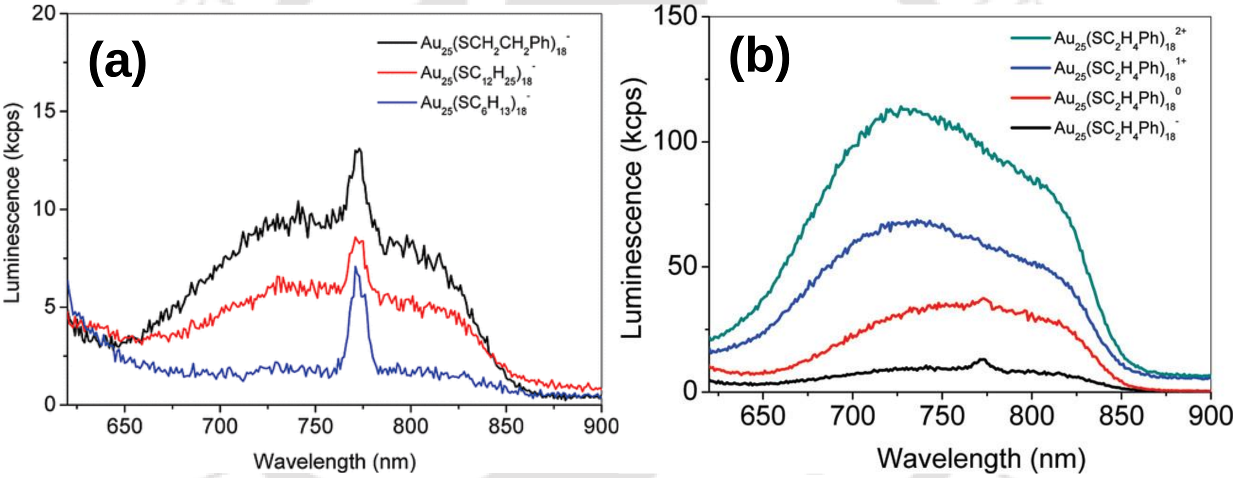

Figure 1.6 (a) Fluorescence spectra of $[Au_{25}(SR)_{18}]^-$ with different R groups ($-C_2H_4Ph$, $-C_{12}H_{25}$, and $-C_6H_{13}$) and (b) Fluorescence spectra of $[Au_{25}(SC_2H_4Ph)_{18}]^q$ (q = −1, 0, +1, +2). Adapted from ref [26] with permission. Copyright 2010 American Chemical Society.

1.2.4 Effect of alloying/doping

Introduction of a heteroatom in homometallic nanoclusters can influence its electronic structure. Precise engineering of the alloy MNCs allow alteration of its photoluminescent property. Doped $AuAg_{24}$(DMBT) exhibits 25 times enhanced emission intensity than undoped Ag_{25}NCs, however a little change has been witnessed in case of doped $PdAg_{24}$(DMBT) **(Figure 1.7a)**[29]. A literature reported doping of series of Ag atoms in rod shaped Au_{25}NCs, which unveiled that even the position of Ag atoms can influence the photophysical properties. It was observed that doping up to 12 Ag atoms (Ag_xAu_{25-x}, x = 1–12) donot alter the PL property of the rod shaped Au_{25}NCs, however, incorporation of the 13th Ag atom dramatically enhances the quantum yield (QY) by 200 times. Here, the 13th Ag atom holds the central position within the biicosahedral $Ag_{13}Au_{12}$NCs alloy, rendering modification of the HOMO-LUMO position[30]. Doping with 5 Au atoms in $Ag_{29}(BDT)_{12}(TPP)_4$NCs results in PL intensity enhancement by 26 times. Though the literature reports unalteration in the structure of the parent Ag_{29}NCs, however, increase in gradual visualization of the red luminescence was seen along with the increment in doping percentage of Au from 0-40% (**Figure 1.7b and 1.7c)**[31]. In another literature, doping of Au(I) in CuNCs led to gradual shifting in emission from 501 nm to 607 nm, visible to naked eye by variation in emission color from blue-green to yellow[32]. Moreover, with increasing mole percentage of Au(I) in CuNCs enhancement in quantum yield was also observed.

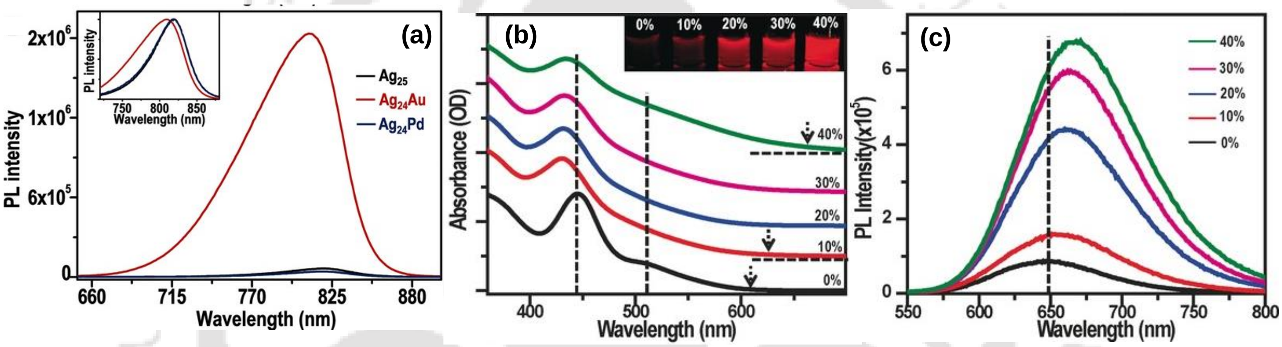

Figure 1.7 (a) photoluminescence spectra of $[Ag_{25}(SPhMe_2)_{18}]^-$, $[Ag_{24}Au(SPhMe_2)_{18}]^-$, and $[Ag_{24}Pd(SPhMe_2)_{18}]^{2-}$ clusters. The dotted lines show the peak shift relative to Ag_{25}. Adapted from ref [29] Copyright 2015 John Wiley and Sons. (b) A) UV/Vis and B) PL spectra of Ag_{29} and Au-doped Ag_{29} clusters synthesized using different amounts (mmol%) of Au. Inset: a photograph of Ag_{29} and Au-doped Ag_{29} clusters under a UV lamp (using 365 nm light). Adapted from ref [31] Copyright 2016 John Wiley and Sons.

1.2.5 Oxidation state of MNC's core

The metal core of MNCs comprises of M(0) species ,while M(I) species constitutes the surface of MNCs core (M denotes metal)[33]. Some literature demonstrated that the relative increase in the M(I) species on the surface of metal core promotes the LMCT (ligand to metal charge transfer) effect inducing enhancement in photoluminescent property of MNCs[33, 34]. Moreover, the increased oxidation state of the metal core in MNCs also provides resistance for further oxidation of MNCs by external presence of oxidants or aerial oxygen, thus providing stability to MNCs along with assisting its luminescent property[33].

1.2.6 Effect of aggregation.

Another interesting finding of the factors responsible for influencing PL properties is aggregation of the MNCs, a phenomena commonly referred as Aggregation induced emission (AIE). Until now, few literatures have explored the primary mechanisms responsible for enhancement of emission in aggregated sates of MNCs. These mechanisms include restriction of intramolecular motion (RIM), intramolecular vibration (RIV) and intramolecular rotation (RIR)[35, 36]. The core-shell structure characterised by long –S-M-S-M-S- influences the emission mechanisms in certain MNCs[37-39]. The degree of aggregation can be regulated via controlling certain factors like polarity, solvent, pH, state of MNCs (solid or liquid), application of pressure, temperature etc[25, 38, 40-42]. In a literature, Xie and coworkers comprehensively elucidated how a non-luminescent Au(I)-SG oligomers can undergo AIE phenonmenon in ethanol medium generating bright orange emission. The increment in ethanol content in the medium eventually allowed Au(I)-SG motifs to condense on Au(0) core forming a core-shell type NCs with bright emission **(Figure 1.8a and 1.8b)**[33]. Soluble Au_2Cu_6 nanoclusters exhibiting a bright red luminescence with an impressive QY of 11.7%, are formed via controlled aggregation of Cu(I)–SR complexes on Au(0)[43]. Few literatures described the influence of solvent polarity and pH of the medium to surface motif regulated AIE mechanism in CuNCs. In a literature, gradual introduction of ethanol solvent manifests regulation of the surface motifs in $Cu_{34-32}(SG)_{16-13}$ NCs resulting 36 fold increment in PL emission. The less polar solvent (ethanol) disrupts the hydration shell around solvated MNCs, allowing formation of compact aggregates of NCs due to higher intra and inter Cu(I)–Cu(I) cuprophilic interactions **(Figure 1.8c and 1.8d)**[25].

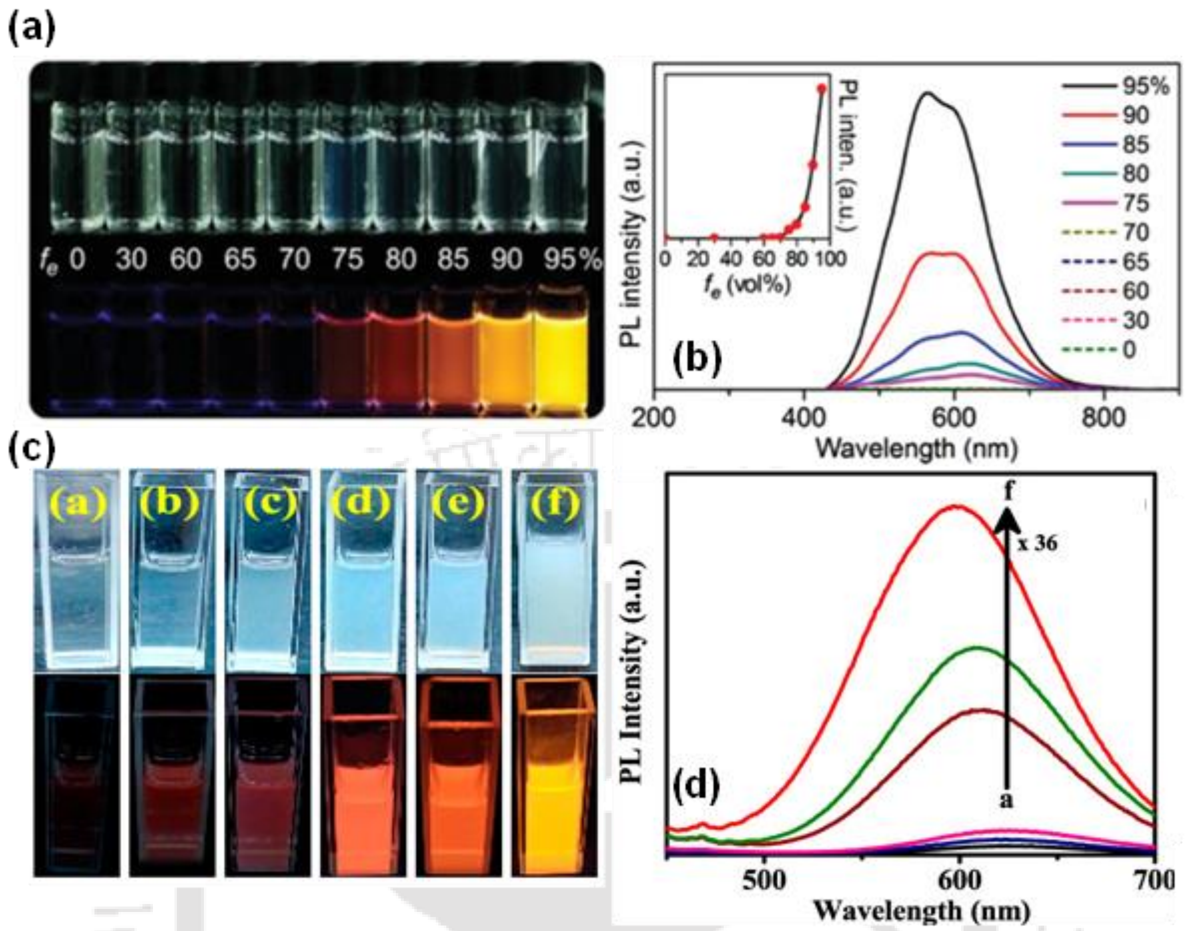

Figure 1.8 (a) Digital photos of Au(I)−thiolate complexes in mixed solvents of ethanol and water with different f_e under visible (top row) and UV (bottom row) light. (b) photo-emission spectra of Au(I)−thiolate complexes in mixed solvents with different fe. (Inset) Relationship between the luminescence intensity and fe. Adapted from ref [33] Copyright 2012 American Chemical Society. (c) Corresponding digital photographs with f_v of (a) 0%, (b) 20%, (c) 40%, (d) 60%, (e) 80%, and (f) 90% under daylight and UV (365 nm) illumination. (D) PL spectra of $Cu_{34-32}(SG)_{16-13}$. Adapted from ref [25] Copyright 2019 American Chemical Society .

Upon dispersing the water soluble AgNCs into hydrogen-bond breaking DMSO solvent, the aggregated state of AgNCs display dual photoluminescent characteristics with fluorescence-phosphorescence emission[44]. In a literature, CuNCs capped by cysteine ligands display bright red luminescence at pH 3.0, however, the luminescence weakens at pH <1.5 or > 4.0. Specifically, formation of insoluble macroscopic aggregates at pH 3.0 rendered red emission, in contrast pH <1.5 or > 4.0 promotes solubilisation of these aggregates[42]. Another literature reported an unique AIE mechanism in the solid or crystal state, involving restriction of TPP ligand dissociation-aggregation process in $Ag_{29}(BDT)_{12}(TPP)_4$ (BDT=1,3-benzenedithiol, TPP= triphenylphosphine), resulting in 13 fold increment in the PL intensity than in the solution state[45]. Additionally, lowering the temperature effectively constrained the dynamic equilibrium process of TPP dissociation and aggregation, leading to a remarkable 25-fold increase in PL intensity. Aggregation of MNCs can also be triggered by introduction of divalent (e.g., Zn^{2+}, Sn^{2+}, Pb^{2+}, Cd^{2+} etc.) or trivalent (e.g., Al^{3+}, Ce^{3+}) metal ions into the system. Introduction of an oppositely charged species into the water soluble MNCs system can trigger assembly via interaction with the terminal functional groups of the ligands that exhibit ionic nature. Such metal ion-induced AIE are often employed to modify the PL properties of MNCs by reducing the non-radiative decay channels[46]. In summary, diverse strategies can be utilized to attain AIE based mechanisms. Thus, AIE based mechanisms offers a versatile means to regulate emissions of MNCs, thereby expanding their applications in the field of biological media, sensing and light emitting diodes.

1.3 SYNTHESIS OF MNCs

Stabilizing agents play a crucial role in the synthesis process of MNCs by providing stabilization along with controlling its size, photoluminescence properties, electronic structure etc. Generally, the synthesis of MNCs is majorly achieved by following two basic approaches, namely bottom-up and top-down processes[47] **(Figure 1.9)**. Top-down synthesis approach involves large sized metal nanoparticles serving as precursors, which then undergo core reduction into ultrasmall sized MNCs in the presence of suitable ligands as etching agent. In bottom-up approach, formation of MNCs involves reduction of metal precursors by using reducing agents such as $NaBH_4$, ascorbic acid etc. in presence of suitable capping agents[48]. Employing these approaches, the PL properties, core size and surface properties of MNCs can be varied by regulating various other synthesis parameters like metal to ligand ratio, nature of reducing agent, chemical structure of capping ligands, reaction time, temperature, pH of the medium, etc[48]. Below are mentioned different methodologies followed for synthesizing stable MNCs.

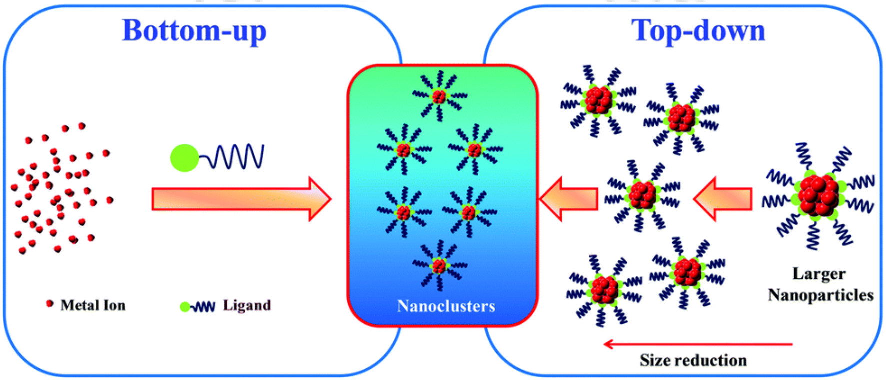

Figure 1.9 Illustration of metal nanocluster synthesis by bottom-up and top-down approaches, respectively. Adapted from ref [48] Copyright 2019 Royal Chemical Society

1.3.1 Chemical reduction

Reduction of metal precursors in presence of suitable reducing agent and capping agent commonly result in the formation of stable MNCs. Typically, reducing agents such as $NaBH_4$, ascorbic acid, and tetrakis-(hydroxymethyl)phosphonium chloride (THPC) are utilized[14]. These agents play a pivotal role in facilitating the reduction of metal ions, followed by nucleation of the zerovalent metal atoms, ensuring uniform growth and enabling the formation of monodispersed MNCs. The use of strong reducing agents like $NaBH_4$ enables effective control of reduction kinetics, however, inadequately regulated reduction kinetics may led to generation of polydispersed MNCs[49]. This reduction strategy has been applied to fabricate MNCs of Au, Ag, Cu and also alloy MNCs. A diverse array of molecules holds the potential for serving as templates in the formation of MNCs. Commonly capping ligands containing –SH, $-NH_2$ and –COOH functional groups are employed for stabilizing clusters of zerovalent metal atoms[48]. Moreover, owing to the strong binding affinity of thiol group[50] with Au, Ag, Cu, numerous thiol containing capping ligands like peptides such as glutathione (GSH), amino acids such as L-cysteine, proteins such as Bovine serum albumin (BSA), Human serum albumin (HSA) and other capping ligands such as histidine, DNA, polymers, polyelectrolytes, dendrimers are adapted to synthesize stable MNCs[51-60] Additionally, some phosphine based molecules are also adapted as an excellent capping ligands for the synthesis of MNCs[61, 62]. Furthermore, certain reports have detailed protocols for synthesizing stable and fluorescent MNCs without the use of external reducing agents. In these procedures, the reaction medium is carefully controlled, allowing the capping ligand to function both as a capping agent and a reducing agent. With the beginning of synthesis of fluorescent AuNCs (QY~6%) capped with BSA by Xie and his co-workers[51], there have been numerous reports on the synthesis of MNCs via direct reduction of metal salts. Kawaski and his co-workers illustrated how pH regulation of the reaction medium enabled formation of pepsin capped AuNCs with tunable emission from blue to red[58]. Blue emitting CuNCs with 13 and 5 Cu atoms in the core were synthesized adopting BSA as a capping ligand[63]. Xie and his co-workers reported a unique CO-reduction method for producing discrete sized AuNCs (Au_{10-12}, Au_{15}, Au_{18} and Au_{25}) capped by GSH and MPA (3-mercaptopropionic acid) via pH regulation[64]. Time-controlled synthesis of size specific AgNCs with 1-4 Ag atoms in the core, exhibiting tunable emission from blue to near-

IR was achieved utilizing DNA as a template[54]. In a literature, Chang and his co-workers demonstrated how three different isomers of mercaptobenzoic acid enabled synthesis of CuNCs with distinct physical and optical properties exhibiting distinct emission colors[60].

1.3.2 Chemical/ligand etching

Etching method is typically classified under top-down approach. The process involves etching of a larger sized MNPs to ultrasmall MNCs by incorporating excess etching agents (e.g., thiolate ligands). Some literatures documented formation of MNCs with distinct photophysical characteristics by controlled regulation of various reaction parameters during etching process like etching temperature, etching time, ratio of etchant to metal precursors. In a literature, Chen *et al*. demonstrated an etching method, where ammonia serves as an etchant for producing CuNCs with green emission from CuNPs[65]. Patra *et al*. in a report described an etching method utilizing MPA as an etchant, for producing AuNCs exhibiting time-controlled tunable emission from 590 nm to 510 nm[66]. A literature reported biomolecule (amino acids, peptides, proteins and DNA) assisted top-down approach for synthesizing Au_8NCs from Au nanocrystals (particles and rods)[67]. Excess GSH-induced temperature and time controlled core-etching of CuNPs by top-down approach has been reported for producing intense blue emissive $Cu_{25}GSH_{20}$ and red emissive $Cu_{34-32}GSH_{16-13}$ at 70°C and room temperature for 36 hr and 30 min respectively[25]. An interfacial etching method comprising of aqueous/organic interface was reported to produce smaller clusters of Ag_8 and Ag_7 from its large sized AgNPs counterparts[24]. In another literature, an interfacial etching method involving water/toluene interface and two etchants (guanine and a thiolate ligand) has been used to synthesize NIR (near infra-red) emitting AgNCs[68]. Another top-down method for synthesizing red luminescent AgNCs has been reported by core-reduction of citrate-capped AgNPs[69]. Xie’s group reported an interesting work on phase transfer based etching method for synthesis of stable, monodisperse and highly fluorescent MNCs of Au, Ag, Pt and Cu[50] **(Figure 1.10)**. Firstly, using $NaBH_4$ as a reducing agent, metal NPs protected by GSH were synthesized in water followed by transferring the MNPs to the organic phase (toluene) by adding cetyltrimethylammonium bromide (CTAB) via the electrostatic interaction between the positively charged CTA^+ and the negatively charged COO^- of GSH. In the toluene phase, mild etching occurs resulting in the formation of MNCs. Thereafter, the fluorescent MNCs can easily be transferred back to the aqueous phase upon addition of a salt, tetramethylammonium decanoate (TMAD), the anionic part of the salt D^- extracted the hydrophobic cation CTA^+ from the surface of GSH-NCs, thus bringing back the MNCs to the aqueous phase.

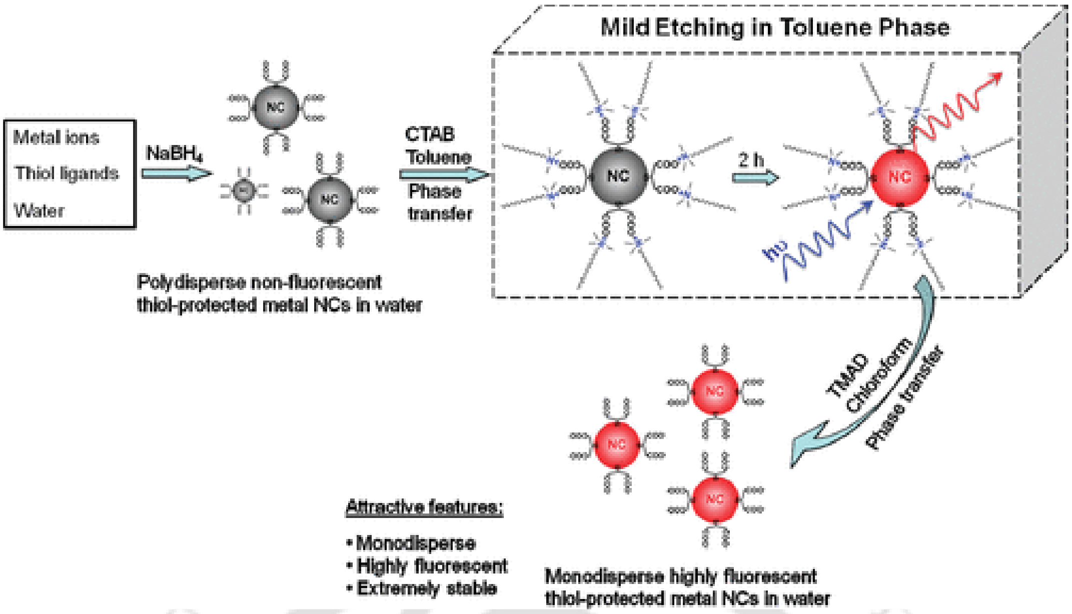

Figure 1.10: Illustration of the process to generate highly fluorescent metal NCs by a etching based phase transfer cycle (aqueous →organic (incubation)→aqueous. Adapted from ref [50] Copyright 2011 American Chemical Society

1.3.3 Ligand exchange

Ligand exchange method of synthesis allows structural and optical modification of a pre-synthesized MNCs. The nature of the newly introduced protecting ligand significantly influence the nuclearity, core size and core electronic structure of the pre-synthesized MNCs resulting in complete transformation of the photophysical properties. At 80°C, for 12 hours, chiral $Au_{38}(PET)_{24}$ NCs undergo complete ligand exchange with 4-tert-butylbenzenethiol (TBBT) ligand, resulting in the formation of entirely distinctly structured achiral $Au_{36}(TBBT)_{24}$ nanoclusters[70]. In another example, simultaneous ligand exchange and core conversion process at different reaction condition in the presence of TBBT ligand leads to the formation $Au_{20}(TBBT)_{16}$ from $Au_{25}(PET)_{18}^{-}$ and $Au_{133}(TBBT)_{52}$ from $Au_{144}(PET)_{60}$ NCs[71, 72]. Phosphine protected Au_{11} NCs undergo exchange method in the presence of GSH ligand to form $Au_{25}(GSH)_{18}$ NCs[73]. Sometime ligand exchange method provides an alternative when chemical reduction mehod fails to synthesize single sized doped MNCs, like, Some alloy NCs like $[PtAg_{28}(BDT)_{12}(TPP)_4]^{4-}$ (BDT= benzenedithiol and TPP=tri-phenylphosphine) is formed by a ligand exchange approach from $Pt_2Ag_{23}Cl_7(TPP)_{10}$ and $BDTH_2$, however, bottom-up reaction results in the formation of mixture of $[Ag_{29}(BDT)_{12}(TPP)_4]^{3-}$ and $[PtAg_{28}(BDT)_{12}(TPP)_4]^{4-}$ NCs[74]. Thus, ligand exchange approach proves to an efficient method for the synthesis of both homo and hetero-metallic NCs.

1.4 APPLICATIONS OF MNCs

The distinctive physicochemical characteristics of MNCs positions them as highly appealing probe for applications in broad range of fields like sensing, biomedical and theranoustic applications, light emitting diodes (LEDs), catalysis etc.

1.4.1 Fabrication of Light emitting devices

Based on light-emitting characteristics, MNCs can serve as light emitters in light-emitting devices, offering as an energy-efficient alternatives to traditional incandescent lamps[75, 76]. A widely adopted down-conversion LED configuration involves utilization of one or multiple light emitters for producing desirable colours or white light when exposed to blue or UV radiation[17]. Mostly commercially adopted phosphors in LEDs are based on rare-earth elements e.g. terbium, yttrium and europium[77]. Nevertheless, owing to current availability shortage and the inability to recycle poses detrimental impact on environment. On the contrary, tunable emissive and large stokes shift nature along with long lifetime offer significant advantage of utilizing MNCs as an efficient phosphor in LEDs[17]. Moreover, fabrication of white light emitting system demands the light emitting source should emit over entire visible range, which require the presence of three primary colour (blue, green and red) or two complementary colour emitting source. In a literature, where NaCl is adapted as a cost-effective and eco-friendly matrix for CuNCs, orange emitting GSH-AuNCs and blue emitting GSH-CuNCs are precisely mixed as colour-emitting phosphors with silicone resin to fabricate a prototype of white-light emitting device (WLED), bearing a CIE coordinate of (0.32, 0.31)[76]. Another literature reported elimination of utilization of rare-earth metals for fabrication of WLED, instead, combination of orange emitting GSH capped CuNCs and blue emitting polyvinylpyrrolidone CuNCs are integrated on a commercially available GaN LED chip with 370 nm excitation to fabricate a CuNCs based down-conversion WLED[78]. Another literature reports co-assembly of MPA capped AuNCs with Zn^{2+} and 2-methyl-imidazole (2M-IM) yielded AuNCs@ZIF-8 displaying orange emission. This AuNCs@ZIF-8 were the mixed with commercially available blue phosphor $BaMgAl_{10}O_{17}$:Eu (BAM) to fabricate WLED[79]**(Figure 1.11)**.

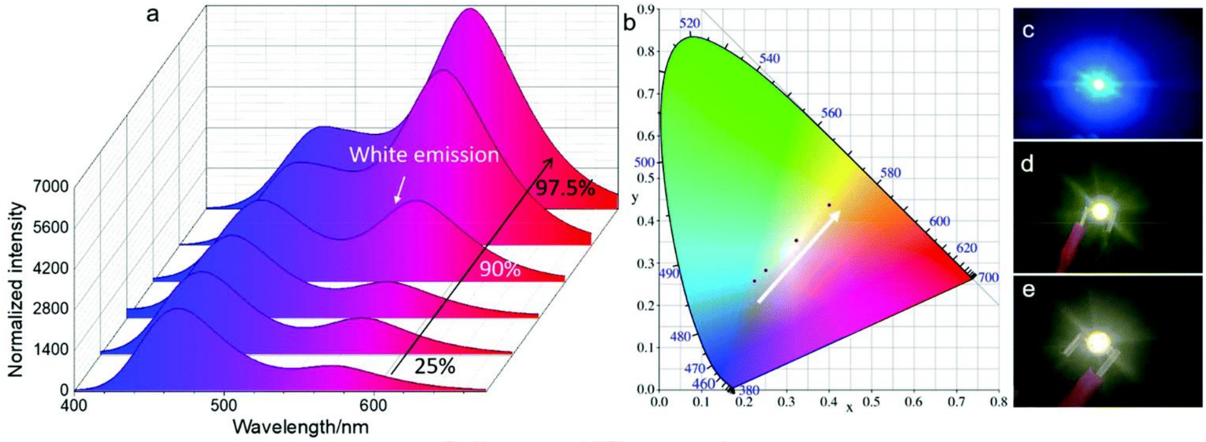

Figure 1.11 (a) PL spectra of hybrid films constituted by BAM and the increasing amount of AuNCs@ZIF-8 doping from 25.0 wt% to 97.5 wt% and (b) the corresponding CIE chromaticity coordinates (BAM : AuNCs@ZIF-8 = 1 : 3, 1 : 7, 1 : 9, 1 : 30). Optical images of LEDs fabricated by (c) BAM, (d) AuNCs@ZIF-8 and (e) 10 wt% BAM/90 wt% AuNCs@ZIF-8. Adapted from ref [79] Copyright 2021 Royal Chemical Society

1.4.2 Sensing applications

Currently, MNCs are widely used for sensing based applications[80]. Based on Fl response signals variation, sensing applications can mainly be classified as (1) on-off mode (2) on-off-on mode and (3) ratiometric mode. The “on-off” mode sensing system typically consists of a luminescent MNCs and an analyte. Here, the luminescence exhibited by MNCs gets quenched in presence of the analyte. In “on-off-on” mode based sensing, the luminescence of MNCs after getting quenched in presence of a complementary species is recovered back by the introduction of an analyte via interacting with either MNCs or the complementary species. On the contrary, the ratiometric mode of detection involves the transformation of one luminescent colour to another one in presence of an analyte. The ratiometric system either consists of mixing of two different emissive species by physical or chemical strategy or simply a single probe with dual emissive nature. Generally, in compared to the other two modes, the ratiometric detection mode offer more precise detection results. Since, the ratiometric based detection approach involves measuring Fl intensity ratio at two different wavelengths, thus factors like matrix background, larger standard deviation of Fl intensity and inefficiency of instruments does not cause interference during data determination.

1.4.2.1 Sensing of biomolecules

Precise detection of biomolecules with sensitivity and selectivity in trace levels is crucial for early stage identification and prevention of diseases. Enough researchers have proved MNCs to be an efficient luminescent probe to serve as a biosensor. A literature reported synthesis of

GSH protected AuNCs exhibiting emission at 570 nm. However introduction of lysine induces aggregation of the terminal 6-primary amino functional group on the surface of GSH-AuNCs, generating a new peak at 473 nm, while leaving the 570 nm peak unaltered, thus developing a ratiometric response signal for detection of lysine[81] **(Figure 1.12a)**. However the GSH-AuNCs also showed sensitivity towards cysteine via strong Au-S interaction, leading to emission enhancement of the 570 m peak. This sensing method allowed detection of lysine and cysteine with LOD values of 2 nM and 50 nM respectively. A DNA capped AgNCs were successfully employed for "turn-on" response signal allowing detection of acetylcholinesterase (AChE). This detection method was based on hydrolysis of acetylthiocholine (ATCh) chloride to thiocholine (TCh) in the presence of AChE. The TCh produced reacts with DNA-AgNCs via Ag-S bond formation leading to emission enhancement of DNA-AgNCs at 635 nm with prolonged incubation[82]. Chen *et al.* developed a weakly green emitting ATT (6-aza-2-thiothymin) capped AuNCs, which on addition of L-arginine led to emission enhancement due to the formation of a host-guest assembly. Later, this host-guest emissive hybrid served as a convenient and cost-effective luminescent probe for detection of arginase, which induces hydrolysis of L-arginine leading to decrement of the emission intensity **(Figure 1.12b)**. Further, incorporation of arginase activity inhibitor, L-norvaline restores the luminescence property of the hybrid system[83]. This detection system allowed detection of arginase with LOD value of 0.056 U/mL. Reactive oxygen species (ROS) represent a vital class of molecules generated during various metabolic processes and are involved in regulation of diverse array of physiological functions. Highly ROS such as peroxynitrite ($ONOO^-$), hypochlorite (OCl^-) and hydroxyl radical (.OH) results in direct oxidation of nucleic acids, lipids and proteins causing permanent damage of living cells. Thus, development of luminescent probes for determining intracellular hROS is highly demanding. In a literature, a dual emitting probe formed by self assembly of GSH-AuNCs with fluorescein isothiocyanate (FTIC) modified hyaluronic acid (HA) was synthesized for ratiometric detection of hROS. This detection method showed efficient results in imaging intracellular hROS[84].

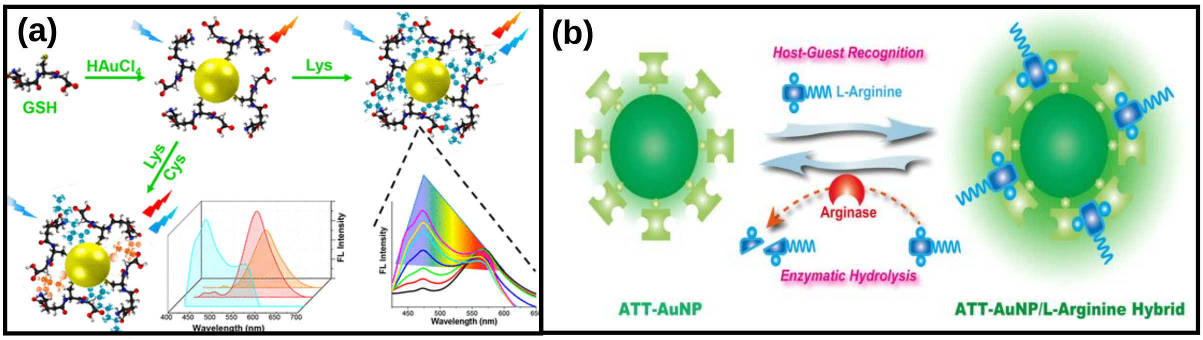

Figure 1.12 (a) Synthesis of Glutathione (GSH)-Stabilized Gold Nanoclusters (GSHAuNCs) and the Detection of Lysine or Cysteine Utilizing Pre-Prepared GSH-AuNCs Adapted from ref [81] Copyright 2017 American Chemical Society (b) ATT-AuNP-Based Fluorescent Assay of Arginase Activity. Adapted from ref [83] Copyright 2018 American Chemical Society

1.4.2.2 Sensing of hazardous molecules.

Detection of bio-hazardous molecules like nitroaromatic compounds, pesticides and herbicides, that can cause detrimental effects on human health and environment is of paramount importance. A green emitting dye, FTIC has been coated on a silica coated Au MFs (mesoflowers) termed as Au@SiO2-FTIC MFs, which is further utilized to develop a hybrid nanostructure displaying dual emission by integrating BSA capped fifteen atom silver clusters on Au@SiO2-FTIC MFs. This dual emitting probe was then employed for ratiometric detection of 2,4,6-trinitrotoluene[85]. Another literature reported an effective co-precipitation separation technique employing zinc hydroxide to remove free proteins from BSA capped AuNCs, for potential sensitive detection of H_2O_2, Hg^{2+} and certain pesticides like dithizone, 2,4-dichlorophenoxyacetic acid, paraoxonethyl and fenitrothion[86]. Picric acid, another nitroaromatic compound having more explosive power than TNT can contribute largely to groundwater and soil contamination posing serious health issues to human kind. A blue emissive copper nanocluster has shown sensitive detection towards picric acid[87]. An alloy nanocluster, BSA-$Ag_{28}Au_{10}$NCs exhibited distinct sensitivity towards a herbicide, propazine. In presence of propazine, two different peaks arising from BSA and AuAgNCs converged into a single peak, accompanied by remarkable increase in fluorescence intensity[88].

1.4.2.3 Sensing of ions

Heavy metal ions (Hg^{2+}, Cd^{2+}, Pb^{2+}) possess affinity to bind with certain cellular components such as proteins, enzymes and nucleic acids, inducing alteration of normal biological functions, eventually causing fatal diseases[89]. Recognition of these ions in complexed biological and environmental systems is crucial, which demands development of potential luminescent probe for easy identification with high sensitivity and selectivity performance. A red luminescent sensor based on l-cysteine capped CuNCs integrated on eggshell membrane (ESM), l-Cys/CuNCs@ESM exhibited sensitive response towards Hg^{2+}. Hg^{2+} induces quenching of the red luminescence, however, introduction of GSH into the quenched system can regenerate the red luminescence of l-Cys/CuNCs@ESM by interacting with Hg^{2+} **(Figure 1.13a)**[90]. Thus, the synthesized nanosystem served as an efficient sensor for both Hg^{2+} and GSH by on-off-on sensing mode. MNCs core with three distinct metal ions (Au, Ag and Cu) has been developed employing dual capping ligands BSA and thiosalicylic acid (TSA). These three distinct MNCs system displays different emissive centres at 700, 624 and 430 nm originating from TSA/BSA-AuNCs, TSA/BSA-AgNCs and TSA/BSA-CuNCs respectively. Thereafter, these MNCs successfully demonstrated sensitivity towards three different heavy metal ions Hg^{2+}, As^{3+} and Cr^{6+} via distinct mechanisms leading to Fl quenching of TSA/BSA-AuNCs, TSA/BSA-AgNCs and TSA/BSA-CuNCs respectively[89] **(Figure 1.13b)**. In another work, adopting GSH as precursor cyan emitting carbon dots (CDs) termed as GSH@CDs has been synthesized. This GSH@CDs were further utilized as stabilizing agent to fabricate dual emitting CDs stabilized CuNCs (GSH@CDs-CuNCs) with emissive centres at 450 and 750 nm. Introduction of $Cr_2O_7^{2-}$ and Cd^{2+} into this dual emitting system generates a ratiometric response by inducing a quenching effect and enhancement effect at 750 nm respectively, while unaltering the Fl intensity at 450 nm[91]. Moreover, numerous toxic anions are also extensively used in various industrial processes thereby contributing significantly to environmental contamination. A red emissive L-amino acid oxidase (LAAOx)-protected Au nanoclusters (LAAOx@AuNCs) was found to be potential sensor for cyanide ion (CN^-). The CN^- ion interacts with the Au(I) present on the surface of the Au(0) core leading to quenching of the red emission of LAAOx@AuNCs[92]. In a literature, aggregated clusters generated by Cu^{2+}-induced aggregation of 3-mercaptopropionic acid capped CuNCs displayed good sensitivity towards detection of sulphide ions (S^{2-}). Cu^{2+} triggered generation of red luminescence from aggregated clusters, which on addition of S^{2-} gets destroyed causing quenching of the generated red luminescence, thus allowing potential detection of S^{2-}[93].

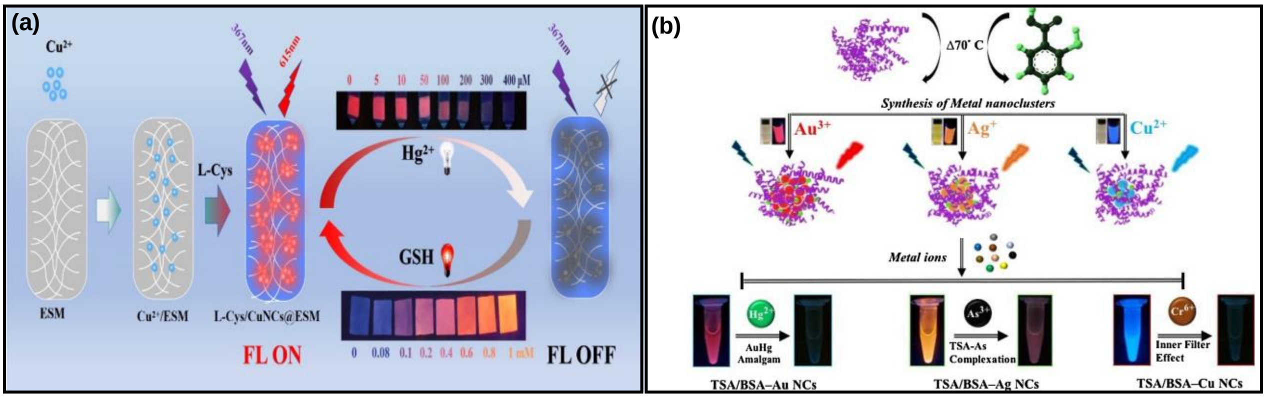

Figure 1.13 (a) Solid-phase copper nanocluster fluorescence membranes with the ESM and cysteine and their application as dual-sensing bands of Hg^{2+} and GSH Adapted from ref [90] Copyright 2023 American Chemical Society (b) synthesis of TSA/BSA–stabilized MNCs and their applications for selective detection of Hg^{2+}, As^{3+}, and Cr^{6+} ions. Adapted from ref [89] Copyright 2020 Elsevier

1.4.3 Biological applications

1.4.3.1 Antimicrobial agents

Recently, grown interest has been seen towards harnessing MNCs of Au, Ag and Cu as a potential antibacterial agents against various bacterial infections. Since decades AgNPs are well known efficient antimicrobial agents. In contrast to AgNPs, AgNCs possess higher surface-to-volume ratio and are expected to show higher efficacy towards microbial species. For example, a literature reported higher efficacy of AgNCs capped by GSH ligand against both *Escherichia coli* (Gram negative) and *Staphylococcus aureus* (Gram positive) bacteria as compared to GSH coated AgNPs[94]. Similarly, Xie group demonstrated higher efficacy of 6-mercaptohexanoic acid (MHA) capped AuNCs against Gram positive (*Staphylococcus aureus*) bacteria compared to MHA-AuNPs and Au(I)-MHA complexes. The bacteria killing efficiencies as demonstrated by MHA-AuNCs, MHA-AuNPs and Au(I)-MHA complexes are 95%, 3% and 5% respectively. For Gram negative (*Escherichia coli*) bacteria, the killing efficiencies are 96, 2 and 3% respectively by MHA-AuNCs, MHA-AuNPs and Au(I)-MHA complexes[95]. Possible mechanisms accounting for antibacterial effects of MNCs include disruption of bacterial membrane on binding, generation of ROS (Reactive oxygen species) radical, bacterial cell disruption by release of metals from MNCs.

1.4.3.2 Bio-imaging

Biomolecules like DNA, proteins, peptides, enzymes, amino acids are widely used as capping ligands to protect MNCs making them an efficient biocompatible agent. The exceptional features of MNCs like non-toxic nature, good water solubility, nanometer size range, long lifetime enables utilization of these luminescent probes as suitable bioimaging agent. Furthermore, luminescent MNCs emitting in red or NIR region offer distinct advantages over blue emissive MNCs due to the lower optical scattering of tissues and bio-molecules within this wavelength range, thereby allowing effective bio-imaging of deep tissues and thus enhancing spatial resolution of images[96]. Zhang *et al.* synthesized a transferrin (Trf) stabilized CuNCs displaying emission at 670 nm. Here, Trf not only served as a capping agent, but also assisted targeting over-expressed transferrin receptors found on specific cancerous cells, aiding targeted bio-imaging of HeLa cells[97]. AuNCs protected by BSA and conjugated with Herceptin serve as an effecient fluorescent probe, facilitating imaging and specific targeting of breast cancer cells[98].

1.4.3.3 Drug delivery

Grown interest among researchers have been seen for employing bio-functionalization strategy of MNCs in order to enhance their physicochemical properties for its applicability in biological media, which includes drug delivery, theranostics and other biomedical applications[99]. Functionalization with specific biomolecules on MNCs surface is vital for targeting biological species. The ultrasmall nanometer size range of these luminescent MNCs not only facilitates easy accumulation within targeted site but also ensures efficient renal clearance from body. Luo and co-workers developed a multifunctionalized AuNCs for live cells in vivo imaging and specific drug-delivery for anticancer treatment. A cyclic tripeptide (arginine-glycine-aspartate) (RGD) was covalently linked with BSA capped AuNCs via reaction between carboxyl groups of BSA and amino groups of the tripeptide forming RGD-BSA@AuNCs. Subsequently, the anticancer drug doxorubicin hydrochloride (DOX) was linked via disulfide bonds to amino groups of BSA in RGD-BSA@AuNCs to form DOX/ RGD-BSA@AuNCs[100]. Li *et al.* adopted a innovative drug delivery approach based on remarkable binding affinity of the antibiotic vancomycin to D-alanine-D-alanine termini. They utilized a synthetic pentapeptide (GSHaa) employing GSH as a capping agent for AuNCs and D-alanine-D-alanine for binding with vancomycin. This engineered vancomycin-integrated GSHaa-coated fluorescent AuNCs allowed precise tracking of drug loading efficiency and release process[101].

1.4.4 Catalytic applications

The escalating environmental pollution and energy scarcity have emerged as a global concern posing serious threat to human lives[102]. This issues are basically stemming due to rapid expansion of population and rise in industrial activities. With the view of attaining sustainability, scientists are constantly finding ways to harness renewable energy sources. Nowadays, introducing MNCs in photocatalysis and electrocatalysis have led to the development in attaining a greener and sustainable way to energy resources[8]. Some literatures represented MNCs as class of catalysts owing to monodisperse nature and high surface-to-volume ratio[103-105] Hu *et al.* developed a hyperstar-$Au_{25}(SR)_{18}$ nanocomposite system consisting of $Au_{25}(SR)_{18}$ encapsulated synthesized hyperstar polymer. This nanocomposite material demonstrates notable stability upto three months offering remarkable catalytic property for reduction of 4-nitrophenol[106]. Furthermore, its catalytic activity can be reused without any loss. Xie *et al.* innovatively adopted wet chemical approach to develop dendrite-like Pt/AuNCs for reduction reaction of oxygen and methanol oxidation. This method involved L-histidine and polyvinyl pyrrolidone as the structure director and dispersing agent respectively[107]. In another literature, novel CuNCs were employed as a catalyst for hydrogen evolution reaction[108].

1.5 FLUORESCENCE QUENCHING MECHANISMS

Fluorescence quenching arises from suppression of emission intensity in the presence of a specific quencher indicating potential interactions between nanoprobe and quencher might induce this phenomenon. Determining the rate of quenching is crucial in the quenching process[109]. The quenching rate constant can be determined from the linear plot obtained by plotting emission intensity ratio against the added concentration of quencher, called the Stern-Volmer (S-V) plot. This can be defined by the following equation

$$\frac{F}{F_0} = 1 + K_{sv}[Q]$$

Here, F and F_0 represents emission intensities of synthesized luminescent nanoprobe before and after addition of quencher. Q is the quencher concentration. K_{sv} is called the S-V constant.

Various mechanisms could contribute to fluorescence quenching like ground-state complex formation, Photo-induced electron transfer, Forster resonance energy transfer, Inner filter effect, anti-galvanic method, etc[110].

1.5.1 Ground-State Complexation

Interaction between the fluorophore (F) and analyte (A) can form a non-fluorescent ground state complex characterised by a distinct absorbance spectrum. Here, the emission intensity is dependent upon analyte concentration and temperature. Elevated temperatures can lead to breakdown of the complex resulting in decrease of the association constant (K_{ass}). In this quenching phenomena, the fluorescence lifetime of the nanoprobe before and after addition of the quencher remains unchanged[109] **(Figure 1.14a and 1.14b)**.

$$F + A \xrightarrow{K_{ass}} [F \cdots A]\ \text{(nonfluorescent complex)}$$

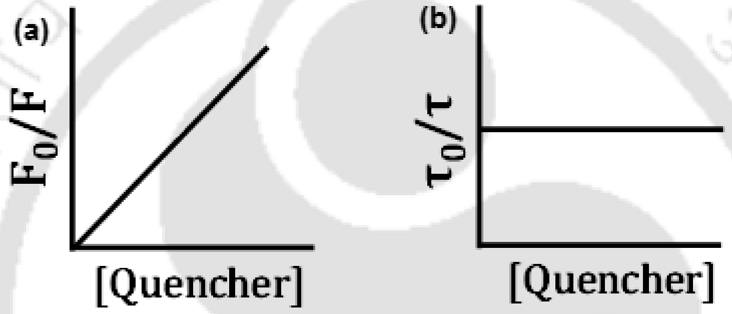

Figure 1.14. (a) The ratio of emission intensity, and (b) The ratio of average lifetime vs. quencher concentration plot.

1.5.2 Photo-Induced Electron Transfer (PET)

PET generally involves a donor (D) and an acceptor (A) forming a complex[111, 112]. MNCs in excited state often donate an electron to the ground-state acceptor molecules particularly metal ions, resulting in formation of $[D^{+}\text{-}A^{-}]$ pair as illustrated in **Figure 1.15**. Subsequently, this complex returns to the ground state through non-radiative transitions, representing a significant phenomenon for fluorescence quenching induced by various metal ions.

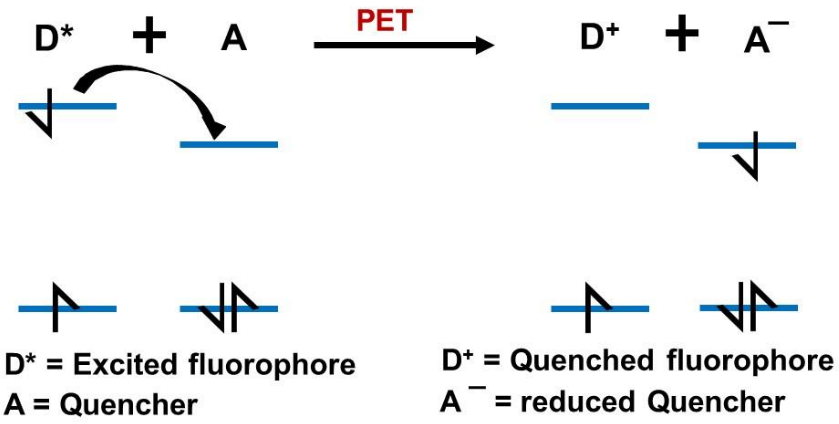

Figure 1.15. Schematic illustration of PET process.

1.5.3 Inner Filter Effect (IFE)

IFE stands as another pivotal phenomenon in spectrofluorometry, wherein the absorber or quencher interferes the emission and/or excitation energy of the nanoprobe[109, 113]. The possibilities of the spectral overlap between the absorption spectra of the quencher and the emission-excitation spectra of the fluorophore that could lead to IFE phenomenon is depicted in **Figure 1.16**

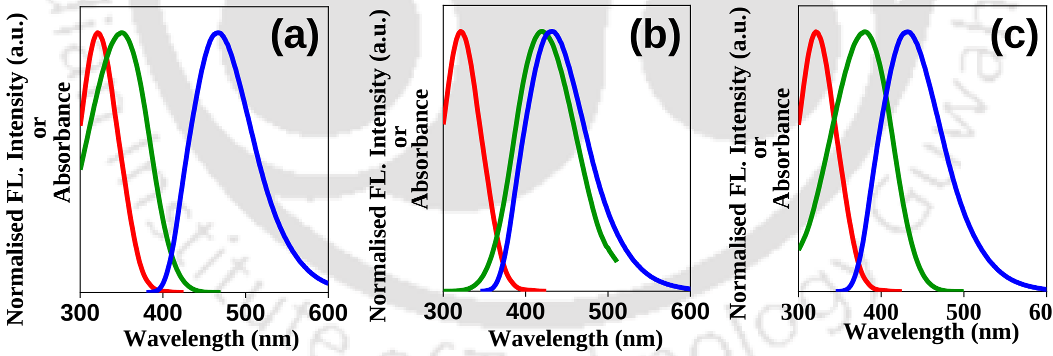

Figure 1.16. Various conditions for IFE: the overlap of the absorption spectrum of the quencher with (a) the excitation spectrum, (b) the emission spectrum and (c) both the excitation and emission spectra of the fluorophore. [red line: Excitation spectra of fluorophore, green line: Absorption spectra of quencher, and blue line: Emission spectra of fluorophore]

While IFE was initially perceived as an error in fluorescence measurement, it has evolved into a non-irradiative energy transformation model within spectroscopy. Consequently, it has been instrumental in the advancement of numerous fluorescence-based detection systems. IFE based phenomena does not require chemical interaction between the quencher and the nanoprobe. For IFE calculation following formula is used

$$\frac{F_{corrected}}{F_{observed}} = \frac{2.3dA_{ex}}{1-10^{-dA_{ex}}} 10^{gA_{em}} \frac{2.3sA_{em}}{1-10^{-sA_{em}}}$$

Here, $F_{corrected}$ and $F_{observed}$ denotes corrected emission intensity after removing the IFE and actual emission intensity. , A_{ex}, and A_{em} stands for the absorbance value of nanomaterials at the excitation wavelength and emission wavelength respectively. 'd', and 's' denotes the thickness of the cuvette and width of the excitation beam. The 'g' stands for the distance between the edges of the cuvette and the excitation beam.

1.5.4 Förster Resonance Energy Transfer (FRET)

The mechanism of FRET is outlined in **Figure 1.17**. In this process, the donor molecule (fluorophore) molecule becomes excited (D*), and upon returning to the ground state, it emits energy. This energy is absorbed by the acceptor molecule, causing it to transition to a higher energy level (A*).

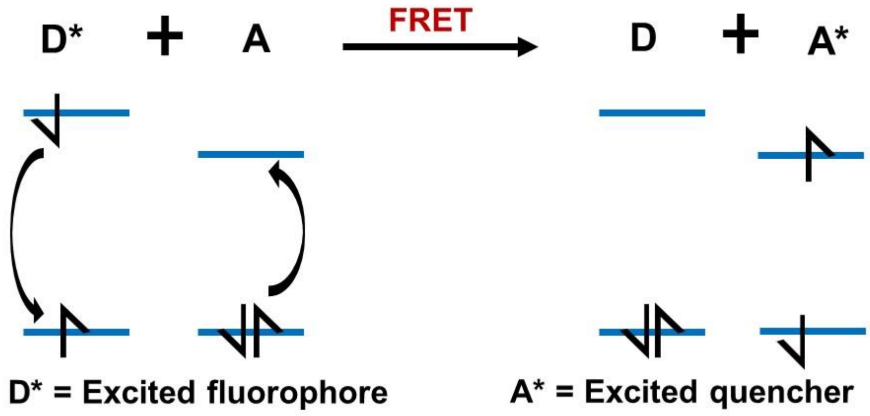

Figure 1.17. Schematic illustration of FRET process.

Three main factors which are mainly responsible for controlling the rate of FRET process are: (1) the distance between the donor-acceptor pair, (2) the dipole orientation, and (3) the extent of spectral overlap between the donor emission and acceptor absorption. The extent of spectral overlap i.e., overlapping integral (J(λ)) is calculated by the following formula[114, 115]

$$\text{Overlapped Integral J}(\lambda) = \frac{\int_0^\infty F_D(\lambda)\varepsilon(\lambda)\lambda^4 d\lambda}{\int_0^\infty F_D(\lambda)d\lambda}$$

Here, $F_D(\lambda)$ denotes corrected FL intensity of the donor in the range λ to λ + Δλ and ε(λ) represented the molar extinction coefficient of the acceptor. The effective FRET efficacies are also calculated by the following equation

$$\text{FRET Efficiency (E)} = 1 - \frac{\tau_{D-A}}{\tau_D}$$

Here, τ_D and τ_{D-A} denote the lifetimes of the MNCs in the presence and absence of a quencher.

FRET pair is also governed by the distance (r_0) between the pair of donor-acceptor and the effective Förster distance is calculated by the equations

$$\text{Förster distance } (R_0) = 8.8 \times 10^{-25}\kappa^2 n^{-4}\varphi\, J(\lambda) \quad \text{in nm}$$

$$E = \frac{1}{1 + (r_0/R_0)^6} \qquad (r_0 \text{ value in nm})$$

where κ^2 is described as the orientation factor between the donor and the transition dipole acceptor, φ is the measured quantum yield of synthesized nanomaterials, n is the refractive index of the solvent, and J(λ) stands for the overlapping integral.

1.5.5 Anti-galvanic method (AGR).

A new sensing method that can induce fluorescence quenching based on AGR phenomena has recently been reported in some literatures. This method becomes particularly relevant when the size of gold or silver particles is reduced to less than 3 nm[116]. The size reduction amplifies their reducing capability, facilitating the reduction of more reactive metal ions (such as Cu^{2+} to Cu^0). For e.g., AgNCs synthesized in a literature were reported to reduce more reactive Cu^{2+} ions based on AGR method thus enabling sensing of Cu^{2+} ions[117]. In this method, the valence state of the MNCs core also plays a significant role in determining the reactivity between MNCs and certain analytes, resulting in changes to the luminescence signal, thereby enabling the detection of these analytes[80, 118-120].

1.6 OBJECTIVE OF THE THESIS

This thesis delivers some strategic synthetic route for the production of some novel metal nanoclusters (MNCs) of silver (Ag) and copper (Cu), commonly referred to as silver nanoclusters (AgNCs) and copper nanoclusters (CuNCs). It comprises of the optical and structural characterization of these novel metal nanoclusters (MNCs), followed by exploring their applicability in optical sensing of analytes in aqueous and biological media, bioimaging and white light emission (WLE). Although MNCs of gold (Au) has been extensively investigated, however MNCs of Ag and Cu are comparatively less explored. The high reactivity and ease of oxidation of Cu and Ag in zero-valent state challenges formation and stability of CuNCs and AgNCs, compared to extensively explored AuNCs. Thus this report primarily aims to document the synthesis of novel AgNCs and CuNCs exhibiting diverse optical characteristics.

1.7 Thesis Overview

In ***Chapter 1***, a systematic overview of the evolution of MNCs, to their identification as potential luminescent materials is discussed. This chapter also describes its distinct photophysical characteristics, various synthesis strategies, methods for tuning its optical characteristics along with its application across diverse fields.

Chapter 2 provides a broad description of the various materials, instrumental techniques, and methodology used throughout the experiments.

In ***Chapter 3***, selective and efficient detection of Cu^{2+} and Vitamin B_{12} (VB12) is achieved using red-emitting AgNCs synthesized within dithiothreitol-reduced lysozyme (LYS) scaffold. A portable paper strip was fabricated using LYS-AgNCs for on-site detection of Cu^{2+} and VB12. The probe was further applied for cell-imaging, with efficient detection capability of Cu^{2+} and VB12 inside cells as well.

In ***Chapter 4***, dithiothreitol-reduced bovine serum albumin (BSA) has been employed as a stabilizing agent to produce AgNCs with a distinct photophysical characteristics. Here, a dual emissive AgNCs with a blue emission band at 450 nm and a far-red emissive band at 650 nm allowed selective and ratiometric detection of Cu^{2+} and IO_4^-. These two analytes display different effects on both the emission bands. A smartphone-based on-site detection of IO_4^- and Cu^{2+} was also achieved.

In ***Chapter 5***, a different synthetic strategy was adopted to synthesize CuNCs via a two-step process. Non emissive copper nanoparticles (CuNPs) were firstly synthesized, followed by time-controlled conversion of these CuNPs to green-emissive (G-CuNCs) and blue-emissive CuNCs (B-CuNCs). This B-CuNCs were then utilized for selective detection of Fe^{3+} and Glutathione (GSH) via fluorescence turn-off-on mechanism. Further, employing B-CuNCs and G-CuNCs a white light emitting (WLE) system was also generated.

In ***Chapter 6***, a glutathione (GSH) capped CuNCs system is reported which showed solvent (ethanol) induced distinct emission property than in aqueous environment. The synthesized GSH-CuNCs in aqueous system displayed fluorescence emission, however with increasing ethanol solvent the GSH-CuNCs displayed delayed fluorescence property. Moreover, on treating the GSH-CuNCs with gadolinium salt (Gd^{3+}) it displayed delayed fluorescence emission in aqueous medium. Both ethanol and Gd^{3+} induced aggregation of GSH-CuNCs, which in turn led to generation of delayed fluorescence propery, thus manifesting Aggregation induced delayed fluorescence (AIDF) phenonmenon. Further, these Gd^{3+} treated GSH-CuNCs were adopted to selectively detect carcinogenic Cr(VI) in aqueous system via delayed fluorescence emission property.

Chapter 7 offers a concise overview of the thesis along with some future directions of the works presented in the thesis.

REFERENCES

1. S. Bayda, M. Adeel, T. Tuccinardi, M. Cordani and F. Rizzolio, *Molecules (Basel, Switzerland)*, 2019, **25**.
2. L. Leon, E. J. Chung and C. Rinaldi, in *Nanoparticles for Biomedical Applications*, eds. E. J. Chung, L. Leon and C. Rinaldi, Elsevier, 2020, DOI: https://doi.org/10.1016/B978-0-12-816662-8.00001-1, pp. 1-4.
3. M. Faraday, *Philosophical Transactions of the Royal Society of London Series I*, 1857, **147**, 145-181.
4. G. Mie, *Annalen der Physik*, 1908, **330**, 377-445.
5. R. P. Feynman, 1960.
6. *ACS Nano*, 2015, **9**, 2215-2217.
7. X. Y. Wong, A. Sena-Torralba, R. Álvarez-Diduk, K. Muthoosamy and A. Merkoçi, *ACS Nano*, 2020, **14**, 2585-2627.
8. S. Maity, D. Bain and A. Patra, *Nanoscale*, 2019, **11**, 22685-22723.
9. L. Shang, S. Dong and G. U. Nienhaus, *Nano Today*, 2011, **6**, 401-418.
10. J. Li, J.-J. Zhu and K. Xu, *TrAC Trends in Analytical Chemistry*, 2014, **58**, 90-98.

11. L. Zhang and E. Wang, *Nano Today*, 2014, **9**, 132-157.
12. Z. Luo, K. Zheng and J. Xie, *Chemical Communications*, 2014, **50**, 5143-5155.
13. M. V. Romeo, E. López-Martínez, J. Berganza-Granda, F. Goñi-de-Cerio and A. L. Cortajarena, *Nanoscale Advances*, 2021, **3**, 1331-1341.
14. L.-Y. Chen, C.-W. Wang, Z. Yuan and H.-T. Chang, *Analytical Chemistry*, 2015, **87**, 216-229.
15. Y. Chen, M. L. Phipps, J. H. Werner, S. Chakraborty and J. S. Martinez, *Accounts of Chemical Research*, 2018, **51**, 2756-2763.
16. I. Díez and R. H. Ras, *Advanced Fluorescence Reporters in Chemistry and Biology II: Molecular Constructions, Polymers and Nanoparticles*, 2010, 307-332.
17. T. Chen, H. Lin, Y. Cao, Q. Yao and J. Xie, *Advanced Materials*, 2022, **34**, 2103918.
18. G. Li, Z.-Q. Zhu, Q. Chen and J. Li, *Organic Electronics*, 2019, **69**, 135-152.
19. Z. Zhao, H. Zhang, J. W. Y. Lam and B. Z. Tang, *Angewandte Chemie International Edition*, 2020, **59**, 9888-9907.
20. J. Zheng, J. T. Petty and R. M. Dickson, *Journal of the American Chemical Society*, 2003, **125**, 7780-7781.
21. J. Zheng, C. Zhang and R. M. Dickson, *Physical Review Letters*, 2004, **93**, 077402.
22. C. P. Joshi, M. S. Bootharaju, M. J. Alhilaly and O. M. Bakr, *Journal of the American Chemical Society*, 2015, **137**, 11578-11581.
23. K. Zheng, X. Yuan and J. Xie, *Chemical Communications*, 2017, **53**, 9697-9700.
24. T. Udaya Bhaskara Rao and T. Pradeep, *Angewandte Chemie International Edition*, 2010, **49**, 3925-3929.
25. S. Maity, D. Bain and A. Patra, *The Journal of Physical Chemistry C*, 2019, **123**, 2506-2515.
26. Z. Wu and R. Jin, *Nano Letters*, 2010, **10**, 2568-2573.
27. Y. Chen, T. Yang, H. Pan, Y. Yuan, L. Chen, M. Liu, K. Zhang, S. Zhang, P. Wu and J. Xu, *Journal of the American Chemical Society*, 2014, **136**, 1686-1689.
28. L. Ai, W. Jiang, Z. Liu, J. Liu, Y. Gao, H. Zou, Z. Wu, Z. Wang, Y. Liu, H. Zhang and B. Yang, *Nanoscale*, 2017, **9**, 12618-12627.
29. M. S. Bootharaju, C. P. Joshi, M. R. Parida, O. F. Mohammed and O. M. Bakr, *Angewandte Chemie International Edition*, 2016, **55**, 922-926.
30. S. Wang, X. Meng, A. Das, T. Li, Y. Song, T. Cao, X. Zhu, M. Zhu and R. Jin, *Angewandte Chemie International Edition*, 2014, **53**, 2376-2380.
31. G. Soldan, M. A. Aljuhani, M. S. Bootharaju, L. G. AbdulHalim, M. R. Parida, A.-H. Emwas, O. F. Mohammed and O. M. Bakr, *Angewandte Chemie International Edition*, 2016, **55**, 5749-5753.
32. J. Liu, Z. Wu, Y. Tian, Y. Li, L. Ai, T. Li, H. Zou, Y. Liu, X. Zhang, H. Zhang and B. Yang, *ACS Applied Materials & Interfaces*, 2017, **9**, 24899-24907.
33. Z. Luo, X. Yuan, Y. Yu, Q. Zhang, D. T. Leong, J. Y. Lee and J. Xie, *Journal of the American Chemical Society*, 2012, **134**, 16662-16670.
34. X. Yuan, M. I. Setyawati, D. T. Leong and J. Xie, *Nano Research*, 2014, **7**, 301-307.
35. J. Mei, N. L. C. Leung, R. T. K. Kwok, J. W. Y. Lam and B. Z. Tang, *Chemical Reviews*, 2015, **115**, 11718-11940.

36. Y. Chen, J. W. Y. Lam, R. T. K. Kwok, B. Liu and B. Z. Tang, *Materials Horizons*, 2019, **6**, 428-433.
37. Y. Yu, Z. Luo, D. M. Chevrier, D. T. Leong, P. Zhang, D.-e. Jiang and J. Xie, *Journal of the American Chemical Society*, 2014, **136**, 1246-1249.
38. N. Goswami, Q. Yao, Z. Luo, J. Li, T. Chen and J. Xie, *The Journal of Physical Chemistry Letters*, 2016, **7**, 962-975.
39. X. Dou, X. Yuan, Y. Yu, Z. Luo, Q. Yao, D. T. Leong and J. Xie, *Nanoscale*, 2014, **6**, 157-161.
40. K. Zheng, X. Yuan, K. Kuah, Z. Luo, Q. Yao, Q. Zhang and J. Xie, *Chemical Communications*, 2015, **51**, 15165-15168.
41. X. Jia, X. Yang, J. Li, D. Li and E. Wang, *Chemical Communications*, 2014, **50**, 237-239.
42. X. Su and J. Liu, *ACS Applied Materials & Interfaces*, 2017, **9**, 3902-3910.
43. X. Kang, S. Wang, Y. Song, S. Jin, G. Sun, H. Yu and M. Zhu, *Angewandte Chemie International Edition*, 2016, **55**, 3611-3614.
44. T. Yang, S. Dai, S. Yang, L. Chen, P. Liu, K. Dong, J. Zhou, Y. Chen, H. Pan, S. Zhang, J. Chen, K. Zhang, P. Wu and J. Xu, *The Journal of Physical Chemistry Letters*, 2017, **8**, 3980-3985.
45. X. Kang, S. Wang and M. Zhu, *Chemical Science*, 2018, **9**, 3062-3068.
46. Y.-e. Shi, J. Ma, A. Feng, Z. Wang and A. L. Rogach, *Aggregate*, 2021, **2**, e112.
47. Y. Lu and W. Chen, *Chemical Society Reviews*, 2012, **41**, 3594-3623.
48. D. Bain, S. Maity and A. Patra, *Physical Chemistry Chemical Physics*, 2019, **21**, 5863-5881.
49. K. Zheng, X. Yuan, N. Goswami, Q. Zhang and J. Xie, *RSC Advances*, 2014, **4**, 60581-60596.
50. X. Yuan, Z. Luo, Q. Zhang, X. Zhang, Y. Zheng, J. Y. Lee and J. Xie, *ACS Nano*, 2011, **5**, 8800-8808.
51. J. Xie, Y. Zheng and J. Y. Ying, *Journal of the American Chemical Society*, 2009, **131**, 888-889.
52. X. Yuan, B. Zhang, Z. Luo, Q. Yao, D. T. Leong, N. Yan and J. Xie, *Angewandte Chemie International Edition*, 2014, **53**, 4623-4627.
53. Y. Negishi, K. Nobusada and T. Tsukuda, *Journal of the American Chemical Society*, 2005, **127**, 5261-5270.
54. J. T. Petty, J. Zheng, N. V. Hud and R. M. Dickson, *Journal of the American Chemical Society*, 2004, **126**, 5207-5212.
55. S. Maity, D. Bain, K. Bhattacharyya, S. Das, R. Bera, B. Jana, B. Paramanik, A. Datta and A. Patra, *The Journal of Physical Chemistry C*, 2018, **122**, 13354-13362.
56. Y. Guo, X. Zhao, T. Long, M. Lin, Z. Liu and C. Huang, *RSC Advances*, 2015, **5**, 61449-61454.
57. X. Yang, M. Shi, R. Zhou, X. Chen and H. Chen, *Nanoscale*, 2011, **3**, 2596-2601.
58. H. Kawasaki, K. Hamaguchi, I. Osaka and R. Arakawa, *Advanced Functional Materials*, 2011, **21**, 3508-3515.
59. H.-H. Deng, X.-Q. Shi, F.-F. Wang, H.-P. Peng, A.-L. Liu, X.-H. Xia and W. Chen, *Chemistry of Materials*, 2017, **29**, 1362-1369.

60. Y.-J. Lin, P.-C. Chen, Z. Yuan, J.-Y. Ma and H.-T. Chang, *Chemical Communications*, 2015, **51**, 11983-11986.
61. B. K. Teo, X. Shi and H. Zhang, *Journal of the American Chemical Society*, 1992, **114**, 2743-2745.
62. P. A. Bartlett, B. Bauer and S. Singer, *Journal of the American Chemical Society*, 1978, **100**, 5085-5089.
63. N. Goswami, A. Giri, M. S. Bootharaju, P. L. Xavier, T. Pradeep and S. K. Pal, *Analytical Chemistry*, 2011, **83**, 9676-9680.
64. Y. Yu, X. Chen, Q. Yao, Y. Yu, N. Yan and J. Xie, *Chemistry of Materials*, 2013, **25**, 946-952.
65. H.-H. Deng, K.-L. Li, Q.-Q. Zhuang, H.-P. Peng, Q.-Q. Zhuang, A.-L. Liu, X.-H. Xia and W. Chen, *Nanoscale*, 2018, **10**, 6467-6473.
66. D. Bain, S. Maity, B. Paramanik and A. Patra, *ACS Sustainable Chemistry & Engineering*, 2018, **6**, 2334-2343.
67. R. Zhou, M. Shi, X. Chen, M. Wang and H. Chen, *Chemistry – A European Journal*, 2009, **15**, 4944-4951.
68. K. V. Mrudula, T. U. Bhaskara Rao and T. Pradeep, *Journal of Materials Chemistry*, 2009, **19**, 4335-4342.
69. L. Dhanalakshmi, T. Udayabhaskararao and T. Pradeep, *Chemical Communications*, 2012, **48**, 859-861.
70. C. Zeng, H. Qian, T. Li, G. Li, N. L. Rosi, B. Yoon, R. N. Barnett, R. L. Whetten, U. Landman and R. Jin, *Angewandte Chemie International Edition*, 2012, **51**, 13114-13118.
71. C. Zeng, C. Liu, Y. Chen, N. L. Rosi and R. Jin, *Journal of the American Chemical Society*, 2014, **136**, 11922-11925.
72. C. Zeng, Y. Chen, K. Kirschbaum, K. Appavoo, M. Y. Sfeir and R. Jin, *Science Advances*, 2015, **1**, e1500045.
73. Y. Shichibu, Y. Negishi, T. Tsukuda and T. Teranishi, *Journal of the American Chemical Society*, 2005, **127**, 13464-13465.
74. M. S. Bootharaju, S. M. Kozlov, Z. Cao, M. Harb, M. R. Parida, M. N. Hedhili, O. F. Mohammed, O. M. Bakr, L. Cavallo and J.-M. Basset, *Nanoscale*, 2017, **9**, 9529-9536.
75. S. Shekhar, P. Mahato, R. Yadav, S. D. Verma and S. Mukherjee, *ACS Sustainable Chemistry & Engineering*, 2022, **10**, 1379-1389.
76. M. Wang, B. Duan, Y. Li, S. Jiang, Z. Huang and W. Yang, *ACS Applied Nano Materials*, 2021, **4**, 7486-7492.
77. H. A. Höppe, *Angewandte Chemie International Edition*, 2009, **48**, 3572-3582.
78. Z. Wang, B. Chen, A. S. Susha, W. Wang, C. J. Reckmeier, R. Chen, H. Zhong and A. L. Rogach, *Advanced Science*, 2016, **3**, 1600182.
79. Y. Zhang, N. Feng, S. Zhou and X. Xin, *Nanoscale*, 2021, **13**, 4140-4150.
80. S. Qian, Z. Wang, Z. Zuo, X. Wang, Q. Wang and X. Yuan, *Coordination Chemistry Reviews*, 2022, **451**, 214268.
81. G. Liu, D.-Q. Feng, D. Hua, T. Liu, G. Qi and W. Wang, *Langmuir*, 2017, **33**, 14643-14648.

82. Y. Zhang, Y. Cai, Z. Qi, L. Lu and Y. Qian, *Analytical Chemistry*, 2013, **85**, 8455-8461.
83. H.-H. Deng, X.-Q. Shi, H.-P. Peng, Q.-Q. Zhuang, Y. Yang, A.-L. Liu, X.-H. Xia and W. Chen, *ACS Applied Materials & Interfaces*, 2018, **10**, 5358-5364.
84. X. Ran, Z. Wang, F. Pu, Z. Liu, J. Ren and X. Qu, *Chemical Communications*, 2019, **55**, 15097-15100.
85. A. Mathew, P. R. Sajanlal and T. Pradeep, *Angewandte Chemie International Edition*, 2012, **51**, 9596-9600.
86. G. Guan, S.-Y. Zhang, Y. Cai, S. Liu, M. S. Bharathi, M. Low, Y. Yu, J. Xie, Y. Zheng, Y.-W. Zhang and M.-Y. Han, *Chemical Communications*, 2014, **50**, 5703-5705.
87. W. J. Zhang, S. G. Liu, L. Han, Y. Ling, L. L. Liao, S. Mo, H. Q. Luo and N. B. Li, *Analytical Methods*, 2018, **10**, 4251-4256.
88. G. Guan, Y. Cai, S. Liu, H. Yu, S. Bai, Y. Cheng, T. Tang, M. S. Bharathi, Y.-W. Zhang and M.-Y. Han, *Chemistry – A European Journal*, 2016, **22**, 1675-1681.
89. A. Nain, Y.-T. Tseng, Y.-S. Lin, S.-C. Wei, R. P. Mandal, B. Unnikrishnan, C.-C. Huang, F.-G. Tseng and H.-T. Chang, *Sensors and Actuators B: Chemical*, 2020, **321**, 128539.
90. C. Zhang, M. Liang, C. Shao, Z. Li, X. Cao, Y. Wang, Y. Wu and S. Lu, *ACS Applied Bio Materials*, 2023, **6**, 1283-1293.
91. H. Bai, Z. Tu, Y. Liu, Q. Tai, Z. Guo and S. Liu, *Journal of Hazardous Materials*, 2020, **386**, 121654.
92. G. Zhang, Y. Qiao, T. Xu, C. Zhang, Y. Zhang, L. Shi, S. Shuang and C. Dong, *Nanoscale*, 2015, **7**, 12666-12672.
93. D. Wang, Z. Wang, X. Wang, X. Zhuang, C. Tian, F. Luan and X. Fu, *Journal of Agricultural and Food Chemistry*, 2020, **68**, 11301-11308.
94. I. Chakraborty, T. Udayabhaskararao, G. K. Deepesh and T. Pradeep, *Journal of Materials Chemistry B*, 2013, **1**, 4059-4064.
95. K. Zheng, M. I. Setyawati, D. T. Leong and J. Xie, *ACS Nano*, 2017, **11**, 6904-6910.
96. X.-W. Hua, Y.-W. Bao, J. Zeng and F.-G. Wu, *ACS Applied Materials & Interfaces*, 2019, **11**, 32647-32658.
97. T. Zhao, X.-W. He, W.-Y. Li and Y.-K. Zhang, *Journal of Materials Chemistry B*, 2015, **3**, 2388-2394.
98. Y. Wang, J. Chen and J. Irudayaraj, *ACS Nano*, 2011, **5**, 9718-9725.
99. Z. Lin, N. Goswami, T. Xue, O. J. H. Chai, H. Xu, Y. Liu, Y. Su and J. Xie, *Advanced Functional Materials*, 2021, **31**, 2105662.
100. C. Ding, Y. Xu, Y. Zhao, H. Zhong and X. Luo, *ACS Applied Materials & Interfaces*, 2018, **10**, 8947-8954.
101. Q. Li, Y. Pan, T. Chen, Y. Du, H. Ge, B. Zhang, J. Xie, H. Yu and M. Zhu, *Nanoscale*, 2018, **10**, 10166-10172.
102. L. Shang, J. Xu and G. U. Nienhaus, *Nano Today*, 2019, **28**, 100767.
103. S. K. Kailasa, S. Borse, J. R. Koduru and Z. V. P. Murthy, *Trends in Environmental Analytical Chemistry*, 2021, **32**, e00140.
104. M. Zhou, C. Zeng, Y. Chen, S. Zhao, M. Y. Sfeir, M. Zhu and R. Jin, *Nature Communications*, 2016, **7**, 13240.

105. M. Valden, X. Lai and D. W. Goodman, *Science*, 1998, **281**, 1647-1650.
106. D. Hu, S. Jin, Y. Shi, X. Wang, R. W. Graff, W. Liu, M. Zhu and H. Gao, *Nanoscale*, 2017, **9**, 3629-3636.
107. X.-W. Xie, J.-J. Lv, L. Liu, A.-J. Wang, J.-J. Feng and Q.-Q. Xu, *International Journal of Hydrogen Energy*, 2017, **42**, 2104-2115.
108. B. Eren, D. Zherebetskyy, L. L. Patera, C. H. Wu, H. Bluhm, C. Africh, L.-W. Wang, G. A. Somorjai and M. Salmeron, *Science*, 2016, **351**, 475-478.
109. in *Principles of Fluorescence Spectroscopy*, ed. J. R. Lakowicz, Springer US, Boston, MA, 2006, DOI: 10.1007/978-0-387-46312-4_2, pp. 27-61.
110. L. K. Fraiji, D. M. Hayes and T. C. Werner, *Journal of Chemical Education*, 1992, **69**, 424-428.
111. M. S. Meaney and V. L. McGuffin, *Analytica Chimica Acta*, 2008, **610**, 57-67.
112. B. Valeur and M. N. Berberan-Santos, *Molecular Fluorescence: Principles and Applications*, Wiley, 2012.
113. S. Chen, Y.-L. Yu and J.-H. Wang, *Analytica Chimica Acta*, 2018, **999**, 13-26.
114. X. Sun, Y. Wang and Y. Lei, *Chemical Society Reviews*, 2015, **44**, 8019-8061.
115. S. W. Thomas, G. D. Joly and T. M. Swager, *Chemical Reviews*, 2007, **107**, 1339-1386.
116. Z. Wu, *Angewandte Chemie*, 2012, **12**, 2988-2992.
117. S. Wang, X. Meng, Y. Feng, H. Sheng and M. Zhu, *RSC Advances*, 2014, **4**, 9680-9683.
118. Z. Gan, N. Xia and Z. Wu, *Accounts of Chemical Research*, 2018, **51**, 2774-2783.
119. X. Yuan, X. Dou, K. Zheng and J. Xie, *Particle & Particle Systems Characterization*, 2015, **32**, 613-629.
120. Y. Wang, L. Liu, L. Gong, Y. Chen and J. Liu, *The Journal of Physical Chemistry Letters*, 2018, **9**, 557-562.

CHAPTER 2

Materials, Methods and Instrumentation

[This page was intentionally left blank]

2.1 Overview

In this chapter, we have thoroughly focused on the synthesis strategy followed and techniques used for the preparation of Metal nanoclusters (MNCs). Additionally, the instrumentation specifications for characterizing the nano-fluorescent MNCs are elaborately described. The surface, morphological and structure analysis are performed by transmission electron microscope (TEM), X-ray photoelectron spectroscopy (XPS), Fourier transformed infrared spectroscopy (FTIR), and Matrix-assisted laser desorption/ionization time-of-flight mass spectrometry (MALDI−TOF−MS). For spectrofluorometric characterization, UV-visible absorption (UV-vis), steady-state fluorescence, time-correlated single photon counting (TCSPC) are used. Lastly, the confocal laser scanning microscope (CLSM) is used for biological purpose.

2.2 Materials and Synthetic Procedures.

Silver nitrate ($AgNO_3$), lysozyme (LYS), bovine serum Albumin (BSA), dithiothreitol (DTT), sinapinic acid, PBS tablet, vitamin B12, vitamin B1, vitamin B3, vitamin B5, vitamin B6, vitamin B7, vitamin B9, ascorbic acid (AA), mercaptopropionic acid (MPA), Cysteine (Cys), Tyrosine (Tyr), Phenylalanine (Phe), Alanine (Ala), Glycine (Gly), Glutathione (GSH), Lysine (Lys), Histidine (His) were purchased from Sigma-Aldrich Chemicals. Sodium hydroxide and Metal salts (Pb^{2+}, Fe^{3+}, Cu^{2+}, Ni^{2+}, Zn^{2+}, Cr^{3+}, Cd^{2+}, Al^{3+}, Mg^{2+}, Hg^{2+}, Fe^{2+}, Ag^{+}, Mn^{2+}, Co^{2+}) and anions (F^-, I^-, HPO_4^{2-}, CN^-, Cl^-, NO_2^-, Br^-, $P_2O_7^{4-}$, S^{2-}, PO_4^{3-}, H_2O_2, ClO^-,ClO_4^- ClO_3^-, NO_3^-) and solvents (absolute ethanol) were purchased from Merck and used without any kind of purification. The aqueous solution was prepared using Milli-Q deionized water (18.2 MΩ).

2.2.1 Synthesis of LYS-AgNCs.

For ***chapter 3***, Synthesis of LYS-AgNCs was carried out under optimized conditions (discussed later) by adding 100 μl 0.1M aqueous $AgNO_3$ solution to 2 mL 15mg/mL lysozyme (LYS) solution at 37°C under vigorous stirring condition. After 5 min, 150 μl 1M NaOH was added to the reaction mixture to maintain the pH of the solution at 11.8, followed by the addition of 500 μl 16.2 mM dithiothreitol (DTT) solution after 2 min. The mixture was incubated for 44 h at 37 °C under constant stirring. The color of the solution appeared light orangish, which showed bright red emission under a 365 nm UV lamp.

2.2.2 Synthesis of BSA-AgNCs.

For ***chapter 4***, In a 10 mL round bottom flask containing 2.5 mL BSA solution (20mg/mL), 100 μL of 0.1 M AgNO3 solution was added at 37 °C. After 5 min of stirring, 100 μL of 1 M NaOH was added, followed by the addition of 500 μL of 10 mM DTT (final solution concentration was 1.56 mM) solution after 2 min. The stirring condition was continued for 21 hr at 37 °C. The final solution displayed bright red luminescence under a 365 nm UV lamp.

2.2.3 Synthesis procedure for luminescent CuNCs with two different emission from non-luminescent CuNPs system.

For ***chapter 5,*** A reported method was adapted for synthesis of non-luminescent CuNPs [1]. Briefly, AA (0.1761 g) was dissolved in water (10 mL) to form a clear solution. Then a $Cu(NO_3)_2$ aqueous solution (0.1 M, 1 mL) was added dropwise into the AA solution under vigorous stirring. The reaction mixture was stirred for 1 h at room temperature in a closed round bottom flask (RB). The resulting solution was non-luminescent under UV-lamp.

For synthesis of CuNCs with two different emission, to 4 mL of the as-prepared CuNPs solution, 200 µL of 0.11 M MPA is added and left under a continuous stirring condition in a closed RB at room temperature. The progress of the reaction was monitored periodically by recording FL spectra. The addition of MPA to the CuNPs system led to a generation of precipitation. So the mixture was centrifuged at 12000 rpm for 10 min. The resulting supernatant showed bright green emission and blue emission at 2h and 43h, respectively, after adding MPA, while the precipitate was found to be non-emissive.

For fabrication of white light emission, GSH-AuNCs was also synthesized according to a previously reported procedure [2]. For the synthesis, aqueous solutions of $HAuCl_4$ (20 mM, 0.50 mL) and GSH (100 mM, 0.15 mL) were mixed with 4.35 mL water. The reaction mixture was heated to 70 °C under gentle stirring for 24 h. Strong orange emitting GSH-AuNCs were formed.

2.2.4 Synthesis of GSH-CuNCs

For ***chapter 6,*** A simple synthesis procedure is followed, where, 500 μL of 10 mM $Cu(NO_3)_2$ is firstly added to 2 mL of 40 mM GSH solution at room temperature under stirring condition. After 5 min 100 μL of 1 M NaOH solution is added followed by incubating the reaction mixture under stirring condition for 1 hr. The resulting clear solution mixture is utilized for various experimental analysis.

For preparing varying volume fraction of ethanol, maintaining a constant volume of the resulting solution of 2500 μL and keeping sample volume constant at 250 μL we varied volume of water and solvent for attaining specific volume fraction (f_d) of ethanol solvent in water.

For Gd^{3+}-GSH-CuNCs synthesis, to the synthesized GSH-CuNCs, we added 100 μL of 40 mM $Gd(NO_3)_3.6H_2O$ solution followed by stirring the mixture for 10 minutes. The resulting solution appeared turbid in nature. For obtaining optimized concentration of Gd^{3+} required for maximum delayed emission from GSH-CuNCs, we prepared different stock concentration (5 , 10 , 20, 30 and 40 mM) of $Gd(NO_3)_3.6H_2O$ solution and added 100 μL of it separately to GSH-CuNCs solution followed by measuring the delayed emission spectra of respective resulting solution mixture.

2.3 Biological Analysis

In ***Chapter 3,*** for Cytotoxicity of LYS-AgNCs was studied on HeLa cells by MTT assay. Cells were seeded in a 96-well plate at a density of 5×10^3 cells/well. After 48 h of treatment with increasing concentrations of the probe (2-40 μg/mL), 0.5 mg/ml of MTT in DMEM was added to each well and incubated for 1.5h. Thereafter, 150 μl DMSO was added to each well. Absorbance was measured at 570 nm for dissolved formazon crystals and at 630 nm as reference. Thereafter, cell viability was calculated as shown.

$$Cell\ viability\ (\%) = \frac{(abs570 - abs630)\ Sample}{(abs570 - abs630)\ Control} \times 100$$

Note: The concentration of LYS-AgNCs calculated here is based on the amount of Ag present in the solution, excluding lysozyme, NaOH and DTT. The amount of Ag is calculated from the initial Ag salt taken, considering the full conversion of the salt to LYS-AgNCs.

In vitro uptake study of LYS-AgNCs

HeLa cells were seeded in glass bottom confocal plates at a density of 1×10^5 cells per plate and allowed to attach for 24 h in a humidified incubator (37˚C, 5% CO_2). In order to study the cellular uptake of LYS-AgNCs and the quenching behaviour of Cu^{2+} and VB12, the cells were treated with 40 μg/mL of LYS-AgNCs, followed by the treatment with 63 μM of Cu^{2+} and 54 μM of VB12 for 7 h. Thereafter, the cells were washed thrice with PBS to remove residual compounds, fixed using 4% formaldehyde and visualized under a confocal laser scanning microscope (Zeiss LSM 880) with an excitation laser source of 405 nm.

2.4 SENSING STUDY

2.4.1 Fluorescence Sensing of VB12 and Cu^{2+} for *chapter 3*.

In order to explore the potential application of the synthesized LYS-AgNCs, their interaction with a large number of metal ions was examined in water. Before proceeding, 2mL of the as-prepared LYS-AgNCs was mixed with 1 mL of Milli-Q water. After that, 2.5mL of this diluted LYS-AgNCs is treated with 50 μM of various common metal ions (Cr^{3+}, Mg^{2+}, Fe^{2+}, Cd^{2+}, Co^{2+},Fe^{3+}, Hg^{2+}, Cu^{2+}, Ni^{2+}, Zn^{2+}, Pb^{2+}) and the Fl spectra of the resulting solutions were recorded after 3 min incubation time. A substantial quenching of emission intensity was noted in the case of Cu^{2+}. For spectrofluorometric titration, incremental amounts of Cu^{2+} (6 -66 μM) were added to 2.5 mL of diluted LYS-AgNCs, and fluorescence spectra were recorded at room temperature after 3min of incubation time at an excitation wavelength of 360 nm.

For VB12 sensing, 2mL of the as-prepared LYS-AgNCs was mixed with 1 mL of PBS solution (pH 7.4, 10 mM). For fluorometric detection of VB12, 2.5 mL of this diluted LYS-AgNCs in PBS was thoroughly mixed with different concentrations of VB12 solutions (6-60 μM), and the fluorescence spectra were monitored at an excitation wavelength of 360 nm. The emission spectra were recorded at room temperature, allowing 1 min incubation time after each titration. Fl spectra were also recorded with various other vitamins (50 μM) like vitamin B12, vitamin B1, vitamin B3, vitamin B5, vitamin B6, vitamin B7, vitamin B9 in the same experimental conditions for selectivity study.

2.4.2 Sensing procedure of Cu^{2+} and IO_4^-, by synthesized AgNCs for *chapter 4*.

2 mL of the synthesized AgNCs was diluted with 1 mL of Milli-Q water. For the selectivity study, 2.5 mL of this diluted solution was treated with 30 μM (stock solution of 5 mM prepared in Milli-Q water) of various cations like (Cu^{2+}, Pb^{2+}, Fe^{3+}, Ni^{2+}, Zn^{2+}, Cr^{3+}, Cd^{2+}, Al^{3+}, Mg^{2+}, Hg^{2+}, Fe^{2+}, Co^{2+}, Ag^{+}, Mn^{2+}) and 160 μM (stock solution of 10 mM prepared in Milli-Q water) of various anions like (IO_4^-, F$^-$, I$^-$, Br$^-$, Cl$^-$, CN$^-$, S^{2-}, HPO_4^-, NO_2^-, $P_2O_7^{4-}$, PO_4^{3-}, H_2O_2, ClO$^-$, ClO_4^-, NO_3^-, ClO_3^-) followed by recording Fl spectra of the resulting solution at 360 nm excitation wavelength, after 4 min and 30 min of incubation time respectively. A substantial ratiometric change in emission intensity was noted in the case of IO_4^- and Cu^{2+}. For

spectrofluorometric titration, incremental amounts of IO_4^- (from 0 to 160 μM) and Cu^{2+} (from 0 to 40 μM) were added separately to 2.5 mL of diluted AgNCs solution. Fl spectra was recorded after 30 min and 4 min of incubation time for IO_4^- and Cu^{2+} respectively at an excitation wavelength of 360 nm. Moreover, selectivity study of AgNCs by adding various other anions (160 μM) in presence of IO_4^- (160 µM) and selectivity study of AgNCs by adding various other cations (30 μM) in presence of Cu^{2+} (30 μM) was also conducted in 2.5 mL of diluted AgNCs solution.

2.4.3 Sensing of Fe^{3+} and Glutathione (GSH) by B-CuNCs in *chapter 5*.

In order to explore the potential application of the synthesized B-CuNCs, their interaction with a large number of metal ions was examined in water. Before proceeding, 20 *uL* of the as-prepared B-CuNCs was mixed with 1.98 mL of Milli-Q water. The diluted B-CuNC solution was treated with 150 μM of various common metal ions (Cr^{3+}, Mg^{2+}, Fe^{2+}, Cd^{2+}, Co^{2+}, Fe^{3+}, Hg^{2+}, Cu^{2+}, Ni^{2+}, Zn^{2+}, Pb^{2+}) and the Fl spectra of the resulting solutions were recorded after 1 min incubation time. A substantial quenching of emission intensity was noted in the case of Fe^{3+}. For spectrofluorometric titration, incremental amounts of Fe^{3+} (10 -200 μM) were added to diluted B-CuNCs, and fluorescence spectra were recorded at room temperature after 1min of incubation time at an excitation wavelength of 370 nm.

Further, in order to acquire Fl based turn off-on detection platform, 200 μM of Fe^{3+} was added to above mentioned diluted B-CuNCs (denoted as B-CuNCs-Fe^{3+}) followed by adding 300 µM of different amino acids (Cysteine (Cys), Tyrosine (Tyr), Phenylalanine (Phe), Alanine (Ala), Glycine (Gly), Glutathione (GSH), Histidine (His), Lysine (Lys)) and the Fl spectra of the resulting solutions were recorded after 6min of incubation time. The quenched emission intensity of B-CuNCs-Fe^{3+} was found to be recovered significantly only in case of GSH. For spectrofluorometric recovery titration, incremental amounts of GSH (25 μM-300 µM) were added to B-CuNCs-Fe^{3+}, and fluorescence spectra were recorded at room temperature after 6min of incubation time at an excitation wavelength of 370nm.

2.4.4 Sensing of Cr^{6+} by Gd^{3+}-GSH-CuNCs for *chapter 6*.

In order to explore the potential application of the synthesized Gd^{3+}-GSH-CuNCs, their interaction with a large number of metal ions was examined in water. Before proceeding, 1mL of the as-prepared Gd^{3+}-GSH-CuNCs was mixed with 1 mL of Milli-Q water, followed by treating the solution mixture with 50 µM of various common metal ions (Cr^{3+}, Mg^{2+}, Fe^{2+}, Cd^{2+}, Co^{2+},Fe^{3+}, Cu^{2+}, Ni^{2+}, Zn^{2+}, Pb^{2+}, Cr^{6+}) and the delayed emission spectra of the resulting solutions were recorded with a delay time of 50 μs. A substantial quenching of delayed emission intensity was noted in the case of Cr^{6+}. For titration, incremental amounts of Cr^{6+} (6 -62 μM) were added to 2 mL of diluted Gd^{3+}-GSH-CuNCs, and delayed emission spectra were recorded at room temperature with a delay time of 50 µs at an excitation wavelength of 360 nm.

2.5 INSTRUMENTATION

2.5.1 UV-visible spectroscopy

UV-absorption spectroscopy is one of most beneficial spectroscopic method which can provides valuable evidence about the electronic transition of various functional moieties. During all the experiments, UV-Vis spectra were recorded in Perkin-Elmer Lamda-750 spectrophotometers. The instrument consists of tungsten, deuterium, halogen light source, high sensitivity R928 PMT and double holographic grating monochromator.

2.5.2 Steady-state fluorescence

Jobin Yvon Fluoromax4 is used for recording all the fluorescence spectra of all the synthesized samples. Here is, the high-pressure 150 W xenon (ozone-free) arc lamp is used as a light source. The emission signal is collected by placing the cuvette at a 90° angle with respect to the incident beam and the emitted signal is identified through a monochromator by an R928P photomultiplier (PMT). The bandwidth of the monochromator during the excitation and emission signals was 5 nm.

Delayed photoluminescent emission spectra and time-resolved delayed photoluminescence decay spectra were acquired in Horiba Jobin Yvon Fluoromax 4P. Parameters for acquisition of delayed photoluminescence emission spectra and decay spectra were set as follows: time per flash= 61 ms; sample window =200 μs; delay after flash = 50 μs; flash count = 100.

2.5.3 Quantum Yield measurement

Quantum yield (QY) can be described as the ratio of the number of emitted photons and the number of absorbed photons.

$$\phi_f = \frac{\text{Number of photons emitted}}{\text{Number of photons absorbed}}$$

QY of the synthesized nano-fluorescent material was taken in a relative manner with the following formula.

$$\text{QY (Sample)} = \frac{I}{I_R} \times \frac{A_R}{A} \times \frac{\eta^2}{\eta_R^2} \times QY_R \qquad \ldots\ldots\ldots\ldots(1)$$

Here QY (sample) is the calculated quantum yield of synthesized material. I and I_R are integrated emission intensities of metal nanoclusters (MNCs) and the references, respectively. η is the refractive index of the solvent used. A_R and A is the optical density at the excitation wavelength of the reference and MNCs respectively. QY_R is the reference quantum yield. While measuring the QY, the absorbance was always kept below 0.1 at the excitation wavelength.

For measuring fluorescence QY in ***Chapter 3, 4, 5 and 6*** Quinine sulfate was used as a reference with QY of 54.4% in 0.1 M H_2SO_4 and for measuring delayed fluorescence QY in ***chapter*** *6*, bis[2-(4,6- difluorophenyl)pyridinato-C2 ,N]- (picolinato)iridium(III), commonly known as FIRPIC, in acetonitrile solution was used as a reference with reported QY of 60%. η_R, refractive index of the reference solution: 1.33 for water,1.34 for acetonitrile and 1.36 for ethanol.

2.5.4 Calculation of corrected Fl intensity

In ***Chapter 3*** and ***Chapter 5,*** the corrected FL intensity is calculated using equation.

$$\frac{F_{\text{corrected}}}{F_{\text{observed}}} = \frac{2.3dA_{ex}}{1-10^{-dA_{ex}}} 10^{gA_{em}} \frac{2.3sA_{em}}{1-10^{-sA_{em}}} \qquad (2)$$

Where F_{observed} is the maximum fluorescence intensity; $F_{\text{corrected}}$ is the corrected fluorescence intensity, which is the fluorescence intensity obtained after removing the IFE; A_{ex} and A_{em} represent the absorbance at the excitation wavelength of sample (In ***Chapter 3***, λ_{ex}^{max} = 360 nm and in ***Chapter 5,*** λ_{ex}^{max} = 370 nm) and maximum emission wavelength (In ***Chapter 3***,λ_{em}^{max} = 640 nm and in ***Chapter 5,*** $\lambda_{em}^{max} = 440\,nm$), respectively.; d is the width of the quartz cell (d=1.00 cm); g is the distance between the edges of the cuvette and the excitation beam (0.40 cm in this case); s is the thickness of excitation light (s = 0.10 cm).

2.5.4 Lifetime measurement of the synthesized MNCs.

The fluorescence lifetime of synthesized MNCs is measured by a time-correlated single-photon-counting (TCSPC) instrument which has a broad time resolution range from picoseconds to nanosecond scale. In ***chapter 3***, ***chapter 4***, and ***chapter 5*** DeltaDiode-375L pulsed laser is used. The full width at half-maximum (FWHM) of these setups was typically ~80 ps measured using a liquid scatter.

In the ***chapter 6,*** delayed decay spectra was measured with parameters set as follows: time per flash= 61 ms; sample window =200 μs; delay after flash = 50 μs; flash count = 100.

All decay curve was fitted into exponential functions as mentioned below

$$\mathrm{I(t)} = \sum_{i=1}^{n} a_i \ \exp\left(\frac{-t}{\tau_i}\right) \qquad (3)$$

Where τ_i is the decay time of components and a_i is the corresponding contributions.

The average decay time can be further calculated by the equation.

$$\boldsymbol{\tau_{avg}} = \frac{\sum_{i=1}^{n} a_i \ \tau_i}{\sum_{i=1}^{n} a_i} \qquad (4)$$

Average decay time for delayed fluorescence decay was calculated using the equation

$$\boldsymbol{\tau_{avg}} = \frac{\sum_{i=1}^{n} a_i \ \tau_i^2}{\sum_{i=1}^{n} a_i \ \ \tau_i} \qquad (5)$$

2.5.5 Field emission transmission electron microscope (FETEM)

To know the formation of MNCs, TEM measurement is a very powerful technique which is accomplished by a JEOL JEM 2100 electron microscope with an operating voltage of 200 kV. Every TEM sample was prepared by drop-casting a very diluted solution of MNCs to a copper grid and allowing it to dry in a cleaned desiccator. For analyzing the size of the samples Image-J software was used.

2.5.6 Fourier transformed infrared spectroscopy (FTIR)

The FTIR spectra of all samples are recorded in attenuated total reflectance or ATR mode with a scanning range from 4000 to 400 cm^{-1} with an average of 4 scans. Here, all the solid samples are placed into the incident IR-light chamber followed by applying the force gauge 45 and recording the spectra. Here, the sample is directly in contact with the incident IR beam which is very advantageous for detecting functional groups.

2.5.7 X-ray photoelectron spectroscopy (XPS)

XPS is the most useful method for anticipating the oxidation state and binding property of elements in MNCs. In this thesis, all XPS characterization was done by ESCALAB Xi+ (Thermo Fisher Scientific Pvt. Ltd., UK) photoelectron spectrometer. For the XPS deconvolution, XPSPEAK4.1 software was used.

2.5.8 Matrix-assisted laser desorption/ionization time-of-flight mass spectrometry (MALDI−TOF−MS)

Matrix-assisted laser desorption ionization (MALDI) mass spectra were measured using a Bruker MALDI-TOF spectrometer with a 355 nm nitrogen pulse laser. Sinapinic acid was used as a matrix for MALDI mass sample preparation, and mass spectra were collected in positive mode. The matrix was prepared by dissolving 10 mg of sinapinic acid in a mixture of 300 μl of acetonitrile and 700 μl of water i.e. in a 1:3 mixture of acetonitrile and water. The samples (LYS and LYS-AgNCs in ***chapter 3*** and BSA and BSA-AgNCs in ***chapter 4***) and the matrix were prepared at 1:30, 1:50, 1:70, and 1:90 molar ratios and then ~ $2\mu l$ of the mixture was spread over the MALDI Mass plate for the measurement.

2.5.9 Confocal laser scanning microscope

For confocal analysis in ***chapter 3*** the cell images are collected by using Zeiss, LSM 880 instrument.

2.5.10 Dynamic light scattering (DLS)

In ***chapter 6,*** DLS measurements were performed in Malvern Nano ZS 90 instrument using 50 mW DPSS laser. The He-Ne Laser (λ = 632.8 nm) was used as the excitation source and scattering was collected at a fixed angle of 90º. Around 1 ml of sample is taken on a thoroughly rinsed dust-free quartz cuvette having 10 mm path length. Thereafter 10 minutes equilibrating time feed in the Malvern software to attain fitted temperature. All experiment was performed at 298 K and hydrodynamic diameters are calculated by taking an average of 30 scans with 60 seconds for each scan.

2.5.11 Zeta potential

In ***chapter 6,*** Zeta potential measurement was carried out in Malvern Nano ZS 90 instrument using 50 mW DPSS laser. Around 1 ml of sample is taken on a Zetasizer cuvette. Thereafter 10 minutes equilibrating time feed in the Malvern software to attain fitted temperature. All experiment was performed at 298 K and zeta potential of samples were calculated.

REFERENCES

1. X. Jia, J. Li and E. Wang, *Small*, 2013, **9**, 3873-3879.
2. Z. Luo, X. Yuan, Y. Yu, Q. Zhang, D. T. Leong, J. Y. Lee and J. Xie, *Journal of the American Chemical Society*, 2012, **134**, 16662-16670.

CHAPTER 3

Red-Emitting Silver Nanoclusters for Dual-Mode Detection of Cu^{2+} and Vitamin B_{12} in Living Cell

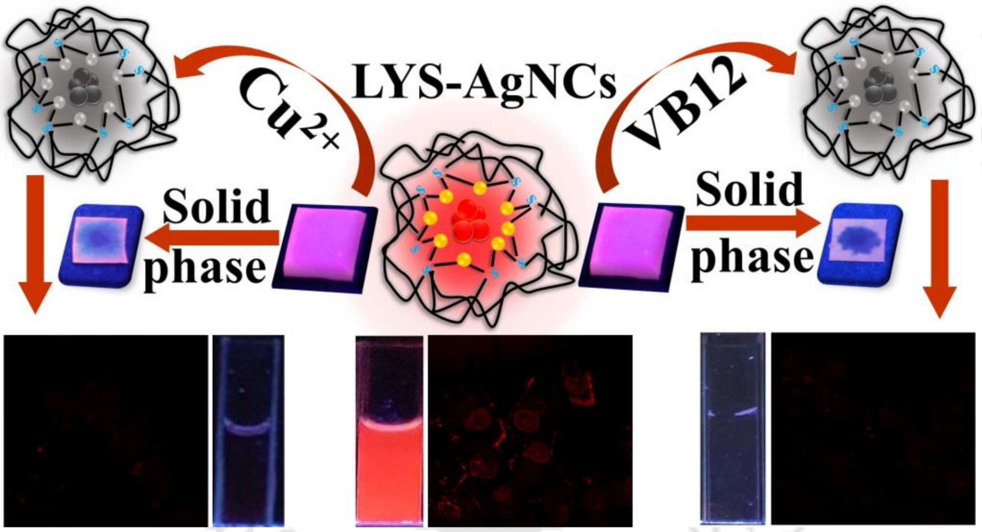

<u>Manuscript</u>: Priyanka Sarkar, Muktashree Saha, Nilanjana Nandi, Dillip Kumar Sahu, and Kalyanasis Sahu, “Red-Emitting Silver Nanoclusters for Dual-Mode Detection of Cu^{2+} and Vitamin B12 in Living Cells” *ACS Appl. Nano Mater. 2022, 5, 7670−7678.*

[This page was intentionally left blank]

ABSTRACT

Biomolecule-stabilized metal nanoclusters (MNCs) exhibit enormous potential as unique luminescent materials in various applications. However, synthesis of highly stable and bio-friendly fluorescent MNCs is still a challenge. Here, we report a facile synthesis of red-emissive silver nanocluster (LYS-AgNCs) within a dithiothreitol-reduced lysozyme (LYS) scaffold. The nanoclusters exhibit uniform size distribution, excellent water solubility, and superior photoluminescence properties featuring a quantum yield of 6.1%, a massive (280 nm) Stokes shift, solid-state emission, and pH stability augments its applicability in dual-mode sensing platforms for Cu^{2+} and vitamin B_{12} (VB12). Two contrasting fluorescence (FL)-quenching mechanisms are responsible for the sensing; Cu^{2+} –induced FL quenching occurs via a multifaceted mechanism involving both static and dynamic quenching, whereas the inner filter effect and Förster resonance energy transfer are mainly responsible for VB12-induced FL quenching. An inexpensive portable paper strip is fabricated using LYS-AgNCs for on-site field application, enabling instrument-free fast and visual detection of Cu^{2+} and VB12. Moreover, LYS-AgNCs also possess favourable biocompatibility against human cervical cancer cells (HeLa), making them a suitable nanoprobe for cell imaging and an efficient agent for detecting Cu^{2+} and VB12 inside live cells as well.

3.1 OVERVIEW

Over the years, atomically precise noble metal nanoclusters (MNCs) have received immense interest due to widespread opportunities in sensing[1-3], multimodal imaging[4, 5], targeted drug delivery[6-8], therapeutic applications[9, 10], biolabeling[11, 12], and so on[13, 14]. These MNCs feature unique molecule-like fluorescence (FL) properties due to the presence of discrete energy levels, unlike their larger plasmonic nanoparticle counterparts.[15] Contrary to most extensively studied gold nanoclusters (AuNCs), silver nanoclusters (AgNCs) remained less explored due to their propensity to aggregate in an aqueous phase because of higher surface energy making the synthesis of AgNCs a bit challenging.[16, 17] Particularly, proteins as stabilizers have come out as a boon to researchers presenting a bio-friendly avenue to produce water-soluble and stable AgNCs[18-23]. However, toxic reducing agents such as $NaBH_4$ are often used to synthesize most red-emitting protein-stabilized AgNCs, which may limit their application in a biological system[24, 25]. Zhou et al. synthesized red-emitting AgNCs using $NaBH_4$ as a reducing agent and lysozyme (LYS) as a stabilizer[21]. However, the quantum yield (QY) was only 1.3%. Subsequently, Sun et al. reported $NaBH_4$ reduced red-emitting AgNCs with a QY of 1.4% to detect sulfide ions[26]. Very recently, Nath et al. have used a biocompatible reducing agent dithiothreitol (DTT) to prepare red-emitting AuNCs, facilitating the cleavage of disulfide bonds of bovine serum albumin (BSA)[27]. We have adopted the DTT reduction method to prepare LYS-stabilized red-emitting AgNCs with much-improved FL properties. Note that long-wavelength, red/near-infrared-emissive MNCs have advantages such as improved tissue penetration, reduced scattering, and better contrast against an autofluorescence background in cells[28]. Thus, a bio-friendly synthetic method is required to develop photostable and chemically stable, nontoxic red-emissive AgNCs for biological applications and targeting.

Copper (Cu^{2+}) is a vital element for the proper functioning of many biological processes. However, excess Cu^{2+} can cause serious harm to the human body by promoting hydroxyl radical generation in cells, causing interference with cellular signaling, damaging cell structures, or inducing apoptosis[29, 30].

Thus, developing a simple and effective sensor for sensitive detection of Cu^{2+} in environmental and biological samples is of utmost importance. Recently, Meng et al. incorporated glutathione-capped bimetallic Au/AgNCs inside the confined space of silica structures (λ_{ex}^{max} = 370 nm; λ_{em}^{max} = 570 nm), which showed an excellent response toward Cu^{2+} in aqueous media and live cells with a limit of detection (LOD) of 60 nM[31]. Yuan et al. also reported FL-based Cu^{2+} detection by polyethyleneimine-capped AgNCs with a Stokes shift of

130 nm (λ_{ex}^{max} =361 nm; λ_{em}^{max} = 490 nm)[32]. Red emissive BSA-capped AuNCs with stokes shift of 165 nm was reported for sensing Cu^{2+} [33]. Very recently, Chen and co-workers have developed a yellow emissive AuNCs (λ_{ex}^{max} = 420 nm and λ_{em}^{max} = 530 nm) using methionine as a stabilizer and reducing agent for Cu^{2+} sensing.[34]

Vitamin B_{12} (VB12) is a water-soluble nutrient indispensable for red blood cell formation, nervous system functioning, and myelin sheath construction. However, a slight imbalance can lead to severe diseases such as pernicious anemia, neurological disorders, and detrimental effects on the liver and kidneys. The acceptable VB12 intake amount is 0.4-2.8 mg/day[35]. Nowadays, fluorescent-based nanomaterials such as quantum dots[36], organic fluorophores[37], and MNCs[38-41] have emerged as attractive and cost-effective platforms for the rapid and facile detection of VB12. Recently, Shanmugaraj et al. have developed a blue-emissive histidine-capped copper nanocluster (CuNCs) for sensing VB12 via Förster resonance energy transfer (FRET)-based FL quenching mechanism[38]. Dual-ligand (BSA and thiosalicylic acid)-based red-emissive bimetallic Au/AgNCs were developed to detect VB12 via the combined FRET and inner filter effect (IFE)-based FL quenching mechanism with a LOD of 71 nM[39]. Samari et al. developed red-emitting BSA-capped AuNCs for selective detection of VB12 via the FRET mechanism with a LOD of 73.8 nM[40]. Qu et al. synthesized polyethyleneimine-capped AgNCs (λ_{ex}^{max} = 375 nm; λ_{em}^{max}= 440 nm), which showed a good response towards VB12 based on IFE-based quenching[41].

In this work, we synthesized bright red-emissive AgNCs capped by LYS (LYS-AgNCs) facilitated by DTT, a biocompatible reducing agent of protein. This strategy was adopted to produce nanoclusters with improved biocompatibility. The LYS-AgNCs display excitation-independent emission spectra centered at 640 nm, featuring superior optical properties such as massive Stokes shift (280 nm), solid-state emission, excellent photophysical stability, broad-range pH stability, and a QY of 6.1%. Moreover, it can effectively serve as an excellent nanosensor to detect Cu^{2+} and VB12 with good selectivity and sensitivity via two contrasting mechanistic pathways. A systematic investigation of the FL suppression mechanisms revealed that both static and dynamic quenchings were responsible for Cu^{2+}, whereas IFE and FRET mechanisms are primarily responsible for VB12. The LODs were 12.8 and 48 nM for Cu^{2+} and VB12, respectively. A filter paper strip of LYS-AgNCs was fabricated, which serves as a quantitative on-site sensor with the gradual disappearance of the red-emission at different concentrations of Cu^{2+} and VB12. Moreover, the long-wavelength emission and massive Stokes shift can be exploited for live-cell imaging. Cellular imaging of HeLa cells with LYS-

AgNCs showed bright red FL under a confocal microscope, which efficiently got quenched in cells enriched with Cu^{2+} and VB12. To the best of our knowledge, the use of protein-based AgNCs for dual-mode detection of Cu^{2+} and VB12 inside live cells has not been reported earlier.

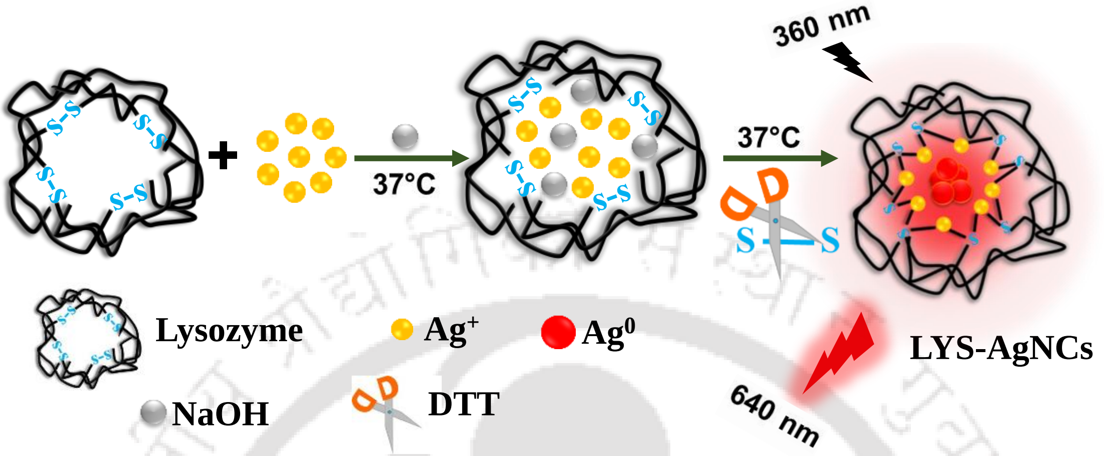

Scheme 3.1. Schematic illustration of the DTT reduced LYS-AgNCs synthesis. Copyright 2022 American Chemical Society

3.2 RESULTS AND DISCUSSIONS

3.2.1. Optical properties of synthesized LYS-AgNCs.

Scheme 3.1 illustrates the bio-friendly synthetic route for the preparation of LYS-AgNCs. Complete optimization of the reaction parameters such as reaction time, LYS concentration, temperature and DTT concentration are elaborately mentioned in **Figure A. 3.1a**, **Figure A. 3.1b**, **Figure A. 3.1c** and **Figure A. 3.1d**. Here, DTT is used to reduce the disulfide bonds (-S-S-) of the cysteine residues present in LYS[42] to produce –SH groups during the synthesis, which help stabilize the cluster core by generating shell of Ag^+-thiol motifs around the core. A high pH (~11.8) medium is requisite for activating the reducing power of protein, which is essential for developing the cluster core by reducing Ag^+ to Ag^0. The UV-vis spectrum of LYS-AgNCs shows a remarkable progressive increase of absorbance at shorter wavelengths below 475 nm **(Figure 3.1a)** indicating the successful synthesis of LYS-AgNCs**.** The emission maximum (λ_{em}^{max}) and the excitation maximum (λ_{ex}^{max}) of Lys-AgNCs are at 640 nm and 360 nm, respectively **(Figure 3.1a).** Moreover, a weak emission band at ~450 nm is also present along with the strong emission at 640 nm on excitation at 360 nm. To investigate the reason for the emergence of weak emission at 450 nm, we performed a blank experiment where the emission spectra of LYS treated with NaOH but no $AgNO_3$ was recorded under the same experimental conditions. As shown in **Figure A. 3.1e**, comparison of the FL spectra of LYS with those of LYS-AgNCs shows that the weak emission at 450 nm appears from the LYS capping the AgNCs[20]. The massive Stokes shift of 280 nm exhibited by LYS-AgNCs is unprecedented and vital to prevent the possibility of any unwanted coupling between excitation and emission signals, which is a prerequisite for a promising fluorescent nanoprobe suited for biological applications[43]. On illuminating with a 365 nm UV lamp, LYS-AgNCs show bright red emissions both in solution and solid-state **(Inset of Figure 3.1a). Figure 3.1b** display that the emission spectra do not shift with the excitation wavelengths[44]. The FL QY, measured using quinine sulfate (54.4% in 0.1 M H_2SO_4) as the standard, was 6.1%. A control experiment was carried out under the same conditions used to synthesize LYS-AgNCs except without DTT addition **(Figure A. 3.1f)**. However, the solution did not show any FL emission, confirming the necessity of the DTT step to reduce the disulfide bonds of LYS-AgNCs for the successful synthesis of LYS-AgNCs at a physiological temperature (37 °C). The lifetime components of LYS-AgNCs calculated using triexponential decay fit at 640 nm was found to be 16.81 (23%), 127.92 (14%) and 0.44 (63%) ns **(Figure 3.1c and Table A.3.1)**.

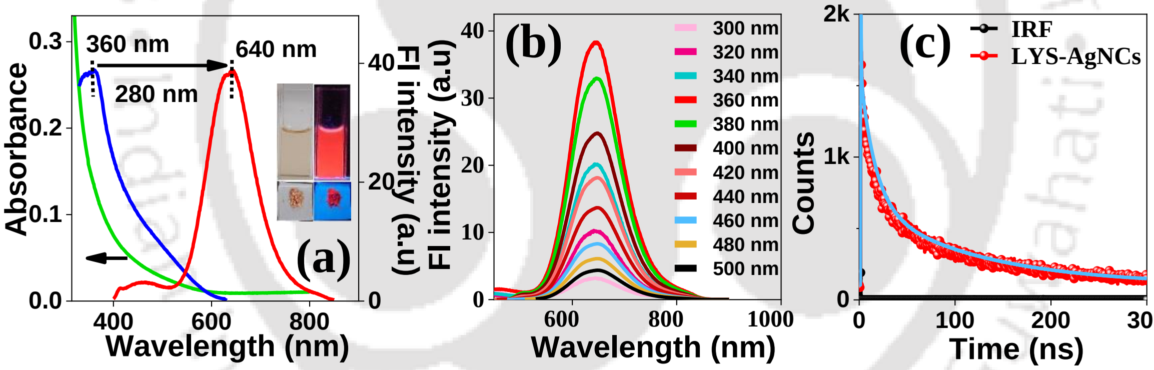

Figure 3.1. (a) UV-vis absorption (green), excitation (λ_{em} = 640 nm) (blue), and fluorescence (λ_{ex} = 360 nm) (red) spectra of LYS-AgNCs. Inset photograph in (a) shows LYS-AgNCs in solution (top) and solid state (bottom) under normal (left) and UV light (365 nm) (right). (b) Fluorescence spectra of LYS-AgNCs at different excitation wavelengths (300 – 500 nm). (c) Fluorescence decay of LYS-AgNCs at 640 nm. Copyright 2022 American Chemical Society

Furthermore**,** the optical stability of LYS-AgNCs was rigorously examined under different conditions such as variable pH (2-12), and UV light treatment **(Figure A.3.1g and A. 3.1h).** However, only 20% decrease in the FL intensity was observed. The LYS-AgNCs remained stable for more than 2 months when preserved at 4 °C, without any change in the emission spectrum **(Figure A.3.1i)**. Thus, the AgNCs possess all the recommended characteristics of a good nanoprobe: excellent photostability, broad range pH stability, a significant Stokes shift, and a long lifetime.

3.2.2. Spectroscopic Characterization of the LYS-AgNCs.

The transmission electron microscopy (TEM) image shows that the LYS-AgNCs were well-dispersed and spherical, with an average size 1.5 ± 0.31 nm **(Figure 3.2a)**. X-ray photoelectron spectroscopy (XPS) revealed the oxidation state of Ag and binding properties in LYS-AgNCs. **Figure 3.2b** indicates the coexistence of both Ag^0 and Ag^+. The peak positioned at 368.9 eV (Ag $3d^{5/2}$) and 374.9 eV (Ag $3d^{3/2}$) correspond to Ag^+ ,while 367.9 eV (Ag $3d^{5/2}$) and 373.9 eV (Ag $3d^{3/2}$) peaks correspond to Ag^0.[45] Ag^0 may form a nanocluster core, while Ag^+ may constitute the shell around the core. Thus, we propose a core-shell structure of LYS-AgNCs, where a network of repeating Ag^+-thiolate bonds formed with the thiol group of LYS stabilizing the core. The N 1S XPS peak at 399.8 eV indicates nitrogen of amide/amine groups present in LYS **(Figure A.3.2a)**. The XPS peak for O 1S was also deconvoluted into two components **(Figure A.3.2b)**; the two peaks at 531.7 eV and 530.8 eV were due to C-O and C=O bonds, respectively[46].

Fourier transform-infrared (FTIR) spectroscopy helps analyze a protein's secondary structure and conformational change. The peaks at 2948 cm^{-1} and 3281 cm^{-1} in LYS and LYS-AgNCs correspond to C-H and O-H/N-H stretching vibrations, respectively **(Figure A.3.2c)**. In LYS, the three signatory peaks at 1653 cm^{-1}, 1531 cm^{-1}, and 1245 cm^{-1} correspond to the stretching and bending vibrations of amide I (primarily –CO stretching) and amide II (primarily –NH bending), and amide III. In LYS-AgNCs, the peak positions of amide II and amide III are nearly the same as those in LYS. However, the amide I band shifts to a lower wavenumber of 1636 cm^{-1} indicating a substantial change of the secondary structure of LYS after AgNCs formation[19].

Matrix-assisted laser desorption/ionization time-of-flight mass spectrometry (MALDI-TOF-MS) is a powerful method for examining the atomicity of metal atoms in MNCs. The protein LYS showed a maximum intensity single peak at m/z~14348 Da, whereas LYS-AgNCs showed an additional shifted peak at m/z ~14870 Da **(Figure 3.2c)**. Thus, the observed m/z difference of ~522 Da indicates the involvement of five silver atoms (Ag_5) in the formation of LYS-AgNCs. However, there is an additional lower intensity peak at m/z~14767 Da with a mass difference of 419 Da from the parent LYS peak, accounting for four silver atoms (Ag_4). Moreover, some very low-intensity peaks appear at m/z~14963 Da and ~15065 Da, which could also account for a small amount of Ag_6 and Ag_7. In 2010, Adhikari et al. reported the formation of AgNCs stabilized by dihydrolipoic acid, which showed a large Stokes shift (200 nm), good photostability, and most importantly, excitation-independent red emission at 652 nm with a narrow emission profile. High-resolution mass spectra showed the presence of two types of clusters: Ag_5 and Ag_4[47]. Thus our synthesized LYS-AgNCs might contain a very narrow distribution of cluster sizes (Ag_4-Ag_7), with the most dominant being Ag_5. Although this result deviates from the consideration of the Jellium model that AgNCs with a significantly higher number of metal atoms emit a red color. However, red emitting AgNCs with very few atoms (Ag_2 to Ag_5) are also reported that emit in the range 610 nm-650 nm[47-50]. The MALDI mass spectra of weakly associated protein complex do not show any mass shift from the parent protein. A plausible explanation could be that the capping protein may be detached from the grown clusters during ionization due to cleavage of S-C or metal-S bonds upon laser irradiation[21]. It has been reported that the growth mechanism of clusters in smaller proteins is different from larger proteins, and the stability of clusters under laser desorption depends on many factors such as the capping agent used and the synthesis procedure used for the preparation of the clusters[51, 52].

The red-emitting LYS-AgNCs synthesized via the DTT-reduction method have many improved features than the usual red-emitting LYS-AgNCs synthesized via $NaBH_4$ reduction[21]. First, the emission maximum of the DTT-reduced AgNCs is at a higher wavelength (640 nm) than the emission maximum (602-605 nm) of $NaBH_4$-reduced AgNCs. [21] The most remarkable change was observed in the excitation spectrum; the excitation maximum of the DTT-reduced AgNCs occurs at a much shorter wavelength (360 nm) than the excitation maximum (450 and 480 nm) of $NaBH_4$- reduced AgNCs. Thus, the Stokes shift is exceptionally large for the DTT-reduced AgNCs (280 nm). Moreover, unlike $NaBH_4$ reduced LYS-AgNCs, which showed stability only in acidic and neutral pH, DTT-reduced LYS-AgNCs were found to be stable over a broad range of pH (2 to 12).[21] The improved feature may originate from the atomicity of metal atoms or the chemical environment around the cluster core. Unfortunately, the atomicity of the $NaBH_4$-reduced LYS-AgNCs was not available. The DTT facilitates the breakage of –S-S- bonds of LYS, resulting in more thiol groups forming the Ag^+-thiolate shell around the core, facilitating ligand-to-metal charge transfer[27, 53, 54].This core-shell nature faciliates the high QY of DTT-reduced LYS-AgNCs (6.1%) compared to $NaBH_4$-reduced LYS-AgNCs (1.3%)[21].

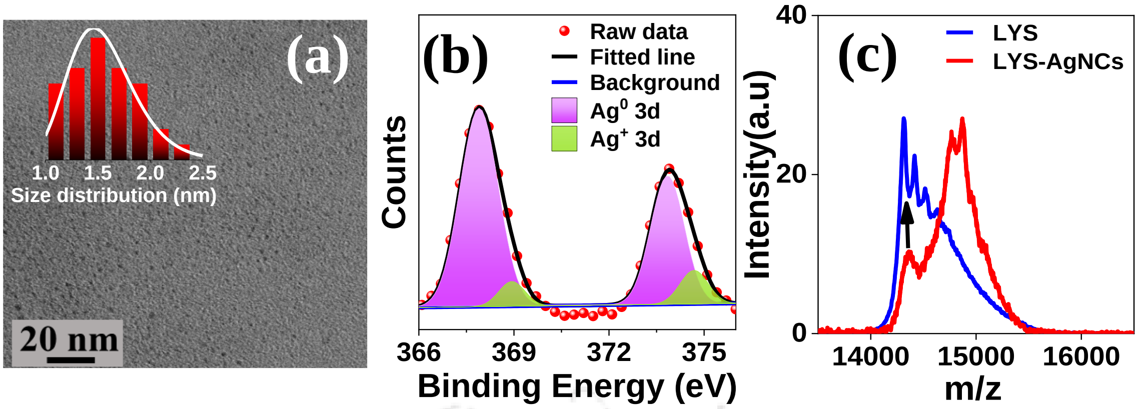

Figure 3.2. (a) TEM image of LYS-AgNCs and the size distribution histogram (b) high-resolution XPS spectra of Ag in LYS-AgNCs (c) MALDI-TOF MS spectra of LYS and LYS-AgNCs. Copyright 2022 American Chemical Society

3.2.3 Fluorescence sensing of Cu^{2+} by LYS-AgNCs.

The FL responses of LYS-AgNCs towards various metal ions were investigated. Interestingly, the emission intensity of the nanoclusters severely decreased only upon the addition of Cu^{2+}; ~80% of the FL intensity was quenched at 66 μM of Cu^{2+} **(Figure 3.3a)**. The bright red emission of LYS-AgNCs under a UV lamp (365 nm) disappears completely in the presence of Cu^{2+} **(Inset of Figure 3.3a)**. The plot of the intensity ratio (F_0/F, where F_0 and F are the Fl intensity in the absence and presence of Cu^{2+}) showed an upward curvature nature at high concentrations of Cu^{2+} **(Figure 3.3b)**, with a linear fit relation observed from 0 to 30 µM with R^2= 0.996 **(Inset of Figure 3.3b)**. Using the standard formula, 3σ/S, where σ is the standard deviation of the blank signal and S is the slope of the linear calibration plot of FL intensity against the analyte concentration; the calculated LOD was 12.8 nM. The selectivity of LYS-AgNCs was studied against other metal ions (Cr^{3+}, Mg^{2+}, Fe^{2+}, Cd^{2+}, Co^{2+}, Fe^{3+}, Hg^{2+}, Ni^{2+}, Zn^{2+}, Pb^{2+}, Eu^{3+}). However, no other metal ions alter the FL intensity significantly like Cu^{2+} **(Figure 3.3c)**. Thus, LYS-AgNCs show great promise as a selective and sensitive sensor for Cu^{2+}.

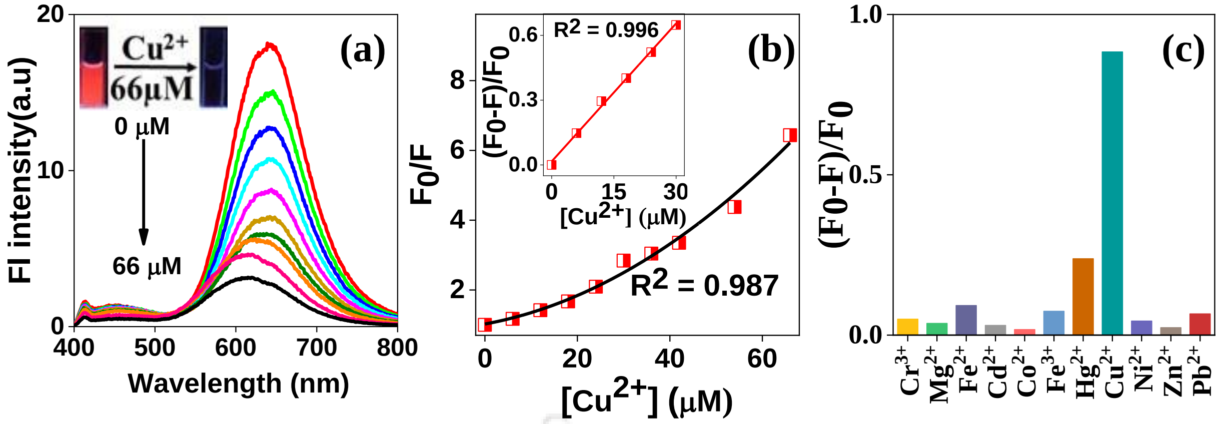

Figure 3.3. (a) Fl spectra of LYS-AgNCs in the presence of various concentrations of Cu^{2+} (0−66 μM). The inset shows the visual fluorescence of LYS-AgNCs and its complete depletion in the presence of 66 μM Cu^{2+} under a 365 nm UV lamp. (b) The ratio of the Fl intensity with different concentrations of Cu^{2+}. The inset shows the ratio of Fl intensity linearly plotted with different concentrations of Cu^{2+}. (c) Selectivity study of LYS-AgNCs in the presence of various metal ions. Copyright 2022 American Chemical Society

3.2.4 Fluorescence sensing of VB12 by LYS-AgNCs.

The LYS-AgNCs were further applied to the detection of VB12 (cyanocobalamin). The addition of only 6 μM VB12 promptly led to a 20% decline in FL intensity, and almost 80% quenching was observed at 60 μM of VB12 **(Figure 3.4a)**. Accordingly, the bright red emission under UV lamp also disappeared **(inset of Figure 3.4a)**. We also observed an upward curvature of the intensity ratio plot (F/F_0, where F and F_0 are the Fl intensity after and before VB12 addition) against the VB12 concentration **(Figure 3.4b)**. The intensity ratio fits linear up to 12 μM VB12 with R^2 =0.994 **(Inset of Figure 3.4b)**, which gives a LOD of 48 nM. Thus, LYS-AgNCs are an effective FL sensor for detecting VB12 with excellent sensitivity. The impact of some other representative vitamins is also evaluated to check the selectivity performance, as the absorbance spectra of all other vitamins (VB1, VB3, VB5, VB6, VB7, VB9) do not overlap with the excitation and emission spectra of LYS-AgNCs **(Figure A.3.4a)**, and the results demonstrated a negligible influence on the emission intensity of LYS-AgNCs **(Figure 3.4c)**.

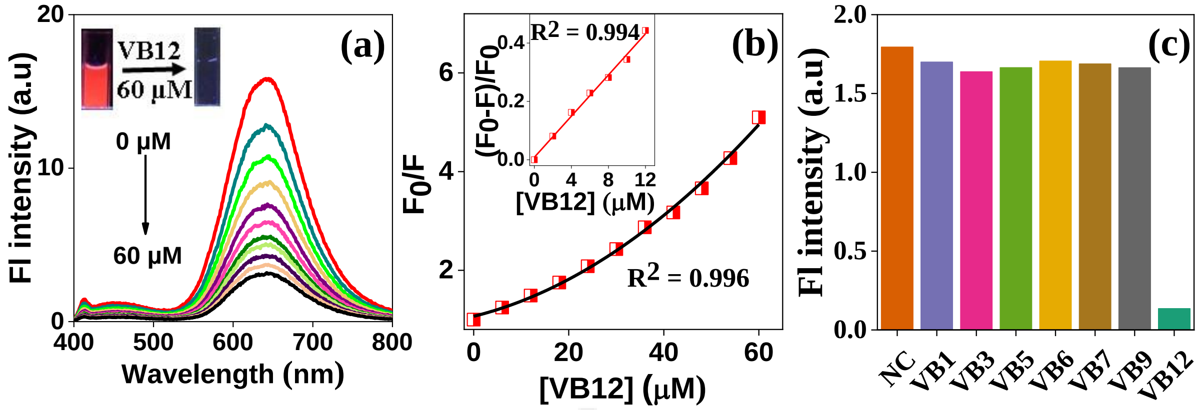

Figure 3.4. (a) Fl spectra of LYS-AgNCs in the presence of various concentrations of VB12 (0−60 µM). The inset shows the visual fluorescence of LYS-AgNC s and its complete depletion in the presence of 60 µM VB12 under a 365 nm UV lamp. (d) The ratio of the Fl intensity with different concentrations of VB12. The inset shows ratio of Fl intensity linearly plotted with different concentrations of VB12. (c) Selectivity study of LYS-AgNCs with various vitamins along with VB12. Copyright 2022 American Chemical Society

3.2.5 Mechanism of Cu^{2+} sensing.

The electron-rich functional groups such as $–NH_2$, -COOH and -OH of protein may precisely coordinate to Cu^{2+} resulting in protein-Cu^{2+} complexation inducing protein aggregation[55]. The UV-vis spectra of LYS-AgNCs showed the emergence of a new broad absorption band at around 450-600 nm range with increasing concentration of Cu^{2+} **(Figure 3.5a)**, indicating complexation between Cu^{2+} and LYS-AgNCs. TEM images further confirmed aggregated structures after adding Cu^{2+} to LYS-AgNCs **(Figure 3.5b)**. The size of the individual nanoclusters increased from ~1.5±0.31 nm to ~5.3±0.72 nm, confirming the formation of self-assembled non-luminescent aggregates induced by complexation. Moreover, the FTIR spectra could also provide insights into the interaction of Cu^{2+} with LYS-AgNCs. A significant change in the spectral nature was observed; the amide II band at 1531 cm^{-1} and amide III band at 1245 cm^{-1} of LYS-AgNCs shift to 1523 cm^{-1} and 1233 cm^{-1} in the presence of Cu^{2+} **(Figure A.3.5a)**. An XPS study can also manifest the interaction of Cu^{2+} with the electron-rich groups of LYS at the surface of LYS-AgNCs. The N 1S and O 1S peaks exhibit distinct changes after adding Cu^{2+} to LYS-AgNCs **(Figure A.3.5b** and **Figure A.3.5c)**. The N 1s peak of the amide/amine group has shifted to higher binding energy (by 0.6 eV) and appears at 400.4 eV. The O 1S peaks for C-O and C=O bonds also shifted slightly to higher binding energy (0.2 eV), i.e., appear at 531.9 eV and 531 eV, respectively, confirming the interaction of Cu^{2+} with –COOH and $–NH_2$ groups of LYS[46]. To clarify the nature of interactive modes of Cu^{2+} with LYS-AgNCs, we measured the FL decays of LYS-AgNCs in the presence of three different concentrations of Cu^{2+} **(Figure 3.5c and Table A.3.2)**.The results clearly shows that the lifetime components of LYS-AgNCs decreases with increasing concentration of Cu^{2+} to 5.03 (11%), 89.35 (4%) and 0.23 (85%) ns at 66 μM of Cu^{2+}**.** The dynamic quenching constant obtained from the linear fit of τ_0/τ vs. Cu^{2+} concentration (τ_0 and τ are the average lifetime of LYS-AgNCs in absence and presence of Cu^{2+}) is $6.60 \pm 0.1 \times 10^4$ M^{-1} **(Figure 3.5d)**. Hence, the overall FL quenching process involves both static and dynamic quenching processes. The static quenching comes from the complexation process between Cu^{2+} and LYS-AgNCs, causing aggregation-induced FL suppression. The dynamic quenching may arise due to electron transfer from LYS-AgNCs to Cu^{2+}, as the incompletely filled d-orbitals of Cu^{2+} ($[Ar]3d^94s^0$) exhibit a greater affinity for electrons from LYS-AgNCs. The static quenching constant can be calculated using the modified Stern-Volmer equation[56, 57].

$$\frac{I_0}{I} = K_{SV}[Q]e^{V[Q]} + 1 \qquad \text{equation (1)}$$

where [Q] signifies the concentration of the quencher (Cu^{2+}), K_{SV} and V signify the dynamic and static quenching constants, respectively. The value of V is found to be 3.38×10^3 M^{-1}. The much larger K_{SV} value implies the dominant role played of dynamic quenching in LYS-AgNCs-Cu^{2+} system.

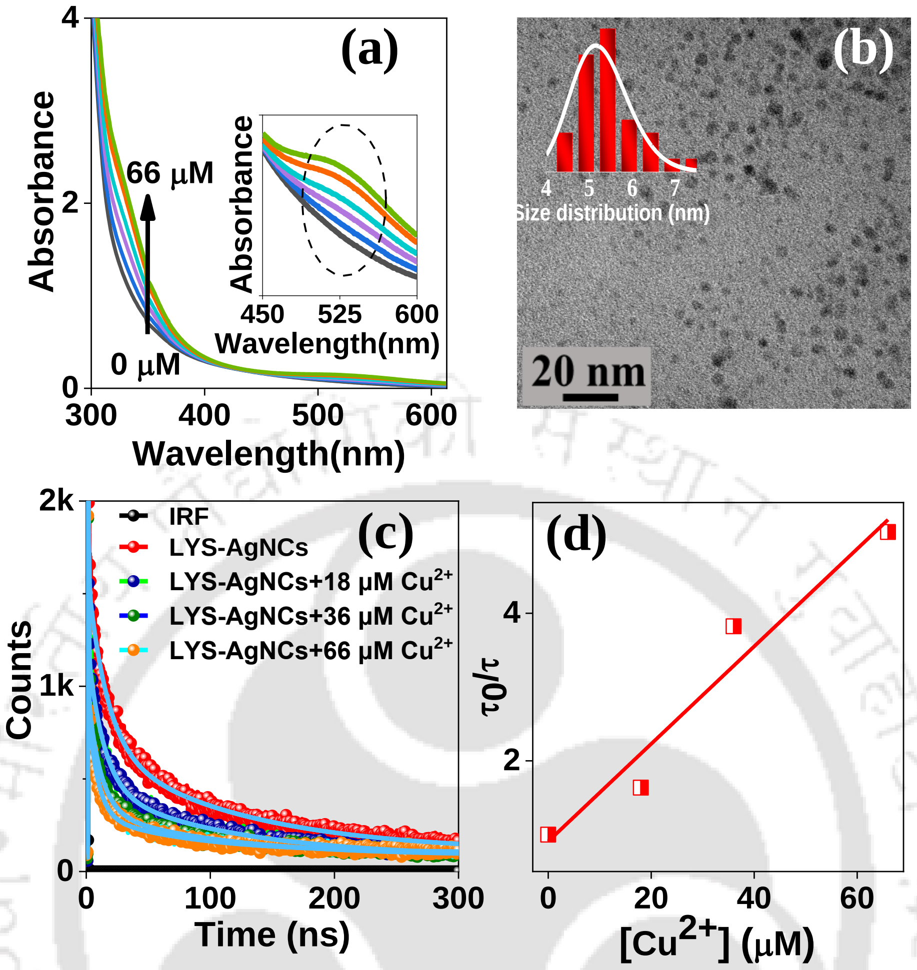

Figure 3.5. (a) Absorption spectra of LYS-AgNCs in the presence of different concentrations of Cu^{2+}. The inset shows the emergence of a new broad absorption band at around 450-600nm with the increase in Cu^{2+} concentration. (b) TEM images of LYS-AgNCs after adding Cu^{2+}; Inset shows size distribution profile. (c) FL decay of LYS-AgNCs at various concentrations of Cu^{2+}(d) The ratio of the average lifetimes against Cu^{2+} concentration. Copyright 2022 American Chemical Society.

3.2.6. Mechanism of VB12 sensing.

The feasibility of the FL-based detection of VB12 by LYS-AgNCs was systematically investigated. Many mechanisms such as ground state complexation, FRET, and IFE were accounted for FL quenching in the literature[58] . Although, IFE was believed to be an error in FL measurement, it has emerged as a non-irradiative energy transformation model in the spectroscopy technique and has been finding use in the development of several FL-based detection systems[59-61]. For a detailed investigation, a series of spectral studies were performed. The absorption spectra of LYS-AgNCs recorded in the presence of several VB12 concentrations did not exhibit any new peak or any spectral shift, thus ruling out the possibility of ground state complexation **(Figure 3.6a)**. Moreover, the absorption spectrum of VB12 displays considerable spectral overlap with both emission and excitation spectra of LYS-AgNCs **(Figure 3.6b),** implying that the FL quenching could likely originate due to FRET and/or IFE based mechanisms. Notably, the FL decays can provide the necessary insights to distinguish between the two mechanisms. The lifetime components of LYS-AgNCs decreases slightly after the addition of three different concentrations of VB12 to 16.02 (18%), 126.5 (12%) and 0.37 (70%) ns at 60 μM of VB12 **(Figure 3.6c and Table A.3.3).** The slight decrease in the average lifetime suggests that FRET may involve in the quenching mechanism but is insufficient to govern the whole quenching mechanism **(Figure A.3.6)**. This observation implies that a considerable contribution also stems from IFE in the LYS-AgNCs-VB12 system. The corrected FL intensity is calculated using **equation 2**[62]. The suppressed efficiency (E=1-F/F_0) for observed and for corrected FL obtained after removal of IFE against each concentration of VB12 added is calculated as shown in **Figure 3.6d**. **Table A.3.4** summarizes the correction factor (CF) values obtained from the ratio of $F_{corrected}$ / $F_{observed}$ for various concentrations of VB12. Thus the remarkable sensitivity of LYS-AgNCs towards VB12 is due to the combined role of IFE and FRET.

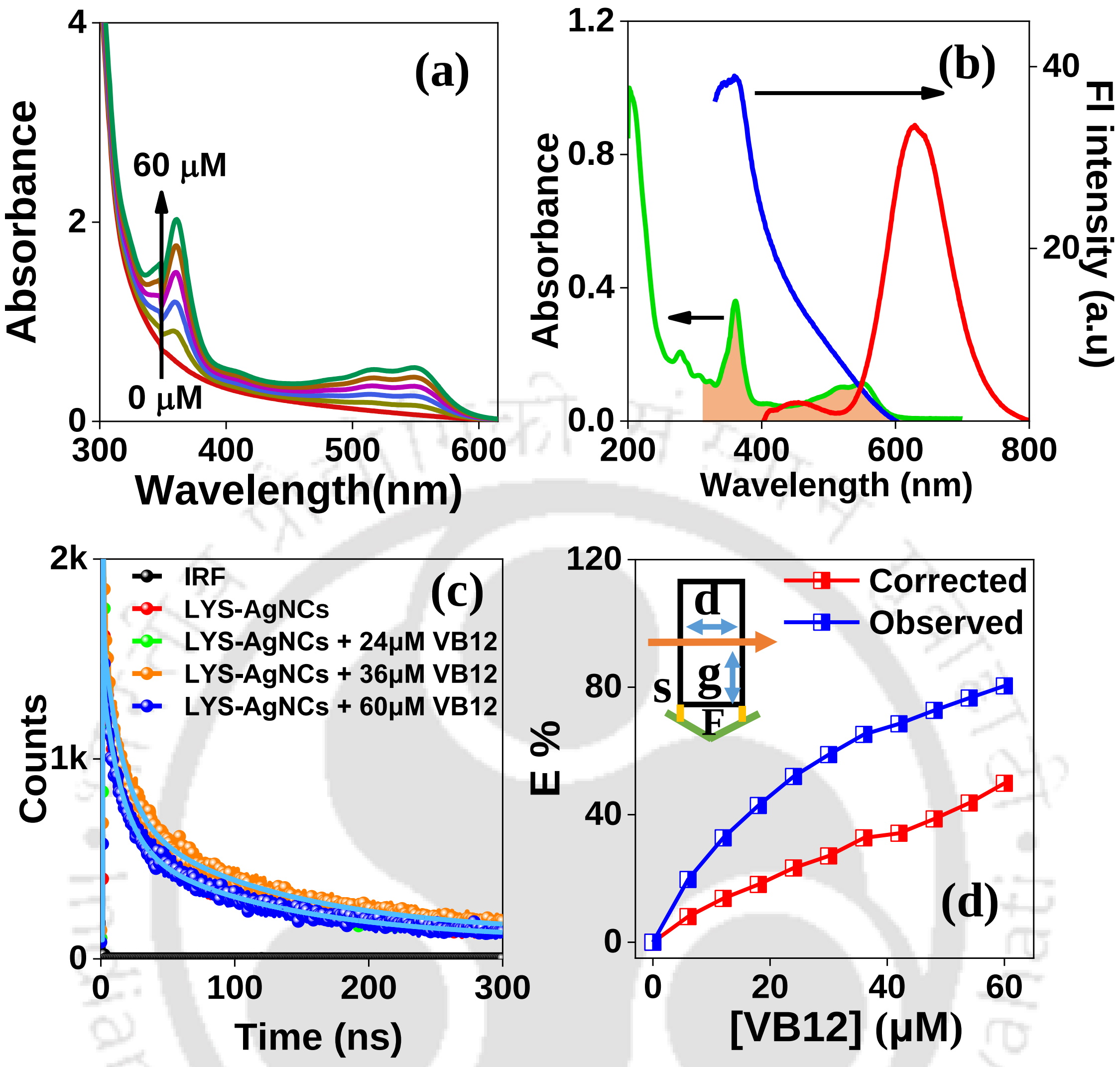

Figure 3.6. (a) Absorption spectra of LYS-AgNCs in the presence of different concentrations of VB12. (b) Spectral overlap between the absorption spectrum of VB12 (green) and the excitation (blue) and emission (red) spectra of LYS-AgNCs. (c) FL decay curve of LYS-AgNCs at various VB12 concentrations. (d) Suppressed efficiency (E%) of observed (blue curve) and modified (red curve) measurements for LYS-AgNCs after each addition of different concentrations of VB12 (The inset shows the parameters used for the IFE equation). Copyright 2022 American Chemical Society

3.2.7. Sensing on paper strips.

Furthermore, owing to solid state property, paper strips were fabricated to extend the practical use of LYS-AgNCs. The strips provide an economically viable and rapid naked-eye detection of Cu^{2+} and VB12. The strips were prepared by immersing Whatman filter paper (cut into the desired size) into LYS-AgNCs solution, followed by air-drying at room temperature. The strips displayed red FL under a 365 nm UV lamp. As shown in **Figures 3.7a and 3.7b,** introducing different concentrations of Cu^{2+} and VB12 (10ul in each strip), the red FL gradually faded away from the centre of the strips giving rise to a spot due to the quenching phenomenon. This spot darkens with an increase in Cu^{2+} and VB12 concentrations. These strips can detect concentrations of both the analytes (Cu^{2+} and VB12) up to 10^{-6} M. This experiment demonstrated the potential role of LYS-AgNCs in developing a portable paper-based sensor for quantitative detection of Cu^{2+} and VB12 under UV lamp.

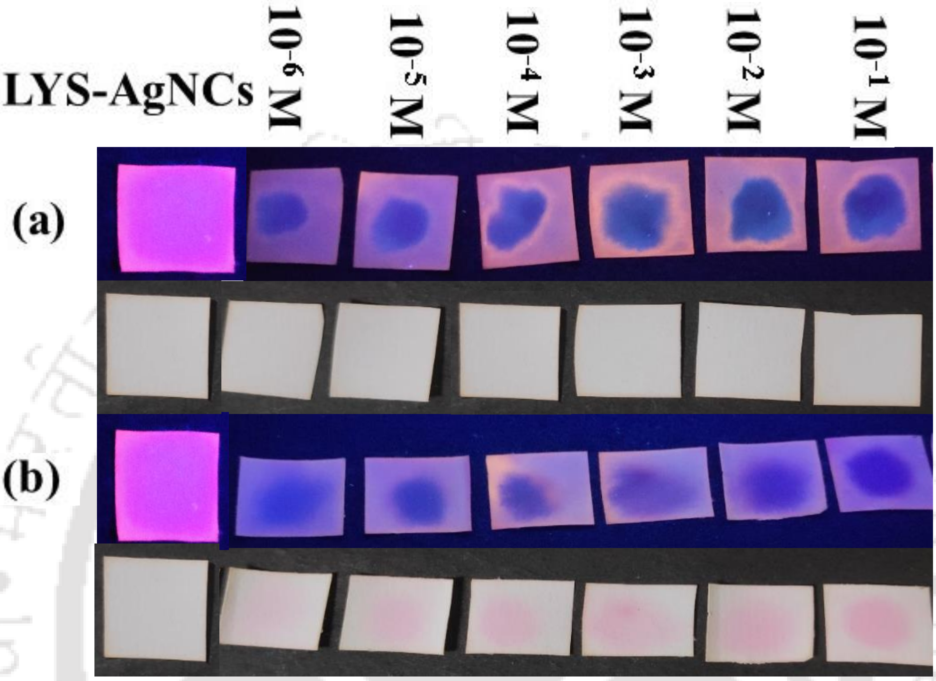

Figure 3.7. LYS-AgNCs paper strips for on-site detection of (a) Cu^{2+} (top, under UV lamp and bottom, under normal light) and (b) VB12 (top, under UV lamp and bottom, under normal light). Copyright 2022 American Chemical Society

3.2.8. Cellular imaging applications.

The MTT assay was conducted on HeLa cells to evaluate the cell viability of LYS-AgNCs, which is a prime requirement for a suitable bioimaging candidate. After exposing the cells to a broad range of LYS-AgNCs concentrations (2-40 μg/mL) for 48 h, the overall cell viability ranges between 70 and 80%, suggesting that the LYS-AgNCs are relatively nontoxic to cells and thus possess considerable biocompatibility for a cellular study **(Figure A.3.8),** Subsequently, to check the potentiality of LYS-AgNCs for cellular imaging, the FL images of the HeLa cells incubated with 40 μg/mL of LYS-AgNCs for 7 h were captured on a confocal microscope using a 405 nm laser source. **Figure 3.8d-f** displays good internalization of LYS-AgNCs inside HeLa cells without affecting the cell morphology. Thus, LYS-AgNCs can be successfully employed as a suitable probe for cell imaging. For further expanding the utility of

LYS-AgNCs as a biosensor, their FL responses towards Cu^{2+} and VB12 inside live cells were monitored. HeLa cells pretreated with LYS-AgNCs for 7 h display bright red luminescence; however, this luminescence drastically reduced in the presence of 54 μM of VB12 **(Figure 3.8g-i)** and 63 μM of Cu^{2+} **(Figure 3.8j-l)**. This result concludes that LYS-AgNCs hold promising potential for the detection of Cu^{2+} and VB12 inside cells as well.

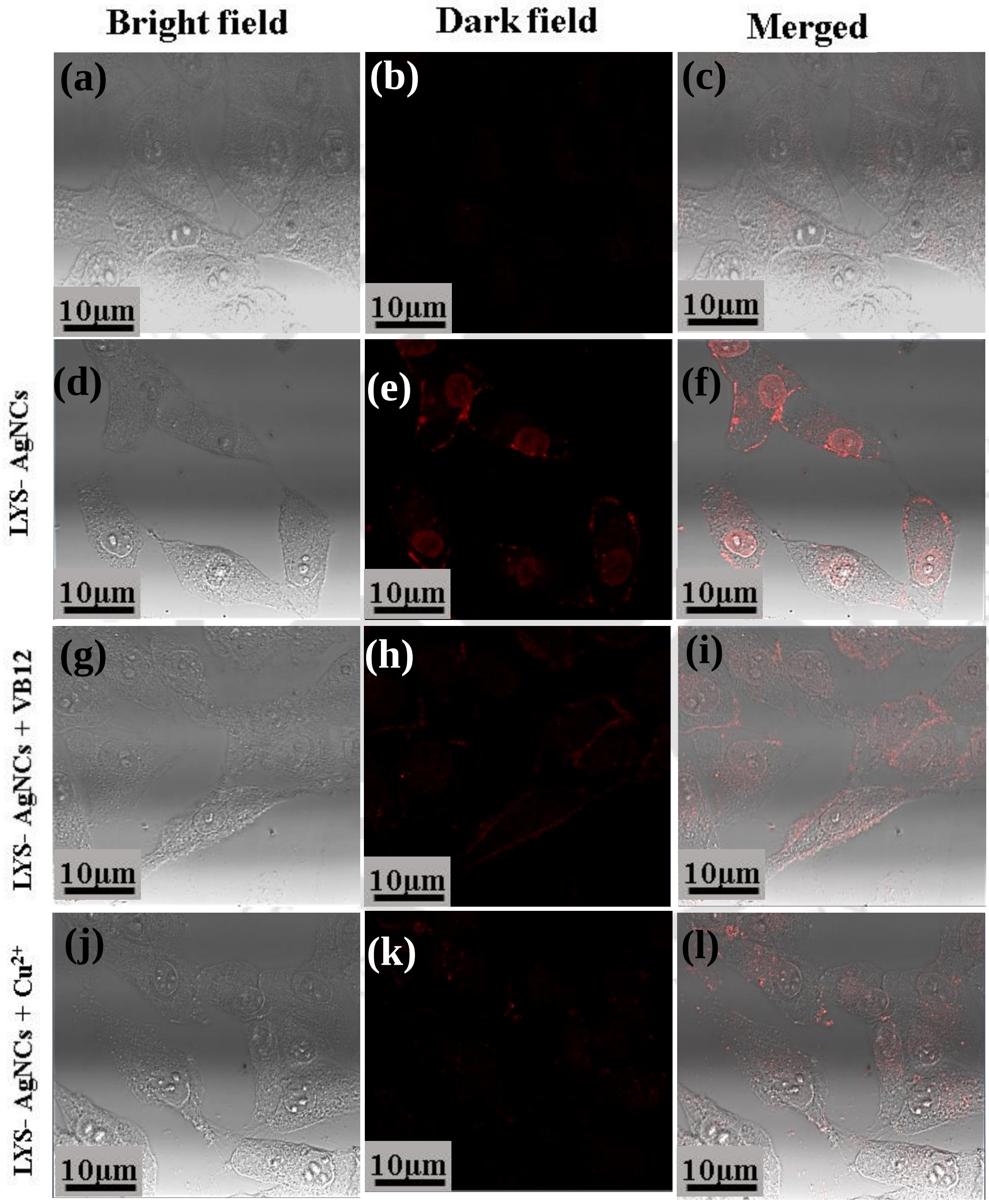

Figure 3.8. Confocal image of HeLa cells (a-c) cell control (d-f) in the presence of LYS-AgNCs (40 µg/mL) treated for 7h (g-i) Cells treated with LYS-AgNCs + 54 µM VB12 (j-l) Cells treated with LYS-AgNCs + 63 µM Cu^{2+}. The excitation source used was 405 nm laser. Copyright 2022 American Chemical Society

3.3 CONCLUSION

In summary, red-emitting LYS-stabilized AgNCs were synthesized using DTT reduction of the disulfide bonds. The synthesized LYS-AgNCs possess solid-state emissive property, excitation-independent emission, and a large Stokes of 280 nm (λ_{ex}^{max}=360 nm, λ_{em}^{max}=640 nm), which may be beneficial to minimize light scattering possibility and reduce interference from auto FL of cells. Moreover, LYS-AgNCs retain their intrinsic FL properties under different conditions, e.g., under pH variation and UV light treatment. The LYS-AgNCs showed a selective response towards Cu^{2+} and VB12 with LOD values of 12.8 nM and 48 nM, respectively. Interaction of Cu^{2+} with electron-rich groups of LYS present on the surface of LYS-AgNCs promoted aggregation of nanoclusters along with transfer of electrons to Cu^{2+} from LYS-AgNCs, resulting in quenching of FL intensity. The VB12-induced FL quenching of LYS-AgNCs is primarily due to IFE, followed by FRET-based quenching phenomenon. Portable paper-strips fabricated using LYS-AgNCs offered FL-based on-site detection of Cu^{2+} and VB12. Moreover, LYS-AgNCs were successfully employed in HeLa cell imaging and served as an effective nanoprobe for detecting Cu^{2+} and VB12 inside live cells.

REFERENCES

1. H. Yang, F. Lu, Y. Sun, Z. Yuan and C. Lu, *Anal. Chem.*, 2018, **90**, 12846-12853.
2. H. Zhao, X. Wen, W. Li, Y. Li and C. Yin, *J. Mater. Chem. B*, 2019, **7**, 2169-2176.
3. W. Zhang, D. Lin, H. Wang, J. Li, G. U. Nienhaus, Z. Su, G. Wei and L. Shang, *Bioconjug. Chem.*, 2017, **28**, 2224-2229.
4. L. Han, J.-M. Xia, X. Hai, Y. Shu, X.-W. Chen and J.-H. Wang, *ACS Appl. Mater. Interfaces*, 2017, **9**, 6941-6949.
5. C. Liu, X. Zhang, X. Han, Y. Fang, X. Liu, X. Wang, G. I. N. Waterhouse, C. Xu, H. Yin and X. Gao, *ACS Appl. Bio Mater.*, 2020, **3**, 1934-1943.
6. Q. Li, Y. Pan, T. Chen, Y. Du, H. Ge, B. Zhang, J. Xie, H. Yu and M. Zhu, *Nanoscale*, 2018, **10**, 10166-10172.
7. X. Yin, B. Yang, B. Chen, M. He and B. Hu, *Anal. Chem.*, 2019, **91**, 10596-10603.
8. M.-M. Xu, T.-T. Jia, B. Li, W. Ma, X. Chen, X. Zhao and S.-Q. Zang, *Chem. Commun.*, 2020, **56**, 8766-8769.

9. L. V. Nair, R. V. Nair, S. J. Shenoy, A. Thekkuveettil and R. S. Jayasree, *J. Mater. Chem. B*, 2017, **5**, 8314-8321.
10. E. Ju, T. Li, S. Ramos da Silva and S.-J. Gao, *ACS Appl. Mater. Interfaces*, 2019, **11**, 34717-34724.
11. X. Song, W. Zhu, X. Ge, R. Li, S. Li, X. Chen, J. Song, J. Xie, X. Chen and H. Yang, *Angew. Chem., Int. Ed.*, 2021, **60**, 1306-1312.
12. C.-A. J. Lin, T.-Y. Yang, C.-H. Lee, S. H. Huang, R. A. Sperling, M. Zanella, J. K. Li, J.-L. Shen, H.-H. Wang, H.-I. Yeh, W. J. Parak and W. H. Chang, *ACS Nano*, 2009, **3**, 395-401.
13. P. Kunwar and P. Soman, *ACS Appl. Nano Mater.*, 2020, **3**, 7325-7342.
14. N. Goswami, K. Zheng and J. Xie, *Nanoscale*, 2014, **6**, 13328-13347.
15. I. Chakraborty and T. Pradeep, *Chem. Rev.*, 2017, **117**, 8208-8271.
16. Y.-P. Xie, Y.-L. Shen, G.-X. Duan, J. Han, L.-P. Zhang and X. Lu, *Mater. Chem. Front.*, 2020, **4**, 2205-2222.
17. T. Zhou, M. Rong, Z. Cai, C. J. Yang and X. Chen, *Nanoscale*, 2012, **4**, 4103-4106.
18. D. K. Sahu, P. Sarkar, D. Singha and K. Sahu, *RSC Adv.*, 2019, **9**, 39405-39409.
19. X. Le Guével, B. Hötzer, G. Jung, K. Hollemeyer, V. Trouillet and M. Schneider, *J. Phys. Chem. C*, 2011, **115**, 10955-10963.
20. F. Liu, T. Bing, D. Shangguan, M. Zhao and N. Shao, *Anal. Chem.*, 2016, **88**, 10631-10638.
21. T. Zhou, Y. Huang, W. Li, Z. Cai, F. Luo, C. J. Yang and X. Chen, *Nanoscale*, 2012, **4**, 5312-5315.
22. U. Anand, S. Ghosh and S. Mukherjee, *J. Phys. Chem. Lett.*, 2012, **3**, 3605-3609.
23. A. Mathew, P. R. Sajanlal and T. Pradeep, *J. Mater. Chem.*, 2011, **21**, 11205-11212.
24. W. Song, R.-P. Liang, Y. Wang, L. Zhang and J.-D. Qiu, *Chem. Commun.*, 2015, **51**, 10006-10009.
25. Z. Luo, K. Zheng and J. Xie, *Chem. Commun.*, 2014, **50**, 5143-5155.
26. H. Sun, D. Lu, M. Xian, C. Dong and S. Shuang, *Anal. Methods*, 2016, **8**, 4328-4333.
27. P. Nath, M. Chatterjee and N. Chanda, *ACS Appl. Nano Mater.*, 2018, **1**, 5108-5118.
28. X.-W. Hua, Y.-W. Bao, J. Zeng and F.-G. Wu, *ACS Appl. Mater. Interfaces*, 2019, **11**, 32647-32658.
29. K. J. Barnham, C. L. Masters and A. I. Bush, *Nat. Rev. Drug Discov.*, 2004, **3**, 205-214.

30. E. Gaggelli, H. Kozlowski, D. Valensin and G. Valensin, *Chem. Rev.*, 2006, **106**, 1995-2044.
31. J. Meng, S. E, X. Wei, X. Chen and J. Wang, *ACS Appl. Mater. Interfaces*, 2019, **11**, 21150-21158.
32. Z. Yuan, N. Cai, Y. Du, Y. He and E. S. Yeung, *Anal. Chem.*, 2014, **86**, 419-426.
33. C. V. Durgadas, C. P. Sharma and K. Sreenivasan, *Analyst*, 2011, **136**, 933-940.
34. H.-H. Deng, L.-N. Zhang, S.-B. He, A.-L. Liu, G.-W. Li, X.-H. Lin, X.-H. Xia and W. Chen, *Biosens. Bioelectron.*, 2015, **65**, 397-403.
35. Y. Jia, Y. Hu, Y. Li, Q. Zeng, X. Jiang and Z. Cheng, *Microchim. Acta*, 2019, **186**, 84.
36. N. Nandi, S. Gaurav, P. Sarkar, S. Kumar and K. Sahu, *ACS Appl. Bio Mater.*, 2021, **4**, 5201-5211.
37. J. Sun, X. Zhu and M. Wu, *J. Fluoresc.*, 2007, **17**, 265-270.
38. K. Shanmugaraj, T. Sasikumar and M. Ilanchelian, *J. Anal. Test*, 2018, **2**, 168-174.
39. Y. Hu, W. Yu, Y. Liao, X. Jiang and Z. Cheng, *Spectrochim. Acta A*, 2021, **263**, 120194.
40. F. Samari, B. Hemmateenejad, Z. Rezaei and M. Shamsipur, *Anal. Methods*, 2012, **4**, 4155-4160.
41. F. Qu, Q. Song and J. You, *Anal. Methods*, 2016, **8**, 4324-4327.
42. J. C. Lukesh, M. J. Palte and R. T. Raines, *J. Am. Chem. Soc.*, 2012, **134**, 4057-4059.
43. L. Tian, W. Zhao, L. Li, Y. Tong, G. Peng and Y. Li, *Sens. Actuators B Chem.*, 2017, **240**, 114-124.
44. V. A. Neacşu, C. Cerretani, M. B. Liisberg, S. M. Swasey, E. G. Gwinn, S. M. Copp and T. Vosch, *Chem. Commun.*, 2020, **56**, 6384-6387.
45. C. Guo and J. Irudayaraj, *Anal. Chem.*, 2011, **83**, 2883-2889.
46. J. Liu, D. Su, J. Yao, Y. Huang, Z. Shao and X. Chen, *J. Mater. Chem. A*, 2017, **5**, 4163-4171.
47. B. Adhikari and A. Banerjee, *Chem. Mater.*, 2010, **22**, 4364-4371.
48. J. Yu, S. A. Patel and R. M. Dickson, *Angew. Chem., Int. Ed.*, 2007, **46**, 2028-2030.
49. I. Díez, M. Pusa, S. Kulmala, H. Jiang, A. Walther, A. S. Goldmann, A. H. Müller, O. Ikkala and R. H. Ras, *Angew. Chem., Int. Ed.*, 2009, **48**, 2122-2125.
50. K. Zheng, X. Yuan, N. Goswami, Q. Zhang and J. Xie, *RSC Adv.*, 2014, **4**, 60581-60596.
51. Y. Lu and W. Chen, *Chem. Soc. Rev.*, 2012, **41**, 3594-3623.

52. P. L. Xavier, K. Chaudhari, A. Baksi and T. Pradeep, *Nano reviews*, 2012, **3**, 14767.
53. K.-T. Chuang and Y.-W. Lin, *J. Phys. Chem. C*, 2017, **121**, 26997-27003.
54. Z. Wu and R. Jin, *Nano Lett.*, 2010, **10**, 2568-2573.
55. M. A. Habeeb Muhammed, P. K. Verma, S. K. Pal, A. Retnakumari, M. Koyakutty, S. Nair and T. Pradeep, *Chem. Eur. J.*, 2010, **16**, 10103-10112.
56. Z. Huang, W. Song, Y. Li, L. Wang, N. K. Pandey, L. Chudal, M. Wang, Y. Li, L. Zhao, W. Yin and W. Chen, *J. Mater. Chem. C*, 2020, **8**, 12935-12942.
57. N. Nandi, S. Gaurav, P. Sarkar, S. Kumar and K. Sahu, *ACS Appl. Bio Mater.*, 2021, **4**, 7605-7614.
58. N. Nandi, P. Sarkar and K. Sahu, *ACS Appl. Nano Mater.*, 2021, **4**, 9616-9624.
59. H. Liu, M. Li, Y. Xia and X. Ren, *ACS Appl. Mater. Interfaces*, 2017, **9**, 120-126.
60. J. Sun, J. Zhao, L. Wang, H. Li, F. Yang and X. Yang, *ACS Sensors*, 2018, **3**, 183-190.
61. H.-C. Chang and J.-a. A. Ho, *Anal. Chem.*, 2015, **87**, 10362-10367.
62. X. Zhu, T. Zhao, Z. Nie, Y. Liu and S. Yao, *Anal. Chem.*, 2015, **87**, 8524-8530.

CHAPTER 4

BSA-Capped Dual Emissive Silver Nanoclusters for Detection of IO_4^- and Cu^{2+} Ions

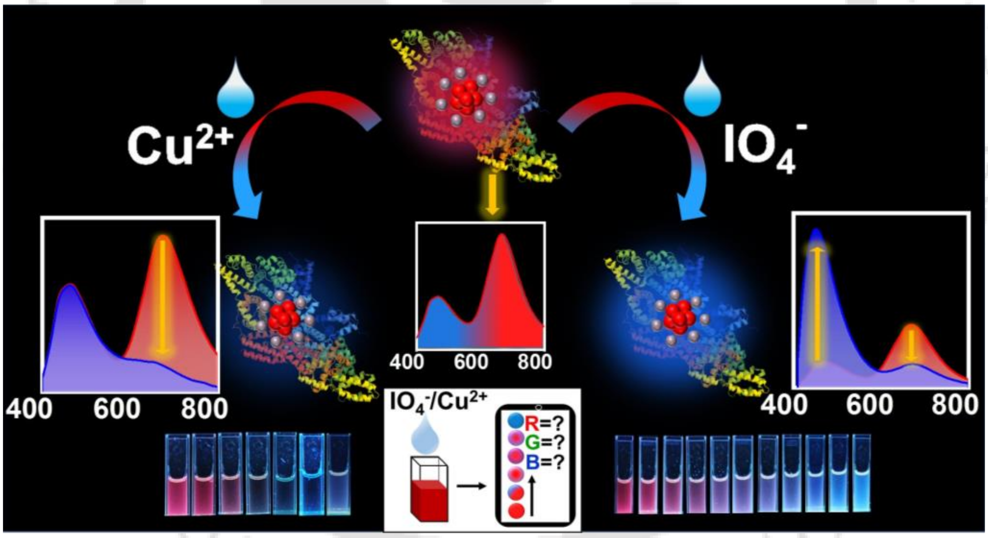

Manuscript: Priyanka Sarkar, Nilanjana Nandi, Neha Barnwal, and Kalyanasis Sahu, "BSA-Capped Dual-Emissive Silver Nanoclusters for Detection of IO_4^- and Cu^{2+} Ions" *ACS Appl. Nano Mater. 2023, 6, 15851−15859.*

[This page was intentionally left blank]

ABSTRACT

Dual-emissive protein-capped metal nanoclusters are emerging nanoprobes for ratiometric sensing. Here, we report a dual-emissive bovine serum albumin (BSA)-capped silver nanoclusters (AgNCs) with a blue emission band at 450 nm and a far-red emission band at 680 nm. The blue emission is attributed to the BSA capping, while the far-red emission originates from the AgNCs. The intensity ratio of the two bands is susceptible to the presence of IO_4^- and Cu^{2+}, allowing selective detection of these analytes with a limit of detection (LOD) of 18.8 nM and 21.6 nM, respectively. These two analytes display different effects on the emission bands. The blue emission band increases with simultaneous diminution of the far-red band in the presence of IO_4^-; however, only the far-red emission band decreases in the presence of Cu^{2+} without altering the blue emission. Both the analytes manifested distinct visual changes in the emission color of the AgNCs solution under a UV-lamp, which also can be evident from the shift of the Commission Internationale d'Eclairage (CIE) coordinates from (0.48, 0.32) to (0.18, 0.17) and (0.24.0.25) for IO_4^- and $Cu^{2+,}$ respectively. IO_4^- induced a conformational change in BSA, intensifying the blue emission band along with a dynamic quenching of the AgNCs emission at 680 nm. In contrast, Cu^{2+} triggered metal exchange method-based quenching of the 680 nm emission with almost no effect on the BSA-capping. A smartphone-based on-site detection of IO_4^- and Cu^{2+} was also achieved. This investigation will provide important insight into the one-pot synthesis of dual-emissive silver nanoclusters and the ratiometric detection mechanism of IO_4^- and Cu^{2+}.

4.1 OVERVIEW

Metal nanoclusters (MNCs) possessing inherent intriguing features, viz. molecule-like discrete energy levels, ultra-small size, and remarkable fluorescence (Fl), continue gaining attention among researchers[1-6]. Their exceptional inherent properties render them an extensive platform for offering various applications like sensing toxic metal ions[7-9] and hazardous molecules[10, 11], bioimaging[12], photodynamic theory[13], catalysis[14], and optoelectronics[15]. MNCs, particularly with red or near-infrared (NIR) emission, possess remarkable advantages in contrast to lower wavelength emitting MNCs due to their benefiting properties like deep cell penetrating power, minimizing the possibility of light-scattering and bypassing autofluorescence[16-18], augmenting their utilization for various applications ranging from sensing of environmental contaminants to biologically hazardous molecules.[19-23] MNCs capped by proteins offer excellent biocompatibility and optical stability.[24-28] Following the first report of bovine serum albumin(BSA) capped AuNCs[29], several other proteins e.g., lysozyme[30], ovalbumin[31], insulin[32], pea protein[33], and pepsin[34] have been utilized for capping many other MNCs. Induction of biocompatible reducing agents like dithiothreitol (DTT) in the synthesis further improves their applicability in biological systems[21]. We previously reported red-emitting silver nanoclusers encapsulated within the DTT-reduced lysozyme, featuring a massive Stokes shift of 280 nm.[35] Ratiometric detection strategies are gaining more attention among researchers[36-38]. The ratiometric detection method involves calculating the fluorescence (Fl) intensity ratio at two different wavelengths, which does not suffer interference from factors like matrix background, a larger standard deviation of Fl intensity, and instrumental efficiency, offering accurate detection results compared to single emissive nanoprobes[39-46]. However, ratiometric nanoprobes usually involve mixing two emissive materials by a chemical or physical strategy. For example, MNCs were mixed with external emissive material like fluorophore[22, 47], carbon dots[48], other MNCs[49], perovskite nanocrystals[19], metal complex[50], and metal-organic framework[51] to construct a suitable ratiometric system for sensing purposes. Thus, a simple strategy of producing MNCs with dual emissive nature in a one-pot system is truly demanding.

Periodate (IO_4^-) anion is a mild oxidant extensively used for various organic reactions facilitating the oxidation of diols and other biomolecules.[52] Moreover, IO_4^- serves as a chemical cross-linker to study interactions between protein-peptide or protein-protein molecules[53, 54]. Additionally, IO_4^- is a potentially hazardous contaminant in the environment and food, inducing singlet oxygen generation.[55] Conventional methods, e.g., electrochemical assay, colorimetric assay, spectrophotometric assay, and UV-vis spectrophotometry, are often employed to detect IO_4^- . However, these methods suffer limitations like low sensitivity, applicability in biological media, and usage of sophisticated instruments.[56-59] Copper (Cu^{2+}) is vital for maintaining the healthy functioning of the human body. An immoderate amount of Cu^{2+} may lead to the generation of reactive oxygen species (ROS), which can lead to the rupture of cellular structures[60] and induce Alzheimer's and Parkinson's diseases [61]. Since Cu^{2+} is also used extensively in industry and agriculture, it can cause severe environmental contamination. Thus, developing a facile Fl-based approach for ratiometric detection of IO_4^- and Cu^{2+} is essential.

This article adopted a facile approach to produce dual-emissive BSA-capped silver nanoclusters (AgNCs) in a one-pot system. The AgNCs possess all the desirable properties like good water solubility, broad range pH stability, high photostability, and long lifetime. The AgNCs show dual emission at blue (450 nm) and far-red (680 nm) regions and proved to be a potential nanoprobe for the ratiometric detection of IO_4^- and Cu^{2+}. IO_4^- induced contrasting responses at two different emission wavelengths. Cu^{2+} induced a significant change in only one emission band, leaving the other unaltered. Mechanistic investigations revealed that IO_4^- induces conformational change in BSA, triggering enhancement in its emission intensity at 450 nm, whereas dynamic quenching may be responsible for the decrease in emission intensity at 680 nm. The Cu^{2+} detection method, on the other hand, involved anti-galvanic based metal-exchange quenching phenomena at 680 nm while leaving emission intensity at 450 nm unaltered. A portable on-site smartphone-aided recognition of IO_4^- and Cu^{2+} was also achieved. To our knowledge, Fl-based ratiometric detection of IO_4^- employing MNCs has not been reported earlier.

4.2 RESULTS AND DISCUSSIONS

4.2.1 Spectroscopic properties of synthesized AgNCs.

Here, a strategic approach was designed utilizing the protein's (BSA) intrinsic blue fluorescence in addition to the far-red emissive AgNCs ($\lambda_{em}^{max} = 680\ nm$) to produce a dual emissive system. The AgNCs were synthesized within a dithiothreitol (DTT)-reduced BSA scaffold. Here, the dual role of BSA protein introduces a unique way of exploring protein-capped MNCs as a ratiometric probe for potential applications. Elaborate optimization of the reaction parameters, e.g., DTT concentration, BSA concentration, and temperature for the synthesis are presented in **Figure A.4.1a, Figure A.4.1b, Figure A.4.1c**. A schematic representation of the synthesis procedure is presented in **Scheme 4.1**.

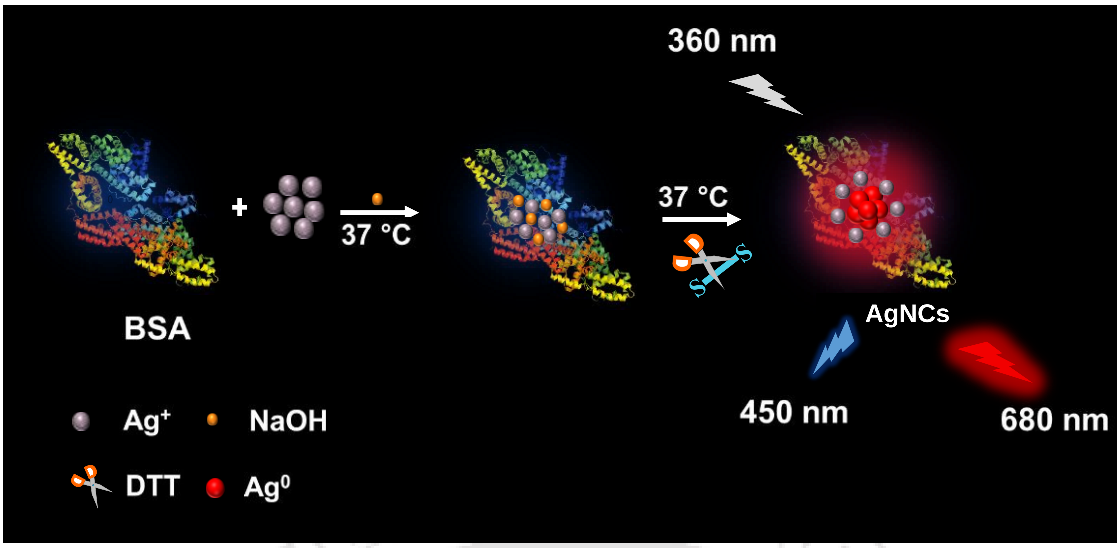

Scheme 4.1. A schematic representation of the synthesis procedure of AgNCs capped within BSA protein. Copyright 2023 American Chemical Society

UV-vis spectrum in **Figure 4.1a** showed an upsurge of the absorbance from 450 nm with a signatory peak of BSA at 280 nm. The Fl spectrum showed a strong emission at a far-red region (680 nm) and a comparatively weaker emission at 450 nm when excited at 360 nm (**Figure 4.1a**). **Figures 4.1b** show that excitation wavelength variation causes a discernible change in emission maxima at a shorter wavelength (440-480 nm) with no alteration of emission maxima at 680 nm. The protein capping under the alkaline condition may contribute to the blue emission at 450 nm, and heterogeneity of the protein conformation around the nanoclusters may give rise to the excitation wavelength-dependent emission maximum for the blue band. A control experiment (BSA protein treated with NaOH without silver nitrate) shows an emission band at 450 nm when excited at 360 nm (**Figure 4.1c**). Quantum yields were 0.5% and 3.6% at 450 nm and 680 nm, respectively, determined employing quinine sulfate (54.4% in 0.1 M H_2SO_4) as reference. The fluorescence decays of the red AgNCs measured at 680 nm follows a tri-exponential fit with components 1.3 ns (50%), 17.0 ns (30%), 118.7 ns (20%) (**Figure 4.1d and Table A.4.1**), whereas fluorescence decay at 450 nm was bi-exponential with components 0.60 ns (80%) and 4.7 ns (20%) (**Figure 4.1e and Table A.4.1**). The prepared AgNCs solution showed deep red emission under a 365 nm UV lamp (**Figure 4.1f**).

Chemical and photostability are essential aspects of any nanomaterial viable for practical application. We measured the emission spectra of the AgNCs over a range of pH (2-12) and with long photo exposure. The Fl intensity ratio (F_{680}/F_{450}) is highest at pH 7 and showed only a 25% decrement when the pH of the medium shifted both ways from neutral value (pH~7) (**Figure A.4.1d**). The Fl intensities of AgNCs at both wavelengths retained the emission intensity under a constant irradiation source for 30 min (**Figure A.4.1e**). Moreover, the emission characteristics were stable upon storing the AgNCs solution at 4 °C (**Figure A.4.1f**), showing almost 80% decrease in intensity after 90 days, which could be likely attributed to the aggregation propensity of AgNCs. Furthermore, the capping ligand BSA may experience environmental intolerance due to prolonged exposure to complicated aqueous environments such as different pH and other materials present in the solution like $AgNO_3$, Dithiothreitol(DTT), which may potentially result in the destabilization of synthesized AgNCs quality after 90 days.

The transmission electron spectroscopy (TEM) image (**Figure 4.1g**) demonstrates the formation of monodispersed spherical AgNCs with an average diameter of 1.0 ± 0.3 nm. The oxidation states of Ag and all other elements (C, N, O, and S) were verified using X-ray photoelectron spectroscopy (XPS). The decomposition of high-resolution XPS spectra of Ag suggests the co-existence of Ag(0) and Ag(+1) states in the synthesized AgNCs (**Figure 4.1h**). The peaks at 367.8 eV (Ag $3d^{5/2}$) and 373.8 eV (Ag $3d^{3/2}$) evince the presence of Ag(0) state, whereas the peaks at 368.6 eV (Ag $3d^{5/2}$) and 374.6 eV (Ag $3d^{3/2}$) evince the presence of Ag(+1) state in AgNCs.[62] Thus, a shell of Ag^+-thiolate bonds may stabilize the Ag(0) present in the core.

Matrix-assisted laser desorption/ionization time-of-flight mass spectrometry (MALDI-TOF-MS) provides vital information about the nuclearity of MNCs. The parent BSA showed a mass peak at m/z ~ 66533 Da, whereas the synthesized AgNCs showed a shifted maximum intensity peak (m/z~ 68424 Da) at a difference of 1891 Da, signifying the predominant formation of Ag_{18} cluster in the core (**Figure 4.1i**). However, the broad nature of the AgNCs mass peak indicates the presence of Ag_{12}-Ag_{25} clusters along with the predominant cluster, Ag_{18}.

Previously Guo et al. synthesized AgNCs utilizing a denatured BSA (dBSA) scaffold to stabilize Ag clusters[62]. Two protein denaturants, tris-(2-carboxyethyl)phosphine hydrochloride (TCEP) and guanidine hydrochloride, were used in tandem to completely denature BSA and to free all 35 cysteine thiol groups. They added $AgNO_3$ to this dBSA, followed by the addition of $NaBH_4$ as an external reducing agent. However, we have utilized dithiothreitol (DTT), a well-known bio-compatible reducing agent for disulfide bonds (-S-S-)[63]. The reaction was performed in an alkaline medium to activate the reducing power of BSA. The –SH groups of BSA form a network shell of Ag^+-thiolate bonds to stabilize the core of Ag^0. Thus, the introduction of DTT assisted BSA in stabilizing the Ag^0 cluster core produced by the reduction of Ag^+. The use of dBSA by Guo et al led to the synthesis of red emissive AgNCs with emission at 637 nm (λ_{ex}= 400 nm), however, our procedure produced AgNCs with far-red emission at 680 nm (λ_{ex}= 360 nm) and a weaker blue emission at 450 nm arising from capped BSA.

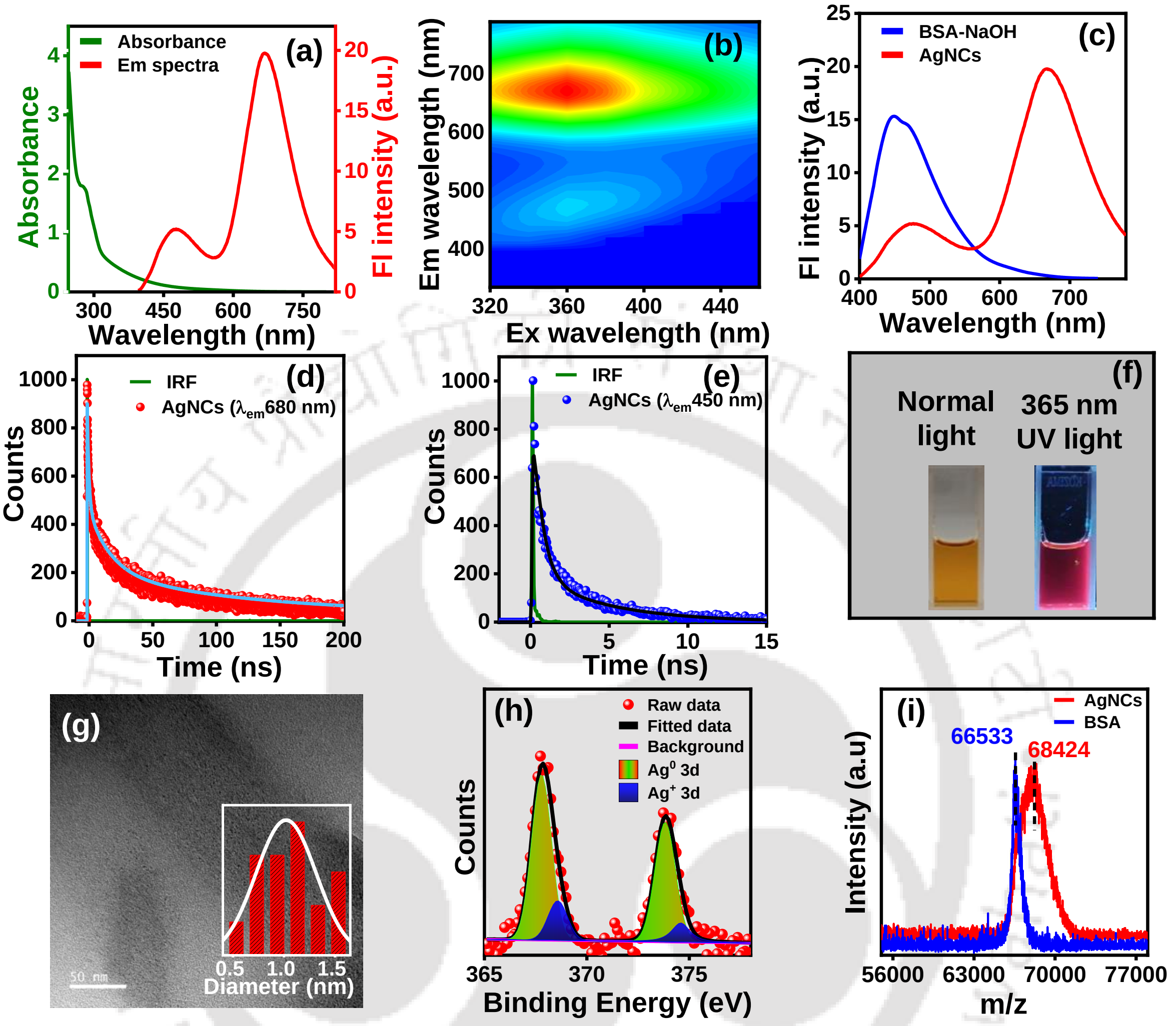

Figure 4.1. (a) UV−vis absorption and Fl (λ_{ex} = 360 nm) spectra of AgNCs. (b) 2D excitation-emission plot of AgNC. (c) Fl (λ_{ex} = 360 nm) spectra of AgNCs and BSA-NaOH. Fl decay of AgNCs at (d) 680 nm and (e) 450 nm emission and (f) photograph of AgNCs under normal light (left) and 365 nm UV lamp (right). (g) TEM image of AgNCs (Inset shows size distribution histogram (upper left) and SAED image (lower right)). (h) high-resolution XPS spectra of Ag in AgNCs and (i) MALDI−TOF MS spectra of BSA and AgNCs. Copyright 2023 American Chemical Society.

4.2.2 Detection of IO_4^-

The dual-emissive AgNCs were exploited for ratiometric detection of some common ions in water. The incorporation of IO_4^- alters the emission intensity of both bands (**Figure 4.2a**). Fl spectra were monitored every 5 min interval after adding 100 μM IO_4^- to AgNCs solution to evaluate response time. A rapid change in the emission intensity ratio was observed up to 30 min (**Figure A.4.2a**), after which the ratio becomes constant. Thus, a response time of 30 min has been considered for all following experiments. Fl spectra recorded with a gradual increment of added concentration of IO_4^- (0 μM to 160 μM) exhibited a gradual decline in emission intensity at 680 nm while a progressive increase and a slight blue shift in the emission intensity at 450 nm. Thus, increasing IO_4^- concentration produced opposite responses at 450 and 680 nm. The CIE plot presented in **Figure 4.2b** represents the change in CIE coordinates of AgNCs (red dot [0.48, 0.32]) after the addition of IO_4^- (160 μM) (blue dot [0.18, 0.17]). Moreover, **Figure 4.2c** demonstrates a distinct visual change in intense red emission of AgNCs solution to intense blue emission with successive addition of IO_4^- under a UV lamp. The intensity ratio plot of F_{450}/F_{680} versus IO_4^- concentration shows adequate linear fit up to 20 μM (**Figure 4.2d**). The LOD (limit of detection) value was 18.8 nM. Selectivity performance is always a crucial factor for sensing applications. **Figure A.4.2b** denotes the emission intensity ratio (F_{450}/F_{680}) in the presence of other potential interfering anions that did not undergo any significant change, unlike in the case of IO_4^-. **Figure A.4.2c** demonstrates the selective nature of IO_4^- in the presence of other relevant anions, illustrating the potential selective nature of the nanoprobe toward ratiometric detection of IO_4^-.

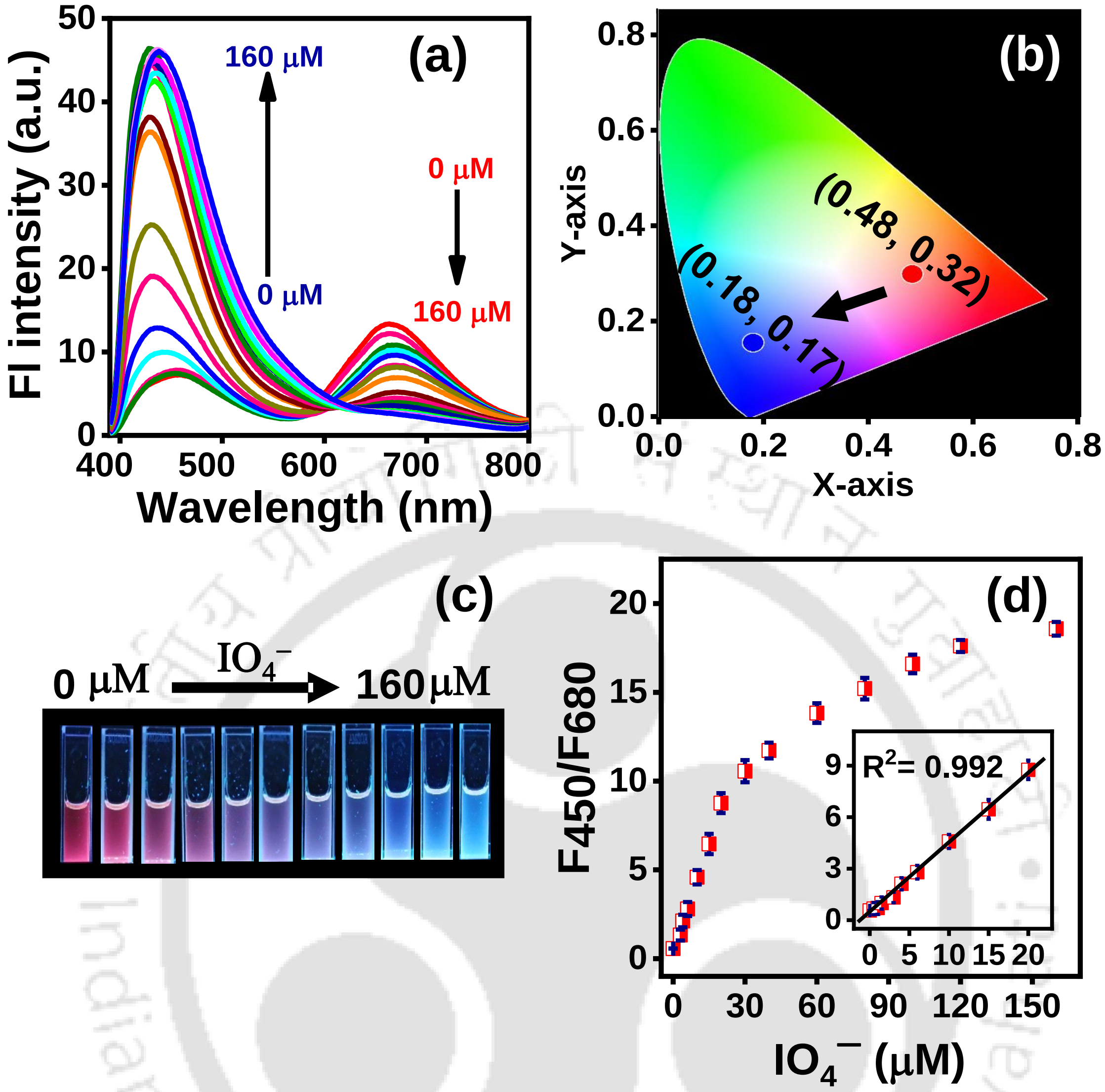

Figure 4.2. (a) Fl spectra of AgNCs in the presence of IO_4^- displaying ratiometric changes. (b) CIE coordinate of AgNCs before and after the addition of 160 μM IO_4^- (c) Photographs of AgNCs solution under 365 nm UV lamp with the gradual addition of IO_4^- (d) Intensity ratio (F_{450}/F_{680}) against IO_4^- concentration (inset shows the linear response up to 20 μM). Copyright 2023 American Chemical Society

4.2.3 Detection of Cu^{2+}

Additionally, on recording the Fl spectra of AgNCs in the presence of different cations, the emission signal was effectively altered only in the case of Cu^{2+}. For response time measurement, Fl spectra of AgNCs recorded every 2min after adding 20 μM of Cu^{2+} denoted that the emission intensity becomes steady after 4 min incubation (**Figure A.4.3a**). The gradual addition of Cu^{2+} (0 μM to 40 μM) induced quenching of emission intensity at 680 nm while the emission intensity at 450 nm remained almost unaltered (**Figure 4.3a**). The CIE plot presented in **Figure 4.3b** shows a change in CIE coordinates of AgNCs (red dot[0.48, 0.32]) after the addition of 40 μM of Cu^{2+} (black dot [0.24,0.25]). **Figure 4.3c** represents the naked eye visual transition of the red emission of AgNCs to light blue emission with a gradually increasing Cu^{2+} concentration under a UV lamp. A linearly fitted intensity ratio plot of F_{450}/F_{680} versus Cu^{2+} concentration up to 40 μM (**Figure 4.3d**) revealed a LOD value of 21.6 nM . **Figure A.4.3b** displays selectivity performance, where the emission intensity ratio of F_{450}/F_{680} in the case of other interfering cations remained unaltered, unlike Cu^{2+}. **Figure A.4.3c** demonstrates the selectivity study of Cu^{2+} in the presence of other relevant interfering cations.

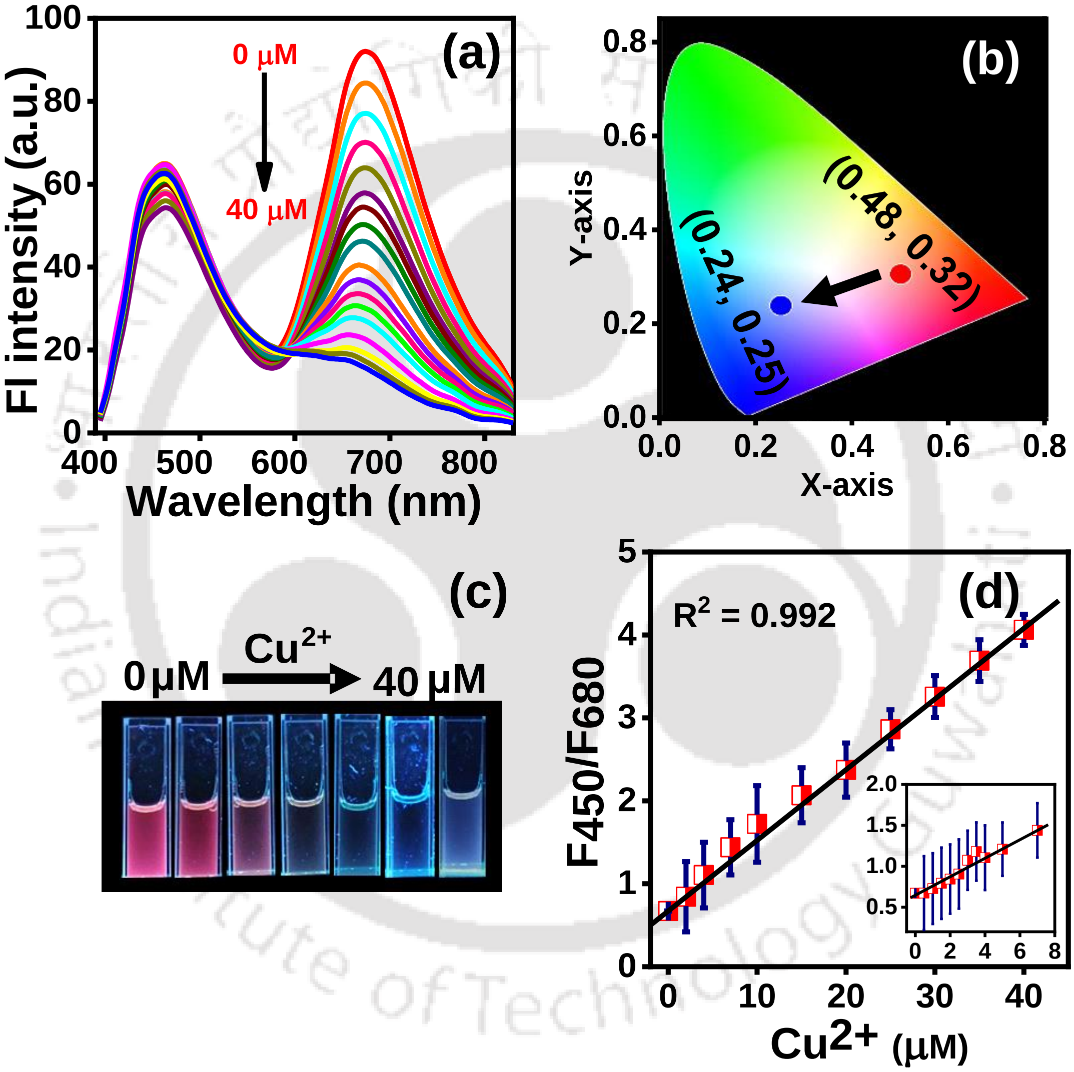

Figure 4.3. (a) Fl spectra of AgNCs in the presence of Cu^{2+} displaying a decrease of the red emission band only. (b) CIE coordinate of AgNCs before and after the addition of 40 μM Cu^{2+}. (c) Photographs of AgNCs solution under 365 nm UV lamp with gradually adding Cu^{2+}. (d) Intensity ratio (F_{450}/F_{680}) against Cu^{2+} concentration. Copyright 2023 American Chemical Society

4.2.4. Mechanism of IO_4^- detection.

To understand the underlying mechanism for the detection of IO_4^- , various experiments were performed. Firstly, UV-vis spectra recorded after each addition of IO_4^- , depicted the absence of any newly emerged notable peak; however, a slight change of absorbance spectra in the region from 240 nm to 260 nm was observed (**Figure 4.4a**). TEM images were taken to confirm whether the addition of IO_4^- induced any change in the core structure of AgNCs. **Figure 4.4b** represents a particle size of 1.1± 0.2 nm, denoting a negligible change in particle size after IO_4^- addition. Further, fluorescence decays were measured at 680 nm and 450 nm after adding 160 μM IO_4^- (**Figure 4.4c and 4.4d**, **Table A.4.2**). The fluorescence decay at 680 nm becomes faster (1.2 (66%) ns, 13.5 (23%) and 99.3 (11%)), whereas the fluorescence decay at 450 nm did not change much (0.7 (69%) and 3.9 (31%) ns). The fluorescence lifetime reduction at 680 nm indicates dynamic quenching. Moreover, to get an in-depth explanation of the enhancement in emission intensity at 450 nm, we performed a control experiment, where Fl spectra of NaOH-treated BSA were measured every 5 min after adding IO_4^- . The addition of IO_4^- gradually enhances the emission intensity along with a slight blue shift of the BSA intrinsic blue emissive band with time (**Figure A.4.4a**). Moreover, the fluorescence decay of the NaOH-treated BSA at 450 nm does not alter before and after adding IO_4^- (**Figure A.4.4b and Table A.4.3**). The fluorescence decay of the NaOH-treated BSA was similar to the BSA-AgNCs fluorescence decay at 450 nm. Thus, these control experiments corroborate that IO_4^- imposes a similar effect on NaOH-treated BSA and BSA-encapsulating AgNCs. IO_4^- can oxidize some residues and cause a conformational change in BSA, triggering emissive enhancement. Moreover, some literature reports mention that IO_4^- can cause protein-protein cross-linking, which may also result in enhanced emission.[53, 54] Thus, combined contribution from the dynamic process and IO_4^- induced conformational changes in BSA caused the ratiometric changes allowing the detection of IO_4^-.

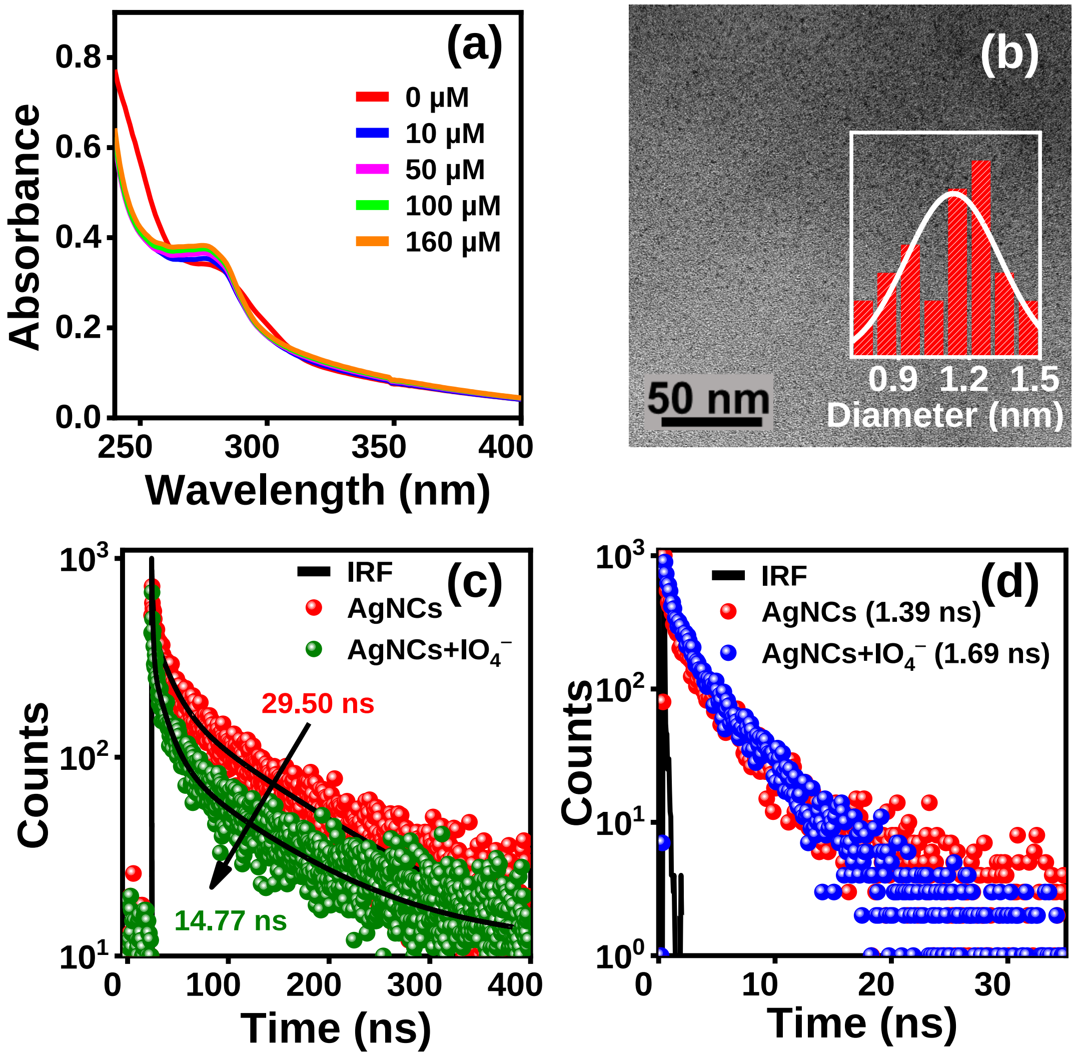

Figure 4.4. (a) UV−vis absorption spectra of AgNCs in the presence of different concentrations of IO_4^-. (b) TEM images of AgNCs after the addition of IO_4^- (Inset shows size distribution histogram). FL decay curve of AgNCs after IO_4^- (160 µM) addition at (c) 680 nm and (d) 450 nm. Copyright 2023 American Chemical Society

4.2.5 Mechanism of Cu^{2+} detection.

Several experiments were undertaken to explore the quenching mechanism responsible for the ratiometric detection of Cu^{2+} by dual-emissive AgNCs. Generally, interaction of metal cations (Cu^{2+}) with the capping ligand BSA protein would result in emergence of a new peak in UV-visible spectra of AgNCs. In our study, the UV-visible spectra obtained while increasing the concentration of Cu^{2+} did not exhibit any new peak (**Figure 4.5a**). However, a slight decrease in absorption at 298 nm and 246 nm, accompanied by a slight increase at 280 nm has been observed with increasing Cu^{2+} concentration. A similar phenomena has also been observed in an earlier literature, where Au_{16}NCs acted as a reductant for Ag^+ and led to the formation of hybrid Au@AgNCs[64]. TEM images after adding Cu^{2+} revealed a particle size of 1.2 ± 0.3 nm, implying a minor change in core size (**Figure 4.5b**). For further exploration of the quenching mechanism, Fl decays measurements were explored (**Figure 4.5c and 4.5d, Table A.4.4**). The tri-exponential decay fit at 680 nm shows a significant decrement in the decay components (1.20 ns (66%), 13.2 ns (24%), and 101.1 ns (10%)); however, the bi-exponential decay fit at 450 nm shows almost no change in the decay components (0.50 ns (79%) and 4.50 ns (21%)). Furthermore, some recent literature reports introduced, that the use of the anti-galvanic method for metal exchange can also induce Fl quenching/enhancement in luminescent MNCs through alloy formation[11, 65, 66]. The anti-galvanic method typically becomes relevant when the size of gold or silver particles is reduced to less than 3 nm. This reduction in size enhances their reducing activity, enabling the reduction of more reactive or less noble metals (such as Cu^{2+} to Cu^0)[67, 68]. Given the size of AgNCs in our case is only 1 nm, it is evident that their enhanced reducing capability can result in the reduction of Cu^{2+}, ultimately leading to the quenching of the Fl intensity of AgNCs at 680 nm. However, the non-coordination of Cu^{2+} with BSA leaves the protein structure intact, resulting in the almost unchanged blue emission.

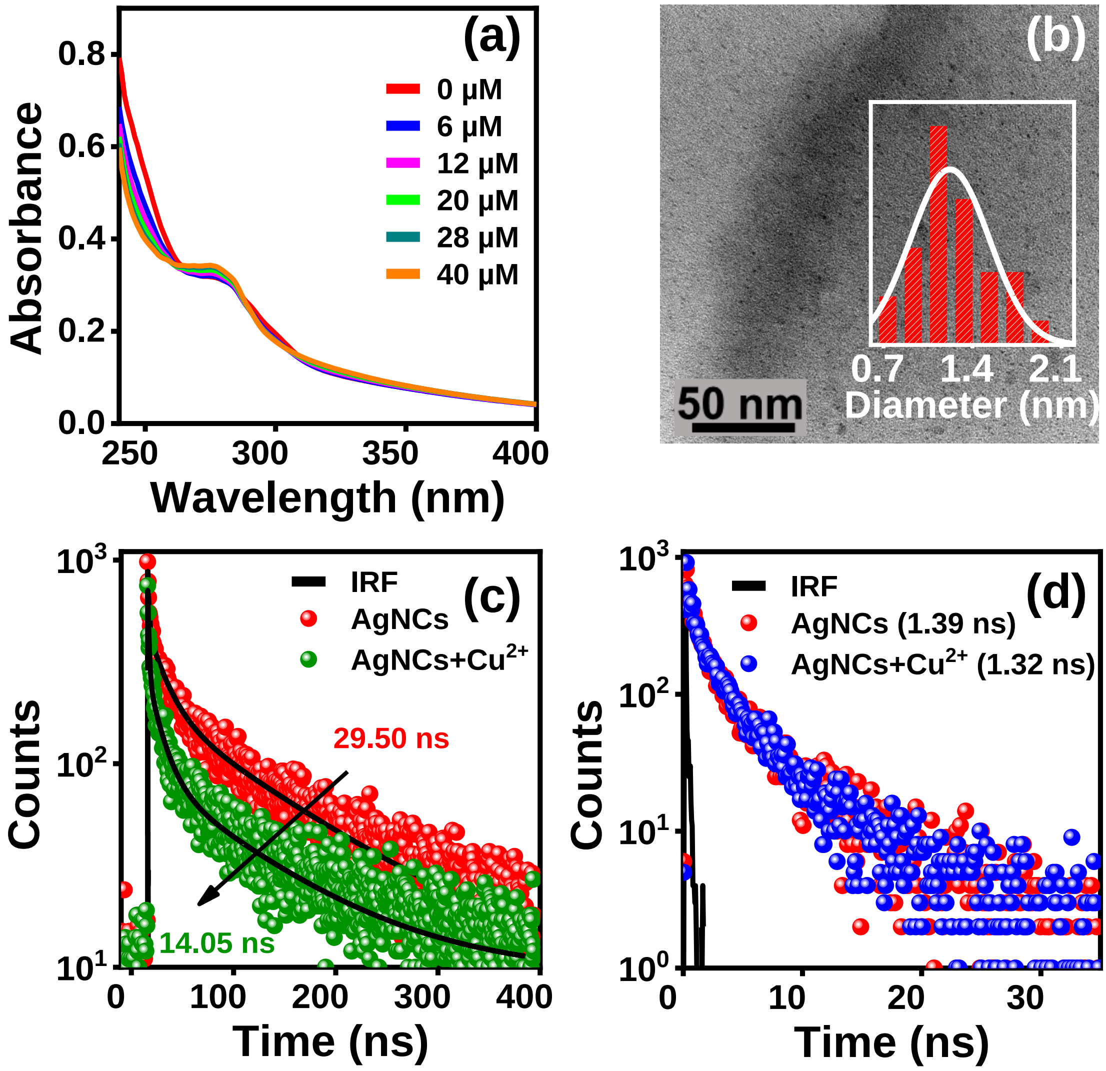

Figure 4.5. (a) UV−vis absorption spectra of AgNCs in the presence of different concentrations of Cu^{2+}. (b) TEM images of AgNCs after adding Cu^{2+} (Inset shows size distribution histogram). FL decay curve of AgNCs after Cu^{2+} (40 µM) addition at (c) 680 nm and (d) 450 nm. Copyright 2023 American Chemical Society

4.2.6 Smartphone-based detection of IO_4^- and Cu^{2+}

A precise quantitative analysis is not possible with bare human eyes. Thus developing a simple, portable, and reliable technique for on-site detection of environmentally toxic analytes is highly desirable. We introduced a smartphone-based convenient method for IO_4^- and Cu^{2+} detection. In this method, a cuvette containing AgNCs solution inside a 365 nm UV chamber was treated with different concentrations of IO_4^- (2-160 μM) and Cu^{2+} (2-40 μM) separately (**Figure 4.6a**). Using a Redmi smart-phone, the observed gradual transition in red emission of AgNCs solution with each added concentration of IO_4^- and Cu^{2+} was translated into relevant RGB value via an installed "RGB Color Detector" app. The obtained ratio of R/G value demonstrated linearity upto 80 μM (**Figure 4.6b**) and 40 μM (**Figure 4.6c**) with detection limits of 1.34 μM and 1.05 μM for IO_4^- and Cu^{2+}, respectively.

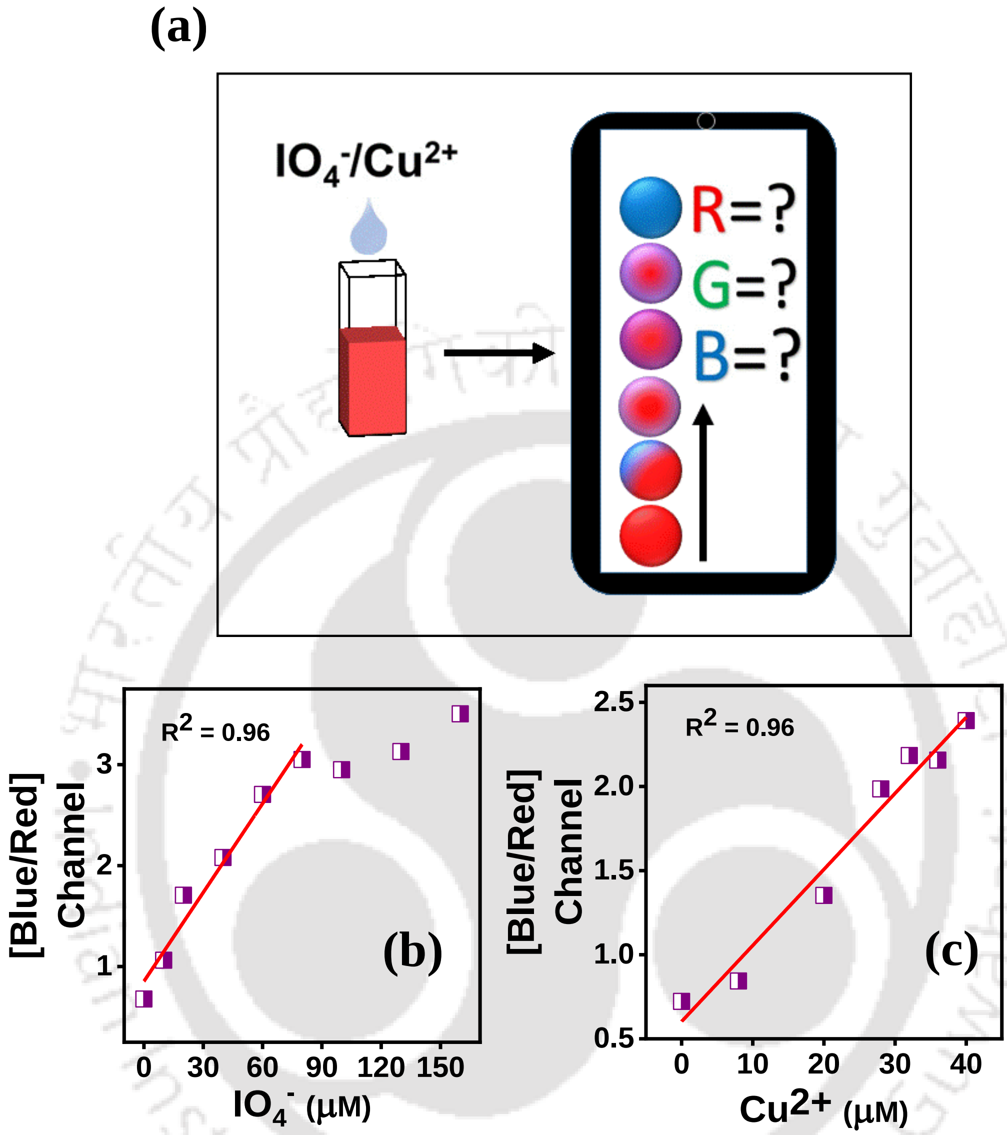

Figure 4.6. (a) Schematic for the smartphone-based detection of IO_4^- and Cu^{2+}. Intensity ratio vs IO_4^- concentration (b) and Cu^{2+} concentration (c). Copyright 2023 American Chemical Society

4.3 CONCLUSION

We report a facile approach for synthesizing BSA-capped AgNCs with blue (450 nm) and far-red (680 nm) emission. The 450 nm emission was attributed to the intrinsic emissive property of BSA, while the 680 nm emission corresponds to the encapsulated AgNCs. MALDI-mass spectrometry revealed that the core consists of Ag_{18} clusters along with a narrow distribution of clusters (Ag_{12}-Ag_{25}). Based on the ratiometric-detection method, the synthesized AgNCs allowed selective recognition of IO_4^- and Cu^{2+} ions with LOD values of 18.8 nM and 21.6 nM, respectively. Concentrations of IO_4^- -assisted conformational change in BSA, enhancing its intrinsic emissive property at 450 nm along with simultaneous quenching of 680 nm emission owing to dynamic quenching phenomena. On the other hand, Cu^{2+} concentrations induced quenching of only 680 nm emission due to a metal exchange phenomena leaving emission at 450 nm unchanged. IO_4^- and Cu^{2+} concentrations also led to a distinct transition in intense red emission of AgNCs solution to intense blue and light blue under a UV lamp. For on-site detection of IO_4^- and Cu^{2+}, a smartphone-based detection method was also introduced via "RGB value" calculation approach.

REFERENCES

1. D. Bain, S. Maity and A. Patra, *Phys. Chem. Chem. Phys.*, 2019, **21**, 5863-5881.
2. Z. Luo, K. Zheng and J. Xie, *ChemComm.*, 2014, **50**, 5143-5155.
3. M. Ghosh, S. Layek, N. Bera, P. K. Nandi, R. Hazra and N. Sarkar, *J. Phys. Chem. C*, 2022, **126**, 21319-21327.
4. S. Kundu, B. Ghosh, S. Nandi, M. Ghosh, A. Pyne, J. Chatterjee and N. Sarkar, *ACS Appl. Bio Mater.*, 2020, **3**, 4282-4293.
5. S. Bhunia, M. Mukherjee and P. Purkayastha, *Langmuir*, 2021, **37**, 3500-3507.
6. N. K. Das, S. Ghosh, A. Priya, S. Datta and S. Mukherjee, *J. Phys. Chem. C*, 2015, **119**, 24657-24664.
7. R. Xie, D. Su, Y. Song, P. Sun, B. Mao, M. Tian and F. Chai, *Talanta*, 2023, **260**, 124573.
8. J. Pang, R. Xie, S. Chua, Y. Zou, M. Tang, F. Zhang and F. Chai, *Spectrochim. Acta A*, 2021, **261**, 120035.
9. X. Yuan, Z. Luo, Y. Yu, Q. Yao and J. Xie, *Chem. Asian J.*, 2013, **8**, 858-871.
10. R. Xie, N. Zhang, Y. Qu, M. Tang, F. Zhang, F. Chai and Z. Su, *Nanotechnology*, 2021, **33**, 025501.
11. S. Qian, Z. Wang, Z. Zuo, X. Wang, Q. Wang and X. Yuan, *Coord. Chem. Rev.*, 2022, **451**, 214268.
12. Z. Wei, Y. Pan, G. Hou, X. Ran, Z. Chi, Y. He, Y. Kuang, X. Wang, R. Liu and L. Guo, *ACS Appl. Mater. Interfaces*, 2022, **14**, 2452-2463.
13. H. Santhakumar, R. V. Nair, D. M. Govindachar, G. Periyasamy and R. S. Jayasree, *ACS Sustain. Chem. Eng.*, 2023, **11**, 2102-2114.
14. L. Primitivo, M. De Angelis, A. Necci, F. Di Pietro, A. Ricelli, D. Caschera, L. Pilloni, L. Suber and G. Righi, *Nanoscale Adv.*, 2023, **5**, 627-632.

15. K. Mondal, A. Pramanik, T. Mondal, S. S. Panja, R. Sarkar and P. Kumbhakar, *J. Phys. Chem. Lett.*, 2022, **13**, 3079-3088.
16. G. Feng, W. Wu, S. Xu and B. Liu, *ACS Appl. Mater. Interfaces*, 2016, **8**, 21193-21200.
17. G. Yang, Z. Wang, F. Du, F. Jiang, X. Yuan and J. Y. Ying, *J. Am. Chem. Soc.*, 2023, **145**, 11879-11898.
18. G. Yang, X. Mu, X. Pan, Y. Tang, Q. Yao, Y. Wang, F. Jiang, F. Du, J. Xie, X. Zhou and X. Yuan, *Chem. Sci*, 2023, **14**, 4308-4318.
19. X. Niu, H. Gao and J. Du, *ACS Appl. Nano Mater*, 2022, **5**, 2350-2357.
20. P. Gao, S. Wu, X. Chang, F. Liu, T. Zhang, B. Wang and K.-Q. Zhang, *Bioconjugate Chem.*, 2018, **29**, 4140-4148.
21. P. Nath, M. Chatterjee and N. Chanda, *ACS Appl. Nano Mater*, 2018, **1**, 5108-5118.
22. C.-H. Chuang, W.-Y. Chen, W.-B. Tseng, A. Lin, C.-Y. Lu and W.-L. Tseng, *ACS Sustain. Chem. Eng.*, 2022, **10**, 2461-2472.
23. S. Li, Q. Ma, C. Wang, K. Yang, Z. Hong, Q. Chen, J. Song, X. Song and H. Yang, *Anal. Chem.*, 2022, **94**, 2641-2647.
24. L. Chen, M. Gharib, Y. Zeng, S. Roy, C. K. Nandi and I. Chakraborty, *Mater. Today Chem.*, 2023, **29**, 101460.
25. K. Qiu, A. Yadav, Z. Tian, Z. Guo, D. Shi, C. K. Nandi and J. Diao, *ACS Mater. Lett.*, 2022, **4**, 1565-1573.
26. A. Yadav, K. Kaushik, S. Sharma, F. Anjum and C. K. Nandi, *ACS Appl. Nano Mater*, 2022, **5**, 9260-9265.
27. A. Chatterjee, A. K. Sharma, S. Pramanick, O. S. Jaykishan and P. Purkayastha, *J. Phys. Chem. C*, 2023, **127**, 797-806.
28. S. Chakraborty, A. Nandy, S. Ghosh, N. K. Das, S. Parveen, S. Datta and S. Mukherjee, *Analyst*, 2021, **146**, 1455-1463.
29. J. Xie, Y. Zheng and J. Y. Ying, *J. Am. Chem. Soc.*, 2009, **131**, 888-889.
30. Y.-H. Lin and W.-L. Tseng, *Anal. Chem.*, 2010, **82**, 9194-9200.
31. J. Qiao, X. Mu, L. Qi, J. Deng and L. Mao, *ChemComm.*, 2013, **49**, 8030-8032.
32. C.-L. Liu, H.-T. Wu, Y.-H. Hsiao, C.-W. Lai, C.-W. Shih, Y.-K. Peng, K.-C. Tang, H.-W. Chang, Y.-C. Chien, J.-K. Hsiao, J.-T. Cheng and P.-T. Chou, *Angew. Chem.*, 2011, **50**, 7056-7060.
33. Z. Li, H. Peng, J. Liu, Y. Tian, W. Yang, J. Yao, Z. Shao and X. Chen, *ACS Appl. Mater. Interfaces*, 2018, **10**, 83-90.

34. H. Kawasaki, K. Hamaguchi, I. Osaka and R. Arakawa, *Adv. Funct. Mater.*, 2011, **21**, 3508-3515.
35. P. Sarkar, M. Saha, N. Nandi, D. K. Sahu and K. Sahu, *ACS Appl. Nano Mater*, 2022, **5**, 7670-7678.
36. C. Zhao, X. Zhang, K. Li, S. Zhu, Z. Guo, L. Zhang, F. Wang, Q. Fei, S. Luo, P. Shi, H. Tian and W.-H. Zhu, *J. Am. Chem. Soc.*, 2015, **137**, 8490-8498.
37. Q. Wan, S. Chen, W. Shi, L. Li and H. Ma, *Angew. Chem.*, 2014, **53**, 10916-10920.
38. Y. J. Ju, N. Li, S. G. Liu, L. Han, N. Xiao, H. Q. Luo and N. B. Li, *Sens. Actuators B Chem.*, 2018, **275**, 244-250.
39. T. Doussineau, A. Schulz, A. Lapresta-Fernandez, A. Moro, S. Körsten, S. Trupp and G. J. Mohr, *Chem. Eur. J.*, 2010, **16**, 10290-10299.
40. P. Li, T. Xie, N. Fan, K. Li and B. Tang, *ChemComm.*, 2012, **48**, 2077-2079.
41. N. Nandi, K. Choudhury, P. Sarkar, N. Barnwal and K. Sahu, *ACS Appl. Nano Mater*, 2022, **5**, 17315-17324.
42. N. Nandi, P. Sarkar and K. Sahu, *ACS Appl. Nano Mater*, 2021, **4**, 9616-9624.
43. N. Nandi, S. Gaurav, P. Sarkar, S. Kumar and K. Sahu, *ACS Appl. Bio Mater.*, 2021, **4**, 7605-7614.
44. N. Nandi, S. Gaurav, P. Sarkar, S. Kumar and K. Sahu, *ACS Appl. Bio Mater.*, 2021, **4**, 5201-5211.
45. N. Nandi, P. Sarkar and K. Sahu, *Mater. Today Chem.*, 2022, **26**, 101015.
46. P. Sarkar, N. Nandi, N. Barnwal and K. Sahu, *Mater. Today Chem.*, 2023, **27**, 101341.
47. X. Ran, Z. Wang, F. Pu, Z. Liu, J. Ren and X. Qu, *ChemComm.*, 2019, **55**, 15097-15100.
48. R. Jiang, Y. Zhang, Q. Zhang, L. Li and L. Yang, *ACS Appl. Nano Mater*, 2021, **4**, 9760-9767.
49. K. Zhong, C. Hao, H. Liu, H. Yang and R. Sun, *J. Photochem. Photobiol. A.*, 2021, **408**, 113100.
50. Y. Li, Q. Du, X. Zhang and Y. Huang, *Talanta*, 2020, **206**, 120202.
51. X.-J. Kong, J.-X. Tian, Y.-Z. Fang, T.-L. Chen, R. Yu, J.-Y. He, Z.-Y. Zhang and Q. Xiao, *Sens. Actuators B Chem.*, 2022, **356**, 131331.
52. K. A. Kristiansen, A. Potthast and B. E. Christensen, *Carbohydr. Res.*, 2010, **345**, 1264-1271.

53. H.-S. Lim, D. Cai, C. T. Archer and T. Kodadek, *J. Am. Chem. Soc.*, 2007, **129**, 12936-12937.
54. B. Liu, L. Burdine and T. Kodadek, *J. Am. Chem. Soc.*, 2006, **128**, 15228-15235.
55. W. Wang, L. Lu, K.-J. Wu, J. Liu, C.-H. Leung, C.-Y. Wong and D.-L. Ma, *Sens. Actuators B Chem.*, 2019, **288**, 392-398.
56. F. Chatraei and H. R. Zare, *Mater. Sci. Eng. C*, 2013, **33**, 721-726.
57. G. Avigad, *Carbohydr. Res.*, 1969, **11**, 119-123.
58. J. J. B. Nevado and P. V. González, *Analyst*, 1989, **114**, 989-990.
59. Y. Ni and Y. Wang, *Microchem. J.*, 2007, **86**, 216-226.
60. J. Emerit, M. Edeas and F. Bricaire, *Biomed. Pharmacother.*, 2004, **58**, 39-46.
61. Y. Fu, C. Ding, A. Zhu, Z. Deng, Y. Tian and M. Jin, *Anal. Chem.*, 2013, **85**, 11936-11943.
62. C. Guo and J. Irudayaraj, *Anal. Chem.*, 2011, **83**, 2883-2889.
63. J. C. Lukesh, III, M. J. Palte and R. T. Raines, *J. Am. Chem. Soc.*, 2012, **134**, 4057-4059.
64. H.-W. Li, Y. Yue, T.-Y. Liu, D. Li and Y. Wu, *J. Phys. Chem. C*, 2013, **117**, 16159-16165.
65. S. Hossain, Y. Niihori, L. V. Nair, B. Kumar, W. Kurashige and Y. Negishi, *Acc. Chem. Res.*, 2018, **51**, 3114-3124.
66. Y. Wang, L. Liu, L. Gong, Y. Chen and J. Liu, *J. Phys. Chem. Lett.*, 2018, **9**, 557-562.
67. Z. Wu, *Angew. Chem.*, 2012, **51**, 2934-2938.
68. X. Yuan, X. Dou, K. Zheng and J. Xie, *Part. Part. Syst. Charact.*, 2015, **32**, 613-629.

CHAPTER 5

Mercaptopropionic acid-assisted synthesis of green and blue emissive copper nanoclusters for multimodal sensing and white light applications

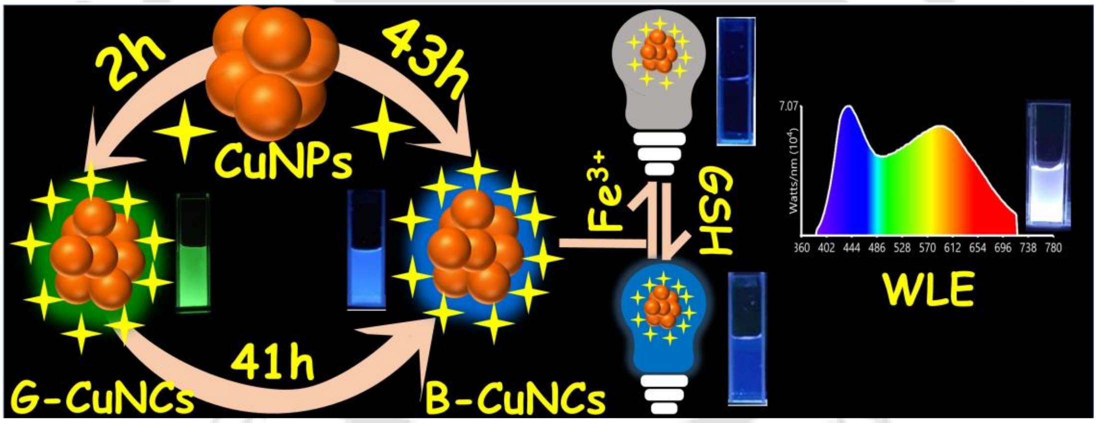

Manuscript: **Priyanka Sarkar**, Nilanjana Nandi, Neha Barnwal and Kalyanasis Sahu, "Mercaptopropionic acid-assisted synthesis of green and blue emissive copper nanoclusters for multimodal sensing and white light applications" *Materials Today Chemistry 27 (2023) 10134.*

[This page was intentionally left blank]

ABSTRACT

A time-controlled synthesis strategy for luminescent copper nanoclusters (CuNCs) was adopted via a two-step process. First, non-emissive copper nanoparticles (CuNPs) were formed by reducing copper salt with ascorbic acid (AA), and then the CuNPs were converted into green (G-CuNCs, λ_{em}= 520 nm) and blue emissive CuNCs (B-CuNCs, λ_{em}= 440 nm) after time-controlled treatment (2h and 43h) with mercaptopropionic acid (MPA). Transmission electron microscopy (TEM) and X-ray photoelectron spectroscopy (XPS) analysis unambiguously demonstrate the etching of CuNPs with the reduction of core size (from 6.09 nm for CuNPs to 2.67 nm and 1.92 nm for G-CuNCs and B-CuNCs, respectively) and a simultaneous lowering of the contribution of the +2 oxidation state of Cu species. Moreover, B-CuNCs showed selectivity and sensitivity towards Fe^{3+} and glutathione (GSH) via fluorescence (Fl) turn-off-on mechanism; the limit of detections (LODs) for respective analytes were 6.2 nM and 281 nM. The Fl turn-off mechanism by Fe^{3+} involves both static and dynamic quenching processes, whereas restoration of the Fl intensity of B-CuNCs was triggered by the GSH-induced reduction of Fe^{3+} to Fe^{2+} and subsequent release of Fe^{3+} from the surface of B-CuNCs. Finally, the synthesized B-CuNCs and G-CuNCs were employed for white light emission (WLE) with Commission Internationale d'Eclairage (CIE) coordinates of (0.33, 0.32) with the aid of another red-emitting GSH-capped gold nanocluster (GSH-AuNCs).

5.1 OVERVIEW

Fluorescent nanomaterials have widespread applications in material chemistry[1], sensing[2-4], photonics[5], bioimaging[6, 7], cancer therapy[8], bio sensing[9], and drug delivery[10]. Over the past few decades, metal nanoclusters (MNCs) have gained burgeoning attention owing to their potential to offer intriguing properties like ultrasmall size, tunable fluorescence, favorably high photostability[11], and biocompatibility[12]. Metal nanoclusters of coinage metals like gold (Au) and silver (Ag) have been explored extensively[13-17]; however, the ease of oxidation of Cu(0) to Cu(II) compared to Ag(0) to Ag(I) and Au(0) to Au(I) makes the synthesis of stable copper nanoclusters (CuNCs) challenging[18]. Cu is a more abundant and cheaper element than the congeners (Ag and Au); hence, synthesizing stable CuNCs demands more profound attention. Primarily, the synthesis of MNCs can be achieved via two strategies: (a) bottom-up method, which involves chemical reduction of metal salts as precursors, and (b) top-down method involves core-etching of pre-formed larger nanomaterials (>3 nm)[19]. Since the top-down method could offer advantages like delicate control over the tuning of emissive nanoclusters within a single system, many research groups have reported the synthesis of AuNCs and AgNCs from their larger counterparts, e.g., nanoparticles and nanorods[20-25]. However, few reports are available to synthesize CuNCs with emission tunability and bright luminescent features. CuNCs synthesized from non-luminescent copper nanocrystals via the size-focusing etching method have been reported[26]. In another literature, CuNCs from non-luminescent CuNPs has been synthesized via core-etching method using excess reduced glutathione[27].

Maintaining adequate levels of metal ions and biologically active molecules in environmental sources and the human body is pivotal. Iron (Fe^{3+}) is integral to the heme group and is crucial for specific biological processes like oxygen transport, electron transport, and enzyme activity[28]. Even a moderate deficiency or surplus levels of Fe^{3+} can lead to life-threatening diseases like anemia, Alzheimer's disease, Parkinson's syndrome, and cancer.[29-32] The tripeptide biomolecule glutathione (GSH) is also crucial to various physiological processes[33, 34]. An abnormal concentration of GSH can prompt many fatal diseases in the human body, like liver damage, cancer, loss of leukocytes, degeneration of neurons, aging, and autism syndrome in children.[35-37] Although a variety of approaches have been applied for Fe^{3+} and GSH detection, including high-performance-liquid chromatography (HPLC)[38], electroanalytical detection[39], electrophoresis[40], electrochemical detection[41], surface-enhanced Raman scattering (SERS)[42], however, Fl-based detection has always benefitted researchers displaying a fast response and superior selectivity.[43-46] The focus on the Fl-based off-on detection principle has attracted considerable attention, where generally, an ion induces the quenched state of the emissive probe, which is further recovered by another analyte, allowing the detection of both analytes within the same system.

Exploring efficient and promising materials for fabricating white light emitting systems has recently gained extensive attention. MNCs are exploited extensively for fabricating white light emission (WLE) [47, 48], defining its potential use in light-emitting diode (LED) based devices.. Developing an efficient white light emitting system demands that the Fl spectrum of the illuminating source should cover the entire visible range (400-700 nm), which can only be achieved from the presence of three primary colors (blue, green, and red) or two complementary colors. Being environmentally benign, MNCs can be a befitting alternative to extensively energy-consuming filament-based devices traditionally used to construct WLE sources. Additionally, most WLE sources are constructed by a precise combination of different colors originating from different emissive sources; thus, a composite made from a similar nanoscale system, covering the full visible wavelength range, is highly preferable.

Herein, we report a strategy to synthesize CuNCs with two distinct emission colors from a one-pot reaction mixture. A thiol ligand, mercaptopropionic acid (MPA), was incorporated into a non-luminescent nanoparticle (CuNPs) system prepared from the ascorbic acid reduction of copper salt. Subsequently, the reduction and etching of the non-luminescent system by MPA produces two types of luminescent CuNCs in a time-controlled manner. The formation kinetics from time-dependent Fl data of the reaction mixture reveals the generation of G-CuNCs ($\lambda_{\mathrm{ex}}^{\mathrm{max}}$=520 nm) and B-CuNCs ($\lambda_{ex}^{max}$=440 nm) after 2 h and 43 h of reduction and etching process by MPA. XPS and TEM analyses were employed to understand the conversion mechanism. The G-CuNCs showed excitation-independent emission, while the emission spectra of B-CuNCs show slight dependency on the excitation wavelength. The B-CuNCs showed a sensitive and selective response towards Fe^{3+} and GSH by successive Fl turn-off and turn-on properties. The LODs for Fe^{3+} and GSH were calculated to be 6.2 nM and 281 nM. B-CuNCs also showed satisfactory results in determining Fe^{3+} and GSH in real samples. Association between the surface ligands of B-CuNCs and Fe^{3+} facilitated the formation of non-luminescent aggregated structures, inducing electron transfer from B-CuNCs to Fe^{3+}, leading to quenching of emission intensity (turn-off state); however, the quenched emission intensity could be restored (turn-on state) after addition of GSH. Mechanistic investigations reveal that GSH leads to the reduction of Fe^{3+} to Fe^{2+}, subsequently releasing Fe^{3+} from the surface of B-CuNCs. Since our synthetic method offers the advantage of producing two differently emissive CuNCs in the blue and green regions, we explored its feasibility for fabricating WLE system.

The optimized concentration of the synthesized CuNCs was later harnessed for white light emission (WLE) with adequate CIE coordinates (0.33, 0.32).

5.2 RESULTS AND DISCUSSION

5.2.1. Structural analysis

Synthesis of the CuNCs was achieved via a two-step reduction and etching mechanism. The first step involves synthesizing a CuNPs system using ascorbic acid (AA)-reduction of copper salt in water at room temperature. Here, AA-assisted partial reduction of Cu^{2+} in the system to Cu^{+}/Cu^{0}, results in a non-luminescent CuNPs system. In the second step, the introduction of mercaptopropionic acid (MPA) to the CuNPs system induces etching and further reduction of the non-luminescent system to green emissive CuNCs (G-CuNCs) and blue emissive CuNCs (B-CuNCs) after 2 h and 43 h, respectively at room temperature. Thus, depending on the reaction time, the synthesis route generates CuNCs that exhibit emission at different wavelengths. A schematic illustration of the synthetic route is presented in **Scheme 5.1.**

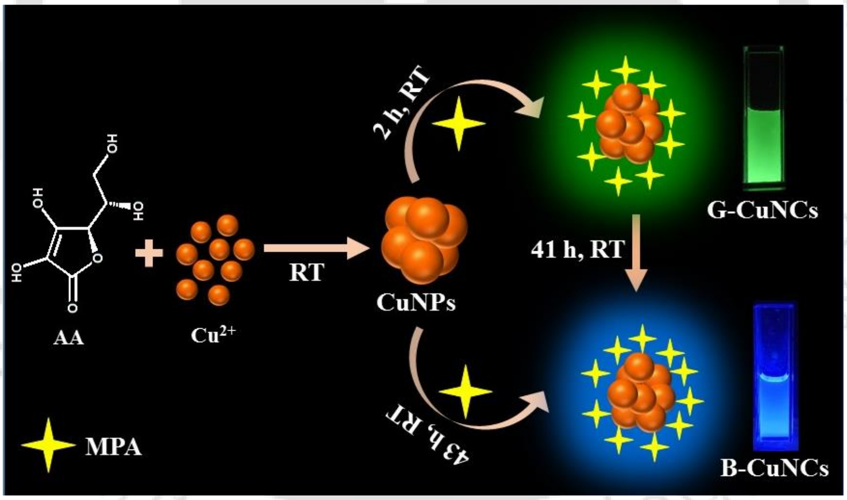

Scheme 5.1. Schematic illustration of the synthesis of G-CuNCs and B-CuNCs. Copyright 2023 Elsevier

We utilized TEM and XPS analysis to confirm the role of MPA as an etchant and a reducing agent in the two-step synthetic route. TEM images of the CuNPs system (**Figure 5.1a**) show the presence of particles with spherical morphology with an average size diameter of 6.09 ± 0.75 nm, whereas TEM images taken after 2 h (**Figure 5.1b**) and 43 h (**Figure 5.1c**) of MPA addition displayed images with much smaller sizes with average diameters of 2.67 ± 0.22 nm and 1.92 ± 0.3 nm, respectively. Thus, TEM analysis indicates that with the introduction of MPA to CuNPs, the core size of the system decreases leading to the generation of green and blue emissive CuNCs after 2 h and 43 h, respectively. Moreover, XPS analysis was employed to study the evolution of the oxidation states of Cu species in the system with time. Deconvolution of the Cu peak in the CuNPs system (**Figure 5.1d**) shows the presence of characteristic $2p_{3/2}$ peak of Cu(II) at 935.4 eV and $2p_{1/2}$ peak of Cu(II) at 955.8 eV along with $2p_{3/2}$ and $2p_{1/2}$ peaks of Cu(0)/Cu(I) at 932.3 eV and 952.2 eV, respectively, indicating the co-existence of a substantial amount of Cu^{2+} in the system along with Cu(0) and Cu(I)[49]. However, the deconvolution of the Cu peak obtained after 2 h from the addition of MPA to the CuNPs system (**Figure 5.1e**) reveals a relative decrement in the amount of Cu^{2+} and further deconvolution of the Cu peak obtained after 43 h from the addition of MPA to CuNPs (**Figure 5.1f**), shows the presence of only $2p_{3/2}$ and $2p_{1/2}$ peaks of Cu(0)/Cu(I) at 932.5 eV and 952.6 eV[50] respectively with no characteristic peak of Cu^{2+} in the system. Thus, the experimental analysis indicates a decrease in the contribution of the +2 oxidation state of Cu species and a reduction in the core size with time, leading to the successful generation of CuNCs with wavelength-dependent emission.

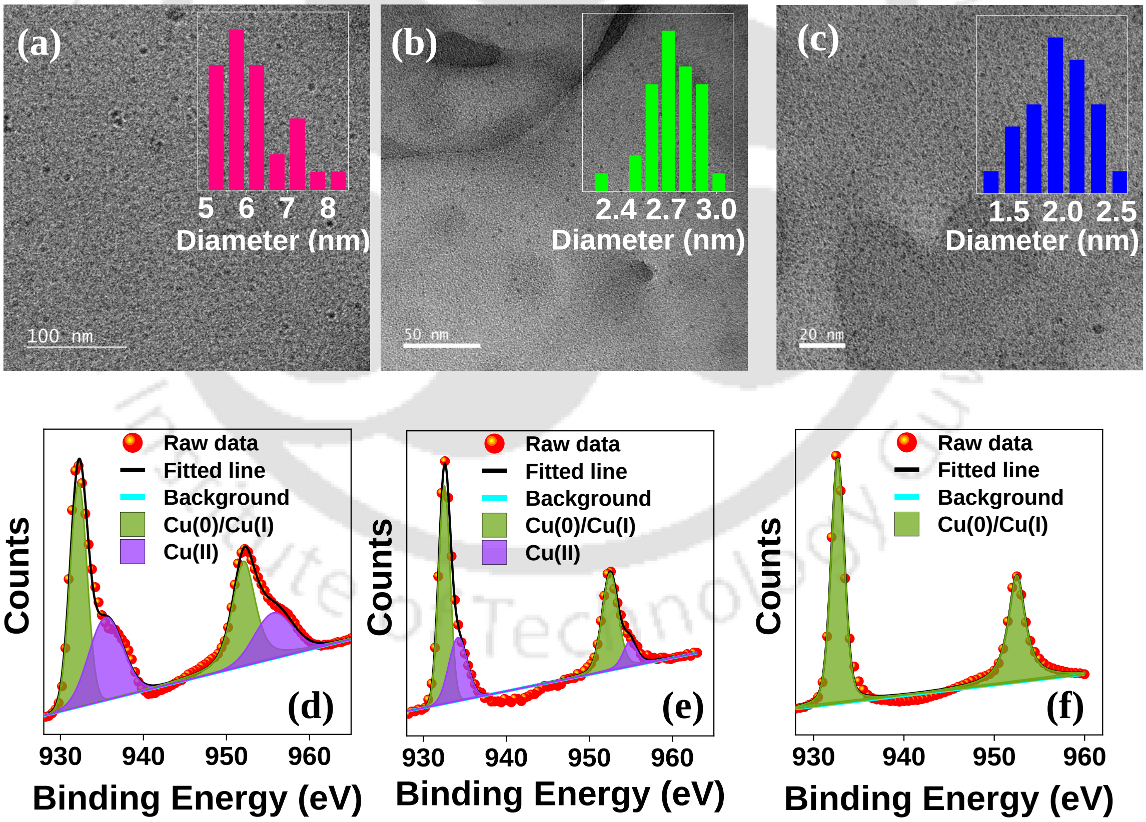

Figure 5.1. TEM images and corresponding size distributions (inset) (a) CuNPs (b) G-CuNCs (c) B-CuNCs. High-resolution XPS spectra of Cu in (d) CuNPs (e) G-CuNCs (f) B-CuNCs. Copyright 2023 Elsevier

We also performed Fourier-transformed infrared spectroscopy (FTIR) to confirm the binding mode of the MPA ligand to B-CuNCs. The FTIR spectrum of free MPA (**Figure A.5.1**) shows a small peak at 2564 cm^{-1}, which is a signature of the –SH bond. However, the FTIR spectrum for B-CuNCs does not show any such peak. Thus this comparison confirms that the MPA molecules are bonded to the surface of B-CuNCs through the Cu-S bond. Moreover, the FTIR spectrum of B-CuNCs also showed characteristic peaks of–C=O, C=C, and C-O stretching vibrations at 1730 cm^{-1}, 1630 cm$^{-1,}$ and 1079-1040 cm^{-1}, respectively.

5.2.2. Optical characterization of G-CuNCs and B-CuNCs

The UV-vis absorption spectrum (**Figure 5.2a**) of the CuNPs system shows a distinct small hump at 320 nm. However, the absorption spectrum did not show any surface plasmon resonance (SPR) peak at around 510 nm, which might be because the size of the particles was not large enough to give rise to a distinct SPR peak. After 2 h from the addition of MPA, slight persistence of the 320 nm absorption hump is still seen; however, the hump disappears in the spectrum recorded at 43 h from the addition of MPA (**Inset of Figure 5.2a**). The absorption spectrum of the as-prepared B-CuNCs exhibits a monotonically increasing nature below 500 nm, which differs from the absorption spectrum of pure MPA and ascorbic acid (**Figure A.5.2a**). Thus, the change in the absorption spectrum of the system with time is indicative of the structural changes occurring in the core of the non-luminescent CuNPs system in the presence of MPA.

Emission spectra were recorded at various times at 370 nm excitation wavelength to monitor the eventual generation of CuNCs with different color emissions. **Figure 5.2b** depicts the emission spectra of the CuNPs system recorded from 2h to 49h after adding MPA to the system. The CuNCs show emission at different wavelengths as time elapsed after adding MPA. After 2h of MPA addition, the CuNCs show an emission maximum at 520 nm and a shoulder peak at 440 nm, indicating a large amount of G-CuNCs and a minimal amount of B-CuNCs in the system. The emission spectrum recorded at 4h also shows the exact spectral nature but of slightly lower intensity, while the emission spectrum recorded at 6h shows a significant onset of fluorescence emission at 440 nm along with a decrease in emission intensity at 520 nm, suggesting a gradual increase in the amount of B-CuNCs and the corresponding decrease in the amount of G-CuNCs with time. From 6h to 43h the emission intensity at 440 nm continues to increase, with a gradual decrease in emission intensity at 520 nm. The emission intensity at 440 nm does not change further after 43 h indicating the completion of the process. The emission spectrum at 43 h shows maximum intensity at 440 nm and a shoulder peak at 520 nm, demonstrating the presence of a large amount of B-CuNCs and very few G-CuNCs in the system. **Figure A.5.2b** shows time versus emission intensity variation at 520 and 440 nm wavelengths.

We have also optimized the concentration of MPA required to synthesize tunable emissive CuNCs to obtain better fluorescence intensity. **Figure A.5.2c and Figure A.5.2d** show that 5.5 mM MPA yields CuNCs with the highest luminescence intensity. **Figure 5.2c** shows that the emission maximum of G-CuNCs at 520 nm does not change with the excitation wavelength. However, the emission spectrum of B-CuNCs was excitation wavelength dependent; the emission wavelength shifts from 430 nm to 480 nm with the change of excitation wavelength from 300 to 420 nm (**Figure 5.2d**). The G-CuNCs and B-CuNCs solutions showed bright green and blue emissions under a 365 nm UV lamp (**Inset of Figure 5.2c and Figure 5.2d)**. The quantum yield (QY), calculated using quinine sulfate (57.7% in 0.1 M H_2SO_4) as the standard, was 1.0% for G-CuNCs and 2.4% for B-CuNCs. The excitation spectra for both G-CuNCs ($\lambda_{em} = 520$ nm) and B-CuNCs ($\lambda_{em} = 440$ nm) show maximum intensity at 370 nm (**Figure 5.2e**). The fluorescence decay measured using a 375 nm laser source for G-CuNCs at 520 nm shows lifetime components of 0.91 ns (12%), 2.75 ns (14%), and 0.04 ns (74%), while for B-CuNCs at 440 nm was found to be 1.03 ns (43%), 0.1 ns (46%) and 2.39 ns(11%) (**Figure 5.2f and Table A.5.1**).

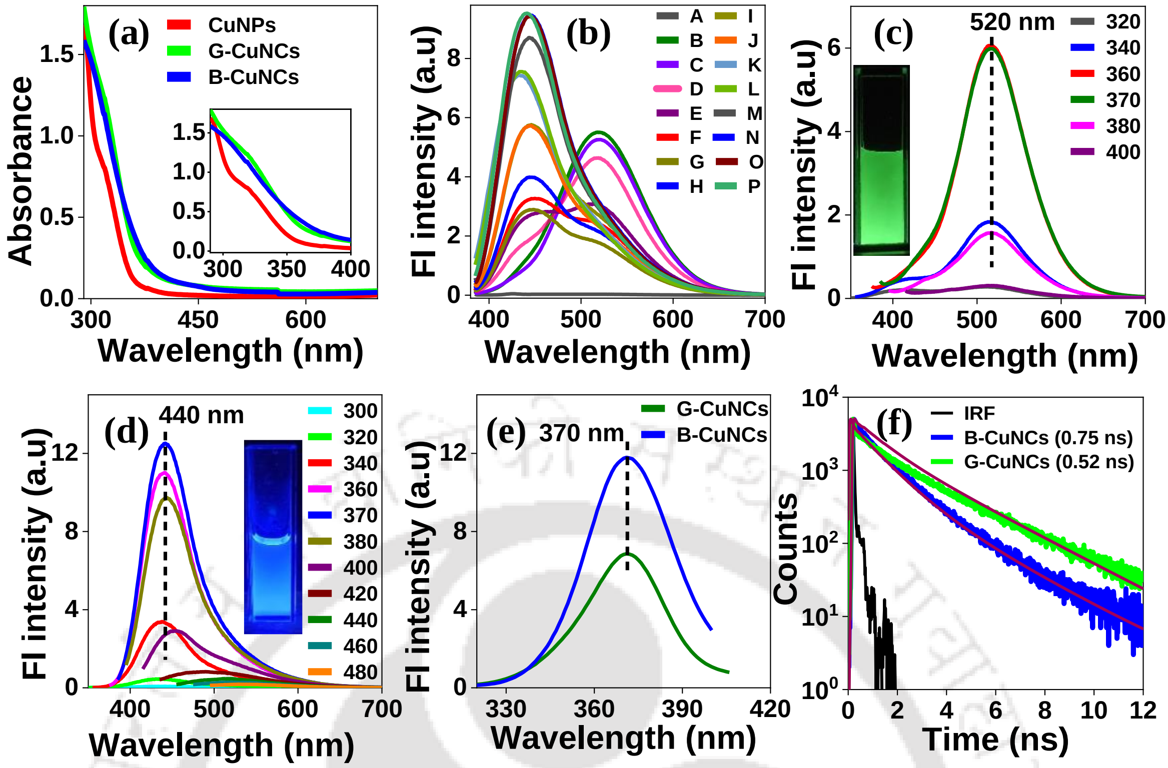

Figure 5.2 (a) UV-vis spectra of CuNPs, G-CuNCs, B-CuNCs .(b) Time-dependent emission spectra (λ_{ex} = 370 nm) ((A) CuNPs, (B) 2h, (C) 4h, (D) 6h, (E) 8h, (F) 10h, (G) 12h, (H) 14h, (I) 18h, (J) 22h, (K) 26h, (L) 31h, (M) 37h, (N) 43h, (O) 46h, (P) 49h. Fl spectra at different excitation wavelengths for (c) G-CuNCs and (d) B-CuNCs. (e) Excitation spectra of G-CuNCs (λ_{em} = 520 nm) and B-CuNCs (λ_{em} = 440 nm). (f) Fl decays of G-CuNCs and B-CuNCs at 520 nm and 440 nm emission wavelengths. Copyright 2023 Elsevier

The optical stability of B-CuNCs was checked for a broad pH range (2-12); **Figure A.5.2e** shows almost negligible alteration of the emission intensity under varying pH conditions. The photostability of G-CuNCs and B-CuNCs was also examined under continuous irradiation by the excitation source for half hour **(. Figure A.5.2f)**. The optical property of B-CuNCs can be successfully preserved for three months when kept at 4°C, and that of G-CuNCs can be preserved for two months when kept at -20°C **(. Figure A.5.2g and Figure A.5.2h)**.

5.2.3. Fluorescence-based on-off-on detection of Fe^{3+} and glutathione (GSH)

The potential of the synthesized B-CuNCs was tested for Fl-based detection of metal ions. **Figure 5.3a** shows that a gradual increase of Fe^{3+} concentrations from 0 to 200 μM induces a significant decrement of Fl intensity at 440 nm and finally leads to 80% quenching at 200 µM of Fe^{3+}. The blue emission under a UV lamp also diminishes **(Inset of Figure 5.3a)**. **Figure A.5.3a** shows an incubation time of only 1 min is sufficient for a significant reduction of Fl intensity in the presence of Fe^{3+}. The intensity ratio plot (F_0/F, where F_0 and F represent emission intensities of B-CuNCs without and with the addition of Fe^{3+}, respectively) shows deviation from linearity at higher concentrations (**Figure 5.3b**); however, at lower concentrations, it follows the Stern-Volmer linearity pattern from 0 to 50 μM. LOD calculated using the conventional $3\sigma/S$ formula (σ signifies the standard deviation of blank signal and S signifies slope of the linear calibration plot of FL intensity against the analyte concentration) was found to be 6.2 nM. The selectivity performance was demonstrated by investigating the impact of other metal ions on the emission intensity of B-CuNCs. **Figure 5.3c** shows that other metal ions do not significantly alter the Fl spectrum of B-CuNCs, illustrating its highly selective nature towards Fe^{3+}. Thus, based on the excellent sensitivity and selectivity, B-CuNCs can be employed as a potential optical sensor for Fe^{3+}.

Interestingly, emission intensity gradually recovers after adding glutathione (GSH) to the quenched B-CuNCs-Fe^{3+} system (**Figure 5.3d**). The fluorescence recovery was easily realized upon illuminating with a UV lamp; the blue emission, which was diminished by adding Fe^{3+}, was seen to regenerate in the presence of GSH (**Inset of Figure 5.3d**). The recovery time was also quite prompt. **Figure A.5.3b** shows that after an incubation time of 6 min from the addition of GSH, the increment in Fl intensity acquires a constant state. The increment in the emission intensity ratio plot (F/F_0, where F and F_0 represent emission intensity of B-CuNCs+Fe^{3+} in the presence and absence of GSH) follows a linear relationship at lower concentrations of GSH from 0 to 100 μM (**Figure 5.3e**). The calculated LOD value was 281 nM. The fluorescence response of B-CuNCs+Fe^{3+} towards other comparative amino acids and reducing agents was also monitored. **Figure 5.3f** shows that the Fl restoration ratio in the case of GSH is notably higher than other competing amino acids. Although cysteine (Cys) and ascorbic acid (AA) showed only a moderate emission intensity restoration, the restoration ratio is only 37-39% in the presence of 300 μM of Cys and AA. Thus, GSH selectively recovers the quenched emission intensity of B-CuNCs from the B-CuNCs+Fe^{3+} system.

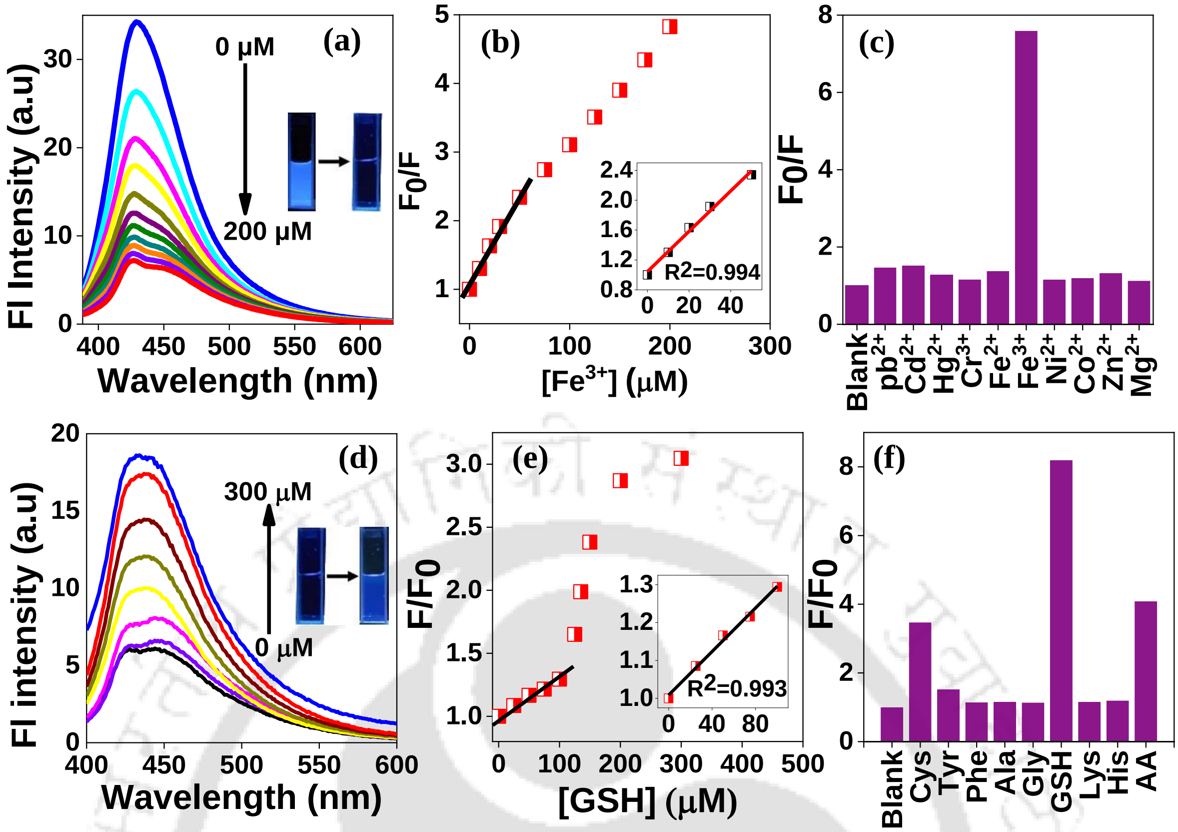

Figure 5.3. (a) Fl spectra of B-CuNCs in the presence of various concentrations of Fe^{3+} (0−200 μM). The inset shows the digital photograph of the visible Fl of B-CuNCs and its complete depletion in the presence of 200 μM Fe^{3+} under a 365 nm UV lamp. (b) The ratio of the Fl intensity with different concentrations of Fe^{3+}. The inset shows the ratio of Fl intensity linearly plotted with different concentrations of Fe^{3+}. (c) Selectivity plot of B-CuNCs in presence of different metal ions (Here F_0 and F represents Fl intensity of B-CuNCs in absence and presence of respective metal ions). (d)Turn-on FL spectra of B-CuNCs-Fe^{3+} system on gradual addition of GSH. The inset shows the digital photograph of the recovery of blue emission of B-CuNCs in the presence of 300 μM of GSH under a 365 nm UV lamp. (e) Turn on the intensity ratio plot with different concentrations of GSH. The inset shows the ratio of recovered Fl intensity linearly plotted with different concentrations of GSH (f) Selectivity plot of B-CuNCs+ Fe^{3+} in presence of different comparative amino acids and reducing agent. (Here F_0 and F represents Fl intensity of B-CuNCs+ Fe^{3+} in absence and presence of respective amino acids). Copyright 2023 Elsevier

5.2.4. Fluorescence turn-off mechanism for Fe^{3+} detection

Several experiments were carried out to unveil the mechanisms responsible for Fe^{3+}-mediated quenching of the emission intensity of B-CuNCs. Fe^{3+} has a broad absorption spectrum in the 260-400 nm range, which has considerable spectral overlap with the absorption spectrum of B-CuNCs (**Figure A.5.4a**). This overlap could likely cause an inner filter effect (IFE) that may lead to Fl suppression of B-CuNCs. The observed quenching efficiency and the corrected quenching efficiency obtained after removing the IFE contribution were calculated for each added concentration of Fe^{3+} to evaluate the contribution of IFE (**Table A.5.2**). As shown in **Figure A.5.4b,** there was no significant difference between the observed and the corrected fluorescence quenching efficiency. The results strongly indicate that IFE has no contribution to the fluorescence quenching process. UV-vis spectrum of B-CuNCs recorded for each added concentration of Fe^{3+} (**Figure 5.4a**) shows that the absorbance increases with the increasing concentration of Fe^{3+}. Moreover, metal ions other than Fe^{3+} do not change the absorption spectrum of B-CuNCs **(Figure A.5.4c)**. TEM images captured after adding Fe^{3+} to B-CuNCs (**Figure 5.4b**) showed the formation of aggregated structures with a diameter of 5.13 ± 0.90 nm. The above results indicate that an association might have occurred between the surface ligands capping B-CuNCs and $Fe^{3+,}$ which further induces the formation of non-luminescent aggregated structures.

Additionally, the fluorescence decays of B-CuNCs in the presence of different concentrations of Fe^{3+} show a gradual decrease in the average lifetime from 0.75 ns to 0.05 ns at 200 μM of Fe^{3+} (**Figure 5.4c and Table A.5.3**). Thus, the results corroborate that quenching of B-CuNCs by Fe^{3+} occurs due to the synergistic effect of static and dynamic processes. Static quenching arises due to the association-induced aggregation of B-CuNCs in the presence of Fe^{3+}. On the other hand, the strong electron-withdrawing capability of the half-filled d-orbitals of Fe^{3+}([Ar]$3d^5 4s^0$) promotes the transfer of electrons from B-CuNCs to Fe^{3+} contributing to the dynamic quenching process occurring in B-CuNCs-Fe^{3+} system.

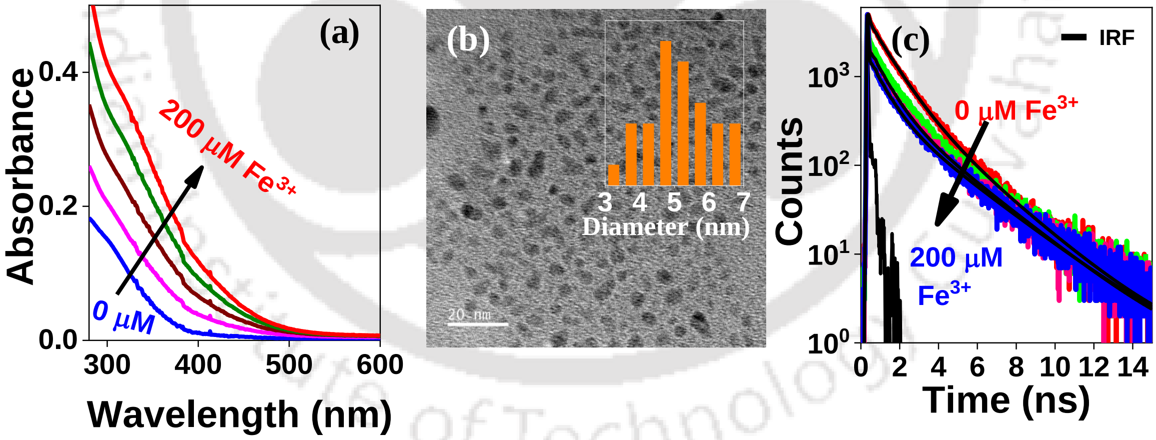

Figure 5.4. (a) UV-vis spectra of B-CuNCs in the presence of different concentrations of Fe^{3+}. (b) TEM images of aggregated B-CuNCs after addition of Fe^{3+}(Inset shows size distribution histogram). (c) Fl decays of B-CuNCs in the presence of different concentrations of Fe^{3+}. Copyright 2023 Elsevier

5.2.5. Fluorescence turn-on mechanism for GSH detection

The quenched emission intensity of B-CuNCs recovers gradually upon adding GSH to the B-CuNCs-Fe^{3+} system. However, GSH has no effect on the emission intensity of pure B-CuNCs; the intensity was almost unaltered upon treatment with excess GSH concentration

(**Figure A.5.5a**). Thus the enhancement of emission intensity of the B-CuNCs-Fe^{3+} system may be attributed to the interaction of GSH with Fe^{3+}. The regeneration of quenched emission intensity can be ascribed to the reducing property of GSH. To investigate this, 1,10-phenanthroline was introduced into B-CuNCs-Fe^{3+}, B-CuNCs-Fe^{3+}-GSH and B-CuNCs-GSH systems. The absorption spectrum shows a hump at around 515 nm for the B-CuNCs-Fe^{3+}-GSH system only (**Figure 5.5a**), which may be attributed to the complexation between Fe^{2+} and 1,10-phenanthroline (**Figure A.5.5b**). The appearance of reddish-orange color upon introduction of 1,10-phenanthroline into the B-CuNCs-Fe^{3+}-GSH system was evident in the photographs taken under normal light (**Figure 5.5b)**. Further, the UV-visible absorption spectrum of the B-CuNCs-Fe^{3+} system recorded in the presence of different concentrations of GSH shows gradual regeneration of the absorbance spectrum of B-CuNCs (**Figure 5.5c**). Thus, many potential heterogenic groups like oxygen, nitrogen, and sulfur in GSH preferentially bind to $Fe^{3+,}$ assisting GSH to reduce Fe^{3+} to Fe^{2+}, which in turn triggers the release of Fe^{3+} from the surface of B-CuNCs, causing regeneration of the quenched emission intensity.

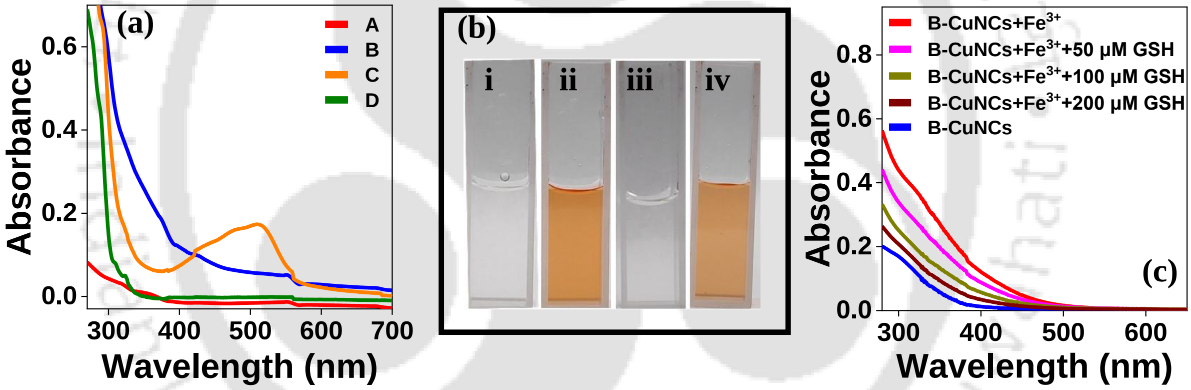

Figure 5.5 (a) UV-vis spectra of (A) B-CuNCs, (B) B-CuNCs+Fe^{3+}+1,10-phenanthroline, (C) B-CuNCs+Fe^{3+}+GSH+1,10-phenanthroline and (D) B-CuNCs+GSH+1,10-phenanthroline. (b) Digital photograph of (i) 1,10-phenanthroline (ii) 1,10-phenanthroline + Fe^{2+} (iii) B-CuNCs+ Fe^{3+}+ 1,10-phenanthroline (iv) B-CuNCs+ Fe^{3+}+GSH+ 1,10-phenanthroline solutions. (c) UV-vis spectra of B-CuNCs+ Fe^{3+} in the presence of different concentrations of GSH. Copyright 2023 Elsevier

5.2.6. Fabrication of white light emission (WLE)

Here, initially, orange-red emitting GSH-AuNCs[51] were mixed with an increasing concentration of blue emitting B-CuNCs to obtain two peaks of almost similar intensity, followed by the gradual addition of green-emitting G-CuNCs. **Figures 5.6a-c** show the emission spectra of B-CuNCs, G-CuNCs, and GSH-AuNCs exhibiting Commission Internationale d'Eclairage (CIE) coordinates of (0.16, 0.11), (0.25,0.49) and (0.52,0.44) respectively at an excitation wavelength of 370 nm. **Figure A.5.6a** and **Table A.5.4** show variation in CIE coordinates corresponding to various combinations of concentrations used during the optimization procedure. Finally, solution phase WLE was achieved at an excitation wavelength of 370 nm by mixing 1 mL of as-synthesized GSH-AuNCs, 40 µL of B-CuNCs, and 40 µL of G-CuNCs in 1 mL of water (**Figures 5.6d**). The solution mixture exhibited CIE coordinates of (0.33, 0.32) (**Figures 5.6e**), which closely represented the chromaticity of perfect white light (0.33, 0.33). The emission spectrum of the solution mixture covered the entire visible range, as shown in **Figures 5.6d,** illuminating WLE under a 365 nm UV lamp (**Inset of Fig. 5.6d**).

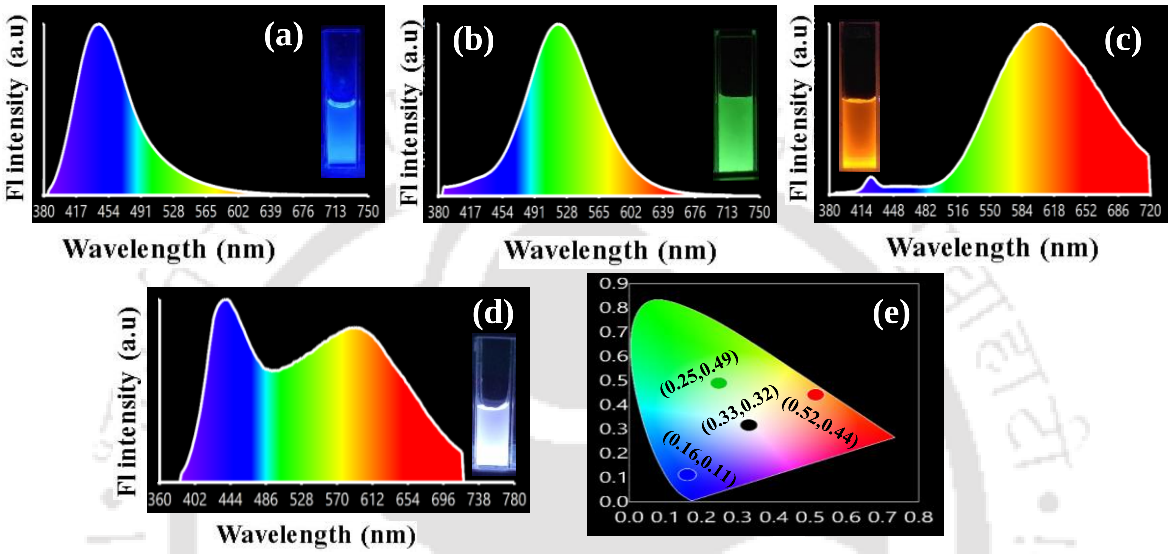

Figure 5.6 Emission spectra of (a) B-CuNCs (b) G-CuNCs (c) GSH-AuNCs (d) optimized mixture of the solution containing B-CuNCs, G-CuNCs and GSH-AuNCs emitting WLE. Inset shows a digital photograph of the respective solutions under a 365 nm UV lamp. (e) CIE chromaticity coordinates of B-CuNCs (blue dot), G-CuNCs (green dot), GSH-AuNCs (red dot), and WLE emitting solution mixture (black dot). Copyright 2023 Elsevier

5.3 CONCLUSION

In summary, a two-step methodology is described to synthesize time-based emission wavelength-dependent blue and green emissive CuNCs from non-emissive CuNPs. The MPA plays a key role in gradually transforming non-luminescent CuNPs to luminescent CuNCs by reducing the core size and the +2 oxidation state of copper in CuNPs. The as-prepared CuNCs display good photostability and water solubility with QY of 1.0% for G-CuNCs and 2.4% for B-CuNCs. The fl-based turn-off-on strategy allowed selective detection of Fe^{3+} and GSH employing B-CuNCs. The sensing method also proved feasible for determining Fe^{3+} and GSH in few real samples with satisfactory results. Quenching of emission intensity of B-CuNCs is caused due to association of Fe^{3+} with the surface ligands of B-CuNCs inducing aggregation of nanoclusters into non-fluorescent structures followed by transfer of electrons from B-CuNCs to Fe^{3+}. Further, the addition of GSH to the B-CuNCs-Fe^{3+} system reduced Fe^{3+} present in the system to $Fe^{2+,}$ prompting the release of Fe^{3+} from the surface of B-CuNCs, thus restoring the quenched emission intensity. Interestingly, the generation of WLE with CIE coordinates of (0.33, 0.32) at an excitation wavelength of 370 nm was accomplished by employing an optimized concentration of the synthesized CuNCs.

REFERENCES

1. G. Schmid, *Clusters and Colloids: From Theory to Applications*, Wiley, 2008.
2. X.-W. Hua, Y.-W. Bao, J. Zeng and F.-G. Wu, *ACS Appl. Mater. Interfaces*, 2019, **11**, 32647-32658.
3. N. Nandi, P. Sarkar and K. Sahu, *ACS Appl. Nano Mater*, 2021, **4**, 9616-9624.
4. L. Fang, M. Wu, C. Huang, Z. Liu, J. Liang and H. Zhang, *J. Mater. Chem. A*, 2020, **8**, 21317-21326.
5. A. Monguzzi, M. Ballabio, N. Yanai, N. Kimizuka, D. Fazzi, M. Campione and F. Meinardi, *Nano Lett.*, 2018, **18**, 528-534.
6. N. Nandi, S. Gaurav, P. Sarkar, S. Kumar and K. Sahu, *ACS Appl. Bio Mater.*, 2021, **4**, 7605-7614.
7. N. Nandi, S. Gaurav, P. Sarkar, S. Kumar and K. Sahu, *ACS Appl. Bio Mater.*, 2021, **4**, 5201-5211.
8. J. Yguerabide and E. E. Yguerabide, *Anal. Biochem.*, 1998, **262**, 137-156.
9. Z. Qiao, J. Zhang, X. Hai, Y. Yan, W. Song and S. Bi, *Biosens. Bioelectron.*, 2021, **176**, 112898.
10. S. Kundu, M. Ghosh and N. Sarkar, *Langmuir*, 2021, **37**, 9281-9301.
11. N. Vilar-Vidal, J. R. Rey and M. A. López Quintela, *Small*, 2014, **10**, 3632-3636.
12. L. Yang, H. Wang, D. Li, L. Li, X. Lou and H. Liu, *Chem. Mater.*, 2018, **30**, 5507-5515.
13. H. Yang, Y. Wu, H. Ruan, F. Guo, Y. Liang, G. Qin, X. Liu, Z. Zhang, J. Yuan and X. Fang, *Anal. Chem.*, 2022, **94**, 3056-3064.
14. D. Maysinger, Ž. Sanader Maršić, E. R. Gran, A. Shobo, J.-R. Macairan, I. Zhang, M. Perić Bakulić, R. Antoine, G. Multhaup and V. Bonačić-Kouteckỳ, *ACS Chem. Neurosci.*, 2022, **13**, 464-476.

15. E. Pensa, L. M. Azofra, R. C. Salvarezza and P. Carro, *J. Phys. Chem. Lett.*, 2022, **13**, 6475-6480.
16. P. Sarkar, M. Saha, N. Nandi, D. K. Sahu and K. Sahu, *ACS Appl. Nano Mater.*, 2022, **5**, 7670-7678.
17. D. K. Sahu, P. Sarkar, D. Singha and K. Sahu, *RSC Adv.*, 2019, **9**, 39405-39409.
18. B. Mondal, K. Basu, R. Jana, P. Mondal, B. Hansda, A. Datta and A. Banerjee, *ACS Appl. Nano Mater.*, 2022, **5**, 7932-7943.
19. I. Chakraborty and T. Pradeep, *Chem. Rev.*, 2017, **117**, 8208-8271.
20. A. Baral, K. Basu, S. Roy and A. Banerjee, *ACS Sustain. Chem. Eng.*, 2017, **5**, 1628-1637.
21. L. Zhu, M. Gharib, C. Becker, Y. Zeng, A. R. Ziefuß, L. Chen, A. M. Alkilany, C. Rehbock, S. Barcikowski, W. J. Parak and I. Chakraborty, *J. Chem. Educ.*, 2020, **97**, 239-243.
22. D. Bain, S. Maity, B. Paramanik and A. Patra, *ACS Sustain. Chem. Eng.*, 2018, **6**, 2334-2343.
23. S. Roy, G. Palui and A. Banerjee, *Nanoscale*, 2012, **4**, 2734-2740.
24. M. A. Habeeb Muhammed, P. K. Verma, S. K. Pal, A. Retnakumari, M. Koyakutty, S. Nair and T. Pradeep, *Chem. Eur. J.*, 2010, **16**, 10103-10112.
25. Y. Bao, H.-C. Yeh, C. Zhong, S. A. Ivanov, J. K. Sharma, M. L. Neidig, D. M. Vu, A. P. Shreve, R. B. Dyer, J. H. Werner and J. S. Martinez, *J. Phys. Chem. C*, 2010, **114**, 15879-15882.
26. X. Jia, J. Li and E. Wang, *Small*, 2013, **9**, 3873-3879.
27. S. Maity, D. Bain and A. Patra, *J. Phys. Chem. C*, 2019, **123**, 2506-2515.
28. N. C. Andrews, *The New England journal of medicine*, 1999, **341**, 1986-1995.
29. J. D. Haas and T. t. Brownlie, *The Journal of nutrition*, 2001, **131**, 676S-688S; discussion 688S-690S.
30. M. Zheng, H. Tan, Z. Xie, L. Zhang, X. Jing and Z. Sun, *ACS Appl. Mater. Interfaces*, 2013, **5**, 1078-1083.
31. S. Altamura and M. U. Muckenthaler, *J Alzheimers Dis*, 2009, **16**, 879-895.
32. L. Zecca, M. B. H. Youdim, P. Riederer, J. R. Connor and R. R. Crichton, *Nat. Rev. Neurosci.*, 2004, **5**, 863-873.
33. J. Yin, Y. Kwon, D. Kim, D. Lee, G. Kim, Y. Hu, J.-H. Ryu and J. Yoon, *J. Am. Chem. Soc.*, 2014, **136**, 5351-5358.
34. H. Sies, *Free Radic Biol Med*, 1999, **27**, 916-921.

35. A. Chauhan and V. Chauhan, *Pathophysiology*, 2006, **13**, 171-181.

36. J. M. Estrela, A. Ortega and E. Obrador, *Crit. Rev. Clin. Lab. Sci.*, 2006, **43**, 143-181.

37. D. M. Townsend, K. D. Tew and H. Tapiero, *Biomed Pharmacother*, 2003, **57**, 145-155.

38. B. Bayram, G. Rimbach, J. Frank and T. Esatbeyoglu, *J. Agric. Food Chem.*, 2014, **62**, 402-408.

39. Y. Wang, J. Lu, L. Tang, H. Chang and J. Li, *Anal. Chem.*, 2009, **81**, 9710-9715.

40. N. Yan, Z. Zhu, N. Ding, L. Zhou, Y. Dong and X. Chen, *Journal of chromatography. A*, 2009, **1216**, 8665-8670.

41. E. J. Pacsial-Ong, R. L. McCarley, W. Wang and R. M. Strongin, *Anal. Chem.*, 2006, **78**, 7577-7581.

42. G. G. Huang, X. X. Han, M. K. Hossain and Y. Ozaki, *Anal. Chem.*, 2009, **81**, 5881-5888.

43. S. Xu, T. Gao, X. Feng, Y. Mao, P. Liu, X. Yu and X. Luo, *J. Mater. Chem. B*, 2016, **4**, 1270-1275.

44. Q. Zhai, H. Xing, D. Fan, X. Zhang, J. Li and E. Wang, *Sens. Actuators B Chem.*, 2018, **273**, 1827-1832.

45. H. Zhao, X. Wen, W. Li, Y. Li and C. Yin, *J. Mater. Chem. B*, 2019, **7**, 2169-2176.

46. L. Tian, W. Zhao, L. Li, Y. Tong, G. Peng and Y. Li, *Sens. Actuators B Chem.*, 2017, **240**, 114-124.

47. S. Shekhar, P. Mahato, R. Yadav, S. D. Verma and S. Mukherjee, *ACS Sustain. Chem. Eng.*, 2022, **10**, 1379-1389.

48. M. Wang, B. Duan, Y. Li, S. Jiang, Z. Huang and W. Yang, *ACS Appl. Nano Mater*, 2021, **4**, 7486-7492.

49. X. Wang, A. Hu, K. Du and F. Feng, *ACS Appl. Bio Mater.*, 2021, **4**, 8004-8012.

50. M.-C. Pan, Y.-M. Lei, Y.-Q. Chai, R. Yuan and Y. Zhuo, *Analytical Chemistry*, 2020, **92**, 13581-13587.

51. Z. Luo, X. Yuan, Y. Yu, Q. Zhang, D. T. Leong, J. Y. Lee and J. Xie, *J. Am. Chem. Soc.*, 2012, **134**, 16662-16670.

CHAPTER 6

Ethanol and Gd^{3+} activated aggregation induced delayed fluorescence in copper nanoclusters

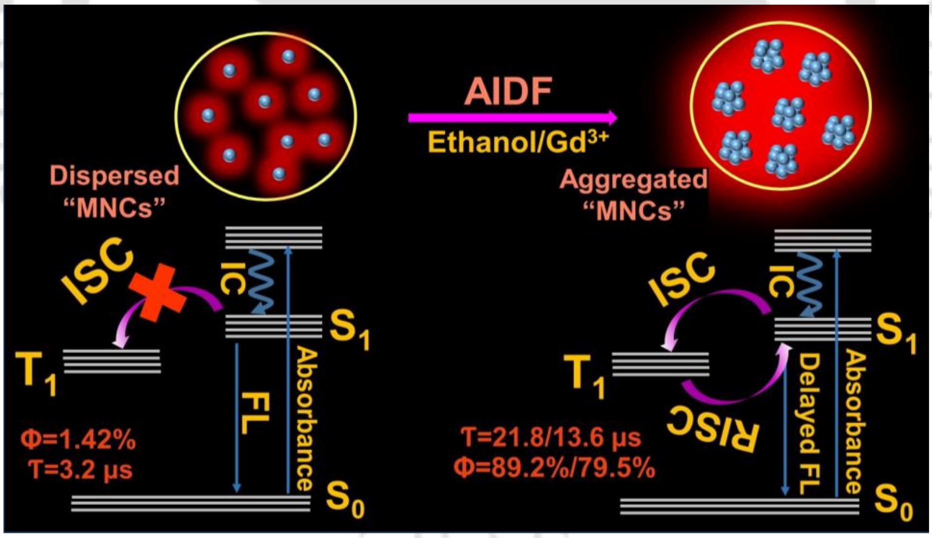

Manuscript: **Priyanka Sarkar**, Neha Barnwal, Nilanjana Nandi, and Kalyanasis Sahu, "Ethanol and Gd^{3+} activated aggregation induced delayed fluorescence in copper nanoclusters" (Under revision)

[This page was intentionally left blank]

ABSTRACT

In recent years, significant emphasis has been dedicated towards investigating Aggregation induced emission (AIE) phenomena and a notable addition to this emerging field is the discovery of Aggregation induced delayed fluorescence (AIDF). Here, we have proposed two different strategy to produce AIDF based luminescent materials at room temperature from widely reported Glutathione (GSH) capped CuNCs (GSH-CuNCs) by (1) simply modifying the solvent environment of the system and (2) by introduction of Gadolinium (Gd^{3+}) ions. The synthesized GSH-CuNCs in aqueous solution displayed weak fluorescence (Fl) emission with negligible delayed lifetime component of 3.2 μs and quantum yield (QY) of 1.42%. However, introducing these GSH-CuNCs to ethanol medium promptly led to emergence of enhanced delayed Fl emission with significant delayed lifetime component of 21.8 μs and high delayed quantum yield (QY) of 89.2%. Further, it was observed that, introduction of Gadolinium (Gd^{3+}) metal ion to GSH-CuNCs in aqueous solution can also induce enhanced delayed Fl emission with delayed lifetime component of 13.6 μs and high delayed quantum yield (QY) of 79.5%. Analysis of Experimental data from TEM and DLS measurements ascribed the fact that both the ethanol solvent and Gd^{3+} endows controlled aggregation of GSH-CuNCs, enabling successful harvesting of triplet states and ultimately leading to AIDF phenomenon. Moreover, the AIDF phenomena harnessed from GSH-CuNCs by Gd^{3+} were successfully employed to detect Cr^{6+} ions in aqueous solution with excellent selectivity.

6.1 OVERVIEW

Delayed fluorescence (DF), a class of photoluminescent (Pl) phenomena other than fluorescence (Fl) and Phosphorescence, is believed to have boost the progression of science and technology in terms of light-emitting diodes (LEDs)[1, 2]. DF phenomena involves a reverse intersystem crossing (RISC) process, enabling transition of photo-excited electrons from triplet excited state to the singlet state followed by radiative relaxation to the ground state. Generally, this RISC process is accessible by thermal activation, a phenomenon termed as TADF (Thermally activated delayed fluorescence), allowing transition between the lowest triplet excited state (T_1) and the lowest singlet excited state (S_1) due to small energy gap (ΔE_{ST}) usually in the range of 0.05-0.2 eV, thus allowing utilization of T_1 state for radiation[3, 4]. DF phenomena not only augments the quantum yield (QY) of an emitter but also contributes to the prolongation of excited state lifetime of the emitting system. However, TADF emitters encounter significant concentration induced emission quenching in an aggregated state[2, 5, 6]. Also, most literatures reports fabrication of luminescent probes with delayed lifetime component mostly involves dopants of heavy metal atoms, restricting their utilization as imaging probes and bio-sensors, while raising environmental concerns as well[7].

Now a days, Aggregation-induced emission (AIE) is considered as a significant phenomenon for harnessing strong photoluminescent molecules in aggregated state[8, 9]. It has been validated that the primary cause of AIE effects stems due to supression of intramolecular motions (RIM) including vibrational and rotational motions, thus blocking the non-radiative decay channel leading to enhanced emission[10]. However, most AIEgens are capable of harnessing only singlet excitons for radiative emission. Hence, focus on developing AIEgens that can efficiently harness triplet excitons would yield significant advantages, also enabling to potentially overcome the limitation associated with common DF materials experiencing aggregation caused emission quenching[1, 4]. Thus, aggregation-induced delayed fluorescence (AIDF) based probes is gearing attention among researchers, potentially opening up novel opportunities in the realm of DF based materials. The AIDF phenomena thus represents a distinctive photophysical process, wherein the materials possess strong emission with significant delayed Fl and lifetime component upon aggregation.

MNCs are composed of number of metal atoms ranging from few to hundreds, with dimensions typically smaller than 2 nm, comparable to fermi wavelength of electrons[11]. MNCs of coinage metals like gold (Au) and silver (Ag) has always received extensive attention compared to

MNCs of copper (Cu). The reason being the high susceptibility of Cu(0) state for aerial oxidation causing instability of CuNCs[12]. Thus, preserving the luminescent property of CuNCs under ambient conditions for extended duration poses significant challenge to researchers. The AIDF phenomenon can hold promising potential to drive advancements in the utilization of MNCs by offering prolonged lifetime, Pl stability and improved QY. AIDF based MNCs can present a promising alternative for fabricating LEDs. Moreover, AIDF based MNCs can also function as an advanced sensor compared to traditional MNCs, which generally exhibits short response times and thus susceptible to interference from background scattering.

Heavy metal ions and their oxo-anions, among water pollutants poses serious threats to human lives, creating critical environmental concern[13]. Chromium (Cr), one of the prevalent heavy metal pollutant commonly exists in two oxidation states, Cr(III) and Cr(VI)[14]. Cr(VI) which is largely utilized in industries like tannery, dyeing, electroplating, etc. poses significant toxicity than Cr(III)[15]. Cr(VI) is categorised as class I carcinogen exhibiting mutagenic properties[16]. Various methods like surface-enhanced Raman spectroscopy (SERS)[17], electrochemical methods[18], high-performance liquid chromatography-inductively coupled plasma mass spectrometry (HPLC-ICP-MS)[19], atomic spectroscopy[20], etc. employed for analytical detection requires sophisticated instruments, longer detection time and portability issue. Thus, developing a AIDF based sensor for potential and selective Cr(VI) detection can be of significant use to researchers.

Here, a tripeptide, glutathione (GSH) is adopted as a stabilizing ligand to synthesize CuNCs in aqueous system. This GSH-CuNCs display weak Fl in aqueous system, however, introducing these CuNCs to ethanol solvent generated notable delayed Fl emission at room temperature with enhanced lifetime of 21.9 μs and quantum yield of 89.2%. TEM and DLS data suggests that the extent and type of aggregation induced by the increasing volume fraction of ethanol solvent in aqueous medium directly influence the generation of delayed Fl emission from GSH-CuNCs. Additionally, introduction of gadolinium (Gd^{3+}) ions into the aqueous solution of GSH-CuNCs also led to unique alteration of its photoluminescent property by generating aggregation induced delayed Fl emission at room temperature with lifetime of 13.6 μs and quantum yield of 79.5%. This Gd-GSH-CuNCs were finally employed for detection of carcinogenic Cr(VI) in aqueous solution with the aid of delayed Fl emission.

Earlier some literatures documented studies on solvent and metal triggered aggregation induced emission enhancement of CuNCs[21-23]. However, to the best of our knowledge, study on generation of delayed Fl emission resulting from alterations in the solvent medium by ethanol and from introduction of a metal ion has not been reported earlier.

6.2 RESULTS AND DISCUSSION

6.2.1 Charaterization of CuNCs

In these work, a tripeptide, Glutathione (GSH) (GSH=Glutamate-cysteine-glycine) is utilized as a thiolate capping ligand to stabilize the synthesized CuNCs. In the first step, a solution of $Cu(NO_3)_2$ is added to the solution of GSH followed by adding NaOH in the second step and maintaining the pH of the reaction mixture to ~4. Transmission electron microscopy (TEM) image of GSH-CuNCs reveals distinct formation of monodispersed spherical morphology structured particles with size diameter of 1.91 ± 0.29 nm **(Figure 6.1a)**. The UV-vis spectra showed an upsurge of absorbance from 360 nm with absence of any SPR peak at 500-600 nm range, clarifying successful formation of GSH-CuNCs with molecule like behaviour **(Figure 6.1b)**. The absorption emergence at 360 nm arises due to electronic transitions occurring between the ligands (GSH) and the metal core. The photoluminescence (Pl) characteristics of GSH-CuNCs exhibits maximum fluorescence (Fl) intensity with weak luminescence at 620 nm **(Figure 6.1b)**. The GSH-CuNCs solution under 365 nm UV lamp illuminates red emission **(Inset of Figure 6.1b).**The excitation dependent emission spectra displays independent nature of the emission maxima, while showing maximum intensity at 360 nm excitation wavelength **(Figure 6.1c)**.. The Fl quantum yield (QY) of GSH-CuNCs measured using quinine sulfate (54.4% in 0.1 M H_2SO_4) as a reference was found to be 1.42%. The GSH-CuNCs solution when stored at 4°C were found to stable for almost 7 days, whereas at room temperature it remained stable for only 1 day. For elemental composition characterization, X-ray photoelectron spectroscopy (XPS) was performed. Deconvolution of the high resolution XPS spectra of Cu represents peaks at 932.5 eV and 952.6 eV corresponding to $2p_{3/2}$ and $2p_{1/2}$ respectively of Cu(0)/Cu(I)[24] **(Figure 6.1d)**. Absence of satellite peak at 942 eV denotes that the GSH-CuNCs core is devoid of Cu(II). Owing to 0.1 eV binding energy difference, precise estimation of Cu(0) and Cu(I) is not possible. FTIR spectra can provide information about the nature of the capped GSH ligand on CuNCs surface **(Figure A.6.1)**. The absence of S-H vibrational peak at 2525 cm^{-1} in the FTIR spectra of GSH-CuNCs assures successful ligation of GSH ligand on the surface of CuNCs via S-H group.

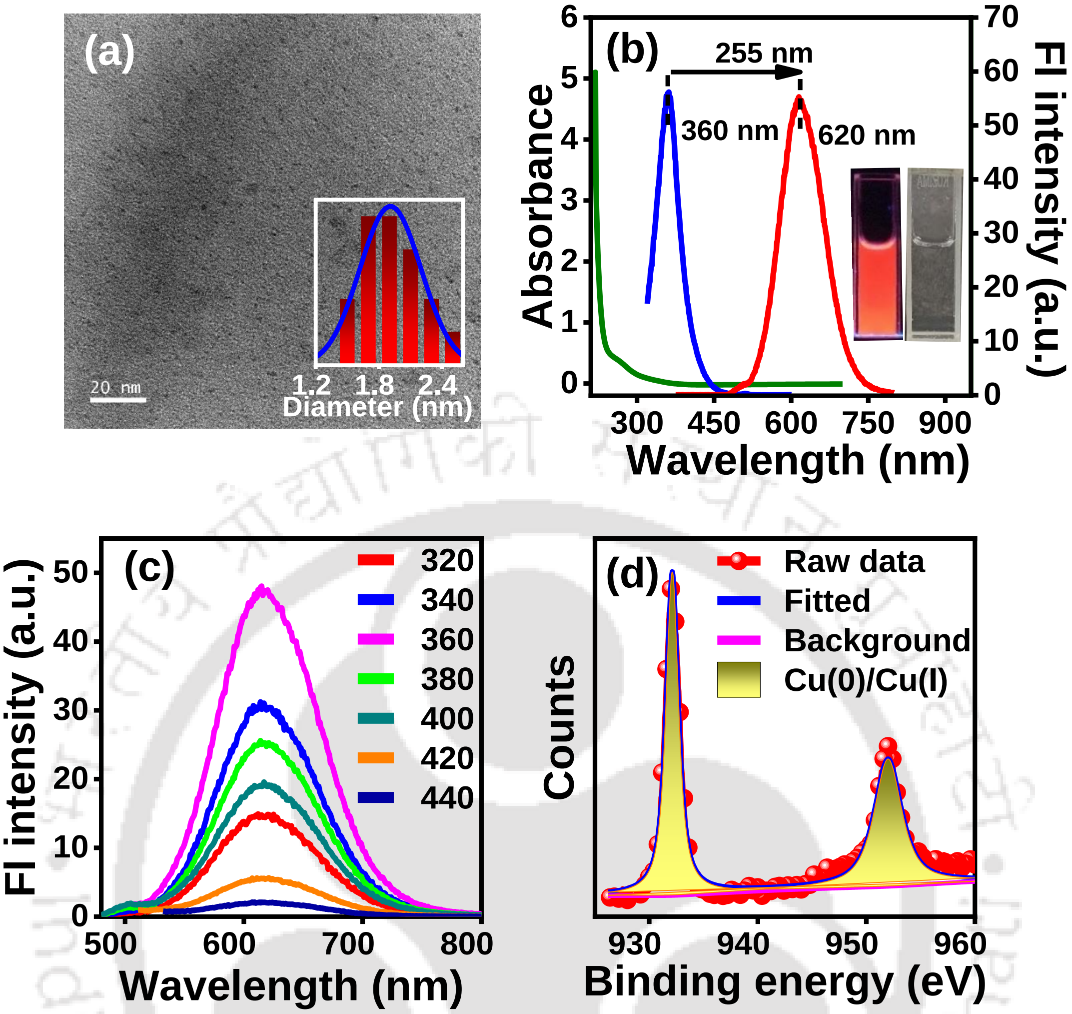

Figure 6.1 (a) TEM image of GSH-CuNCs and the size distribution histogram (b) UV−vis absorption (green), excitation (λem = 620 nm) (blue), and Fl (λex = 360 nm) (red) spectra of GSH-CuNCs. Inset shows solution of GSH-CuNCs under normal light (right) and under 365 nm UV lamp (left) (c) Fl spectra of GSH-CuNCs at different excitation wavelengths (320−440 nm) and (d) high-resolution XPS spectra of Cu in GSH-CuNCs.

6.2.2 Ethanol induced AIDF of GSH-CuNCs.

In aqueous solution, the synthesized CuNCs exhibited weak fl emission, however introducing these GSH-CuNCs to ethanol solvent led to emergence of distinct photoluminescent property. Interestingly, gradual increment in the volume fraction (f_d) of ethanol solvent in water (f_d = $Vol_{ethanol}/Vol_{ethanol+water}$), led to intriguing emergence of delayed fluorescence (Fl) emission property in GSH-CuNCs from f_d =70% (**Figure 6.2a**). Notably, it is worth highlighting that, until f_d =60%, no delayed Fl emission property were observed from GSH-CuNCs. The increment in delayed Fl property is accompanied by slight blue shift in photoluminescent intensity, with a shift of 20 nm at f_d =90%, in comparison to Fl emission of GSH-CuNCs in aqueous solution. With increasing volume fraction of ethanol UV-vis spectra of GSH-CuNCs shows hyperchromic shift, however as the volume fraction reaches f_d = 70%, the turbidity of the solution caused sudden change in the nature of absorption spectra (**Figure 6.2b)**. Further increase in f_d = 80%, the absorption spectra regained its nature and finally at f_d = 90%, the extreme turbidity of the solution caused the absorbance values to increase abruptly. Digital images of GSH-CuNCs solution under normal light shows with increasing volume fraction of ethanol the solution appears clear and transparent until f_d = 60%, however, a hint of turbidity emerges from f_d = 70% and becoming fully turbid at f_d = 90%. Under 365 nm UV lamp, the digital images illustrates clear emission enhancement and transformation of colour from deep red to bright yellowish-orange with increasing ethanol volume fraction (**Figure 6.2c)**. TEM images at f_d = 60%, revealed well dispersed assemblies of GSH-CuNCs with diverse sizes, ranging between 132 ± 57 nm in diameter **(Figure 6.2d)**. In contrast, at f_d = 90%, denser agglomeration of these assemblies was observed, with comparatively smaller and narrower size variation (57 ± 10 nm) **(Figure 6.2e)**, magnified version TEM image at f_d = 90% is shown in **Figure A.6.2a**. Employing single exponential equation, lifetime of GSH-CuNCs was determined to be 3.2 μs (**Figure A.6.2b and Table A.6.1)**, however with increasing volume fraction of ethanol, the delayed component of lifetime increased simultaneously, reaching a value of 21.8 μs at f_d = 90% **(Figure 6.2f and Table A.6.1)**. Thus, the fact of emergence of delayed fluorescence, coupled with the increased delayed lifetime component and the predominant observation of compact aggregates, indicates manifestation of AIDF property of GSH-CuNCs in an ethanol medium. Further evidence that corroborates the fact of assembly formation in accordance with the obtained TEM data is presented by dynamic light scattering experiment (DLS) results. **From Figure A.6.2c**, it can be seen that with increasing ethanol content in the medium the size of aggregates increases until f_d = 60%, however, from f_d = 70% the aggregates size decreases. A similar kind of aggregation pattern has also been reported earlier for AuNCs[25].Therefore, both TEM and DLS data illustrates development of larger dispersed aggregates of GSH-CuNCs until f_d = 60%, while from f_d = 70% denser aggregates with comparatively smaller size were observed. Additionally, UV-vis spectra and digital images of GSH-CuNCs solution under normal light further corroborated this change in the property of GSH-CuNCs solution. The delayed fluorescence quantum yield of aggregated state of GSH-CuNCs in ethanol solvent was calculated to be 89.2% (measured considering FIRPIC as reference with delayed fluorescence quantum yield of 60% in acetonitrile solution). It is assumed that the increasing volume of a weakly polar solvent, ethanol induces disruption of the hydration shell around GSH-CuNCs resulting in formation of aggregates. Notably, the DF emission from the aggregated GSH-CuNCs in ethanol solvent exhibited remarkable stability at room temperature, lasting nearly for 2 months (**Figure A.6.2d**), thus, providing us with a compelling approach for generating stable AIDF based phenonmenon using copper nanoclusters.

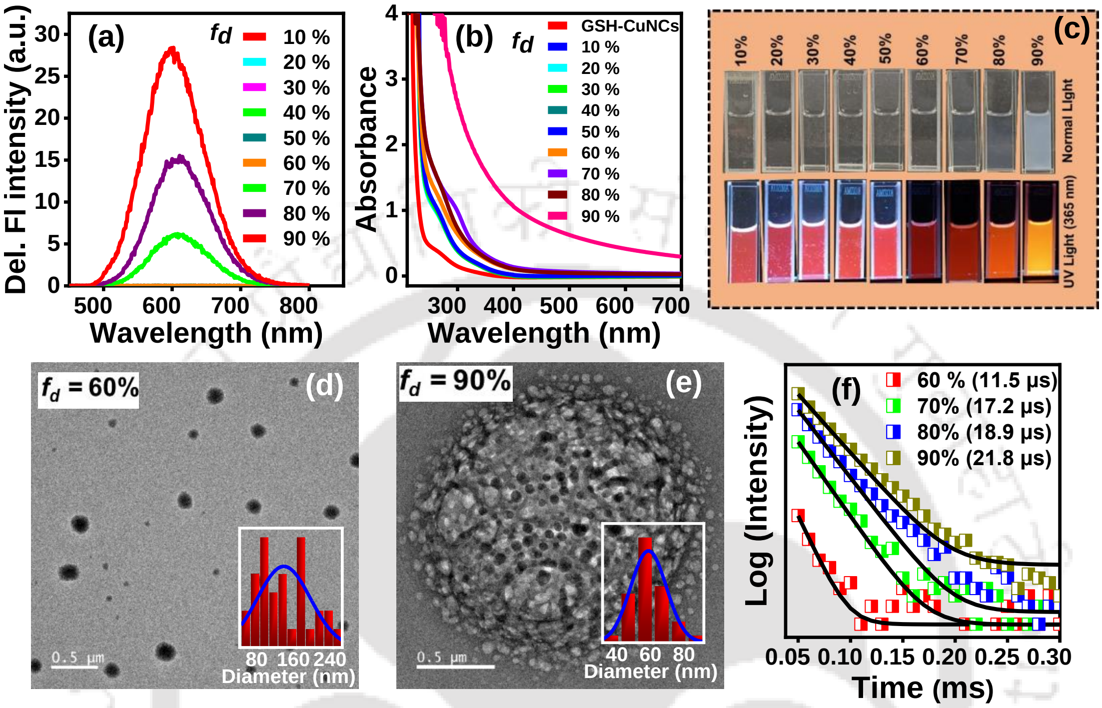

Figure 6.2. (a) Delayed emission spectra of GSH-CuNCs with increasing volume fraction of ethanol (f_d) (b) UV-vis spectra of GSH-CuNCs with increasing volume fraction of ethanol (c) Digital images of GSH-CuNCs with increasing volume fraction of ethanol (up) under normal light (down) under 365 nm UV lamp (d) TEM images of GSH-CuNCs at f_d = 60% (e) TEM images of GSH-CuNCs at f_d = 90% and Inset shows size distribution histogram and (f) Time-resolved delayed photoluminescence decay profiles of GSH-CuNCs at f_d = 60%, 70%, 80% and 90%.

We measured temperature dependent delayed Fl emission spectra at f_d = 90% to observe and analyse its behaviour at low and high temperature. **Figure A.6.2e** shows abrupt increase in the delayed emission spectra of the aggregated state at lower temperature. The delayed Fl decay spectra measured using single exponential equation also showed increment in the delayed lifetime component with decreasing temperature from 60°C to 10°C **(Figure A.6.2f and Table A.6.2)**. Researchers now widely accepted the fact that AIE originates from restriction of intramolecular rotational and vibrational motions, which can arise due to rigidification of structure induced by high viscosity of the medium, lowering the temperature or incorporating the luminogens within some rigid matrices, ultimately leading to reduced probability of nonradiative relaxation of the excited state and resulting in emission enhancement[10, 26]. Further, in a recent literature it is well elucidated that in the aggregated state, restricted molecular motions and nonradiative internal conversion (IC) channel blockage amplifies the ISC and RISC process, facilitating delayed Fl emission phenomena[2]. Thus, the above temperature dependent delayed Fl spectra ascribes the fact that lowering temperature induces greater rigidity within the aggregated medium, thereby facilitating the RISC process and resulting in enhanced delayed emission.

6.2.3 Gd^{3+}-triggered AIDF of GSH-CuNCs

The introduction of gadolinium (Gd^{3+}) into the clear and transparent GSH-CuNCs solution at room temperature promptly led to formation of turbid solution. This turbid Gd^{3+}-GSH-CuNCs solution displays UV-vis spectral nature akin to bare GSH-CuNCs but with increased absorbance values, attributed to increased scattering resulting from turbidity of the solution **(Figure 6.3a)**. This behaviour accounts due to strong coordination between Gd^{3+} and COO^- ions of GSH ligand stabilizing the CuNCs, which led to the formation of aggregates. This interaction was substantiated by zeta potential data, which revealed a notable shift in the zeta potential of GSH-CuNCs from -20.1 mV to -2.75 mV upon introduction of Gd^{3+} (**Figure A.6.3a**). Further, TEM images taken after addition of Gd^{3+} clearly dictated assembly formation with average diameter size of 5.0 ± 1.5 nm **(Figure 6.3b)**. Thus, this multivalent metal ion (Gd^{3+}) besides neutralizing the negatively charged surface ligand GSH, also served as a cross-linker to bring GSH-CuNCs closer forming aggregates. This synthesized Gd^{3+}-GSH-CuNCs displayed distinct photoluminescent nature in aqueous solution. While, GSH-CuNCs typically lack pronounced delayed emission characteristics in aqueous solution, the introduction of Gd^{3+} induced emergence of strong delayed Fl features from GSH-CuNCs **(Figure 6.3a)**. The aqueous solution of Gd^{3+}-GSH-CuNCs under normal light showed turbid nature of the solution and under 365 nm UV lamp it showed bright yellowish-orange emission **(Inset of Fig 3a)**. The optimised concentration of Gd^{3+} required to generate strong delayed Fl characteristics from the aqueous solution of GSH-CuNCs was also evaluated, as depicted in **Figure A.6.3b**. Notably, It was observed that 40 mM of Gd^{3+} induced maximum intensification of delayed emission characteristics. Moreover, we examined the influence of few additional metal ions from f-block like Europium (Eu^{3+}) and from d-block like Platinum (Pt^{3+}), Silver (Ag^+) and Gold (Au^{3+}) on the photoluminescent spectra of GSH-CuNCs. However, none of the above metal ions except Gd^{3+} induced delayed Fl emission charateristics from GSH-CuNCs (**Figure A.6.3c**). The delayed Fl quantum yield of Gd^{3+}-GSH-CuNCs was calculated to be 79.5%. Using single exponential equation lifetime of delayed photoluminescent decay was calculated to be 13.6 μs

(Figure 6.3c and Table A.6.3). The delayed Fl emission of Gd^{3+}-GSH-CuNCs remained stable at room temperature for about 2 months **(Figure A.6.3d)**. Thus, incorporation of Gd^{3+} not only poses alteration in photophysical property of GSH-CuNCs, but also presents a viable strategy for rapid development of AIDF materials with augmented stability.

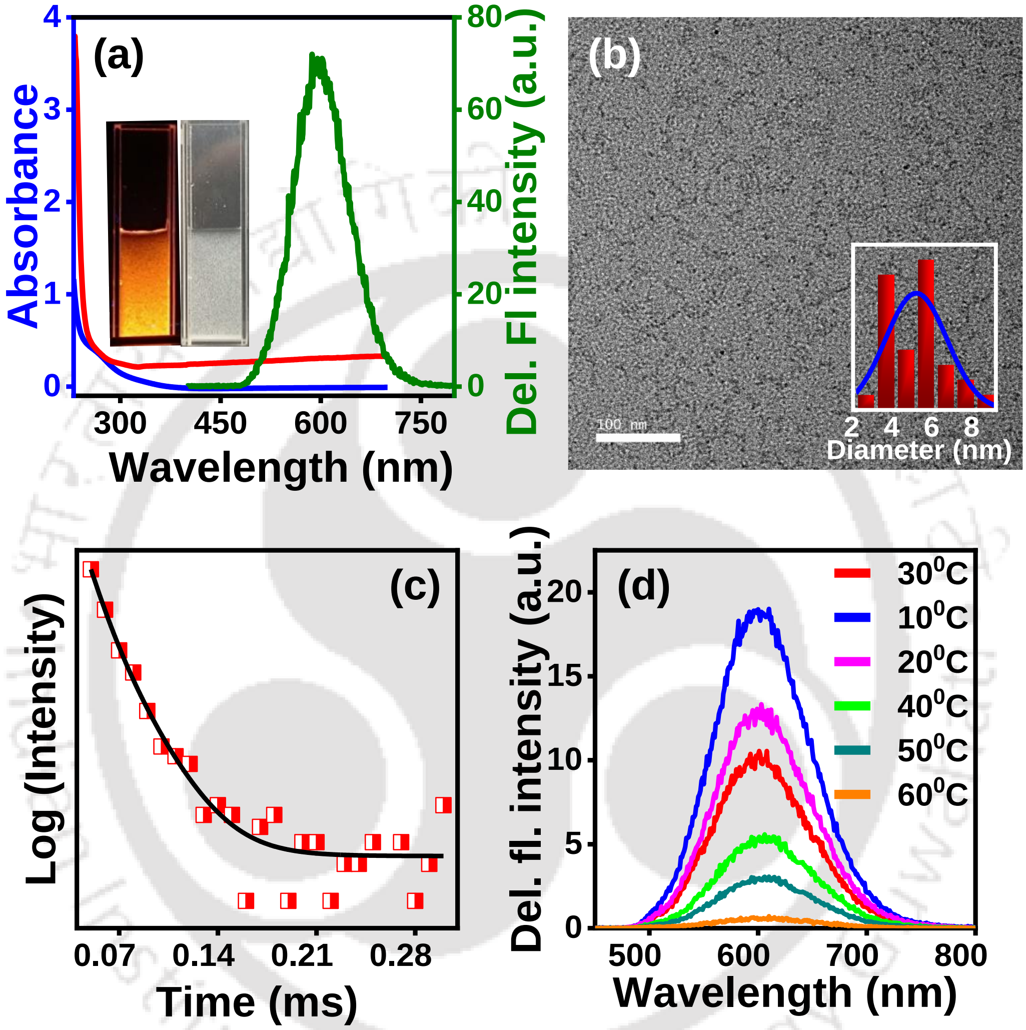

Figure 6.3. (a) UV-vis spectra of GSH-CuNCs (blue), Gd^{3+}-GSH-CuNCs (red) and delayed emission spectra of Gd^{3+}-GSH-CuNCs (green) (Inset shows digital images of Gd^{3+}-GSH-CuNCs under 365 nm UV lamp (left) and under normal light (right) (b) TEM image of Gd^{3+}-GSH-CuNCs and the size distribution histogram (c) Time-resolved delayed photoluminescence decay profiles of Gd^{3+}-GSH-CuNCs and (d) Temperature dependent delayed emission study of Gd^{3+}-GSH-CuNCs.

We also measured temperature dependent delayed Fl emission spectra of Gd^{3+}-GSH-CuNCs. **Figure 6.3d** shows abrupt increase in the delayed emission spectra of the aggregated Gd^{3+}-GSH-CuNCs at lower temperature. The delayed Fl decay spectra measured using single exponential equation also showed increment in the delayed lifetime component with decreasing temperature from 60°C to 10°C **(Figure A.6.3e and Table A.6.4)**. Thus, the above observation indicates that the fact that low temperature facilitates further rigidification of Gd^{3+}-GSH-CuNCs aggregated system, which in turn intensifies the AIDF phenomena.

6.2.4 Delayed Fl sensing of Cr^{6+} by Gd^{3+}-GSH-CuNCs

The delayed Fl emission property of Gd^{3+}-GSH-CuNCs were subsequently utilized to access their reactivity in aqueous solutions containing various metal ions. Upon recording delayed emission spectra in presence of various metal ions, it was observed that the spectra exhibited sensitivity solely towards Chromium (Cr^{6+}) ions. Intriguingly, it was noted that with increase in concentration of Cr^{6+} ions in the aqueous solution of Gd^{3+}-GSH-CuNCs, there was gradual quenching in the delayed emission spectra (**Figure 6.4a)**. After adding about 63 μM of Cr^{6+} ion, notable 80% reduction in the delayed emission spectra was observed. Intensity ratio plot (F_0/F, where F_0 and F signifies delayed emission intensities of Gd^{3+}-GSH-CuNCs before and after addition of Cr^{6+}) as displayed in **Figure 6.4b** demonstrates deviation from linearity at higher concentration of Cr^{6+}, while following Stern-Volmer linearity pattern within lower concentrations (0 to 25 μM) of Cr^{6+} (**Inset of Figure 6.4b**). LOD (Limit of detection) value calculated using conventional formula of 3σ/S was 108 nM (σ signifies standard deviation of blank signal and S signifies slope of the linear calibration plot obtained from intensity ratio plot of F/F_0 upto 25 μM). The selectivity test conducted in presence of various other comparative metal ions is presented in **Figure A.6.4**, which showed that these metal ions did not induce significant change in the delayed emission spectra of Gd^{3+}-GSH-CuNCs.

To gain insight into the quenching mechanism of the delayed Fl emission, we measured the UV-vis spectra of Gd^{3+}-GSH-CuNCs with increasing concentration of Cr^{6+}. **Figure 6.4c** shows that there is hardly any change in the spectral nature of Gd^{3+}-GSH-CuNCs, however a slight increase in absorbance value was observed. Further, lifetime of delayed photoluminescent decay of Gd^{3+}-GSH-CuNCs measured after introducing varying concentrations of Cr^{6+} showed notable decrease in delayed lifetime values indicating involvement of triplet excited state in the quenching phenomena **Figure 6.4d and Table A.6.5**. Thus, the quenching phenomena of delayed Fl emission of Gd^{3+}-GSH-CuNCs by Cr^{6+} ions can be attributed to Cr^{6+} inducing changes in the triplet excited state electronic structure of Gd^{3+}-GSH-CuNCs, ultimately resulting in quenching of the delayed emission characteristics.

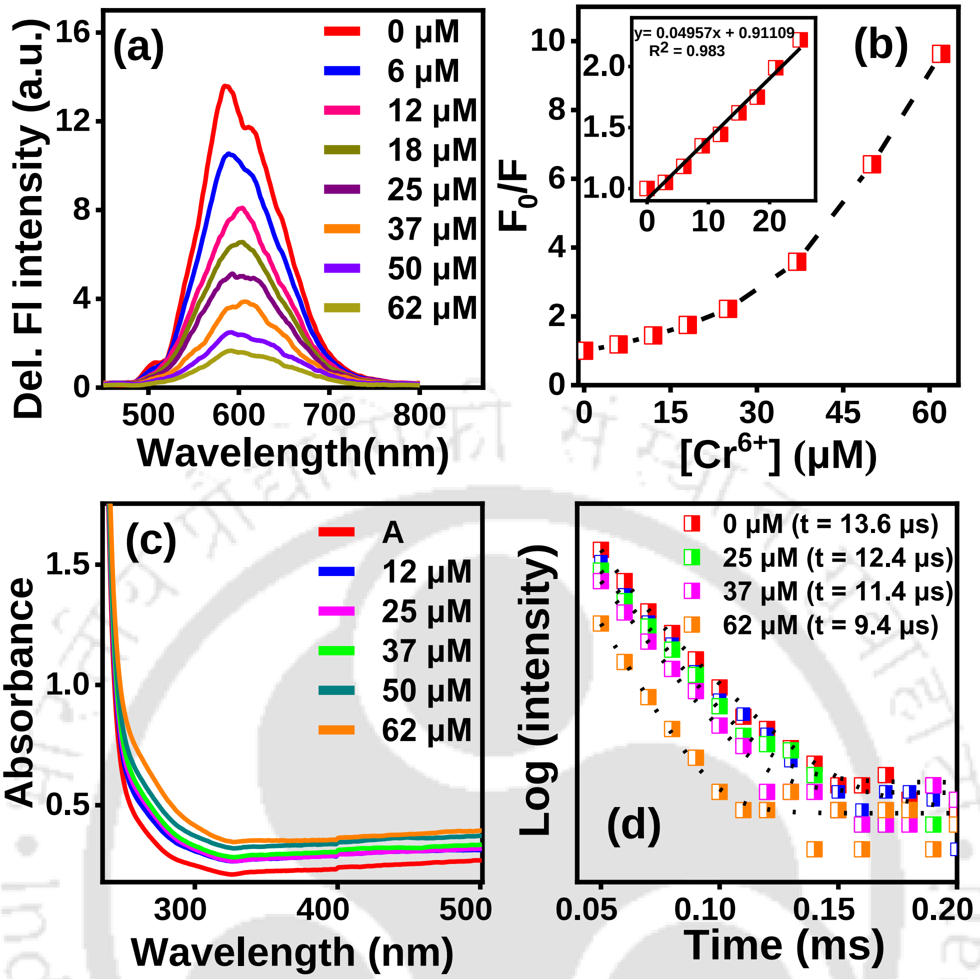

Figure 6.4. (a) Delayed emission spectra of Gd^{3+}-GSH-CuNCs after adding various concentration of Cr^{6+} (b) Delayed emission intensity ratio plot where F_0 and F represents delayed emission intensity before and after adding various concentrations of Cr^{6+} ions. Inset shows linearly plotted intensity plot (c) UV-vis spectra of Gd^{3+}-GSH-CuNCs (represented by A) and after adding various concentration of Cr^{6+} and (d) Time-resolved delayed photoluminescence decay profiles of Gd^{3+}-GSH-CuNCs after adding various concentration of Cr^{6+}.

6.3 CONCLUSION

In summary, two interesting and simple strategy for producing AIDF based luminogens from weakly fluorescent GSH-CuNCs system is proposed. This study demonstrates how controlled aggregation induced by either solvent or a metal ion can led to generation of delayed emission property. Ethanol, which is a weakly polar solvent induces aggregation of GSH-CuNCs. It was observed that larger sized dispersed aggregates at lower ethanol volume fraction (f_d) upto f_d = 60% did not generate delayed emission characteristics from GSH-CuNCs, however, at f_d = 70% and beyond, compact and smaller sized aggregates induced manifestation of the prominent delayed emission property, showing a noticeable enhancement with increasing ethanol volume fraction. Further, introduction of Gd^{3+} to the aqueous solution of GSH-CuNCs also generated delayed emission induced through aggregate formation. Temperature dependent study for both the delayed emission systems described similar pattern: With decreasing temperature both the delayed emission property and associated delayed lifetime component demonstrated an increment in its value. This pattern suggests that elevated temperature destabilizes the aggregated system, ultimately diminishing the propensity for the AIDF phenomenon. Lastly, the delayed emission from Gd^{3+}-GSH-CuNCs showed efficient sensitivity towards Cr^{6+} ions in aqueous solution with LOD value of 108 nM.

REFERENCES

1. S. Gan, W. Luo, B. He, L. Chen, H. Nie, R. Hu, A. Qin, Z. Zhao and B. Z. Tang, *Journal of Materials Chemistry C*, 2016, **4**, 3705-3708.
2. J. Guo, Z. Zhao and B. Z. Tang, *Advanced Optical Materials*, 2018, **6**, 1800264.
3. G. Li, Z.-Q. Zhu, Q. Chen and J. Li, *Organic Electronics*, 2019, **69**, 135-152.
4. S. Xu, T. Liu, Y. Mu, Y.-F. Wang, Z. Chi, C.-C. Lo, S. Liu, Y. Zhang, A. Lien and J. Xu, *Angewandte Chemie International Edition*, 2015, **54**, 874-878.
5. S. Gan, J. Zhou, T. A. Smith, H. Su, W. Luo, Y. Hong, Z. Zhao and B. Z. Tang, *Materials Chemistry Frontiers*, 2017, **1**, 2554-2558.
6. J. Zeng, J. Guo, H. Liu, J. W. Y. Lam, Z. Zhao, S. Chen and B. Z. Tang, *Chemistry – An Asian Journal*, 2019, **14**, 828-835.
7. T. Chatterjee and K.-T. Wong, *Advanced Optical Materials*, 2019, **7**, 1800565.
8. S. Chakraborty, D. Bain, S. Maity, S. Kolay and A. Patra, *The Journal of Physical Chemistry C*, 2022, **126**, 2896-2904.
9. B. Kuppan and U. Maitra, *Nanoscale*, 2017, **9**, 15494-15504.
10. Z. Zhao, H. Zhang, J. W. Y. Lam and B. Z. Tang, *Angewandte Chemie International Edition*, 2020, **59**, 9888-9907.
11. Z. Luo, K. Zheng and J. Xie, *Chemical Communications*, 2014, **50**, 5143-5155.
12. B. Mondal, K. Basu, R. Jana, P. Mondal, B. Hansda, A. Datta and A. Banerjee, *ACS Applied Nano Materials*, 2022, **5**, 7932-7943.
13. S. Dutta, S. Let, M. M. Shirolkar, A. V. Desai, P. Samanta, S. Fajal, Y. D. More and S. K. Ghosh, *Dalton Transactions*, 2021, **50**, 10133-10141.

14. C. M. Stern, T. O. Jegede, V. A. Hulse and N. Elgrishi, *Chemical Society Reviews*, 2021, **50**, 1642-1667.
15. M. Tumolo, V. Ancona, D. De Paola, D. Losacco, C. Campanale, C. Massarelli and V. F. Uricchio, *International Journal of Environmental Research and Public Health*, 2020, **17**, 5438.
16. M. Costa and C. B. Klein, *Critical Reviews in Toxicology*, 2006, **36**, 155-163.
17. C. Wang, M. Shang, H. Wei, M. Zhang, W. Zou, X. Meng, W. Chen, H. Shao and Y. Lai, *Sensors and Actuators B: Chemical*, 2021, **346**, 130594.
18. K. Zhao, L. Ge, T. I. Wong, X. Zhou and G. Lisak, *Chemosphere*, 2021, **281**, 130880.
19. A. Roig-Navarro, Y. Martinez-Bravo, F. López and F. Hernández, *Journal of Chromatography A*, 2001, **912**, 319-327.
20. J. Nan and X.-P. Yan, *Analytica Chimica Acta*, 2005, **536**, 207-212.
21. X. Jia, J. Li and E. Wang, *small*, 2013, **9**, 3873-3879.
22. Y.-e. Shi, J. Ma, A. Feng, Z. Wang and A. L. Rogach, *Aggregate*, 2021, **2**, e112.
23. Z. Wang, B. Chen, A. S. Susha, W. Wang, C. J. Reckmeier, R. Chen, H. Zhong and A. L. Rogach, *Advanced Science*, 2016, **3**, 1600182.
24. P. Sarkar, N. Nandi, N. Barnwal and K. Sahu, *Materials Today Chemistry*, 2023, **27**, 101341.
25. Z. Luo, X. Yuan, Y. Yu, Q. Zhang, D. T. Leong, J. Y. Lee and J. Xie, *Journal of the American Chemical Society*, 2012, **134**, 16662-16670.
26. Y. Chen, J. W. Y. Lam, R. T. K. Kwok, B. Liu and B. Z. Tang, *Materials Horizons*, 2019, **6**, 428-433.

CHAPTER 7

Summary and Prospects

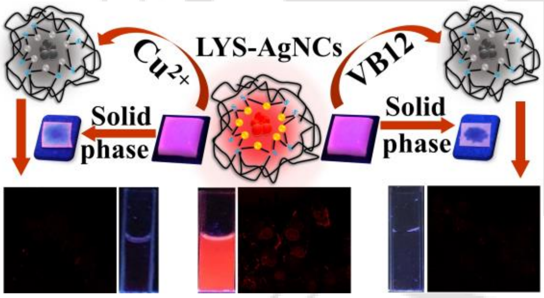

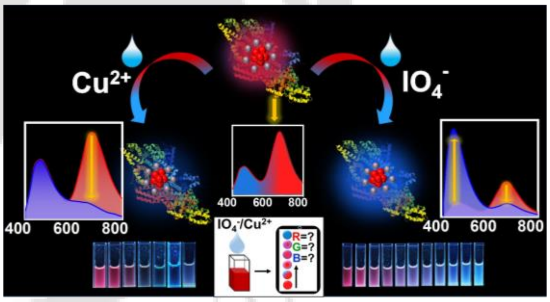

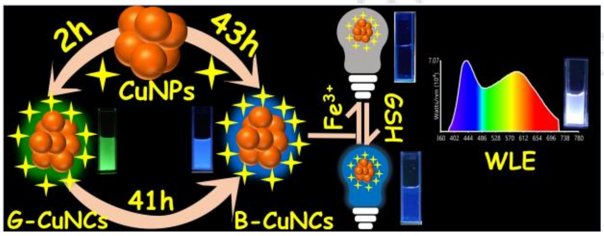

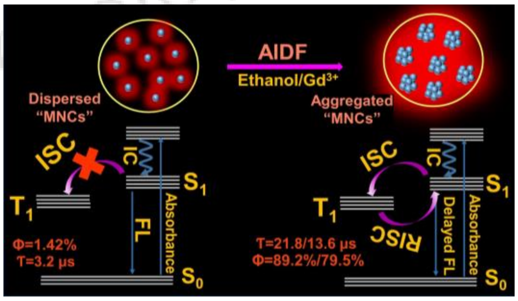

[This page was intentionally left blank]

7.1 Summary

Metal nanoclusters (MNCs) have drawn interests among researchers due to their distinctive characteristics, such as discrete energy levels resembling those found in molecules, leading to distinct HOMO-LUMO transitions, tunable fluorescence, outstanding photostability, and minimal toxicity. Furthermore, due to their biocompatibility and extremely small size, MNCs find extensive applications in biological systems.

In this thesis, a detailed discussion on the synthesis methods of MNCs accompanied by in-depth exploration of their photophysical properties and various applications have been provided. The thesis starts with an introductory overview about the evolution of MNCs to elucidating its photo-physical properties, factors affecting its properties and finally mentioning some of their major applications. The second chapter of the thesis is about experimental methodologies, describing the instrumentation and research approaches utilized. Subsequently, the thesis mentions four working chapters which are summarized below.

In ***Chapter 3***, selective and efficient detection of Cu^{2+} and Vitamin B_{12} (VB12) is achieved using red-emitting AgNCs synthesized within dithiothreitol-reduced lysozyme (LYS) scaffold. Two contrasting fluorescence (FL)-quenching mechanisms are responsible for the sensing. A portable paper strip was fabricated using LYS-AgNCs for on-site detection of Cu^{2+} and VB12. The probe was further applied for cell-imaging and detection capability of Cu^{2+} and VB12 inside cells as well.

In ***Chapter 4***, dithiothreitol-reduced bovine serum albumin (BSA) has been employed as a stabilizing agent to produce AgNCs with dual emission: a blue emission band at 450 nm and a far-red emissive band at 680 nm, allowing selective and ratiometric detection of Cu^{2+} and IO_4^-. These two analytes display different effects on both the emission bands. A smartphone-based on-site detection of IO_4^- and Cu^{2+} was also achieved. This investigation provided important insight into the one-pot synthesis of dual-emissive silver nanoclusters and the ratiometric detection mechanism of IO_4^- and Cu^{2+}.

In ***Chapter 5***, a different synthetic strategy was adopted to synthesize CuNCs via a two-step process. Non emissive copper nanoparticles (CuNPs) were firstly synthesized, followed by introduction of mercaptopropionic acid (MPA), which prompted time-controlled conversion of these CuNPs to green-emissive (G-CuNCs) and blue-emissive CuNCs (B-CuNCs). This B-CuNCs were then utilized for selective detection of Fe^{3+} and Glutathione (GSH) via fluorescence turn-off-on mechanism. Further, employing B-CuNCs and G-CuNCs a white light emitting (WLE) system was also generated.

In ***Chapter 6***, two different strategy to produce AIDF based luminescent materials at room temperature was reported, from widely reported Glutathione (GSH) capped CuNCs (GSH-CuNCs) by (1) simply modifying the solvent environment of the system and (2) by introduction of Gadolinium (Gd^{3+}) ions. The synthesized GSH-CuNCs in aqueous solution displayed weak fluorescence (Fl) emission. However, introducing these GSH-CuNCs to ethanol medium led to emergence of enhanced delayed Fl emission with significant delayed lifetime component and high delayed quantum yield (QY). Further, it was observed that, introduction of Gd^{3+} to GSH-CuNCs in aqueous solution can also induce enhanced delayed Fl emission with delayed lifetime component and high delayed QY. Lastly, the AIDF phenomena harnessed from GSH-CuNCs by Gd^{3+} were successfully employed to detect Cr^{6+} ions in aqueous solution with excellent selectivity.

Finally, this thesis is concluded with a comprehensive summary and an outline of future endeavors, elucidating the potential trajectories of the research presented herein.

7.2 Prospects

In recent times, numerous studies have been carried out for the synthesis of MNCs, aiming to address various challenges by enhancing both selectivity as well and sensitivity. Generally, MNCs of gold (Au) has been extensively investigated, however due to the high reactivity and ease of oxidation of Cu and Ag in zero-valent state, MNCs of Ag and Cu are comparatively less explored. Thus, these limitations challenges stable formation of CuNCs and AgNCs, limiting their potential applications across diverse fields. This thesis delivered the strategic synthesis of some novel CuNCs and AgNCs with superior optical properties. The photo-physical properties of these MNCs have been studied systematically. Furthermore, these MNCs have been applied as multimode sensing platform. I firmly believe that the advancement elucidated in this thesis about synthetic strategy and sensing mechanisms will serve to inspire future researchers to further enhance the efficiency of comparatively less explored CuNCs and AgNCs. Furthermore, exploring sensing based applications by employing ultrafast spectroscopic techniques can provide profound insights into the sensing mechanism, paving the way for strategic synthesis method to expand the scope of their applications. Moreover, in-depth spectroscopic studies including steady state and time-resolved optical spectroscopies can provide critical information on the electronic structure and relaxation dynamics of MNCs.

Appendix Chapter 3

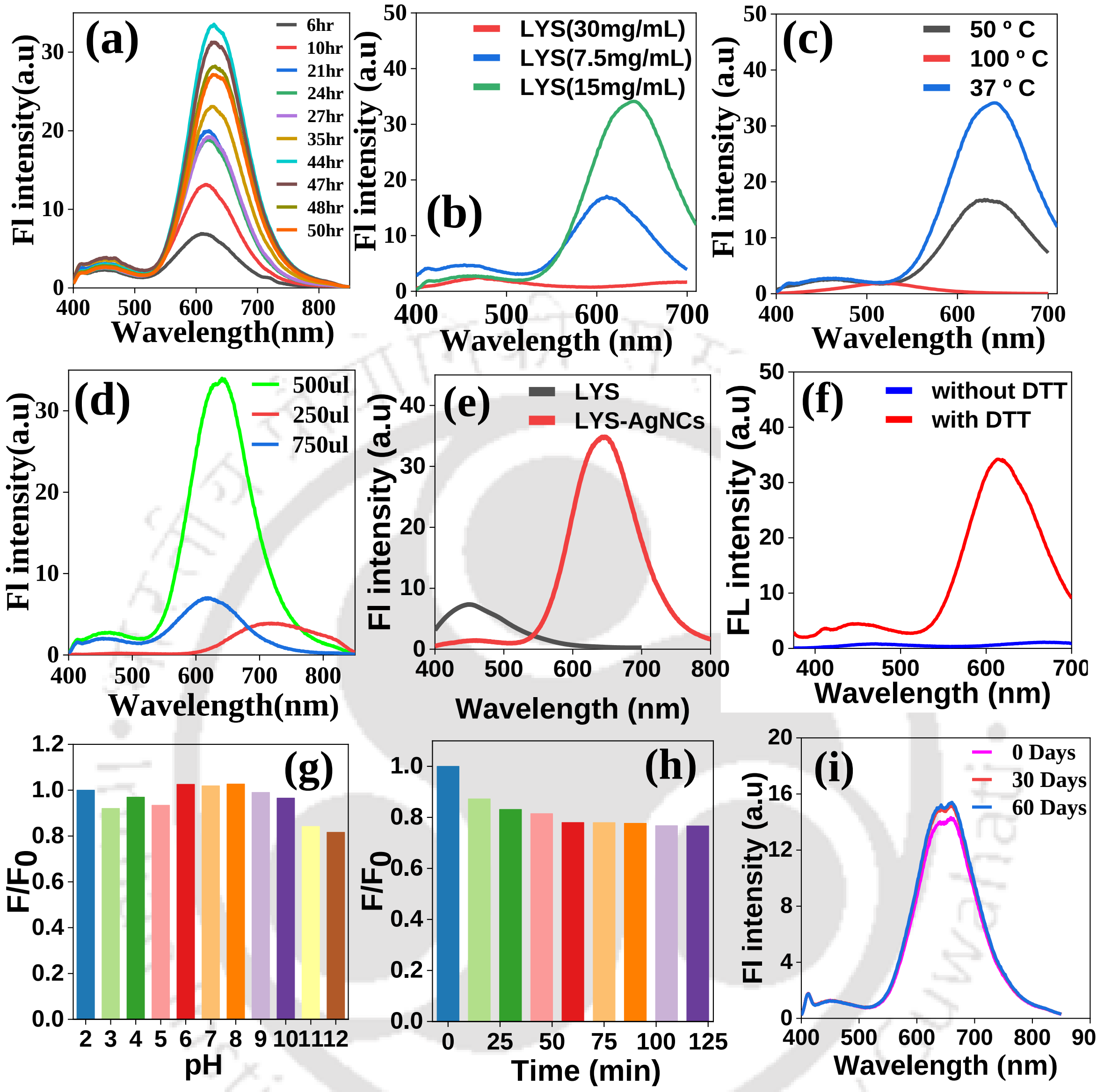

Figure A.3.1. Fl spectra of LYS-AgNCs.measured at different conditions to obtain the optimal conditions: (a) at different reactions times. (b) at different LYS concentrations (c) at various reaction temperatures and (d) at different DTT concentrations (e) Fluorescence spectra of Lysozyme and LYS-AgNCs measured at 360 nm excitation wavelength (f) Fl spectra of LYS-AgNCs with and without DTT addition (g) The variation of fluorescence intensity LYS-AgNCs.(F represents Fl intensity at particular pH and F_0 represents Fl intensity at pH 7) at different pHs. (h) UV light treatment of LYS-AgNCs (i) Fl intensity stability check of LYS-AgNCs for 60 days

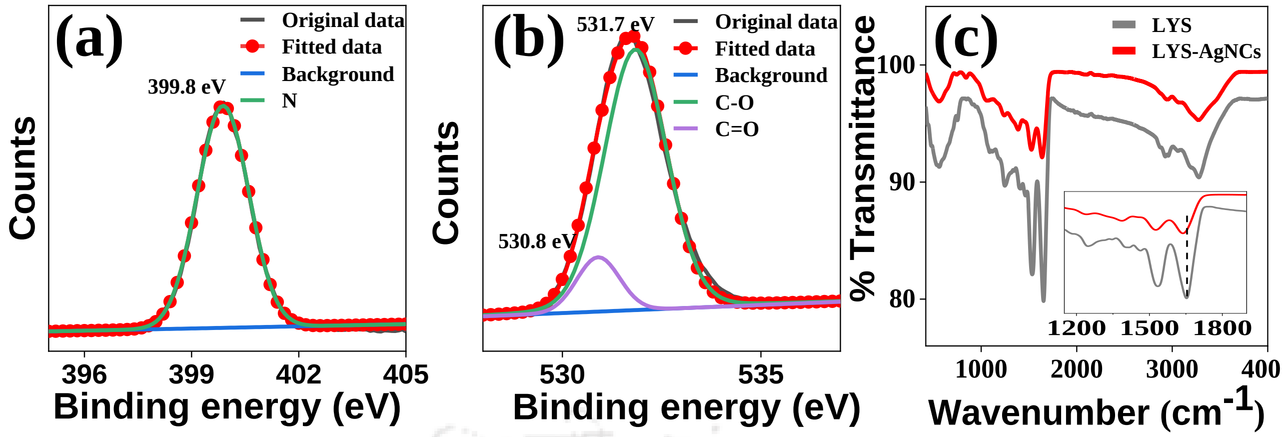

Figure A.3.2. High resolution XPS spectra of (a) N 1S (b) O 1S (c) FTIR spectra of LYS and LYS-AgNCs (Inset shows spectral shift of amide I band).

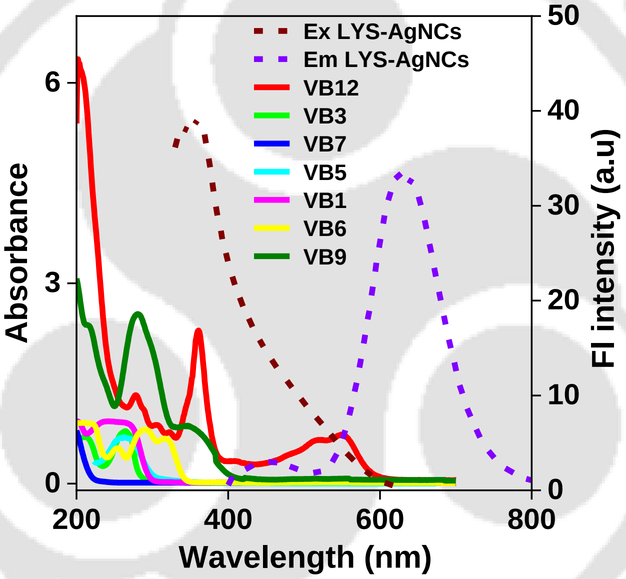

Figure A.3.4 Absorbance spectra of all vitamins and excitation and emission spectra of LYS-AgNCs.

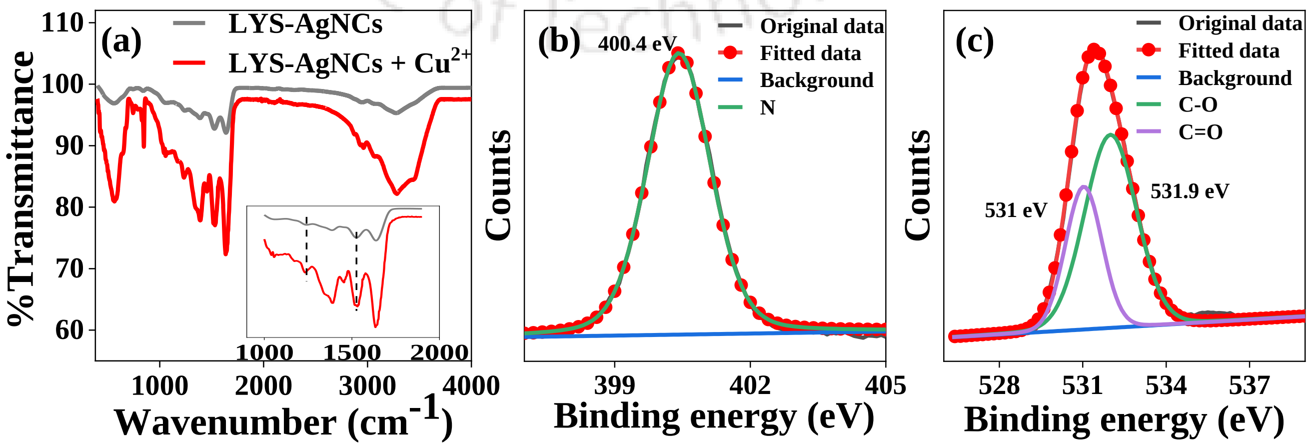

Figure A.3.5. (a) FTIR spectra of LYS-AgNCs before and after addition of Cu^{2+}. Inset shows shifting of amide II and amide III bands. High-resolution XPS spectra of (b) N 1S (c) O 1S of LYS-AgNCs after addition of Cu^{2+}

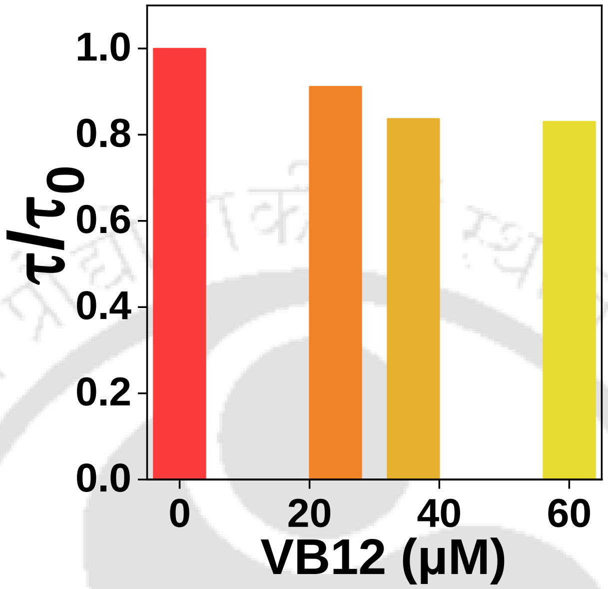

Figure A.3.6. Ratios of the average lifetime of LYS-AgNCs with different concentrations of VB12.

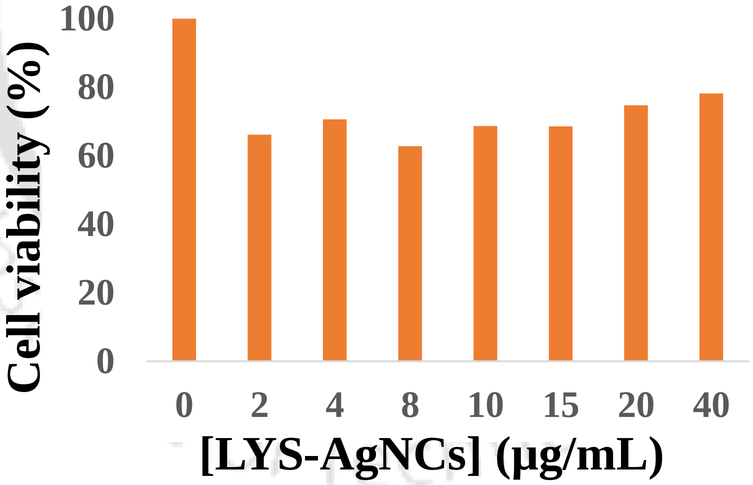

Figure A.3.8. Cell viability for measuring the cytotoxicity of LYS-AgNCs on HeLa cells was measured after 48 h of incubation.

Table A.3.1. Fl decay fitting parameters of LYS-AgNCs measured using 375 nm laser source with IRF value 80 ps.

	A_1	A_2	A_3	τ_1(ns)	τ_2(ns)	τ_3(ns)	τ_{avg}(ns)	χ^2

LYS-AgNCs	0.23	0.14	0.63	16.81	127.92	0.44	22.05	1.24

Table A.3.2. Fluorescence decay fitting parameter of LYS-AgNCs with different concentration of Cu^{2+} measured using 375 nm laser source with IRF value 80 ps.

	A_1	A_2	A_3	τ_1(ns)	τ_2(ns)	τ_3(ns)	τ_{avg}(ns)	χ^2
LYS-AgNCs	0.23	0.14	0.63	16.81	127.92	0.44	22.05	1.24
LYS-AgNCs + 18µm Cu^{2+}	0.17	0.09	0.74	13.91	120.34	0.38	13.48	1.35
LYS-AgNCs + 36µMCu^{2+}	0.11	0.04	0.85	11.15	108.66	0.23	5.77	1.43
LYS-AgNCs +66 µM Cu^{2+}	0.11	0.04	0.85	5.03	89.35	0.23	4.32	1.43

Table A.3.3. Fluorescence decay fitting parameter of LYS-AgNCs with different concentrations of VB12 measured using 375 nm laser source with IRF value 80 ps.

	A_1	A_2	A_3	τ_1(ns)	τ_2(ns)	τ_3(ns)	τ_{avg}(ns)	χ^2
LYS-AgNCs	0.23	0.14	0.63	16.81	127.9	0.44	22.05	1.24
LYS-AgNCs + 24µm VB12	0.21	0.13	0.66	16.13	126.5	0.43	20.11	1.28
LYS-AgNCs + 36 µM VB12	0.17	0.12	0.71	16.16	129.0	0.33	18.46	1.23
LYS-AgNCs + 60µM VB12	0.18	0.12	0.7	16.02	126.5	0.37	18.32	1.28

Table A.3.4. IFE correction table for VB12.

[VB12] (μM)	A_{ex}	A_{em}	CF	$F_{observed}$	$F_{corrected}$	$F_{corrected(0)}/F_{corrected}$
0	0.60201	0.00108	1.846227	1577723.188	2912835.09	1
6	0.75744	0.00197	2.113097	1267749.885	2678878.462	1.087334
12	0.89849	0.00195	2.367466	1061620.366	2513350.471	1.158945
18	1.04515	0.0028	2.646655	901225.8787	2385233.993	1.221195
24	1.19696	0.00372	2.94784	758089.9302	2234727.712	1.303441
30	1.35419	0.00452	3.270427	649701.5206	2124801.488	1.370874
36	1.49569	0.00466	3.566773	549545.4924	1960103.955	1.486062
42	1.6315	0.00413	3.854355	497460.8696	1917390.679	1.519166
48	1.76313	0.00544	4.145058	430958.3236	1786347.436	1.630609
54	1.89973	0.00534	4.444679	369276.4787	1641315.524	1.774695
60	2.02252	0.00616	4.721152	309395.3206	1460702.246	1.994133

Appendix Chapter 4

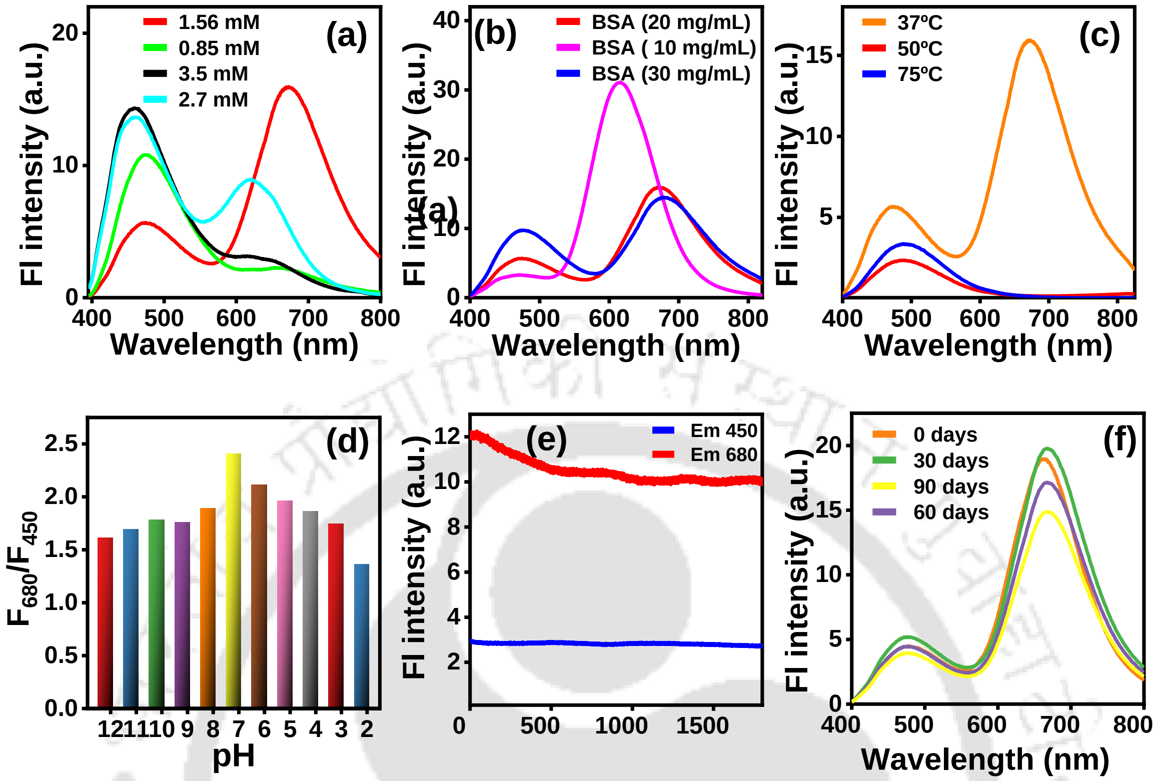

Figure A.4.1. Fl spectra of AgNCs measured at different conditions to obtain the optimal conditions (a) at different DTT concentrations (b) at different BSA concentrations (c) at various reaction temperatures (d) Intensity ratio (F_{450}/F_{680}) at different pH values. (e) Photostability plot at 450 nm and 680 nm emission wavelength under constant excitation source (360 nm) for 30 min. (f) The emission spectra at different days showed almost no change in the emission spectrum for 90 days.

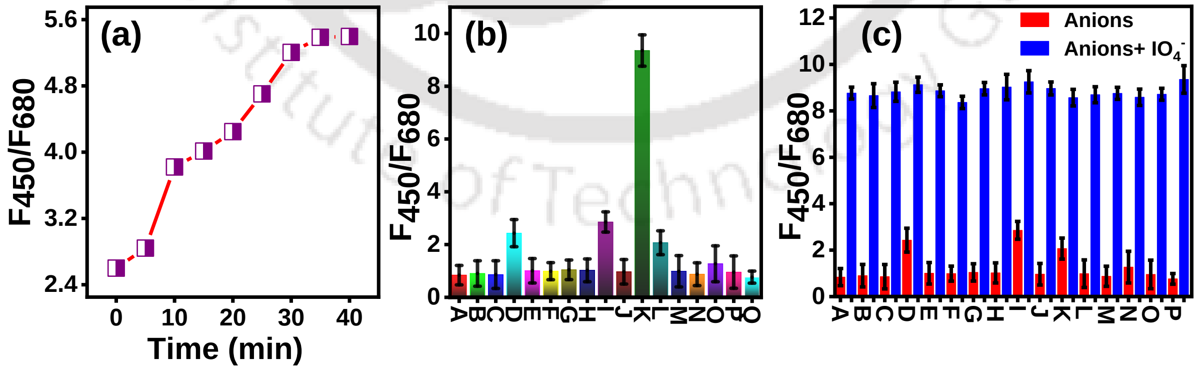

Figure A.4.2. (a) Fl response time of AgNCs in the presence of 100 µM of IO_4^- (b) Selectivity plot of AgNCs in the presence of 160 µM of various anions (A, B, C, D, E, F, G, H, I, J, K, L, M, N, O, P and Q represents F^-, I^-, HPO_4^{2-}, CN^-, Cl^-, NO_2^-, Br^-, $P_2O_7^{4-}$, S^{2-}, PO_4^{3-}, IO_4^-, H_2O_2, ClO^-,ClO_4^- ClO_3^-, NO_3^-, and AgNCs respectively). (c) Selectivity plot of AgNCs by adding various anions (160 µM) in absence and presence of 160 µM of IO_4^- (A, B, C, D, E, F, G, H, I, J, K, L, M, N, O and P represents F^-, I^-, HPO_4^{2-}, CN^-, Cl^-, NO_2^-, Br^-, $P_2O_7^{4-}$, S^{2-}, PO_4^{3-}, H_2O_2, ClO^-,ClO_4^- ClO_3^-, NO_3^- and AgNCs respectively).

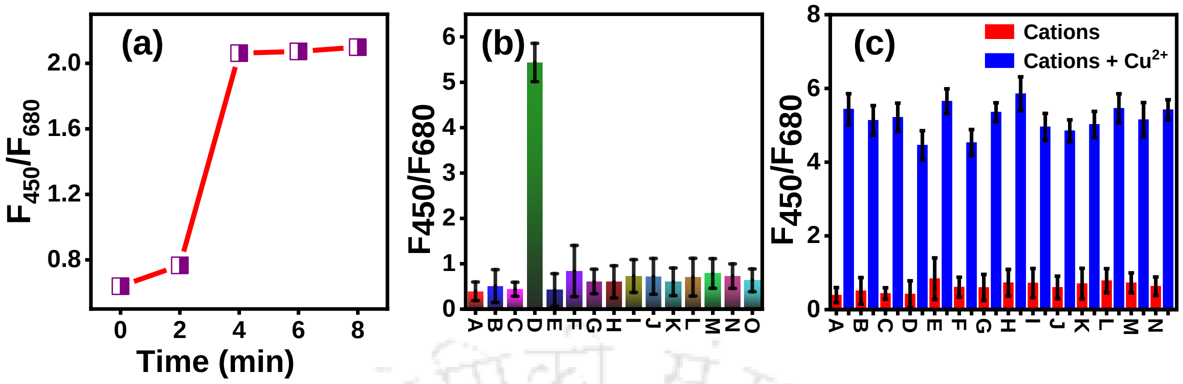

Figure A.4.3. (a) Fl response time of AgNCs in the presence of 20 µM of Cu^{2+} (b) Selectivity plot of AgNCs in the presence of 30 µM of various cations (A, B, C, D, E, F, G, H, I, J, K, L, M, N and O represents AgNCs, Pb^{2+}, Fe^{3+}, Cu^{2+}, Ni^{2+}, Zn^{2+}, Cr^{3+}, Cd^{2+}, Al^{3+}, Mg^{2+}, Hg^{2+}, Fe^{2+}, Ag^{+}, $Mn^{2+}$and Co^{2+} respectively). (c) Selectivity plot of AgNCs by adding various cations(30 µM) in absence and presence of 30 µM of Cu^{2+} (A, B, C, D, E, F, G, H, I, J, K, L, M and N represents AgNCs, Pb^{2+}, Fe^{3+}, Ni^{2+}, Zn^{2+}, Cr^{3+}, Cd^{2+}, Al^{3+}, Mg^{2+}, Hg^{2+}, Fe^{2+}, Ag^{+}, $Mn^{2+}$and Co^{2+} respectively).

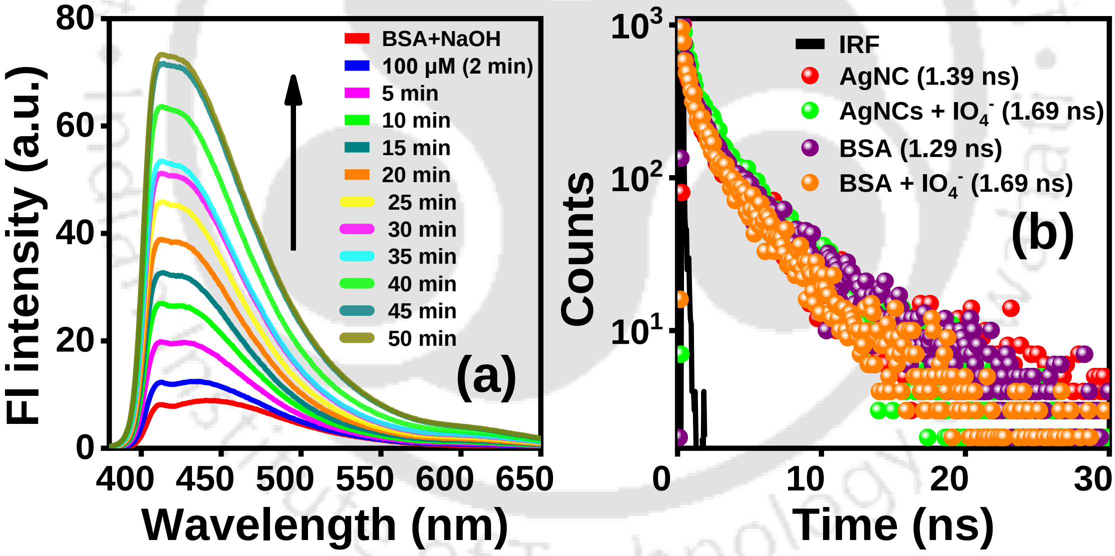

Figure A.4.4. (a) Fl spectra of BSA+ NaOH (100 µl of 1M) recorded every 5 min after the addition of 100 µM of IO_4^- (b) FL decays of AgNCs and BSA+ NaOH before and after IO_4^- (160 µM) addition at 450 nm.

Table A.4.1. Fl decay fitting parameters of AgNCs measured using 375 nm laser source.

λ_{em}	a_1	a_2	a_3	τ_1 (ns)	τ_2 (ns)	τ_3 (ns)	τ_{avg} (ns)	χ^2
680 nm	0.30	0.20	0.50	17.0	118.7	1.34	29.50	1.12

450 nm	0.80	0.20		0.57	4.67		1.39	1.01

Table A.4.2. Fluorescence decay fitting parameters of AgNCs before and after adding IO_4^- (160 μM).

	λ_{em}	a_1	a_2	a_3	τ_1 (ns)	τ_2 (ns)	τ_3 (ns)	τ_{avg} (ns)	χ^2
AgNCs	450 nm	0.80	0.20		0.57	4.67		1.39	1.01
	680 nm	0.30	0.20	0.50	16.98	118.71	1.34	29.506	1.12
AgNCs+IO_4^-	450 nm	0.69	0.31		0.71	3.88		1.6927	1.06
	680 nm	0.23	0.11	0.66	13.45	99.33	1.15	14.7788	1.24

Table A.4.3. Fl decay fitting parameters of AgNCs and NaOH treated BSA before and after adding IO_4^- (160 μM) at the 450 nm emission.

	a_1	a_2	τ_1 (ns)	τ_2 (ns)	τ_{avg} (ns)	χ^2
AgNCs	0.80	0.20	0.57	4.67	1.39	1.01
AgNCs + IO_4^-	0.69	0.31	0.71	3.88	1.6927	1.06
BSA	0.75	0.25	0.48	3.69	1.2825	1.03
BSA + IO_4^-	0.78	0.22	0.76	5.07	1.7082	1.03

Table A.4.4. Fl decay fitting parameters of AgNCs before and after adding Cu^{2+} (40 μM).

	λ_{em}	a_1	a_2	a_3	τ_1 (ns)	τ_2 (ns)	τ_3 (ns)	τ_{avg} (ns)	χ^2
AgNCs	450	0.80	0.20		0.57	4.67		1.39	1.01
	680	0.30	0.20	0.50	16.98	118.71	1.34	29.506	1.12
	450	0.79	0.21		0.49	4.46		1.3237	1.08

AgNCs+ Cu^{2+}	680	0.24	0.1	0.66	13.17	101.11	1.19	14.0572	1.25

Appendix Chapter 5

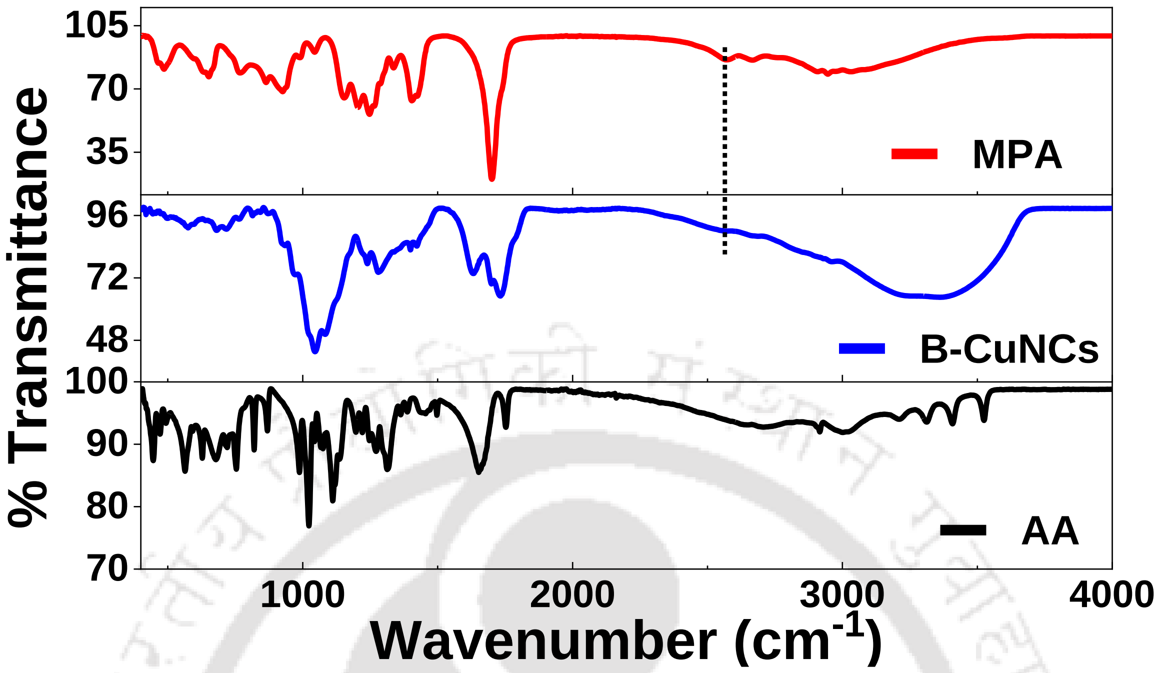

Figure A.5.1. FTIR spectra of Ascorbic acid (AA), B-CuNCs and Mercaptopropionic acid (MPA).

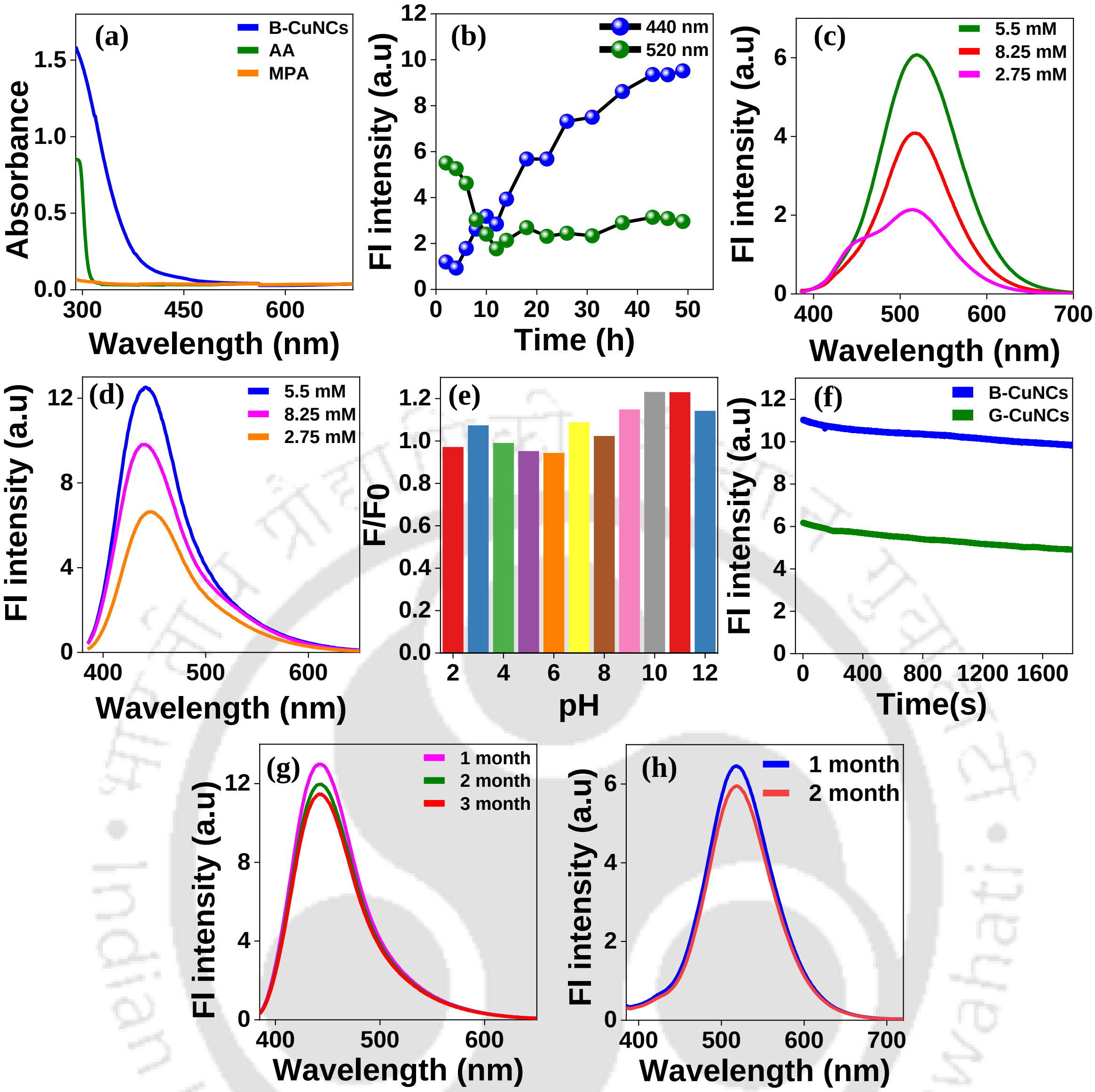

Figure A.5.2. (a) UV-vis spectra of B-CuNCs, AA and MPA. (b) Time versus emission intensity variation at 520 and 440 nm wavelength. Fl spectra of (c) G-CuNCs (d) B-CuNCs at 370 nm excitation with different concentrations of MPA. (e) pH stability of B-CuNCs (f) optical stability of B-CuNCs and G-CuNCs. storage stability of (g) B-CuNCs at 4°C and (h) G-CuNCs at -20°C.

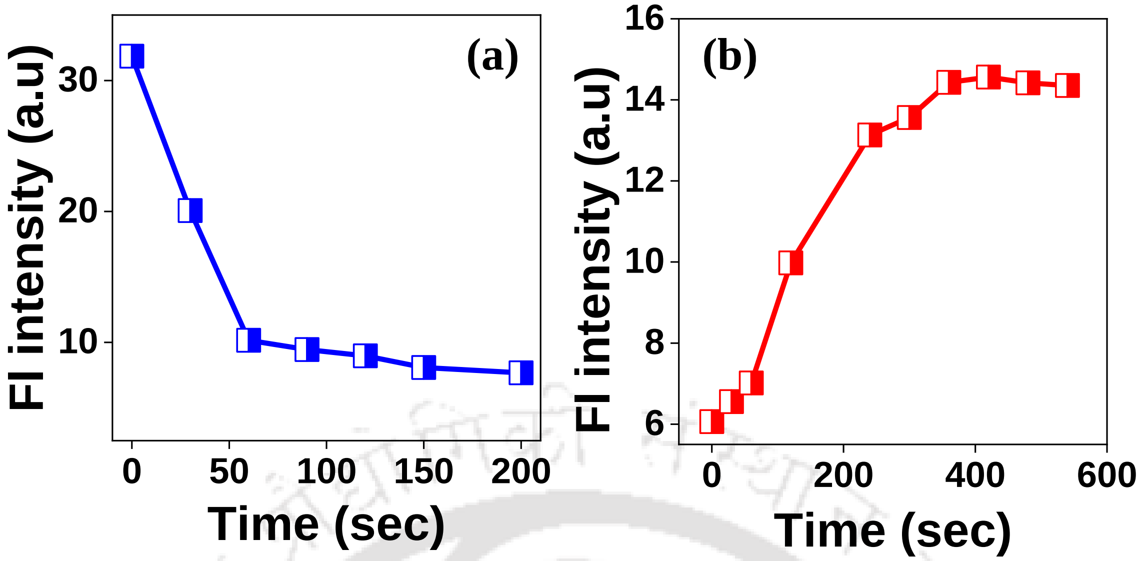

Figure A.5.3: (a) Fl response time of B-CuNCs in presence of 100 μM of Fe^{3+} (b) Fl response time of B-CuNCs+Fe^{3+} in presence of 200 μM of GSH.

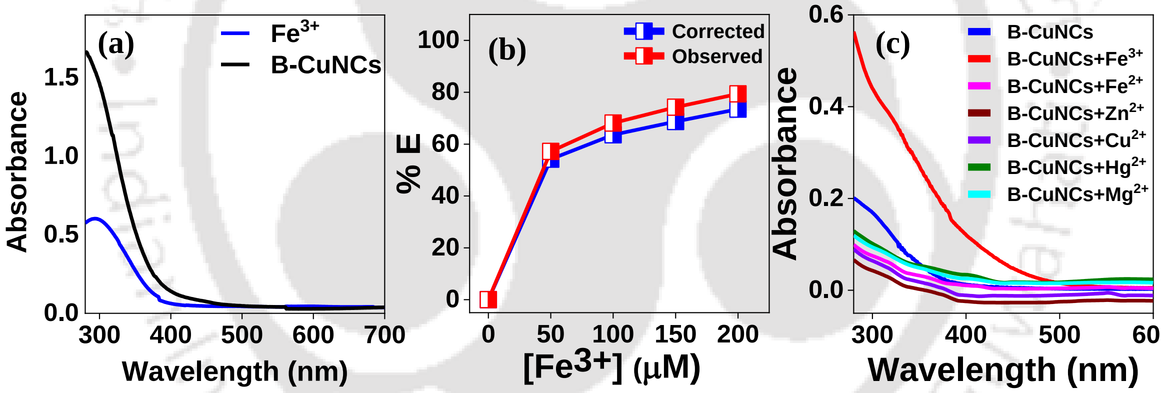

Figure A.5.4: (a) UV-vis spectra of Fe^{3+} and B-CuNCs. (b) Suppressed efficiency (E%) of observed and corrected measurements for B-CuNCs after each addition of different concentrations of Fe^{3+} (The inset shows the parameters used for the IFE equation). (c) Absorbance spectra of B-CuNCs in presence of 200 μM of different metal ions.

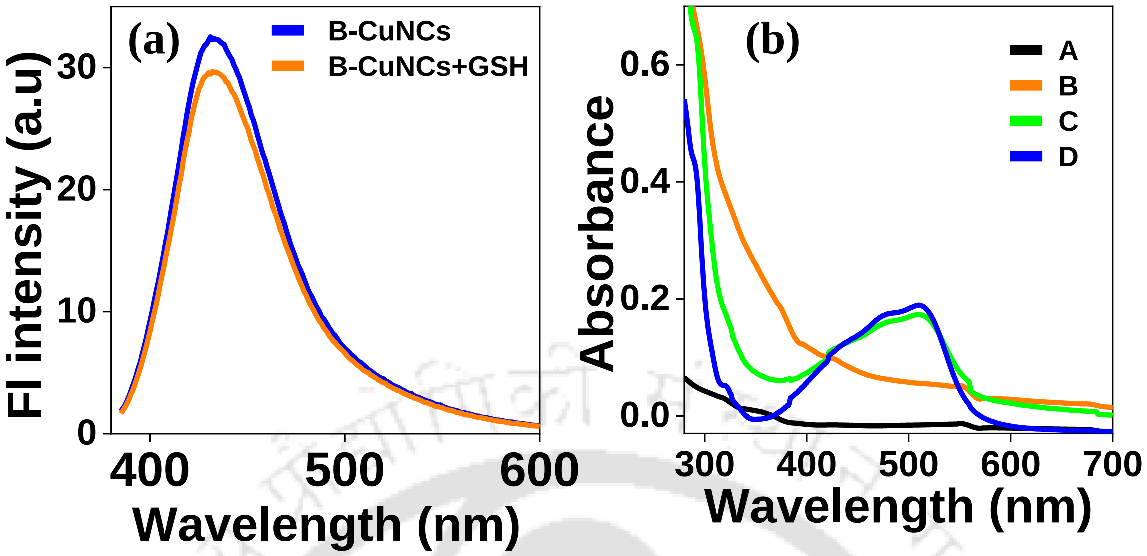

Figure A.5.5: (a) Fl spectra of B-CuNCs in absence and presence of GSH. (b) UV- vis spectra of (A) B-CuNCs (B) B-CuNCs+Fe^{3+}+1,10-phenanthroline(C) B-CuNCs+Fe^{3+}+GSH+1,10-phenanthroline (D) 1,10-phenanthroline + Fe^{2+}.

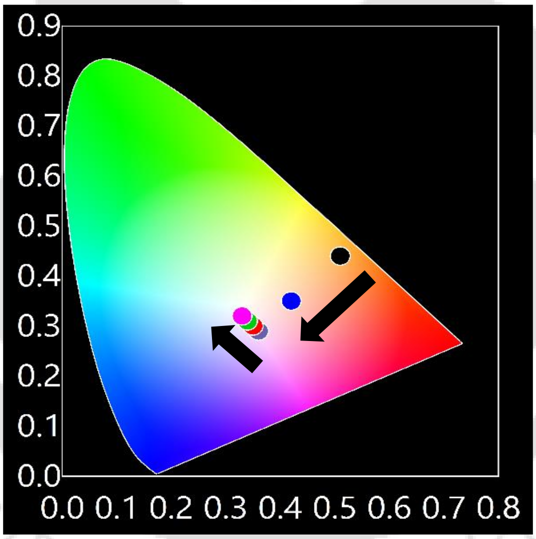

Figure A.5.6: CIE coordinates for different combination of concentrations used during optimization procedure (Table A.5.4).

Table A.5.1. Fl decay fitting parameters of G-CuNCs and B-CuNCs measured using 375 nm laser source at 520 nm and 440 nm respectively.

	A_1	A_2	A_3	τ_1 (ns)	τ_2 (ns)	τ_3 (ns)	τ_{avg} (ns)	χ^2
G-CuNCs	0.12	0.14	0.74	0.91	2.75	0.04	0.52	1.07
B-CuNCs	0.43	0.46	0.11	1.03	0.10	2.39	0.75	1.09

Table A.5.2: IFE correction table for different concentration of Fe^{3+}.

Fe^{3+} (µM)	A_{ex}	A_{em}	CF	$F_{observed}$ (× 10^6)	$F_{corrected}$ (× 10^6)	$F_{corrected(0)}/F_{corrected}$
0	0.0291	0.0067	1.04	3.42	3.56	1
50	0.073	0.0241	1.11	1.46	1.63	2.18
100	0.116	0.041	1.19	1.09	1.29	2.74
150	0.158	0.057	1.26	0.88	1.11	3.19
200	0.195	0.073	1.33	0.71	0.94	3.77

Table A.5.3. Fluorescence decay fitting parameter of B-CuNCs with different concentrations of Fe^{3+} at 440 nm measured using 375 nm laser source.

	A_1	A_2	A_3	τ_1 (ns)	τ_2 (ns)	τ_3 (ns)	τ_{avg} (ns)	χ^2
B-CuNCs	0.43	0.46	0.11	1.03	0.10	2.39	0.75	1.09
B-CuNCs + 50 µM Fe^{3+}	0.09	0.03	0.88	0.87	2.59	0.02	0.17	1.01
B-CuNCs+ 100 µM Fe^{3+}	0.05	0.02	0.93	0.80	2.53	0.02	0.10	1.01
B-CuNCs+ 150 µM Fe^{3+}	0.03	0.01	0.96	0.78	2.54	0.01	0.06	1.09
B-CuNCs+ 200 µM Fe^{3+}	0.02	0.01	0.97	0.77	2.65	0.01	0.05	1.00

Table A.5.4: CIE coordinates corresponding to various combination of GSH-AuNCs, B-CuNCs and G-CuNCs in 1 mL water. Colour of dots mentioned is represented in CIE coordinate diagram shown in Fig. S11.

GSH-AuNCs	B-CuNCs	G-CuNCs	CIE coordinate
1 mL	0 µL	0 µL	(0.52,0.44) (Black dot)

1 mL	20 µL	0 µL	(0.42,0.35) (Blue dot)
1 mL	40 µL	0 µL	(0.36,0.29) (Grey dot)
1 mL	40 µL	15 µL	(0.35,0.30) (Red dot)
1 mL	40 µL	30 µL	(0.34,0.31) (Green dot)
1 mL	40 µL	40 µL	(0.33,0.32) (Pink dot)

Appendix Chapter 6

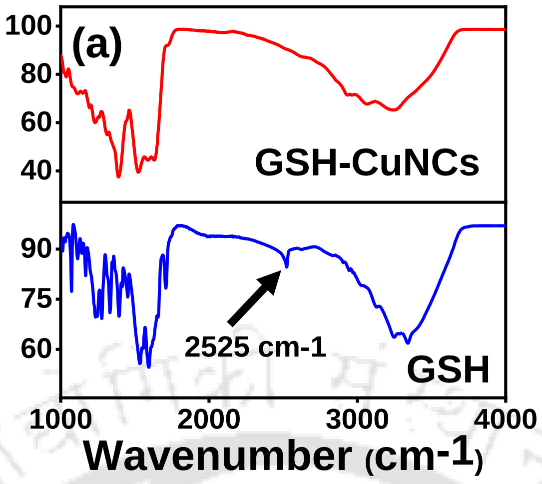

Figure A.6.1. FTIR spectra of GSH and GSH-CuNCs.

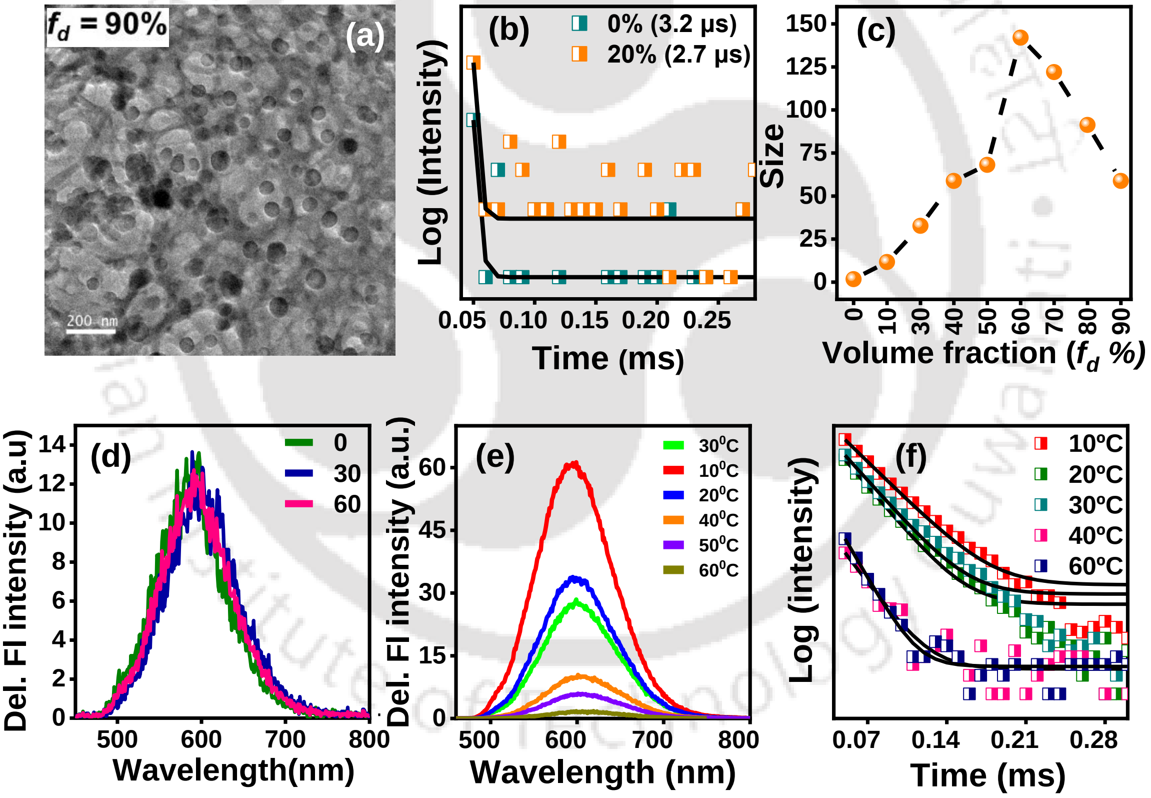

Figure A.6.2. (a) Magnified TEM image of GSH-CuNCs at f_d = 90% (b) Time-resolved delayed photoluminescence decay profiles of GSH-CuNCs at f_d = 0% and 20% (c) size of the aggregates of GSH-CuNCs with increasing volume fraction of ethanol obtained from DLS study (d) Delayed emission check of GSH-CuNCs at f_d = 90% for 60 days on storing at room temperature (e) Temperature dependent delayed emission study of GSH-CuNCs in ethanol solvent and (f) Temperature dependent time-resolved delayed photoluminescence decay profiles of GSH-CuNCs

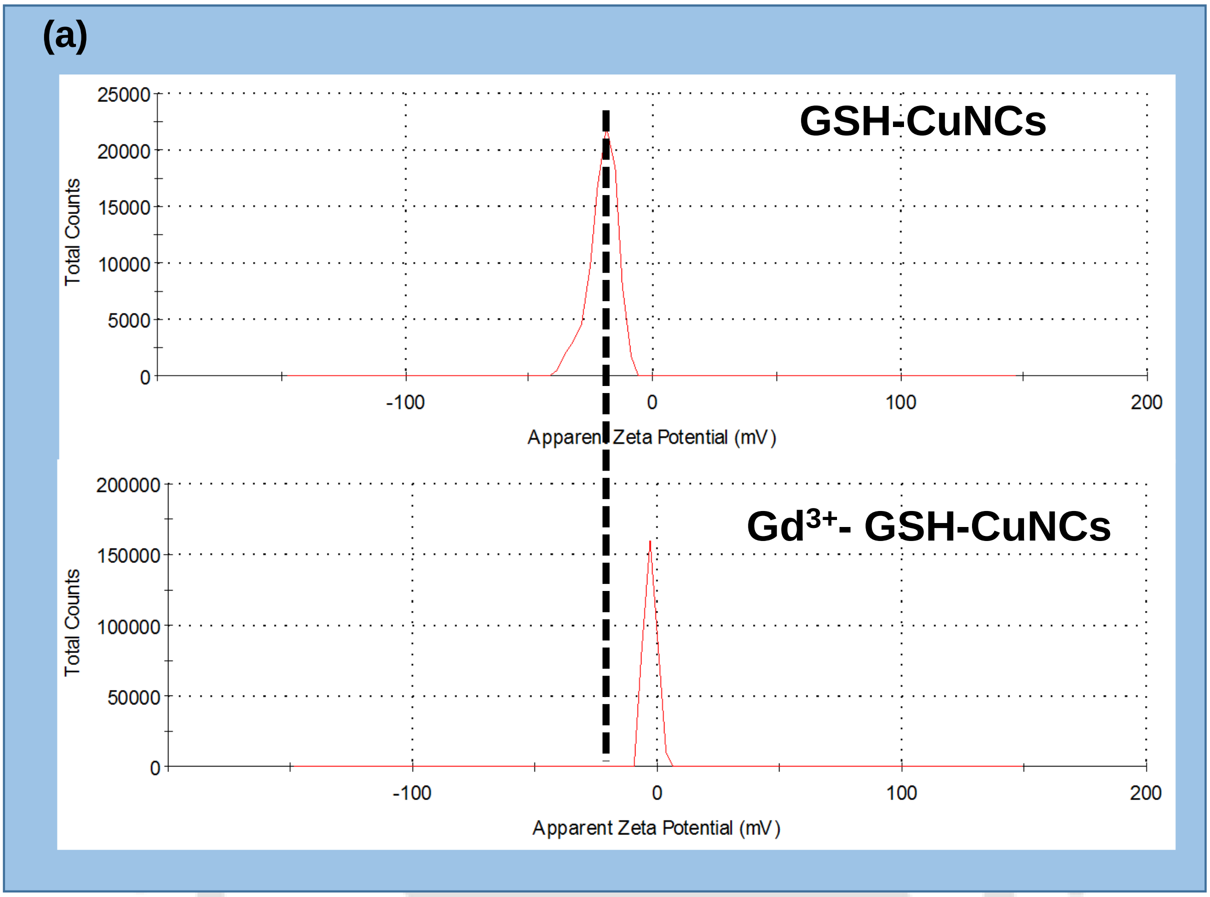

Figure A.6.3a. Zeta potential data of GSH-CuNCs and Gd^{3+}-GSH-CuNCs

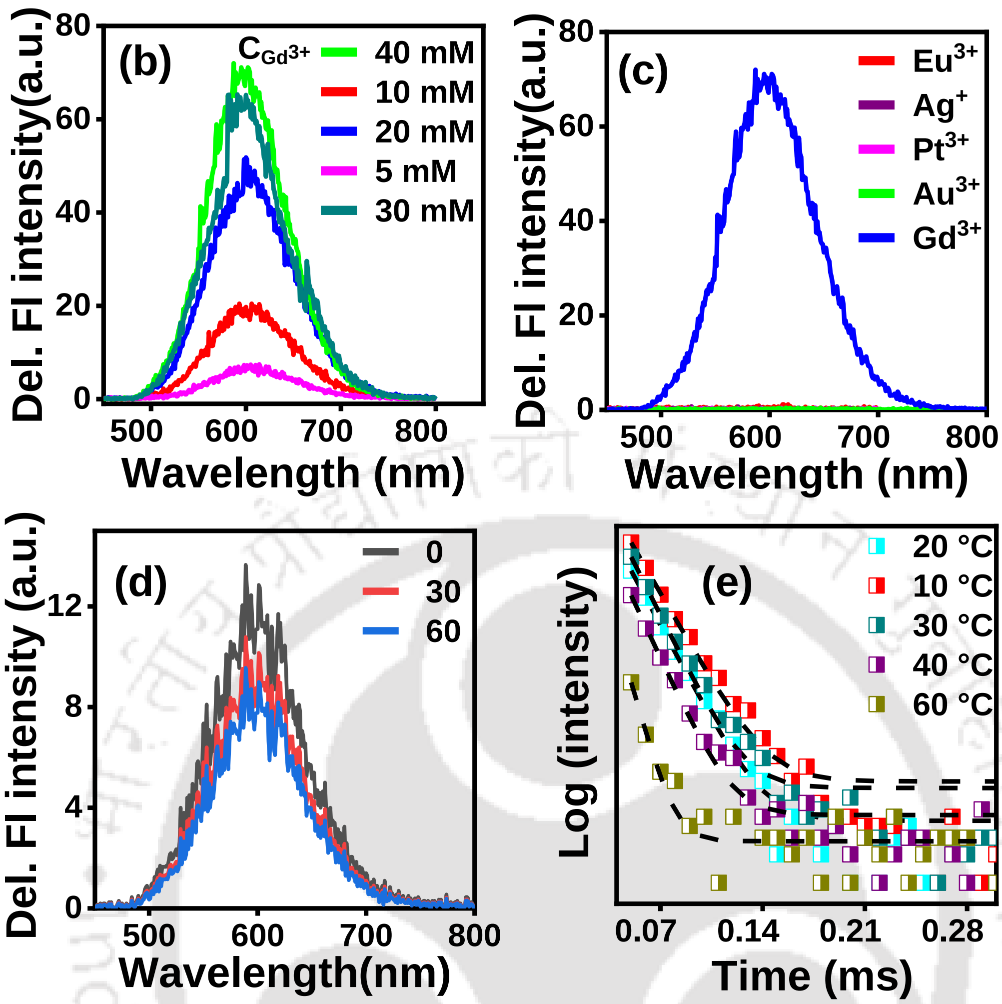

Figure A.6.3. (b) Delayed emission spectra of GSH-CuNCs after adding various concentration of Gd^{3+} (c) Delayed emission spectra of GSH-CuNCs after adding various metal ions (d) Delayed emission check of Gd^{3+}-GSH-CuNCs for 60 days on storing at room temperature and (e) Temperature dependent time-resolved delayed photoluminescence decay profiles of Gd^{3+}-GSH-CuNCs.

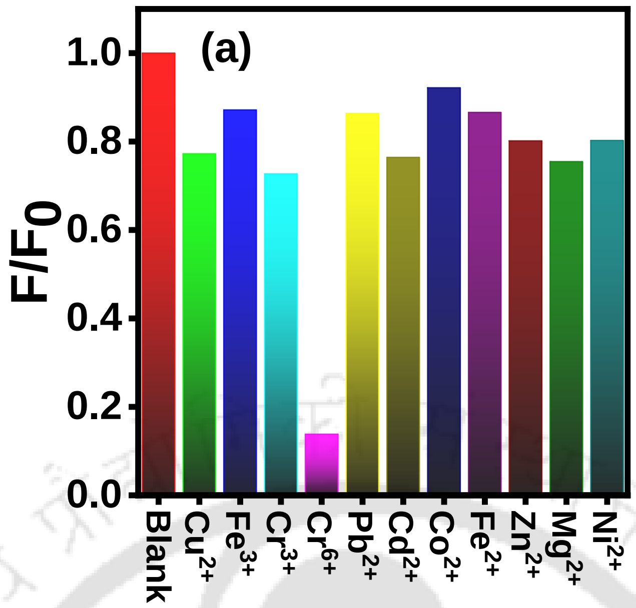

Figure A.6.4 Selectivity plot of the delayed emission of Gd^{3+}-GSH-CuNCs towards various metal ions.

Table A.6.1. Calculated parameters as-obtained from time resolved delayed photoluminescence decay study of GSH-CuNCs in varying volume fraction (f_d) of ethanol.

f_d	A_1	τ_1 (ms)	χ^2
GSH-CuNCs (0%)	1.00×10^{11}	0.0032	0.48
20 %	2.47×10^{12}	0.0027	0.60
60 %	2.55×10^{7}	0.0115	0.98
70 %	1.08×10^{8}	0.0172	0.99
80 %	2.87×10^{8}	0.0189	0.99
90 %	3.74×10^{8}	0.0218	0.99

Table A.6.2. Calculated parameters as-obtained from time resolved delayed photoluminescence decay study of temperature dependent study of GSH-CuNCs in f_d = 90 %.

Temperature (°C)	A_1	τ_1 (ms)	χ^2
10 °C	5.12×10^{8}	0.0242	0.99
20 °C	3.68×10^{8}	0.0201	0.99
30 °C	3.83×10^{8}	0.0212	0.99

40 °C	1.62×10^7	0.0176	0.99
60 °C	6.47×10^7	0.0135	0.99

Table A.6.3. Calculated parameters as-obtained from time resolved delayed photoluminescence decay study of Gd^{3+}- GSH-CuNCs.

	A_1	τ_1 (ms)	χ^2
Gd^{3+}- GSH-CuNCs	9.64×10^7	0.0136	0.99

Table A.6.4. Calculated parameters as-obtained from time resolved delayed photoluminescence decay study of temperature dependent study of Gd^{3+}- GSH-CuNCs.

Temperature (°C)	A_1	τ_1 (ms)	χ^2
10 °C	4.44×10^8	0.0161	0.99
20 °C	2.84×10^8	0.0149	0.99
30 °C	4.99×10^8	0.0140	0.99
40 °C	2.57×10^8	0.0130	0.99
60 °C	3.51×10^8	0.0079	0.99

Table A.6.5. Calculated parameters as-obtained from time resolved delayed photoluminescence decay study with increasing concentration of Cr^{6+} in Gd^{3+}- GSH-CuNCs.

$[Cr^{6+}]$ (μM)	A_1	τ_1 (ms)	χ^2
0	9.64×10^7	0.0136	0.99
25	6.67×10^8	0.0124	0.99
37	1.20×10^9	0.0114	0.99
62	5.65×10^8	0.0094	0.99

Publications

1. **Priyanka Sarkar,** Muktashree Saha, Nilanjana Nandi, Dillip Kumar Sahu, Kalyanasis Sahu***** "Red-Emitting Silver Nanoclusters for Dual-Mode Detection of Cu^{2+} and Vitamin B12 in Living Cells" *ACS Appl. Nano Mater.* 2022, 5, 6, 7670–7678.

2. **Priyanka Sarkar,** Nilanjana Nandi, Neha Barnwal, Kalyanasis Sahu***** "BSA-Capped Dual-Emissive Silver Nanoclusters for Detection of IO_4^- and Cu^{2+} Ions" *ACS Appl. Nano Mater.* 2023, 6, 17, 15851–15859.

3. **Priyanka Sarkar,** Nilanjana Nandi, Neha Barnwal, Kalyanasis Sahu***** "Mercaptopropionic acid-assisted synthesis of green and blue emissive copper nanoclusters for multimodal sensing and white light applications" *Materials Today Chemistry* 27 (2023) 101341.

4. **Priyanka Sarkar,** Neha Barnwal, Nilanjana Nandi, Kalyanasis Sahu***** "Ethanol and Gd^{3+} Induced Aggregation Induced Delayed fluorescence in Copper Nanoclusters" *(Under revision).*

5. Nilanjana Nandi, Konika Choudhury, **Priyanka Sarkar**, S. S. Ghosh, Kalyanasis Sahu* "Ratiometric Multimode Detection of pH and Fe^{3+} by Dual-Emissive Heteroatom-Doped Carbon Dots for Living Cell Applications" *ACS Appl. Nano Mater*. 2022, 5, 17315−17324.

6. Nilanjana Nandi, **Priyanka Sarkar**, Kalyanasis Sahu* "N-doped carbon dots: triple mode excitation emission features for dual channel sensing and logic gate application" *Materials Today Chemistry* 26 (2022) 101015.

7. Nilanjana Nandi, Shubham Gaurav, **Priyanka Sarkar**, Sachin Kumar, Kalyanasis Sahu* "Hit Multiple Targets with One Arrow: Pb^{2+} and ClO^- Detection by Edge Functionalized Graphene Quantum Dots and Their Applications in Living Cells" *ACS Appl. Bio Mater.* 2021, 4, 10, 7605–7614.

8. Nilanjana Nandi, Shubham Gaurav, **Priyanka Sarkar**, Sachin Kumar, Kalyanasis Sahu* "Multifunctional N-Doped Carbon Dots for Bimodal Detection of Bilirubin and Vitamin B12, Living Cell Imaging, and Fluorescent Ink" *ACS Appl. Bio Mater.* 2021, 4, 5201−5211.

9. Nilanjana Nandi, **Priyanka Sarkar**, Kalyanasis Sahu* "N-Doped Carbon Dots for Visual Recognition of 4-Nitroaniline and Use in Fluorescent Inks" *ACS Appl. Nano Mater.* 2021, 4, 9616−9624.

10. Dillip Kumar Sahu, **Priyanka Sarkar**, Debabrata Singha and Kalyanasis Sahu* "Protein-activated transformation of silver nanoparticles into blue and red-emitting nanoclusters" *RSC Adv.*, 2019, 9, 39405.

Conferences

1. Frontiers in Chemical Sciences 2022 held at Indian Institute of Technology Guwahati, Assam, 2-4th December 2022. (Poster Presentation)

2. Research Conclave'22 held at IIT Guwahati, Guwahati, Assam, 20-23rd January 2022. (Poster Presentation)

3. North-East Research Conclave-2022 held at Indian Institute of Technology Guwahati, Assam, May 20-22th, 2022. (Oral Presentation)

4. The ChemSci2021: Leaders in the Field Symposium organised by RSC's flagship journal Chemical Science & JNCASR Bangalore, 13th to 15th December 2021. (Poster Presentation)

5. International Conference on Progress and Challenges in Modern Day Science (PCMDS-2021) organized by B. Barooah College, Guwahati, Assam, India during 17-18 June, 2021 (Poster Presentation)

6. 6th International Conference on Advanced Nanomaterials and Nanotechnology (ICANN2019) held at Indian Institute of Technology Guwahati, Assam, India December 18-21, 2019. (Poster Presentation)